

Head-Disk-Suspension Dynamics

by

Yong Hu

B.S. (Harbin Shipbuilding Engineering Institute, Harbin, China) 1983  
M.S. (Tsinghua University, Beijing, China) 1986

A dissertation submitted in partial satisfaction of the

requirements for the degree of

Doctor of Philosophy

in

Engineering-Mechanical Engineering

in the

GRADUATE DIVISION

of the

UNIVERSITY of CALIFORNIA at BERKELEY

Committee in charge:

Professor David B. Bogy, Chair  
Professor Panayiotis Papadopoulos  
Professor C. Keith Miller

1996

The dissertation of Yong Hu is approved:

Al Soygy Apr. 16, 1996  
Chair Date

P Papadopoulos April 16, 1996  
Date

Keith Miller April 15, 1996  
Date

University of California at Berkeley

1996

**Head-Disk-Suspension Dynamics**

© 1996

by

**Yong Hu**

## **ABSTRACT**

### **Head-Disk-Suspension Dynamics**

by

Yong Hu

Doctor of Philosophy in Engineering-Mechanical Engineering

University of California at Berkeley

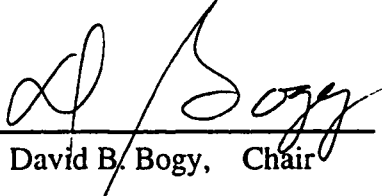
Professor David B. Bogy, Chair

This dissertation focuses on the development of a general purpose numerical simulation program for studying the dynamics of the head-disk-suspension assembly of magnetic hard disk drives. This program, called the CML Air Bearing Dynamic Simulator, employs an additive correction based multigrid control volume method, with superior efficiency, to solve the Reynolds equation, and it can simulate a variety of dynamic effects including partial contact, suspension dynamics and laser texture. Using the simulator we investigate a collection of dynamic head-disk interface problems.

The dynamic flying characteristics of three sub-25nm fly height sliders and a pseudo-contact tripad slider are studied. The results indicate that the spacing modulation induced by disk roughness decreases with an increase in air bearing stiffness and decrease in slider size. It is concluded that the extent of the roll motion and contact force modulation during track accessing and crash events strongly depends on the air bearing roll stiffness and the inertial force of the moving head. The contact force of tripad sliders increases with altitude and decreases after burnishing. The power spectral density plots of impulse responses indicate that the tripad slider's roll and vertical/pitch motions are decoupled. A mixed lubrication model is developed for investigating various air bearing

and other design parameter effects on a slider's take-off performance. The criterion for take-off from a disk is defined as a specified percent of the suspension preload. The slider's crown and disk surface roughness are the two important parameters affecting the take-off velocity. Larger crowns and smoother disk surfaces reduce the take-off velocity.

Several dynamic effects related to zone texturing are studied. The simulations of a slider flying across a transition zone show that the maximum slider/disk spacing reduction occurs at the outer rail trailing edge. The combination that produces the least spacing modulation is increased zone width, decreased zone height, and constant slope transition plane. The effects of the circumferentially ridged disk surfaces on a slider's flying characteristics are also studied. Adding the circumferential ridge surfaces increases the trailing edge fly height and decreases the pitch because of the reductions in the effective flow area and restrictions in side-flows. The rates of fly height and pitch change increase rapidly as the disk velocity decreases. The ridged disk surfaces increase the air bearing damping ratios more in the vertical and roll directions than the pitch direction through the enhancement of the viscous shearing across the circumferential ridges. The effects of laser bumps and laser textured disk surfaces on a slider's flying characteristics are also modeled. The moving laser texture generates moving stippled pressure peaks embedded on a smooth pressure profile. These moving pressure peaks increase the slider's trailing edge fly height and effect a constant magnitude fly height modulation. Flying the outer rail over the smooth data zone, while keeping the inner rail over the textured landing zone, decreases the fly height gain and fly height modulation, but increases the roll loss and roll modulation.

  
David B. Bogy, Chair

*To my parents,  
my wife and daughter*

# TABLE OF CONTENTS

<b>List of Figures</b> .....	ix
<b>List of Tables</b> .....	xvii
<b>Chapter 1 Introduction</b> .....	1
<b>Chapter 2 Solution of the Rarefied Gas Lubrication Equation Using An Additive Correction Based Multigrid Control Volume Method</b> .....	6
2.1 Introduction .....	6
2.2 Mathematical Formulation .....	11
2.2.1 Generalized Reynolds Equation .....	11
2.2.2 Control-Volume Formulation .....	13
2.2.3 Shaped Rail and Clearance Discontinuities .....	14
2.2.4 Convection and Diffusion .....	15
2.2.5 Unsteady Term .....	18
2.2.6 Discretization Equations .....	18
2.3 Solution Procedure .....	18
2.3.1 The Line-by-Line Method .....	18
2.3.2 Convergence Criterion .....	19
2.3.3 The Multigrid Method .....	20
2.4 Results and Discussions .....	23
2.4.1 Tripad Slider .....	23
2.4.2 Headway AAB Slider .....	25

2.5	Summary .....	25
	Appendix .....	27
<b>Chapter 3</b>	<b>The CML Air Bearing Dynamic Simulator .....</b>	<b>38</b>
3.1	Introduction .....	38
3.2	Numerical Models .....	39
3.2.1	Generalized Reynolds Equation .....	39
3.2.2	Dynamics of the Slider .....	40
3.2.3	Slider/Disk Contact Mechanics .....	41
3.2.4	Incorporation of Surface Roughness .....	43
3.2.5	Transition Zone Profile .....	44
3.3	Main Features .....	44
3.4	Summary .....	48
<b>Chapter 4</b>	<b>Dynamic Stability and Spacing Modulation of Sub-25nm</b>	
	<b>Fly Height Sliders .....</b>	<b>49</b>
4.1	Introduction .....	49
4.2	Numerical Simulation .....	51
4.3	Results and Discussions .....	52
4.3.1	Air Bearing Stiffness .....	52
4.3.2	Impulse Responses .....	53
4.3.3	Fly Height Modulation over a Supersmooth Disk .....	53
4.3.4	Bump Responses .....	54
4.3.5	Track Seeking Dynamics .....	55



4.4	Summary .....	57
<b>Chapter 5</b>	<b>Numerical Study of a Slider’s Contact Take-off Process .....</b>	<b>70</b>
5.1	Introduction .....	70
5.2	Mixed Lubrication Model .....	72
5.3	Results and Discussions .....	72
5.3.1	Effect of Slider Crown .....	74
5.3.2	Effect of Slider Camber .....	75
5.3.3	Effect of Slider Twist .....	75
5.3.4	Effect of Slider Taper Angle .....	75
5.3.5	Effect of Disk Surface Roughness .....	76
5.3.6	Effect of Head/Disk Interface Friction Coefficient .....	76
5.4	Summary .....	77
<b>Chapter 6</b>	<b>Spacing Modulation of a Slider Flying Across a Transition Between Landing and Data Zones .....</b>	<b>91</b>
6.1	Introduction .....	91
6.2	Numerical Simulation .....	93
6.3	Results and Discussions .....	93
6.3.1	Effect of Transition Zone Width .....	95
6.3.2	Effect of Transition Zone Height .....	95
6.3.3	Effect of Transition Zone Shape .....	96
6.4	Summary .....	96
<b>Chapter 7</b>	<b>Flying Characteristics of a Slider Over Textured</b>	

	<b>Surface Disks</b> .....	103
7.1	Introduction .....	103
7.2	Numerical Simulation .....	106
7.3	Results and Discussions .....	106
	7.3.1 Effect of the Ridge Height .....	110
	7.3.2 Effect of the Ridge Area Ratio .....	110
7.4	Summary .....	111
<b>Chapter 8</b>	<b>Dynamics of Tripad Slider Partial Contact Air Bearings</b> .....	127
8.1	Introduction .....	127
8.2	Numerical Models .....	128
8.3	Results and Discussions .....	129
	8.3.1 Fly Height, Pitch and Contact Force .....	130
	8.3.2 Partial Contact Air Bearing Stiffness .....	131
	8.3.3 Bump and Impulse Responses .....	131
	8.3.4 Fly Height Modulation over a Supersmooth Disk .....	133
	8.3.5 Track Seeking Dynamics .....	133
	8.3.6 Crash Stop Impact Performance .....	134
	8.3.7 Analysis of Accessing Across a Transition Between Landing and Data Zones .....	136
	8.3.8 Contact Take-off Simulation .....	137
8.4	Summary .....	138

<b>Chapter 9</b>	<b>Effects of Laser Textured Disk Surfaces on a Slider's Flying</b>	
	<b>Characteristics</b> .....	152
9.1	Introduction .....	152
9.2	Numerical Simulation .....	153
9.3	Results and Discussions .....	154
	9.3.1 Laser Bump Responses .....	155
	9.3.2 Effect of the Laser Textured Disk Surfaces .....	156
	9.3.3 Effect of Outer Rail Fly Condition .....	158
9.4	Summary .....	158
<b>Chapter 10</b>	<b>Conclusion</b> .....	171
<b>References</b>	.....	176

## LIST OF FIGURES

### Chapter 2

- Fig. 2.1 Schematic of the control volume
- Fig. 2.2 Schematic showing the assembly of control volumes on the fine grid into blocks (denoted by the hatched block) that defines the coarse grid
- Fig. 2.3 50% tripad slider air bearing surface
- Fig. 2.4 50% Headway AAB slider air bearing surface
- Fig. 2.5 3D non-dimensional air bearing pressure profile of the 50% tripad slider. The disk rotates at 5400 rpm. The nominal trailing edge center fly height, pitch and roll are 40 nm, 180  $\mu$ rad and 0 rad, respectively. The grid is 194 $\times$ 194
- Fig. 2.6 Comparison of the convergence rates between the multigrid and single-grid methods for the 50% tripad slider with the finest grids of 98 $\times$ 98 and the rotation speed of 5400 rpm
- Fig. 2.7 Comparison of the convergence rates between the multigrid and single-grid methods for the 50% tripad slider with the finest grids of 194 $\times$ 194 and the rotation speed of 5400 rpm
- Fig. 2.8 Comparison of the convergence rates between the multigrid and single-grid methods for the 50% tripad slider with the finest grids of 194 $\times$ 194 and the rotation speed of 2700 rpm
- Fig. 2.9 3D non-dimensional air bearing pressure profile of the 50% Headway AAB slider. The disk rotates at 5400 rpm. The nominal trailing edge center fly height, pitch and roll are 40 nm, 48.78  $\mu$ rad and 0 rad, respectively. The grid is 194 $\times$ 194
- Fig. 2.10 Comparison of the convergence rates between the multigrid and single-grid methods for the 50% Headway AAB slider with the finest grids of 98 $\times$ 98 and the rotation speed of 5400 rpm
- Fig. 2.11 Comparison of the convergence rates between the multigrid and single-grid methods for the 50% Headway AAB slider with the finest grids of 194 $\times$ 194 and the rotation speed of 5400 rpm
- Fig. 2.12 Comparison of the convergence rates between the multigrid and single-grid methods for the 50% Headway AAB slider with the finest grids of 194 $\times$ 194 and the rotation speed of 2700 rpm

### Chapter 4

- Fig. 4.1 Three sub-25 nm fly height slider designs
- Fig. 4.2 3D non-dimensional air bearing pressure profiles
- Fig. 4.3 Impulse responses. Initial vertical velocity = 10 mm/s for vertical impulse responses, initial pitch angular velocity = 20 rad/s for pitch impulse

- responses, initial roll angular velocity = 20 rad/s for roll impulse responses
- Fig. 4.4 Power spectral magnitude plots of vertical impulse responses. Initial vertical velocity = 10 mm/s, 50%/25nm design (solid line), 50%/15 nm design (dash line) and 30%/15 nm design (dash dot line)
- Fig. 4.5 Power spectral magnitude plots of pitch impulse responses. Initial pitch angular velocity = 20 rad/s, 50%/25nm design (solid line), 50%/15 nm design (dash line) and 30%/15 nm design (dash dot line)
- Fig. 4.6 Power spectral magnitude plots of roll impulse responses. Initial roll angular velocity = 20 rad/s, 50%/25nm design (solid line), 50%/15 nm design (dash line) and 30%/15 nm design (dash dot line)
- Fig. 4.7 Fly height modulation
- Fig. 4.8 Bump responses. Bump height = 10 nm, width = 25  $\mu$ m
- Fig. 4.9 FEM mesh of a HTI 1650E type suspension
- Fig. 4.10 FEM mesh of a HTI FX30U type suspension
- Fig. 4.11 Track seeking profile
- Fig. 4.12 Fly characteristics during a track seeking event. The dotted lines represent the steady state flying characteristics calculated using the effective skew angle and the relative disk velocity as seen from the head at the radius appropriate to the time shown
- Fig. 4.13 Pitch during a track seeking event for the 50%/25nm slider

## Chapter 5

- Fig. 5.1 Air bearing surface for the Nutcracker slider
- Fig. 5.2 FEM mesh of a Hutchinson 1650E type suspension
- Fig. 5.3 Flying characteristics during the contact start-up (up to the disk speed of 0.0018 m/s). Crown = 15 nm, camber = 10 nm, twist = 0, taper angle = 0.01 rad,  $\gamma = 0.2$  and  $\sigma = 3$  nm
- Fig. 5.4 Flying characteristics during the contact start-up (up to the disk speed of 0.072 m/s). Crown = 15 nm, camber = 10 nm, twist = 0, taper angle = 0.01 rad,  $\gamma = 0.2$  and  $\sigma = 3$  nm
- Fig. 5.5 Fly characteristics after the start-up. Crown = 15 nm, camber = 10 nm, twist = 0, taper angle = 0.01 rad,  $\gamma = 0.2$  and  $\sigma = 3$  nm
- Fig. 5.6 Take-off velocity versus crown. Camber = 10 nm, twist = 0, taper angle = 0.01 rad,  $\gamma = 0.2$  and  $\sigma = 3$  nm
- Fig. 5.7 Take-off fly height versus crown. Camber = 10 nm, twist = 0, taper angle = 0.01 rad,  $\gamma = 0.2$  and  $\sigma = 3$  nm
- Fig. 5.8 Fly height and pitch oscillations during the contact start-up for two crown heights. Crown = 0 (solid lines) and crown = 30 nm (dash lines)
- Fig. 5.9 Take-off velocity versus camber. Crown = 15 nm, twist = 0, taper angle = 0.01 rad,  $\gamma = 0.2$  and  $\sigma = 3$  nm

- Fig. 5.10 Take-off fly height versus camber. Crown = 15 nm, twist = 0, taper angle = 0.01 rad,  $\gamma = 0.2$  and  $\sigma = 3$  nm
- Fig. 5.11 Fly height and pitch oscillations during the contact start-up for two camber heights. Camber = 10 nm (solid lines) and camber = 20 nm (dash lines)
- Fig. 5.12 Take-off velocity versus twist. Crown = 15 nm, camber = 10 nm, taper angle = 0.01 rad,  $\gamma = 0.2$  and  $\sigma = 3$  nm
- Fig. 5.13 Take-off fly height versus twist. Crown = 15 nm, camber = 10 nm, taper angle = 0.01 rad,  $\gamma = 0.2$  and  $\sigma = 3$  nm
- Fig. 5.14 Fly height and pitch oscillations during the contact start-up for two twist values. Twist = 0 (solid lines) and twist = 5 nm (dash lines)
- Fig. 5.15 Take-off velocity versus taper angle. Crown = 15 nm, camber = 10 nm, twist = 0,  $\gamma = 0.2$  and  $\sigma = 3$  nm
- Fig. 5.16 Take-off fly height versus taper angle. Crown = 15 nm, camber = 10 nm, twist = 0,  $\gamma = 0.2$  and  $\sigma = 3$  nm
- Fig. 5.17 Fly height and pitch oscillations during the contact start-up for two taper angles. Taper angle = 0.01 rad (solid lines) and taper angle = 0.02 rad (dash lines)
- Fig. 5.18 Take-off velocity versus the standard deviation of surface roughness. Crown = 15 nm, camber = 10 nm, twist = 0, taper angle = 0.01 rad and  $\gamma = 0.2$
- Fig. 5.19 Take-off fly height versus the standard deviation of surface roughness. Crown = 15 nm, camber = 10 nm, twist = 0, taper angle = 0.01 rad and  $\gamma = 0.2$
- Fig. 5.20 Fly height and pitch oscillations during the contact start-up for two  $\sigma$  values.  $\sigma = 3$  nm (solid lines) and  $\sigma = 6$  nm (dash lines)
- Fig. 5.21 Take-off velocity versus friction coefficient. Crown = 15 nm, camber = 10 nm, twist = 0, taper angle = 0.01 rad and  $\sigma = 3$  nm
- Fig. 5.22 Take-off fly height versus friction coefficient. Crown = 15 nm, camber = 10 nm, twist = 0, taper angle = 0.01 rad and  $\sigma = 3$  nm
- Fig. 5.23 Fly height and pitch oscillations during the contact start-up for two friction coefficients.  $\gamma = 0.2$  (solid lines) and  $\gamma = 0.5$  (dash lines)

## Chapter 6

- Fig. 6.1 Air bearing surface for the Nutcracker slider
- Fig. 6.2 3D non-dimensional air bearing pressure profile
- Fig. 6.3 FEM mesh of a Hutchinson 1650E type suspension
- Fig. 6.4 Accessing profile
- Fig. 6.5 Flying characteristics of a slider flying across a transition zone. The transition zone is a constant slope plane with a height of 20 nm and a width of 0.4 mm

- Fig. 6.6 IRTE and ORTE fly heights of a slider flying across a transition zone. The transition zone is a constant slope plane with a height of 20 nm and a width of 0.4 mm
- Fig. 6.7 The contributions of a transition zone to the fly characteristics. The transition zone is a constant slope plane with a height of 20 nm and a width of 0.4 mm
- Fig. 6.8 The effect of the zone width on the transition zone induced ORTE spacing modulation. width = 0 (solid lines), 0.2 mm (dash lines) and 0.4 mm (dash dotted lines)
- Fig. 6.9 The effect of the zone height on the transition zone induced ORTE spacing modulation. height = 20 nm (solid lines), 30 nm (dash lines) and 40 nm (dash dotted lines)
- Fig. 6.10 The effect of the zone shape on the transition zone induced ORTE spacing modulation. The height of middle point = 10 nm(solid lines), 5 nm(dash lines) and 15 nm (dash dotted lines)

## Chapter 7

- Fig. 7.1 The circumferential ridge disk surface
- Fig. 7.2 A schematic of two mechanisms of the texture effects: side-flow restriction and reduced flow area
- Fig. 7.3 Air bearing surface of the taper-flat slider
- Fig. 7.4 Fly height increase versus the disk velocity for three circumferential ridge disk surfaces
- Fig. 7.5 Pitch decrease versus the disk velocity for three circumferential ridge disk surfaces
- Fig. 7.6 Dimensionless 3-D air bearing pressure profile beneath the inner rail for the smooth disk surface. The disk velocity is 2 m/s
- Fig. 7.7 Dimensionless 3-D air bearing pressure profile beneath the inner rail for the circumferential ridge disk surface with a ridge height of 20 nm and a ridge area ratio of 25%. The disk velocity is 2 m/s
- Fig. 7.8 Dimensionless 3-D air bearing pressure profile beneath the inner rail for the circumferential ridge disk surface with a ridge height of 40 nm and a ridge area ratio of 25%. The disk velocity is 2 m/s
- Fig. 7.9 Dimensionless 3-D air bearing pressure profile beneath the inner rail for the circumferential ridge disk surface with a ridge height of 40 nm and a ridge area ratio of 50%. The disk velocity is 2 m/s
- Fig. 7.10 Vertical, pitch and roll impulse responses at the disk velocity of 10 m/s. Initial vertical velocity = 2 mm/s for vertical impulse response, initial pitch angular velocity = 2 rad/s for pitch impulse response, initial roll angular velocity = 4 rad/s for roll impulse response
- Fig. 7.11 Power spectral magnitude plots of the vertical impulse responses at the disk velocity of 10 m/s. Initial vertical velocity = 2 mm/s, smooth surface (solid line), ridge area ratio = 25%, height = 40 nm (dash dot line)

- Fig. 7.12 Power spectral magnitude plots of the pitch impulse responses at the disk velocity of 10 m/s. Initial pitch angular velocity = 2 rad/s, smooth surface (solid line), ridge area ratio = 25%, height = 40 nm (dash dot line)
- Fig. 7.13 Power spectral magnitude plots of the roll impulse responses at the disk velocity of 10 m/s. Initial roll angular velocity = 4 rad/s, smooth surface (solid line), ridge area ratio = 25%, height = 40 nm (dash dot line)
- Fig. 7.14 Vertical, pitch and roll impulse responses at the disk velocity of 2 m/s. Initial vertical velocity = 2 mm/s for vertical impulse response, initial pitch angular velocity = 2 rad/s for pitch impulse response, initial roll angular velocity = 4 rad/s for roll impulse response
- Fig. 7.15 Power spectral magnitude plots of the vertical impulse responses at the disk velocity of 2 m/s. Initial vertical velocity = 2 mm/s, smooth surface (solid line), ridge area ratio = 25%, height = 20 nm (dash line), ridge area ratio = 25%, height = 40 nm (dash dot line)
- Fig. 7.16 Power spectral magnitude plots of the pitch impulse responses at the disk velocity of 2 m/s. Initial pitch angular velocity = 2 rad/s, smooth surface (solid line), ridge area ratio = 25%, height = 20 nm (dash line), ridge area ratio = 25%, height = 40 nm (dash dot line)
- Fig. 7.17 Power spectral magnitude plots of the roll impulse responses at the disk velocity of 2 m/s. Initial roll angular velocity = 4 rad/s, smooth surface (solid line), ridge area ratio = 25%, height = 20 nm (dash line), ridge area ratio = 25%, height = 40 nm (dash dot line)
- Fig. 7.18 Effects of the ridge height on the fly height increase for two disk velocities of 5 and 10 m/s. The ridge area ratio is 25%
- Fig. 7.19 Effects of the ridge height on the pitch decrease for two disk velocities of 5 and 10 m/s. The ridge area ratio is 25%
- Fig. 7.20 Effects of the ridge area ratio on the fly height increase for two disk velocities of 5 and 10 m/s. The ridge height is 20 nm
- Fig. 7.21 Effects of the ridge area ratio on the pitch decrease for two disk velocities of 5 and 10 m/s. The ridge height is 20 nm
- Fig. 7.22 Vertical, pitch and roll impulse responses at the disk velocity of 2 m/s. Initial vertical velocity = 2 mm/s for the vertical impulse response, initial pitch angular velocity = 2 rad/s for the pitch impulse response, initial roll angular velocity = 4 rad/s for the roll impulse response
- Fig. 7.23 Power spectral magnitude plots of the vertical impulse responses at the disk velocity of 2 m/s. Initial vertical velocity = 2 mm/s, ridge area ratio = 25%, height = 40 nm (solid line), ridge area ratio = 50%, height = 40 nm (dash line)
- Fig. 7.24 Power spectral magnitude plots of the pitch impulse responses at the disk velocity of 2 m/s. Initial pitch angular velocity = 2 rad/s, ridge area ratio = 25%, height = 40 nm (solid line), ridge area ratio = 50%, height = 40 nm (dash line)
- Fig. 7.25 Power spectral magnitude plots of the roll impulse responses at the disk velocity of 2 m/s. Initial roll angular velocity = 4 rad/s, ridge area



ratio = 25%, height = 40 nm (solid line), ridge area ratio = 50%, height = 40 nm (dash line)

## Chapter 8

- Fig. 8.1 Tripad slider air bearing surface
- Fig. 8.2 FEM mesh of a Hutchinson 850AK type suspension
- Fig. 8.3 3D non-dimensional air bearing pressure profile. Radial position = 20.73 mm,  $\sigma = 6$  nm, glide height = 25 nm and altitude = 0
- Fig. 8.4 3D non-dimensional contact pressure profile. Radial position = 20.73 mm,  $\sigma = 6$  nm, glide height = 25 nm and altitude = 0
- Fig. 8.5 Bump response. Bump height = 30 nm, width = 25  $\mu$ m,  $\sigma = 6$  nm, glide height = 25 nm, radial position = 20.73 mm and altitude = 0
- Fig. 8.6 Vertical, pitch and roll impulse responses and their corresponding power spectral density plots. Initial vertical velocity = 2 mm/s, initial pitch and roll angular velocities = 2 rad/s, radial position = 20.73 mm,  $\sigma = 6$  nm, glide height = 25 nm, altitude = 0
- Fig. 8.7 Fly height, roll and contact force modulations. Radial position = 20.73 mm and altitude = 0
- Fig. 8.8 Track seeking profile
- Fig. 8.9 Roll motion during track seeking.  $\sigma = 6$  nm, glide height = 25 nm and altitude = 0
- Fig. 8.10 Fly height during track seeking.  $\sigma = 6$  nm, glide height = 25 nm and altitude = 0
- Fig. 8.11 Contact force during track seeking.  $\sigma = 6$  nm, glide height = 25 nm and altitude = 0
- Fig. 8.12 Deceleration and velocity profiles for the two crash stop processes
- Fig. 8.13 Roll motions during the two crash stop processes.  $\sigma = 6$  nm, glide height = 25 nm and altitude = 0. Maximum deceleration = 800G (solid line), 500G (dash line)
- Fig. 8.14 Pitch motions during the two crash stop processes.  $\sigma = 6$  nm, glide height = 25 nm and altitude = 0. Maximum deceleration = 800G (solid line), 500G (dash line)
- Fig. 8.15 Fly heights at the rear pad during the two crash stop processes.  $\sigma = 6$  nm, glide height = 25 nm and altitude = 0. Maximum deceleration = 800G (solid line), 500G (dash line)
- Fig. 8.16 Fly heights of back center point of the outer rail during the two crash stop processes.  $\sigma = 6$  nm, glide height = 25 nm and altitude = 0. Maximum deceleration = 800G (solid line), 500G (dash line)
- Fig. 8.17 Contact forces during the two crash stop processes.  $\sigma = 6$  nm, glide height = 25 nm and altitude = 0. Maximum deceleration = 800G (solid line), 500G (dash line)

- Fig. 8.18 Fly height and contact force during accessing across a transition zone.  $\sigma = 6$  nm, glide height = 25 nm and altitude = 0
- Fig. 8.19 Flying characteristics during the contact start-up (up to the disk speed of 0.072 m/s).  $\sigma = 6$  nm, radial position = 20.73 mm, glide height = 25 nm and altitude = 0
- Fig. 8.20 Flying characteristics during the early moments of the contact start-up (up to the disk speed of 0.00097717 m/s).  $\sigma = 6$  nm, radial position = 20.73 mm, glide height = 25 nm and altitude = 0

## Chapter 9

- Fig. 9.1 50% Headway AAB slider air bearing surface
- Fig. 9.2 Headway AAB slider's 3D non-dimensional air bearing pressure profile for smooth disk surface
- Fig. 9.2 Headway AAB slider's 3D non-dimensional air bearing pressure profile for smooth disk surface
- Fig. 9.4 A 3D representation of "Sombrero" type laser bump. Center height = 30 nm, rim height = 20 nm and rim diameter = 40  $\mu\text{m}$
- Fig. 9.5 A 3D representation of ridge type laser bump. Rim height = 20 nm and rim diameter = 40  $\mu\text{m}$
- Fig. 9.6 Bump response versus laser bump type. Center height = 30 nm ("Sombrero" type), rim diameter = 40  $\mu\text{m}$  and rim height = 20 nm
- Fig. 9.7 Bump response versus center height. "Sombrero" type laser bump, rim height = 20 nm and rim diameter = 40  $\mu\text{m}$
- Fig. 9.8 Bump response versus rim diameter. "Sombrero" type laser bump, center height = 30 nm and rim height = 20 nm
- Fig. 9.9 Contact bump response. "Sombrero" type laser bump with center height = 50 nm, rim diameter = 40  $\mu\text{m}$  and rim height = 20 nm
- Fig. 9.10 A 3D representation of "Sombrero" type laser texture. Bump spacing = 100 $\times$ 50  $\mu\text{m}$ , center height = 30 nm, rim height = 20 nm and rim diameter = 40  $\mu\text{m}$
- Fig. 9.11 A 3D representation of ridge type laser texture. Bump spacing = 100 $\times$ 50  $\mu\text{m}$ , rim height = 20 nm and rim diameter = 40  $\mu\text{m}$
- Fig. 9.12 Slider's fly height settling history over a laser textured ("Sombrero" type) disk surface. Bump spacing = 100 $\times$ 50  $\mu\text{m}$ , center height = 30 nm, rim height = 15 nm and rim diameter = 40  $\mu\text{m}$
- Fig. 9.13 3D non-dimensional air bearing pressure profile beneath the inner rail. "Sombrero" type laser texture, bump spacing = 100 $\times$ 50  $\mu\text{m}$ , center height = 30 nm, rim height = 15 nm and rim diameter = 40  $\mu\text{m}$
- Fig. 9.14 2D non-dimensional air bearing pressure contour. "Sombrero" type laser texture, bump spacing = 100 $\times$ 50  $\mu\text{m}$ , center height = 30 nm, rim height = 15 nm and rim diameter = 40  $\mu\text{m}$

- Fig. 9.15 2D non-dimensional air bearing pressure contour. ridge type laser texture, bump spacing =  $100 \times 50 \mu\text{m}$ , rim height = 15 nm and rim diameter =  $40 \mu\text{m}$
- Fig. 9.16 2D non-dimensional air bearing pressure contour. "Sombrero" type laser texture, bump spacing =  $200 \times 100 \mu\text{m}$ , center height = 30 nm, rim height = 15 nm and rim diameter =  $40 \mu\text{m}$
- Fig. 9.17 2D non-dimensional air bearing pressure contour. "Sombrero" type laser texture, bump spacing =  $100 \times 50 \mu\text{m}$ , center height = 20 nm, rim height = 15 nm and rim diameter =  $40 \mu\text{m}$
- Fig. 9.18 2D non-dimensional air bearing pressure contour. "Sombrero" type laser texture, bump spacing =  $100 \times 50 \mu\text{m}$ , center height = 30 nm, rim height = 15 nm and rim diameter =  $20 \mu\text{m}$
- Fig. 9.19 2D non-dimensional air bearing pressure contour with inner rail flying over the textured landing zone and outer rail flying over the smooth data zone. "Sombrero" type laser texture, bump spacing =  $100 \times 50 \mu\text{m}$ , center height = 30 nm, rim height = 15 nm and rim diameter =  $40 \mu\text{m}$

## LIST OF TABLES

### Chapter 2

- Table 2.1 Comparison of DEC ALPHA 3000/800 CPU time between the multigrid and single-grid methods for the 50% tripod slider
- Table 2.2 Comparison of DEC ALPHA 3000/800 CPU time between the multigrid and single-grid methods for the 50% Headway AAB slider

### Chapter 4

- Table 4.1 Air bearing stiffness
- Table 4.2 Air bearing forces: lifting force, suction force and net force
- Table 4.3 Summary of fly height modulation
- Table 4.4 Minimum spacing and maximum bump height for the slider to fly over without contact

### Chapter 8

- Table 8.1 Fly height, pitch and contact force versus radial positions.  $\sigma = 6$  nm, glide height = 25 nm and altitude = 0
- Table 8.2 Fly height, pitch and contact force versus roughness. Radial position = 20.73 mm and altitude = 0
- Table 8.3 Fly height, pitch and contact force versus glide height.  $\sigma = 6$  nm, radial position = 20.73 mm and altitude = 0
- Table 8.4 Fly height, pitch and contact force versus altitude.  $\sigma = 6$  nm, glide height = 25 nm and radial position = 20.73 mm
- Table 8.5 Partial contact air bearing stiffnesses versus radial positions.  $\sigma = 6$  nm, altitude = 0 and glide height = 25 nm
- Table 8.6 Partial contact air bearing stiffnesses versus roughness. Altitude = 0 and radial position = 20.73 mm
- Table 8.7 Partial contact air bearing stiffnesses versus glide height.  $\sigma = 6$  nm, altitude = 0 and radial position = 20.73 mm
- Table 8.8 Partial contact air bearing stiffnesses versus altitude.  $\sigma = 6$  nm, radial position = 20.73 mm and glide height = 25 nm
- Table 8.9 Partial contact air bearing resonant frequencies versus radial positions.  $\sigma = 6$  nm, altitude = 0 and glide height = 25 nm
- Table 8.10 Partial contact air bearing resonant frequencies versus roughness. Altitude = 0 and radial position = 20.73 mm
- Table 8.11 Partial contact air bearing resonant frequencies versus altitude.  $\sigma = 6$  nm, glide height = 25 nm and radial position = 20.73 mm

Table 8.12 Partial contact air bearing resonant frequencies versus glide height.  $\sigma = 6$  nm, altitude = 0 and radial position = 20.73 mm

Table 8.13 Summary of the fly height, roll and contact force modulations

## Chapter 9

Table 9.1 Fly height increase and modulation versus laser texture type. Bump spacing =  $100 \times 50 \mu\text{m}$ , rim height = 15 nm, rim diameter =  $40 \mu\text{m}$  and center height = 30 nm (“Sombrero” type)

Table 9.2 Fly height increase and modulation versus laser bump spacing. “Sombrero” type, center height = 30 nm, rim height = 15 nm and rim diameter =  $40 \mu\text{m}$

Table 9.3 Fly height increase and modulation versus laser bump center height. “Sombrero” type, bump spacing =  $100 \times 50 \mu\text{m}$ , rim height = 15 nm and rim diameter =  $40 \mu\text{m}$

Table 9.4 Fly height increase and modulation versus rim diameter. “Sombrero” type, bump spacing =  $100 \times 50 \mu\text{m}$ , rim height = 20 nm and center height = 30 nm

Table 9.5 Fly height increase, roll decrease and their modulations versus outer rail flying condition. Inner rail flies over the laser textured landing zone, “Sombrero” type, bump spacing =  $100 \times 50 \mu\text{m}$ , rim height = 20 nm and center height = 30 nm

## Acknowledgments

I would like to express my sincere gratitude to my advisor, Professor David B. Bogy, for his continuous guidance and support throughout my career at Berkeley. I would also like to thank Professors Panayiotis Papadopoulos and C. Keith Miller for reviewing this manuscript. This research was supported by the Computer Mechanics Laboratory at the University of California at Berkeley. Portions were also supported by the National Storage Industry Consortium (NSIC).

I am indebted to Ryan Jurgenson, Jim Mahoney and Roger Resh of Hutchinson Technology, for providing the FEM meshes of various suspensions that I needed in order to carry out my work. Thanks also go to Dr. Brian Strom of Seagate Technology, for supplying zone texture/transition zone parameters. Over the years, I received much helpful feedback regarding the CML Air Bearing Dynamic Simulator from Dr. Ciuter Chang and Dr. Mark Donovan of Read-Rite Corporation, Peter Griffin of Quantum Corporation. I appreciate their aid.

I want to thank my colleagues at the Computer Mechanics Laboratory for their friendship and support. In particular, I am thankful to Matthew A. O'Hara for many enjoyable conversations and kind help. I also appreciate the valuable discussions that I had with Sha Lu concerning the implementation of the multigrid control volume method. I would also like to acknowledge these two colleagues as the complement of the "three-headed dragon".

Any acknowledgment would not be complete without mentioning my family. My parents teach me the value of education and give me endless support. My deepest appreciation belongs to my wife, Jianping, for her love, patience and comfort. Finally, I would like to thank my daughter, Bonnie, for her love and for giving me something to look forward to every day.

# CHAPTER 1

## INTRODUCTION

The ever growing technological and economical importance of massive data recording in today's information era demands inexpensive, highly reliable, quickly accessible and high-density data storage systems. This has been made possible, in part, by the invention of the magnetic hard disk drives. Since their introduction in 1957, magnetic hard disk drives have become the predominant form for the storage of digital information. Magnetic recording is accomplished by the relative motion between a magnetic medium and a magnetic recording head. Over the past three decades, the disk drive industry has posted unprecedented growth in capacity and performance. The magnetic hard disk drive has shrunk from early, bulky refrigerator sized units to the current battery powered units that can fit into a shirt pocket (Harker *et al.*, 1981), with wristwatch sized drives being part of a cellular video phone predicted sometime early in the next century. Areal densities meanwhile increase from the order of 5 Kb/in<sup>2</sup> in 1960 to 1 Gb/in<sup>2</sup> in current state-of-the-art production drives, with 10 Gb/in<sup>2</sup> drives projected in just ten years.

In magnetic hard disk drives, one or more magnetic media hard disks are mounted on a spindle that rotates at high speed. The read/write transducers are attached to sliders which are loaded onto the disk surface by a spring suspension. The air flow between the slider and spinning disk generates a hydrodynamic air bearing which provides a small spacing between the head and disk. Each suspension is attached to an arm. The arms are

then fixed together to form a head stack assembly. This assembly is driven by an electromagnetic actuator that can position the heads at any track on the disk surface.

Throughout the history of hard disk magnetic recording, most evolutionary advances achieved from a mechanical engineering perspective have begun with the supposition that higher storage density implies lower spacing between the read/write head and the disk (Wallace, 1951). Mechanical engineers have responded by lowering this spacing approximately two orders of magnitude over the past 40 years, and now are beginning to view with anxious anticipation the contact recording which represents the ultimate in head-disk spacing, namely zero. The rapid decrease in head-disk spacing and progressive miniaturization, along with the growing portable and field applications of disk drives are making the drive's performance more and more sensitive to the head/disk interface dynamics. Therefore, a detailed understanding of the head-disk-suspension dynamics is critical in determining drive performance and achieving long term reliability.

Numerical simulation has been a powerful and versatile tool for the study of the head-disk-suspension dynamics. The simulation enables us to investigate those more complicated dynamic problems in the disk drive than would otherwise be currently feasible by experimental means. It offers a fast and accurate prediction of the dynamic flying characteristics of the different head/disk interface designs. It also provides the flexibility needed for examining effects of large number of drive design parameters. Indeed, a well-tested numerical code can greatly facilitate the design of the reliable head/disk interface and reduce the development cost.

The primary goal of this dissertation is to develop an air bearing dynamic



simulator that can simulate almost every dynamic effect associated with today's head/disk interface. Using this simulator, we investigate a collection of head-disk-suspension dynamic problems to better understand the dynamic behavior of the head/disk interface in a hard disk drive. The main results are summarized in this dissertation.

In Chapter 2, the generalized Reynolds equation that governs the air bearing pressure distribution between the slider and the disk is presented, and a brief overview of numerical methods used for solving this equation is given. An additive correction based multigrid control volume method is developed for the solution of the very high bearing number and shaped rail air bearing problems associated with high speed and ultra-low head/disk spacing in current magnetic hard disk drives. The control volume schemes for discretizing the Reynolds lubrication equation are based on convection-diffusion formulations including the central difference, upwind, hybrid, power-law and exponential schemes. The comparison study using the 50% tripad and Headway AAB sliders\* demonstrates the solver's performance improvements by a factor ranging from 3.9 to 39.7 depending on the slider type, grid number and bearing number as compared to the single-grid method. Chapter 3 describes the CML Air Bearing Dynamic Simulator that employs the solver developed in Chapter 2. The code is developed for analyzing the head-suspension assembly dynamics for arbitrarily shaped-rail sliders with multiple recess levels including wall profile and edge blend. In addition, the simulator's main features including partial contact, suspension dynamics and laser texture are briefly discussed.

A variety of head-disk-suspension dynamic problems are studied using the CML

---

\* Note that it is common in the disk drive industry to refer to sliders with lateral dimensions of 4 mm by 3.2 mm as 100% sliders. Smaller sliders with dimensions of 70%, 50% and 30% are now commonly used.

Air Bearing Dynamic Simulator, and their results are presented in Chapters 4 to 9. In Chapter 4, the dynamic flying characteristics of three shaped-rail negative pressure sub-25 nm fly height sliders are investigated. The transient fly height histories over a “supersmooth” disk are simulated by directly incorporating a measured disk track profile into the simulator. The sliders’ responses to passing bumps are correlated with their air bearing stiffness and damping characteristics. The head seeking dynamics are also simulated by integrating the suspension dynamics into the air bearing simulator. Mechanical durability of the contact start/stop (CSS) is an important issue to a successful drive design. Chapter 5 presents a newly developed mixed lubrication model for characterizing CSS performance. We use a pre-defined percent of the suspension load as a criterion to determine a slider’s take-off from a disk. The effects of the air bearing and other design parameters on the slider’s take-off velocity, fly height and other initial flying characteristics are investigated using this model. The zone texturing/transition zone is a very good alternative to the conventional CSS because it effectively decouples disk magnetics from tribological issues. In Chapter 6, we study the spacing modulation of a sub-25 nm fly height slider flying across a transition zone, and the effects of the transition zone height, width and shape on transition zone induced spacing modulation are discussed. Besides meeting the required tribological properties, disk surface texturing must possess the favorable effects on the head/disk interface dynamics. Chapter 7 investigates the effects of well-defined surface texture on the slider’s flying characteristics in conjunction with the experimental work done by Tanaka and Bogy (1994). The texture effect mechanisms on the steady state fly height and slider’s air

bearing damping characteristics are examined. Partial contact recording is currently being pursued by the hard disk drive industry. Conceptually, partial contact recording occurs in the region where the suspension load is supported by both the slider's air bearing and head/disk contact. One of the partial contact slider designs is the so-called tripad pseudo-contact slider. Chapter 8 is dedicated to the investigation of the dynamics of tripad slider partial contact air bearings. In this study, the Greenwood-Williamson asperity-based contact model (1966) is employed to model the slider/disk contact. Recently, laser texturing has captured the attention of head/media interface engineers because it provides precision in the landing zone placement while eliminating the transition zone of a mechanically textured landing zone. It also offers excellent tribological performance in terms of low CSS stiction and good durability. These advantages make it the solution of choice for high-end disk drives. Chapter 9 models the effects of laser bumps and laser textured disk surfaces on Headway AAB slider's flying characteristics. Two commonly used laser bump profiles ("Sombrero" and ridge types) and various texture patterns are numerically generated in the simulator. The effects of bump shape on the slider's bump responses are studied. The slider's flying dynamics over the laser textured disk surface are simulated. The laser texture effect mechanism is explained using the local air bearing pressure profiles induced by the moving laser bumps. The slider's flying characteristics with one rail over the laser textured landing zone and another rail over the smooth data zone are also simulated.

Finally, Chapter 10 summarizes the conclusions of this study.

## CHAPTER 2

# SOLUTION OF THE RAREFIED GAS LUBRICATION EQUATION USING AN ADDITIVE CORRECTION BASED MULTIGRID CONTROL VOLUME METHOD

### 2.1 Introduction

The application of numerical methods to solve high speed, low spacing gas-lubricated slider bearing problems has received considerable attention in the past three decades. An early excellent review paper was presented by Castelli and Pirvics (1963). Since that time, the spacing between the head and disk in magnetic hard disk drives has consistently decreased in order to meet the continual demand for higher data storage density. The flying height reduction in new designs has recently accelerated and the head/disk interface is quickly approaching the near-contact condition. The challenge of decreasing the fly height while improving reliability requires a departure from typical straight rail air bearing designs. It has been demonstrated that shaped rail sub-ambient pressure slides exhibit high air bearing stiffness and fast take-off characteristics (Kogure, *et al.*, 1983; White, 1983; Yoneoka, *et al.*, 1987). Both of them improve reliability. In addition, by designing the sub-ambient pressure region properly it is possible to achieve a constant flying height across the entire radius of the disk. With improvements in ion-beam etching techniques, arbitrary air bearing surface shapes can now be manufactured. This has amplified the numerical problems that were identified with the early straight rail designs.

The differential equation governing the pressure distribution in the lubricating gas

film that separates the slider and disk is known as the compressible Reynolds equation (Gross, *et al.*, 1980). To account for the rarefaction of the air at ultra-low spacing, the classical Reynolds equation is generalized by introducing molecular slip modifications. The Reynolds equation can be derived directly from the principle of mass conservation that demands that the rate at which mass accumulates in the control volume must be equal to the difference between the rates at which mass enters and leaves. There are two types of flows, the Poiseuille flow terms describe the net flow rates due to pressure gradients within the lubricated area, while the Couette flow terms represent the net entraining flow rates due to relative surface velocities. For the high bearing numbers associated with high speed and ultra-low head/disk spacing, the Poiseuille flow is minor compared to the Couette flow. In the differential form of the mass flow rate, the generalized Reynolds equation can be interpreted as a convection-(nonlinear) diffusion transport problem. The physical quantity, pressure times spacing, (PH) is convected by the sliding surface with the non-dimensional velocity (bearing number). In high bearing number flows the convective terms dominate the diffusive terms.

The solution methods normally applied to the generalized Reynolds equation with a large bearing number require very high spatial resolution in the pressure boundary layer to prevent numerical instabilities. The use of a variable spatial grid in the boundary layer decreases the local Peclet number ( $P_e$ ), where  $P_e$  can be viewed as the ratio of the strength of convection to diffusion, and therefore reduces the convective dominant condition. White and Nigam (1981) demonstrated that a variable mesh size could be used to resolve the steep pressure gradient regions if a logical geometric progression in grid size is

employed. Although it is, in principle, possible to refine the grid until the Peclet number is small enough for the central-difference scheme to yield reasonable solutions, in most practical problems, however, this strategy requires excessively fine grids, and therefore it is not feasible on economic grounds. In any case, in order to face the challenge of numerical analysis of today's high speed ultra-thin air bearings, different schemes must be sought that can give physically realistic solutions.

Air bearing pressure calculations of shaped-rail sliders at very high bearing number require the solution of the rarefied gas lubrication equation on a large number of grid points in the computational domain. The currently popular iterative methods performed on a single-grid system show strong convergence when a small number of grid points are involved, but when the number of grid points increases the convergence deteriorates. Consequently, the computational cost and time requirements become enormous and make the solutions on such fine grids unattractive and in many cases impractical. In order to reduce this difficulty associated with the single-grid solution procedure, the multigrid technique has been identified as a very powerful means for improving the convergence rate of iterative methods.

One of the factors affecting the convergence of a scheme is the ability to smooth out errors of all frequencies in the solution. With conventional iterative methods such as the line-by-line method, rapid convergence can be obtained only during the first few iterations. By considering a Fourier analysis of the error reduction process of typical relaxation procedures, Brandt (1977) showed that they are only efficient in smoothing out those error components whose wavelengths are comparable to the mesh size; error

components with longer wavelengths are removed at progressively slower rates. The motivation for the multigrid methods is to solve the equations on a hierarchy of grids so that all frequency components of the error are reduced at comparable rates. Inexpensive iteration on the coarse grid rapidly diminishes exactly those components of the error that are so difficult and expensive to reduce by fine grid iteration alone.

The superior performance of the multigrid methods over the single-grid methods has been demonstrated for a variety of cases by Brandt (1977) and Vanka (1986). There are two main approaches in the application of the multigrid methods. The first approach, designed (Brandt, 1977) for the nonlinear problems, is called the FAS (Full Approximation Storage) method. The method primarily involves computation and storage of all the discretization coefficients and solutions at every level. The solutions are then interpolated (restricted) or extrapolated (prolongated) depending on the cycle stage of whether the procedure is switching to a coarser grid or from a coarser grid.

In the second approach, the discretization equation coefficients are computed only on the finest grid and the coefficients for the coarser grids are obtained by appropriately combining the fine grid coefficients. The solution on a particular grid level are corrections to the next finer grid level and simply added to them when the residuals are below an acceptable level. Thus, this method does not involve any interpolation or extrapolation. This approach was first suggested by Settari and Aziz (1973) and employed by Patankar (1981) to accelerate the convergence of the line-by-line iteration method for the solution of nominally linear equations. A multigrid method based on the additive correction strategy was proposed by Hutchinson *et al.* (1986, 1988).

Considerable research has been conducted on the numerical solution of air bearing slider problems in the Computer Mechanics Laboratory over the past decade. Using work based in fluid flow and heat/mass transfer phenomena, Garcia-Suarez *et al.* (1984) proposed an upwind finite element scheme for air bearing simulation. Miu and Bogoy (1986b) implemented the factored implicit scheme of White and Nigam (1980) for the numerical simulation of taper-flat sliders. Ruiz and Bogoy (1990a) made several improvements to Miu and Bogoy's work. They implemented the second order slip and the Fukui and Kaneko (1988) modification to the classical Reynolds equation. More recently, Cha and Bogoy (1995) developed a finite difference scheme to solve the generalized lubrication equation using the factored implicit scheme for irregular rail geometry. The method is based on a control volume formulation of the linearized Reynolds equation. The power-law scheme is implemented in calculating the mass flows. The resulting equation is solved using the alternating direction implicit method.

In this chapter, control volume schemes based on convection-diffusion formulations are developed for the numerical air bearing analysis of shaped-rail sub-ambient pressure sliders at high speed and ultra-low spacing. These schemes use the original nonlinear governing equation. The discretization equation is derived by representing the total flux (convection and diffusion) at the control volume interfaces using the different convection-diffusion formulations which include the central difference, upwind, hybrid, power-law and exponential schemes. By doing so, the four rules (consistency at control-volume faces, positive coefficients, negative-slope linearization of the source term and sum of the neighboring coefficients), which constitute the underlying guiding principles for a



physically realistic solution (Patankar, 1980), are guaranteed to be satisfied (except when using the central difference). An additive correction based multigrid method is implemented for the solution of the resulting discretization equations. The present multigrid formulation follows the approach proposed by Hutchinson *et al.* (1986, 1988) with a few minor modifications and uses the line-by-line solver as the base solver at all grid levels. To smooth out the errors of the lowest frequency, the block-correction procedure is used once followed the iterations at the finest level. The multigrid method is applied to the 50% tripad slider and Headway advanced air bearing (AAB) slider. The convergence rates of the present calculations are compared with those of the single-grid calculations for two bearing numbers and two sets of grid numbers, measured by the number of fine grid iteration and the total CPU time.

## 2.2 Mathematical Formulation

**2.2.1 Generalized Reynolds Equation.** The compressible Reynolds equation, which governs the pressure distribution between the slider and the disk can be written as

$$\frac{\partial}{\partial x} \left[ ph^3 \frac{\partial p}{\partial x} \right] + \frac{\partial}{\partial y} \left[ ph^3 \frac{\partial p}{\partial y} \right] = 6U\mu \frac{\partial}{\partial x} [ph] + 6V\mu \frac{\partial}{\partial y} [ph] + 12\mu \frac{\partial}{\partial t} [ph] \quad (2.1)$$

where  $p$  is pressure,  $h$  is the local slider-disk separation,  $\mu$  is the viscosity of the air;  $U$  and  $V$  are the sliding velocities in the  $x$  and  $y$  directions. This equation is derived by assuming negligible inertial and body forces, laminar flow, Newtonian viscosity, no-slip boundary condition at the wall, and small film thickness.

Even though the Reynolds equation is based on the assumption of small film

thickness, when the air bearing separation is very small, i.e., on the order of the mean free path of the gas molecules, which is very common in today's magnetic recording applications, the no-slip boundary condition at the wall is no longer satisfied. Then the Reynolds equation should be modified to accommodate the slip flow. Various molecular slip modifications include the first order slip model (Burgdorfer, 1959), second order slip model (Hsia and Domoto, 1983) and higher order slip models (Gans, 1985). Fukui and Kaneko (1988) introduced yet another modification of the Reynolds equation based on the linearized Boltzmann equation. They formulated the Poiseuille- and Couette-like flow for arbitrary bearing spacing. A recent particle-based simulation study (Alexander, *et al.*, 1994) demonstrated that Fukui and Kaneko slip correction is applicable to air bearings with nanometer spacing. If we define the following non-dimensionalized variables

$$X = \frac{x}{L}, Y = \frac{y}{L}, H = \frac{h}{h_m}, P = \frac{p}{p_a}, T = \omega t$$

where  $L$ ,  $h_m$ ,  $p_a$ ,  $\omega$  are the slider's length, minimum spacing, ambient pressure, and appropriate angular frequency, then all of the above generalized forms of the Reynolds equation can be written as (Ruiz and Bogy, 1990a)

$$\frac{\partial}{\partial X} \left[ \hat{Q} P H^3 \frac{\partial P}{\partial X} - \Lambda_x P H \right] + \frac{\partial}{\partial Y} \left[ \hat{Q} P H^3 \frac{\partial P}{\partial Y} - \Lambda_y P H \right] = \sigma \frac{\partial}{\partial T} [P H] \quad (2.2)$$

where  $\Lambda_x = 6\mu UL/p_a h_m^2$  and  $\Lambda_y = 6\mu VL/p_a h_m^2$  are the bearing numbers in the x and y directions, and  $\sigma = 12\mu\omega L^2/p_a h_m^2$  is the squeeze number.  $\hat{Q}$  is the Poiseuille flow factor, which reflects the type of slip-flow modification used, i.e.,

$$\hat{Q} = 1 \quad \text{Continuum model}$$

$$\hat{Q} = 1 + 6a \frac{K_n}{PH} \quad \text{First order slip model}$$

$$\hat{Q} = 1 + 6 \frac{K_n}{PH} + 6 \left[ \frac{K_n}{PH} \right]^2 \quad \text{Second order slip model}$$

$$\hat{Q} = f \left( \frac{K_n}{PH} \right) \quad \text{Fukui-Kaneko model}$$

where  $K_n = \lambda/h_m$  is the Knudsen number,  $\lambda$  is the mean free path of the gas molecules, and  $a=(2-\alpha)/\alpha$  in which  $\alpha$  is the accommodation factor.  $f(K_n/PH)$  is as given by Fukui and Kaneko (1988). A database method of implementing the scheme is also introduced by them (Fukui and Kaneko, 1990).

**2.2.2 Control-Volume Formulation.** To solve the time-dependent generalized Reynolds equation numerically, an implicit control volume scheme, based on the convection-diffusion formulations, is employed here. A control volume is assigned as the rectangular region surrounding each grid point with its boundaries located midpoint between the neighboring grids as shown in Fig. 2.1. To convert equation (2.2) to a control volume form, the equation is rewritten as

$$\frac{\partial F}{\partial X} + \frac{\partial G}{\partial Y} = \sigma \frac{\partial}{\partial T} [PH] \quad (2.3)$$

where  $F = QH^2 \partial P / \partial X - \Lambda_x PH$  and  $G = QH^2 \partial P / \partial Y - \Lambda_y PH$  are the mass flow in the x and y directions, respectively, and  $Q = \hat{Q}PH$ . The integration of equation (2.3) over the control volume  $\Sigma$  and application of the divergence theorem give

$$\int_{\partial \Sigma} [F n_x + G n_y] ds = \int_{\Sigma} \sigma \frac{\partial}{\partial T} [PH] dA \quad (2.4)$$

where  $\partial\Sigma$  denotes the boundary of the control volume, and  $n_x$  and  $n_y$  are the components of the outer unit normal vector on the control volume boundary.

**2.2.3 Shaped Rail and Clearance Discontinuities.** For solving equation (2.4) in the presence of clearance discontinuities, the technique introduced by Kogure *et al.* (1983) is implemented in this scheme. The technique involves averaging the mass flow across the discontinuity by appropriately weighting the mass flow contribution from different clearance heights. The average mass flows  $M$  and  $N$  are defined as,

$$\begin{aligned} M &= [\eta F + (1 - \eta)\bar{F}] \Delta Y \\ N &= [\xi G + (1 - \xi)\bar{G}] \Delta X \end{aligned} \quad (2.5)$$

where  $\Delta X$  and  $\Delta Y$  represent the length of the sides of the control volume in the  $x$  and  $y$  directions, respectively, and  $\xi$  and  $\eta$  are weighting factors obtained by averaging the height discontinuities into the two different heights along the sides of the control volume in  $x$  and  $y$  directions.  $F$  and  $G$  are defined as the mass flow corresponding to the clearance height  $l$ , and  $\bar{F}$  and  $\bar{G}$  are the mass flow for another clearance height.

Following the same idea, the accumulation mass flow inside the control volume can be averaged as

$$\int_{\Sigma} \sigma \frac{\partial}{\partial T} [PH] dA = \sigma \frac{\partial}{\partial T} [PH_{av}] \Delta X \Delta Y \quad (2.6)$$

where  $H_{av}$  is the averaged clearance height across the whole control volume region.

Using the average mass flows in equations (2.5) and (2.6), and carrying out the integration over the control volume ( $i, j$ ) yields:

$$M_{i+1/2,j} - M_{i-1/2,j} + N_{i,j+1/2} - N_{i,j-1/2} = \sigma \frac{\partial}{\partial T} [PH_{av}]_{i,j} \Delta X_i \Delta Y_j \quad (2.7)$$

where  $i+1/2$  denotes the right control volume face, and  $i-1/2$  denotes the left face. The top and bottom faces of the control volume are denoted by  $j+1/2$  and  $j-1/2$ , respectively.

**2.2.4 Convection and Diffusion.** Equation (2.7) consists of convection and diffusion terms with strong convection occurring in the region of very high bearing number. The accurate representation of sharp gradients caused by strong convection presents a challenge for the numerical air bearing analysis. The formulation has direct consequences on the accuracy of the solution for the pressure field. Conventional schemes such as the central-differences tend to become unstable at high bearing number. The ability to obtain a converged solution of the problem is dependent on the underlying convection-diffusion formulation. If the solution contains an excessive amount of the numerical error known as false diffusion, the results may not converge to the correct solution. In many cases, it is almost impossible to refine the grid sufficiently so that the numerical errors will be reduced to acceptable levels. Thus, there is a need for convection-diffusion formulations that lead to stable and accurate results with grids of modest fineness. Well-known convection-diffusion schemes include the upwind, hybrid, power-law and exponential schemes (Patankar, 1980). The upwind scheme recognizes that the weak point in the central-difference formulation is the assumption that the convected property at the interface is the average of the two neighboring point values, and it proposes that the convected property should be the upstream neighboring point value. A hybrid scheme is a combination of the central-difference and upwind schemes. It is identical with the central-difference scheme for Peclet numbers in the range  $-2 \leq P_e \leq 2$ ; outside this range

it reduces to the upwind scheme. The exponential scheme is based on the exact solution of the one-dimensional diffusion problem, which has an exponential behavior. When the exponential scheme is used for the steady one-dimensional problem, it is guaranteed to produce the exact solution for any value of the Peclet number and for any number of grid points. Despite its highly desirable behavior, it is not widely used because exponentials are expensive to compute. A better and not particularly expensive-to-compute representation of the exponential behavior of the one-dimensional exact solution is the power-law scheme. Instead of assuming that the convected property at the interface is the average of the two neighboring point values, the power-law scheme proposes that the convected property should be based on the exact solution of the one-dimensional diffusion problem, which has an exponential behavior.

To arrange the equation more compactly, the following variables are introduced (Patankar, 1980):

$$D_x = \frac{QH^2}{\Delta X} \quad , \quad D_y = \frac{QH^2}{\Delta Y}$$

$$P_{ex} = \frac{\Lambda_x H \Delta X}{QH^2} \quad , \quad P_{ey} = \frac{\Lambda_y H \Delta Y}{QH^2} \quad (2.8)$$

where  $D$  is the diffusion conductance, while  $P_c$  is the Peclet number which indicates the ratio of the strengths of convection to diffusion. The subscripts here represent the components in the specified directions. With these new variables, the mass flows  $F$  and  $G$  can be expressed as

$$-F = D_x \left[ P_{ex} P - \Delta X \frac{\partial P}{\partial X} \right]$$

$$-G = D_y \left[ P_{ey} P - \Delta Y \frac{\partial P}{\partial Y} \right] \quad (2.9)$$

$\bar{F}$  and  $\bar{G}$  have similar expressions.

To proceed, the mass flows F and G crossing the control volume boundaries need to be represented in terms of the pressure values at neighboring grid points. In the power-law scheme formulation, the mass flows F and G are represented as:

$$\begin{aligned} -F_{i+1/2,j} &= D_{x_{i+1/2,j}} \left\{ \left[ A \left( \left| P_{ex_{i+1/2,j}} \right| \right) + \text{MAX} \left( P_{ex_{i+1/2,j}}, 0 \right) \right] P_{i,j} \right. \\ &\quad \left. - \left[ A \left( \left| P_{ex_{i+1/2,j}} \right| \right) + \text{MAX} \left( -P_{ex_{i+1/2,j}}, 0 \right) \right] P_{i+1,j} \right\} \\ -F_{i-1/2,j} &= D_{x_{i-1/2,j}} \left\{ \left[ A \left( \left| P_{ex_{i-1/2,j}} \right| \right) + \text{MAX} \left( P_{ex_{i-1/2,j}}, 0 \right) \right] P_{i-1,j} \right. \\ &\quad \left. - \left[ A \left( \left| P_{ex_{i-1/2,j}} \right| \right) + \text{MAX} \left( -P_{ex_{i-1/2,j}}, 0 \right) \right] P_{i,j} \right\} \\ -G_{i,j+1/2} &= D_{y_{i,j+1/2}} \left\{ \left[ A \left( \left| P_{ey_{i,j+1/2}} \right| \right) + \text{MAX} \left( P_{ey_{i,j+1/2}}, 0 \right) \right] P_{i,j} \right. \\ &\quad \left. - \left[ A \left( \left| P_{ey_{i,j+1/2}} \right| \right) + \text{MAX} \left( -P_{ey_{i,j+1/2}}, 0 \right) \right] P_{i,j+1} \right\} \\ -G_{i,j-1/2} &= D_{y_{i,j-1/2}} \left\{ \left[ A \left( \left| P_{ey_{i,j-1/2}} \right| \right) + \text{MAX} \left( P_{ey_{i,j-1/2}}, 0 \right) \right] P_{i,j-1} \right. \\ &\quad \left. - \left[ A \left( \left| P_{ey_{i,j-1/2}} \right| \right) + \text{MAX} \left( -P_{ey_{i,j-1/2}}, 0 \right) \right] P_{i,j} \right\} \end{aligned} \quad (2.10)$$

The various schemes can now be thought of as merely different choices of the function  $A(|P_e|)$ . Expressions of  $A(|P_e|)$  for the different schemes are (Patankar, 1980)

$$\begin{aligned} A(|P_e|) &= 1 - 0.5|P_e| && \text{central-difference} \\ A(|P_e|) &= 1 && \text{upwind} \end{aligned}$$

$$\begin{aligned}
A(|P_e|) &= \text{MAX}[0, 1 - 0.5|P_e|] && \text{hybrid} \\
A(|P_e|) &= \text{MAX}\left[0, (1 - 0.1|P_e|)^5\right] && \text{power-law} \\
A(|P_e|) &= |P_e| / [\exp(|P_e|) - 1] && \text{exponential}
\end{aligned} \tag{2.11}$$

**2.2.5 Unsteady Term.** For any time step  $\Delta T$ , the fully implicit scheme satisfies the requirements of simplicity and physically satisfactory behavior. For this reason, it is adopted to describe the unsteady term in the generalized Reynolds equation. The unsteady term from time step  $n$  to  $n+1$  can be given by

$$\sigma \frac{\partial}{\partial T} [PH_{av}] \Delta X \Delta Y = \frac{\sigma \Delta X \Delta Y}{\Delta T} [P^{n+1} H_{av}^{n+1} - P^n H_{av}^n] + O(\Delta T) \tag{2.12}$$

**2.2.6 Discretization Equations.** The main principle of the fully implicit scheme is that the new variable values prevail over the entire time step. Thus, the  $P$  and  $H$  values on the left hand side are replaced by their values at time step  $n+1$ . Substituting equations (2.10) and (2.12) into equation (2.7) gives the following discretization equation

$$a_{i,j} P_{i,j}^{n+1} + a_{i-1,j} P_{i-1,j}^{n+1} + a_{i+1,j} P_{i+1,j}^{n+1} + a_{i,j-1} P_{i,j-1}^{n+1} + a_{i,j+1} P_{i,j+1}^{n+1} = b_{i,j} \tag{2.13}$$

where the complete expressions of the coefficients of the above equation are given in the Appendix (page 27).

## 2.3 Solution Procedure

**2.3.1 The Line-by-Line Method.** The resulting discretization equations at every grid level are solved using the line-by-line method. In this method, we choose a grid line, assume that the  $P$ 's along the neighboring lines are known from their "latest" values, and solve for  $P$ 's along the chosen line by the tri-diagonal matrix algorithm. This procedure is



followed for all the lines in one direction and repeated for all the lines in the other direction. This iterative process is terminated when some chosen convergence criterion is satisfied. To improve the convergence, the sweep is from upstream to downstream. The convergence of the line-by-line method is faster, because the boundary-condition information from the ends of the line is transmitted at once to the interior of the domain, no matter how many grid points lie along the line. The rate of transmission of information in the other direction is similar to that of the point-by-point method. By alternating the sweep directions, the information from all boundaries can be quickly brought to the interior.

**2.3.2 Convergence Criterion.** An appropriate convergence criterion depends on the nature of the problem and on the objectives of the computation. The relative change in the grid-point values of all the dependent variables is commonly used to formulate the convergence criterion, but this type of criterion can sometimes be misleading. When heavy under-relaxation is used, the change in the dependent variable is retarded; this may create an illusion of convergence although the computed solution may be far from converged. A more meaningful method of monitoring convergence is to examine how closely the discretization equations are satisfied by the current values of the dependent variables, that is to examine the size of the residual  $R$ . For grid point  $(i, j)$ , the residual  $R$  can be calculated from

$$R = a_{i,j}P_{i,j}^{n+1} + a_{i-1,j}P_{i-1,j}^{n+1} + a_{i+1,j}P_{i+1,j}^{n+1} + a_{i,j-1}P_{i,j-1}^{n+1} + a_{i,j+1}P_{i,j+1}^{n+1} - b_{i,j} \quad (2.14)$$

Obviously, when the discretization equation is satisfied,  $R$  will be zero. A suitable

convergence criterion is to require that the largest absolute value of  $R$  be less than a certain small number.

**2.3.3 The Multigrid Method.** Like the classical multigrid methods, the additive correction multigrid (ACM) method attempts to uniformly diminish all frequency error components by iteration on a sequence of grids. But unlike those multigrid methods, the ACM method obtains the equations on a coarse grid directly from the finest grid equations by application of the additive correction strategy of Settari and Aziz (1973).

This distinction is important for two reasons. First, discretization is required on the finest grid only, thus reducing complexity and cost as well as eliminating the possibility of discretization inconsistencies between the coarse and fine grids. Second, because the fine grid equations are conservative and the coarse grid equations are formed by simply combining the fine grid equations, the resulting coarse grid equations are also conservative. The coarse grid equations thus retain the important conservation property of the fine grid. Solution of the coarse grid equations and subsequent adjustment of the fine grid solution field yields a field that is conservative over each block. The task of the local solver is then to affect minor adjustments within each block to eventually obtain conservation over each control volume. Clearly, communication between the coarse and fine grids preserves the overall conservative nature of the scheme. It should also be noted at the outset that once the ACM method is selected, there are no further decisions to be made related to the treatment of boundary conditions, the transfer of residuals, or the interpolation and extrapolation of the dependent variables.

Figure 2.2 shows the block continuity control volume. The blocks are formed from

the four contiguous control volumes, as denoted in Fig. 2.2 by the hatched block. To form the additive correction equation for the  $(k, l)$  block, equations (2.13), one for each control volume in the block, are summed. To facilitate this, equation (2.13) is rewritten as

$$\begin{aligned} a_{i,j}P_{i,j}^{n+1} + \bar{a}_{i-1,j}P_{i-1,j}^{n+1} + \bar{a}_{i+1,j}P_{i+1,j}^{n+1} + \bar{a}_{i,j-1}P_{i,j-1}^{n+1} + \bar{a}_{i,j+1}P_{i,j+1}^{n+1} \\ + \hat{a}_{i-1,j}P_{i-1,j}^{n+1} + \hat{a}_{i+1,j}P_{i+1,j}^{n+1} + \hat{a}_{i,j-1}P_{i,j-1}^{n+1} + \hat{a}_{i,j+1}P_{i,j+1}^{n+1} = b_{i,j} \end{aligned} \quad (2.15)$$

where  $a_{i-1,j} = \hat{a}_{i-1,j} + \bar{a}_{i-1,j}$  and  $\hat{a}_{i-1,j} = 0$  if  $P_{i-1,j}^{n+1}$  is in the  $(k, l)$  block and  $\bar{a}_{i-1,j} = 0$  if  $P_{i-1,j}^{n+1}$  is not in the  $(k, l)$  block. Summing the four equations for the four control volumes within the block yields

$$\begin{aligned} \sum_4 (a_{i,j} + \bar{a}_{i-1,j} + \bar{a}_{i+1,j} + \bar{a}_{i,j-1} + \bar{a}_{i,j+1}) P_{i,j}^{n+1} \\ + \sum_4 (\hat{a}_{i-1,j} P_{i-1,j}^{n+1} + \hat{a}_{i+1,j} P_{i+1,j}^{n+1} + \hat{a}_{i,j-1} P_{i,j-1}^{n+1} + \hat{a}_{i,j+1} P_{i,j+1}^{n+1}) = \sum_4 b_{i,j} \end{aligned} \quad (2.16)$$

If  $\tilde{P}_{i,j}^{n+1}$  is the best estimate of  $P_{i,j}^{n+1}$  on the fine grid, the correction of  $\Delta P_{k,l}^{n+1}$  obtained on the coarser grid is added to  $\tilde{P}_{i,j}^{n+1}$  to obtain an improved value  $P_{i,j}^{n+1}$ .

Inserting  $P_{i,j}^{n+1} = \tilde{P}_{i,j}^{n+1} + \Delta P_{k,l}^{n+1}$  into equation (2.16) gives

$$\tilde{a}_{k,l} \Delta P_{k,l}^{n+1} + \tilde{a}_{k-1,l} \Delta P_{k-1,l}^{n+1} + \tilde{a}_{k+1,l} \Delta P_{k+1,l}^{n+1} + \tilde{a}_{k,l-1} \Delta P_{k,l-1}^{n+1} + \tilde{a}_{k,l+1} \Delta P_{k,l+1}^{n+1} = \tilde{b}_{k,l} \quad (2.17)$$

where

$$\tilde{a}_{k,l} = \sum_4 (a_{i,j} + \bar{a}_{i-1,j} + \bar{a}_{i+1,j} + \bar{a}_{i,j-1} + \bar{a}_{i,j+1})$$

$$\tilde{a}_{k-1,l} = \sum_4 \bar{a}_{i-1,j}, \quad \tilde{a}_{k+1,l} = \sum_4 \bar{a}_{i+1,j}$$

$$\tilde{a}_{k,l-1} = \sum_4 \bar{a}_{i,j-1} , \tilde{a}_{k,l+1} = \sum_4 \bar{a}_{i,j+1}$$

$$\tilde{b}_{k,l} = \sum_4 \left( b_{i,j} - a_{i,j} \tilde{P}_{i,j}^{n+1} - a_{i-1,j} \tilde{P}_{i-1,j}^{n+1} - a_{i+1,j} \tilde{P}_{i+1,j}^{n+1} - a_{i,j-1} \tilde{P}_{i,j-1}^{n+1} - a_{i,j+1} \tilde{P}_{i,j+1}^{n+1} \right)$$

The solution of equation (2.17) yields the value of  $\Delta P_{k,l}^{n+1}$  that is added to each  $\tilde{P}_{i,j}^{n+1}$  value that lies within the  $(k, l)$  block to obtain the improved estimate  $P_{i,j}^{n+1}$ .

The multigrid algorithm provides the framework for the solution procedure to switch back and forth between various grid levels. The calculation is begun on the finest grid (level 0) by sweeping the grid once in both directions, followed by the block-correction procedure which is used here to smooth out the error components of the lowest frequency. The solution is then sought at level 1 grid. If the residual before iteration  $k$  on this mesh is  $R^k$  and the residual after the iteration is  $R^{k+1}$ , another iteration on this grid is performed if

$$R^{k+1} \leq \gamma R^k \tag{2.18}$$

where the value for  $\gamma$  is chosen to be 0.5. If the residual is not reduced by the specified factor, solution is sought on the coarser level grid. When the coarsest grid is reached, the solution is driven to a tight convergence. This step is inexpensive since only a few grid points are present on the coarsest level. The procedure, thus, moves up and down the grid levels annihilating residuals of the discrete equations on all the coarser levels. When the finest level 0 grid is corrected by the converged level 1 corrections, one more sweep is performed on the finest level, followed by another block-correction procedure. This constitutes one nonlinear fine grid iteration and the algorithm returns to compute the

discretization coefficients using the latest fine grid values.

## 2.4 Results and Discussions

The performances of both the single-grid and the 4-level additive correction based multigrid techniques are evaluated using two 50% air bearing sliders. They are the Read-Rite tripod slider and the Headway AAB slider shown in Figs. 2.3 and 2.4, respectively. The sliders are chosen to show the performance comparison of the multigrid method over the single grid method for straight rails and shaped rails. Since the well-tested power-law scheme is used, the emphasis of the present chapter is on the convergence performance of the methods and no figures of accuracy are mentioned. The sliders are located at the radial position of 25 mm measured from the disk center with zero skew. The nominal trailing edge center fly height, pitch and roll are fixed at 40 nm, 180  $\mu$ rad and 0 rad, respectively. The air bearing forces are calculated for two disk rotating speeds of 2700 rpm and 5400 rpm which correspond to the nominal (at slider's center) bearing number of 9,598.02 and 19,196.04, respectively. To examine the effect of the problem scale, two hierarchies of grids adapted on the basis of pressure gradient are used in the simulation. They are (194 $\times$ 194, 98 $\times$ 98, 50 $\times$ 50, 26 $\times$ 26) and (98 $\times$ 98, 50 $\times$ 50, 26 $\times$ 26, 14 $\times$ 14). All the simulations are run on DEC ALPHA 3000/800 workstations. In our simulation the Fukui-Kaneko model is used.

**2.4.1 Tripad Slider.** The 3D non-dimensional air bearing pressure profile at the rotation speed of 5400 rpm is shown in Fig. 2.5. Figure 2.6 illustrates the convergence histories of the multigrid and single-grid methods with the finest grids of 98 $\times$ 98. The disk rotates

at the speed of 5400 rpm. For the single-grid method, Figure 2.6a shows the rapid reduction of the residuals in the initial iterations and subsequent reduction of the convergence rate. It is this reduction in the convergence rate, attributed to the persistence of the low frequency error components in the solution, that the multigrid methods try to address. Using the multigrid method, it takes only 8 fine-grid iterations to achieve roughly one order of residual reduction, whereas to reduce the residual by the same amount using the single-grid method it takes more than 8 times as many iterations. It is also seen that the slope of the residual reduction with respect to iterations for the multigrid method is approximately constant. The convergence histories of the air bearing force are shown in Fig. 2.6b. Table 2.1 details the total CPU times required to achieve the given convergence. Figure 2.7 shows the convergence histories with the grids of  $194 \times 194$  and at the rotation speed of 5400 rpm. With the increased grids, the residual reduction rate becomes very slow for the single-grid method, while the multigrid method has about the same slope of residual reduction with respect to the iterations as the coarse grids. The results indicate that more gains in CPU time and computing cost can be expected for larger scale problems using the multigrid method over the single-grid method. To study the effect of the bearing number on the convergence performance, the simulations with the same grids but the disk rotation speed of 2700 rpm are performed. The results are presented in Fig. 2.8 and Table 2.1. By comparing the results for the speed of 5400 rpm, it is observed that convergence performance of the multigrid method is much less sensitive to the bearing number than that of the single-grid method, therefore resulting in higher efficiency. The multigrid method is found to be 7 times faster than the

single-grid method for the case with the finest grids of  $194 \times 194$  and the disk rotation speed of 5400 rpm.

**2.4.2 Headway AAB Slider.** This slider has been chosen to illustrate the performance of the multigrid method for the shaped sub-ambient pressure sliders. The 3D non-dimensional air bearing pressure distribution at the rotating speed of 5400 rpm is shown in Fig. 2.9. It is noted that a sub-ambient pressure develops in the reverse step region. The exact same cases as in the tripad slider are simulated and the convergence histories are presented in Figs. 2.10, 2.11 and 2.12; respectively. As anticipated, the convergence rate is slower than that of the tripad slider due to the existence of the sub-ambient pressure zones. The results indicate similar trends as in the tripad slider. Using the multigrid method, convergence is achieved in relatively few iterations and steep residual reduction rates compared to the single-grid method are obtained with better performance for higher bearing number and larger grid numbers. Table 2.2 shows that the total CPU times required by the two methods and the multigrid method are 15.2 to 39.7 times faster depending on the number of grids and the bearing number. The acceleration provided by the multigrid method for the Headway AAB slider is therefore significantly more than that provided by the multigrid method for the tripad slider.

## 2.5 Summary

An additive correction based multigrid control volume method is developed for the solution of the rarefied gas lubrication equation. The control volume schemes for discretizing the lubrication equation are based on convection-diffusion formulations

including the central difference, upwind, hybrid, power-law and exponential schemes. To improve the solver's efficiency, an additive correction based multigrid method is implemented for the solution of the resulting discretization equations. The method is based on the principle of deriving the coarser grid discretization equations from the fine grid discretization equations. An adaptive-cycling version of the multigrid method is described and applied to the 50% tripad and Headway AAB sliders. The convergence rates of the present calculations are compared with those of the single-grid calculations for two bearing numbers and two sets of grid numbers, measured by the number of fine grid iteration and the total CPU times. The study demonstrates the current method to be rapidly convergent with savings in CPU requirements by a factor ranging from 3.9 to 39.7 depending on the slider type, grid number and bearing number as compared to the single-grid method. The performance gets better as the increases of the grid number and the bearing number. The efficiency of the multigrid method over the single-grid method is further dramatically improved for today's shaped rail sub-ambient pressure sliders.



## APPENDIX

The coefficients of the discretized Reynolds equation for the control volume (i, j)

are:

$$\begin{aligned}
 a_{i-1,j} &= -\Delta Y_j \left\{ \eta_{i-1/2,j} D_{x_{i-1/2,j}}^{n+1} \left[ A \left( \left| P_{ex_{i-1/2,j}}^{n+1} \right| \right) + \text{MAX} \left( P_{ex_{i-1/2,j}}^{n+1}, 0 \right) \right] + \right. \\
 &\quad \left. (1 - \eta_{i-1/2,j}) \bar{D}_{x_{i-1/2,j}}^{n+1} \left[ A \left( \left| \bar{P}_{ex_{i-1/2,j}}^{n+1} \right| \right) + \text{MAX} \left( \bar{P}_{ex_{i-1/2,j}}^{n+1}, 0 \right) \right] \right\} \\
 a_{i+1,j} &= -\Delta Y_j \left\{ \eta_{i+1/2,j} D_{x_{i+1/2,j}}^{n+1} \left[ A \left( \left| P_{ex_{i+1/2,j}}^{n+1} \right| \right) + \text{MAX} \left( -P_{ex_{i+1/2,j}}^{n+1}, 0 \right) \right] + \right. \\
 &\quad \left. (1 - \eta_{i+1/2,j}) \bar{D}_{x_{i+1/2,j}}^{n+1} \left[ A \left( \left| \bar{P}_{ex_{i+1/2,j}}^{n+1} \right| \right) + \text{MAX} \left( -\bar{P}_{ex_{i+1/2,j}}^{n+1}, 0 \right) \right] \right\} \\
 a_{i,j-1} &= -\Delta X_i \left\{ \xi_{i,j-1/2} D_{y_{i,j-1/2}}^{n+1} \left[ A \left( \left| P_{ey_{i,j-1/2}}^{n+1} \right| \right) + \text{MAX} \left( P_{ey_{i,j-1/2}}^{n+1}, 0 \right) \right] + \right. \\
 &\quad \left. (1 - \xi_{i,j-1/2}) \bar{D}_{y_{i,j-1/2}}^{n+1} \left[ A \left( \left| \bar{P}_{ey_{i,j-1/2}}^{n+1} \right| \right) + \text{MAX} \left( \bar{P}_{ey_{i,j-1/2}}^{n+1}, 0 \right) \right] \right\} \\
 a_{i,j+1} &= -\Delta X_i \left\{ \xi_{i,j+1/2} D_{y_{i,j+1/2}}^{n+1} \left[ A \left( \left| P_{ey_{i,j+1/2}}^{n+1} \right| \right) + \text{MAX} \left( -P_{ey_{i,j+1/2}}^{n+1}, 0 \right) \right] + \right. \\
 &\quad \left. (1 - \xi_{i,j+1/2}) \bar{D}_{y_{i,j+1/2}}^{n+1} \left[ A \left( \left| \bar{P}_{ey_{i,j+1/2}}^{n+1} \right| \right) + \text{MAX} \left( -\bar{P}_{ey_{i,j+1/2}}^{n+1}, 0 \right) \right] \right\} \\
 a_{i,j} &= \frac{\sigma H_{avi,j}^{n+1} \Delta X_i \Delta Y_j}{\Delta T} - a_{i-1,j} - a_{i+1,j} - a_{i,j-1} - a_{i,j+1} \\
 &\quad - \Delta Y_j \left[ \eta_{i-1/2,j} D_{x_{i-1/2,j}}^{n+1} P_{ex_{i-1/2,j}}^{n+1} + (1 - \eta_{i-1/2,j}) \bar{D}_{x_{i-1/2,j}}^{n+1} \bar{P}_{ex_{i-1/2,j}}^{n+1} \right] \\
 &\quad + \Delta Y_j \left[ \eta_{i+1/2,j} D_{x_{i+1/2,j}}^{n+1} P_{ex_{i+1/2,j}}^{n+1} + (1 - \eta_{i+1/2,j}) \bar{D}_{x_{i+1/2,j}}^{n+1} \bar{P}_{ex_{i+1/2,j}}^{n+1} \right] \\
 &\quad - \Delta X_i \left[ \xi_{i,j-1/2} D_{y_{i,j-1/2}}^{n+1} P_{ey_{i,j-1/2}}^{n+1} + (1 - \xi_{i,j-1/2}) \bar{D}_{y_{i,j-1/2}}^{n+1} \bar{P}_{ey_{i,j-1/2}}^{n+1} \right] \\
 &\quad + \Delta X_i \left[ \xi_{i,j+1/2} D_{y_{i,j+1/2}}^{n+1} P_{ey_{i,j+1/2}}^{n+1} + (1 - \xi_{i,j+1/2}) \bar{D}_{y_{i,j+1/2}}^{n+1} \bar{P}_{ey_{i,j+1/2}}^{n+1} \right] \\
 b_{i,j} &= \frac{\sigma H_{avi,j}^n \Delta X_i \Delta Y_j}{\Delta T}
 \end{aligned}$$

Grid	Disk Speed (rpm)	Multigrid CPU Time (s)	Single-grid CPU Time (s)	Ratio of CPU Time (Single-grid/Multigrid)
98×98	5400	7.9	30.5	3.9
194×194	5400	35.1	246.2	7.0
194×194	2700	29.9	157.2	5.3

**Table 2.1** Comparison of DEC ALPHA 3000/800 CPU time between the multigrid and single-grid methods for the 50% tripad slider

Grid	Disk Speed (rpm)	Multigrid CPU Time (s)	Single-grid CPU Time (s)	Ratio of CPU Time (Single-grid/Multigrid)
98×98	5400	16.5	250.2	15.2
194×194	5400	73.9	2936.6	39.7
194×194	2700	69.0	2657.4	38.5

**Table 2.2** Comparison of DEC ALPHA 3000/800 CPU time between the multigrid and single-grid methods for the 50% Headway AAB slider

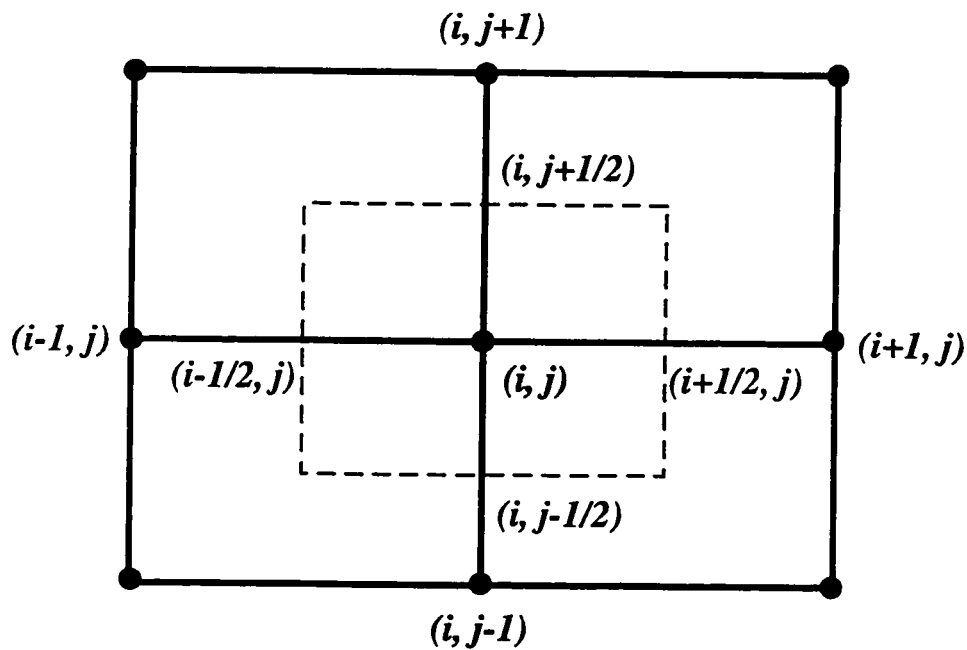


**Fig. 2.1** Schematic of the control volume

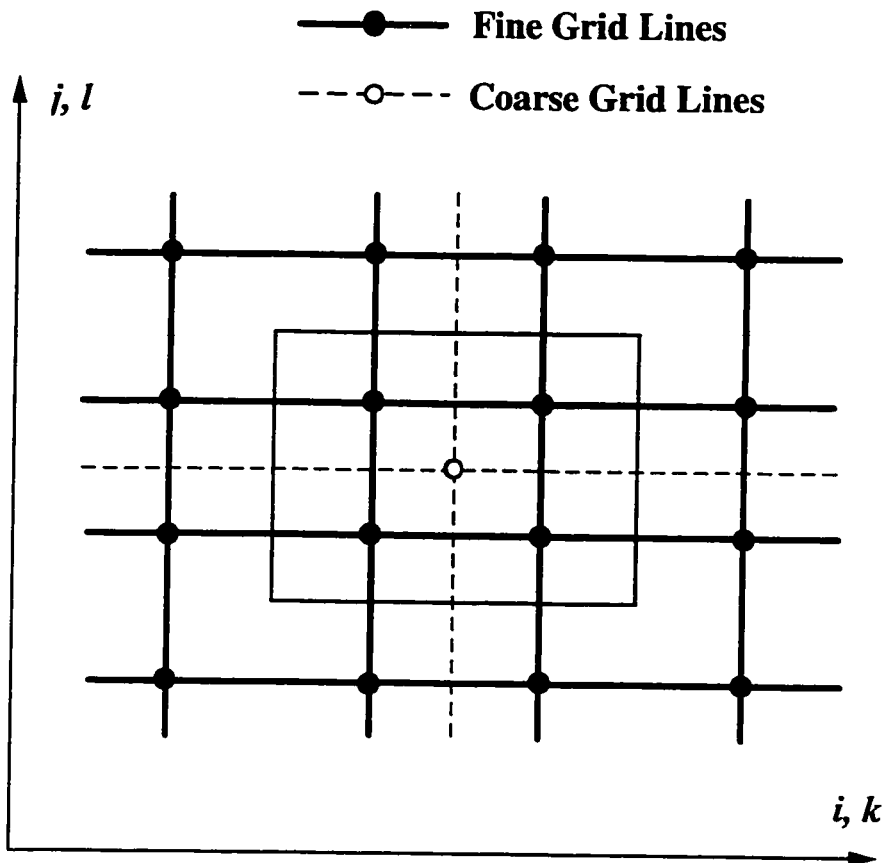


**Fig. 2.2** Schematic showing the assembly of control volumes on the fine grid into blocks (denoted by the hatched block) that defines the coarse grid

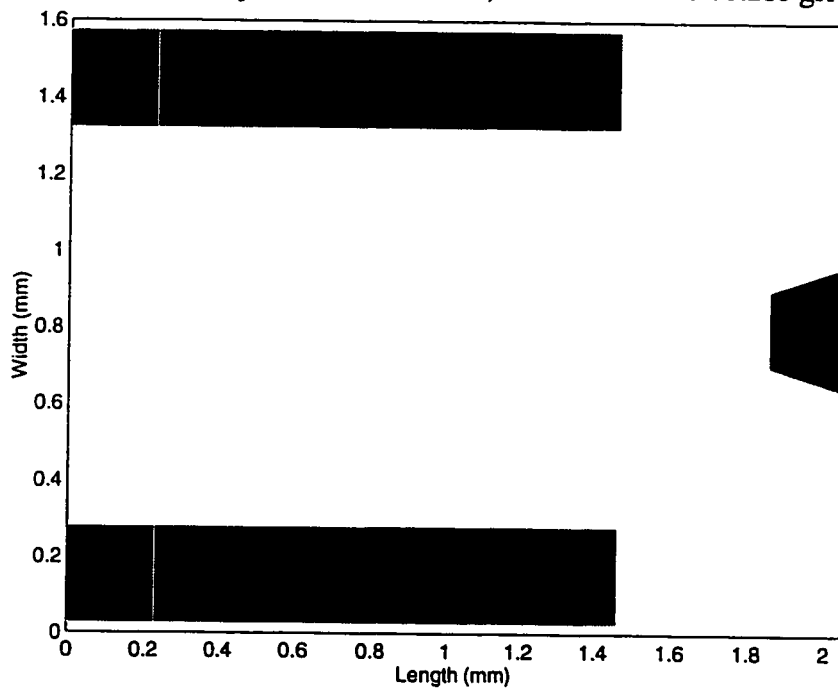


**Fig. 2.3** 50% tripad slider air bearing surface

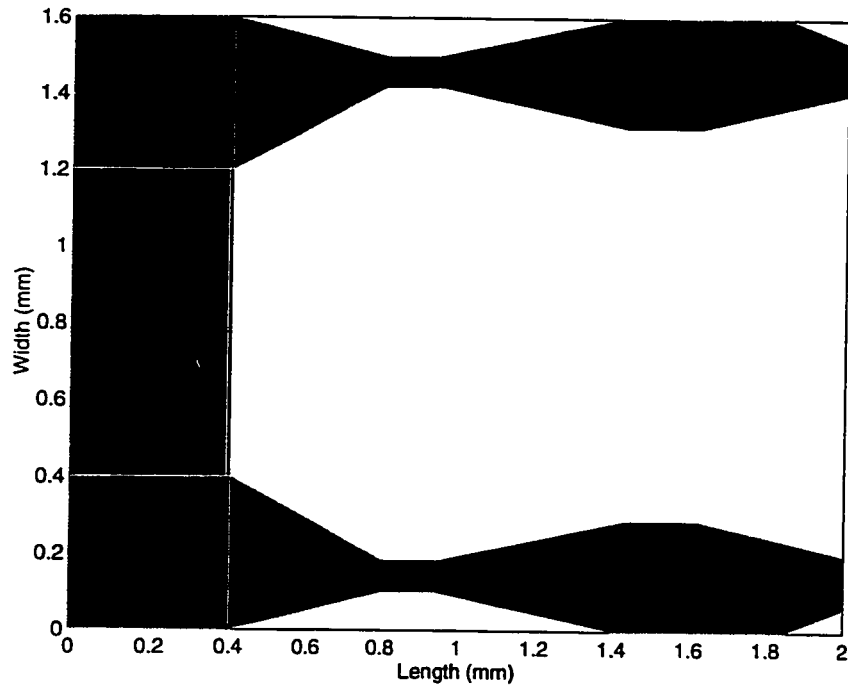


**Fig. 2.4** 50% Headway AAB slider air bearing surface

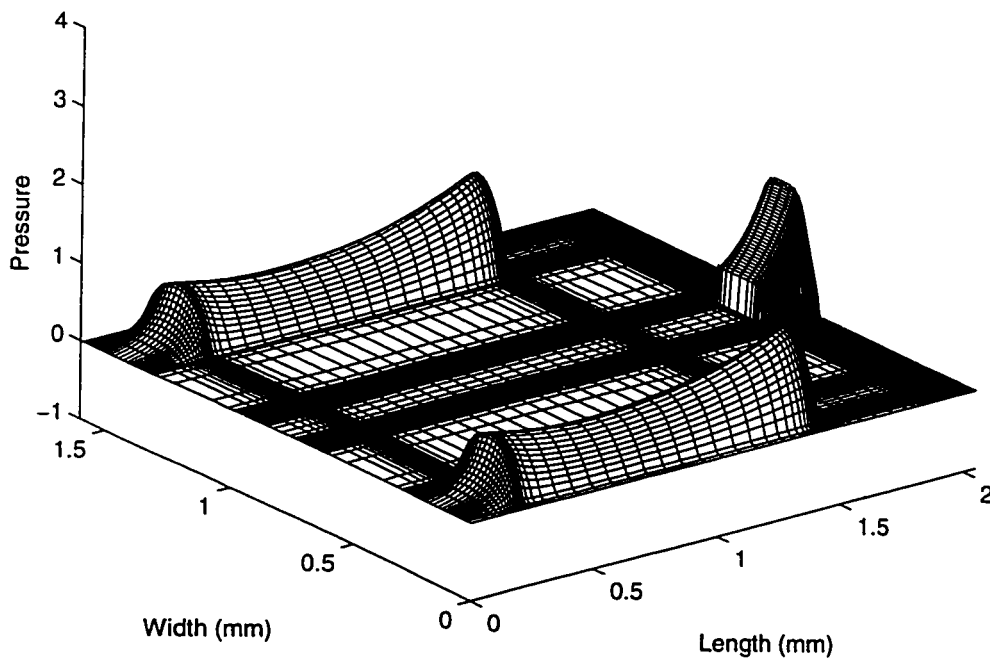
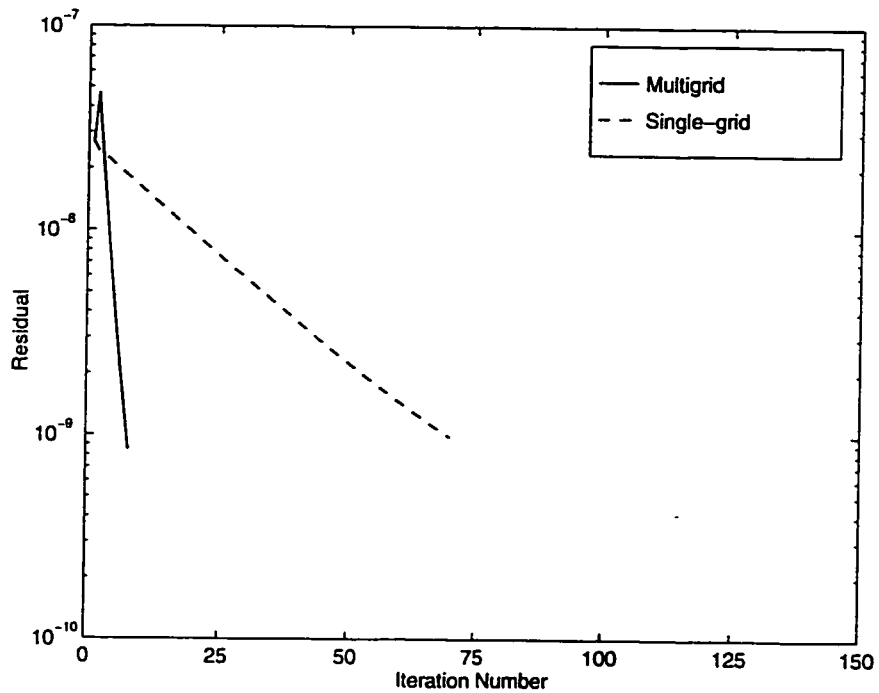
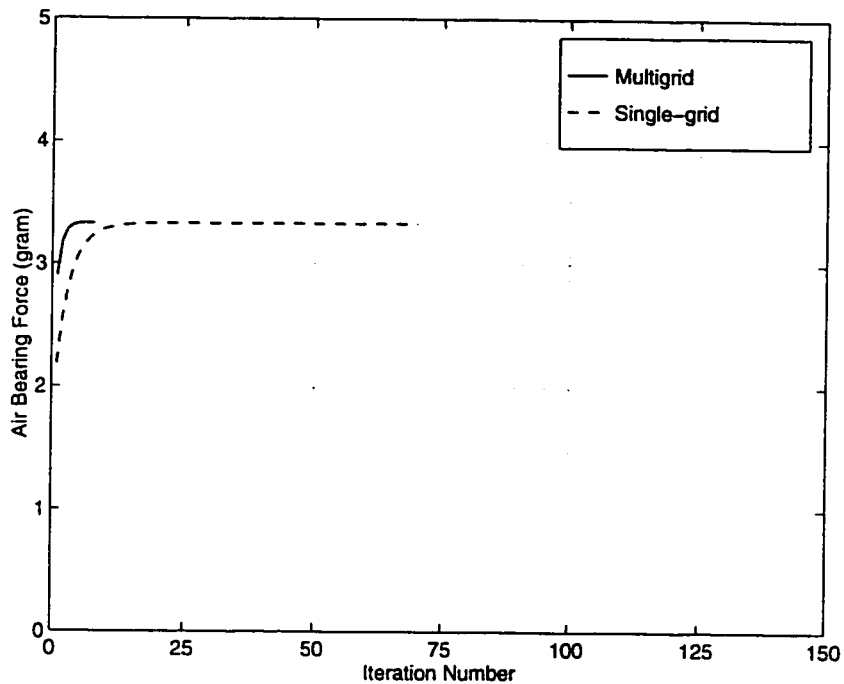


**Fig. 2.5** 3D non-dimensional air bearing pressure profile of the 50% tripad slider. The disk rotates at the speed of 5400 rpm. The nominal trailing edge center fly height, pitch and roll are 40 nm, 180  $\mu$ rad and 0 rad, respectively. The grid is 194 $\times$ 194

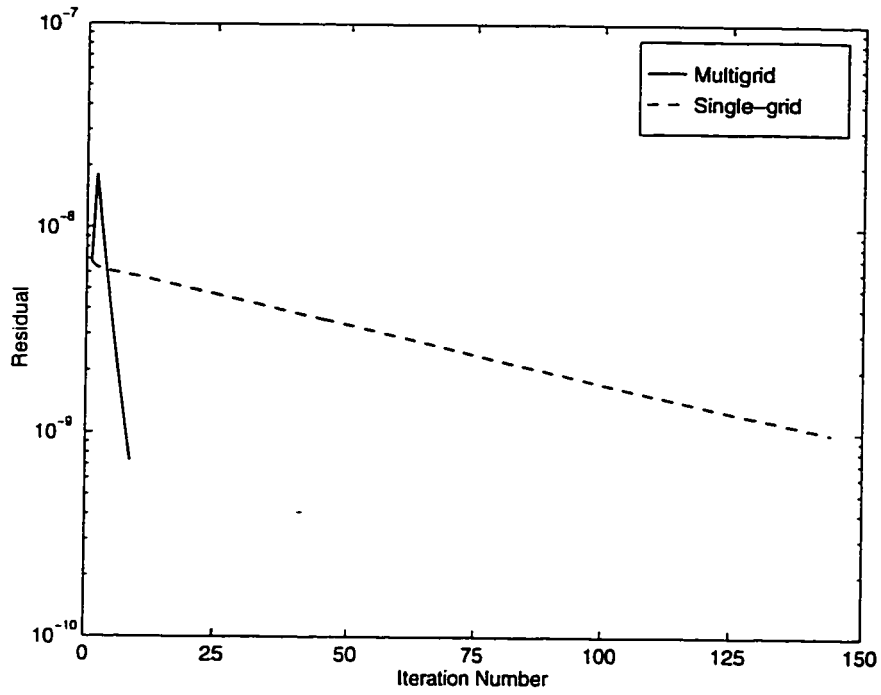


(a) Residual

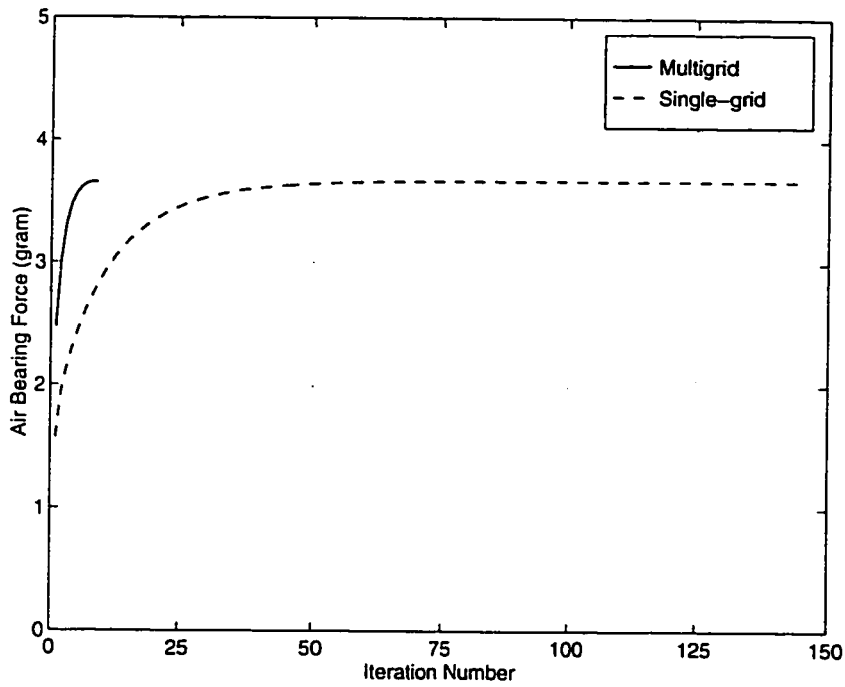


(b) Air bearing force

**Fig. 2.6** Comparison of the convergence rates between the multigrid and single-grid methods for the 50% tripad slider with the finest grids of  $98 \times 98$  and the rotation speed of 5400 rpm

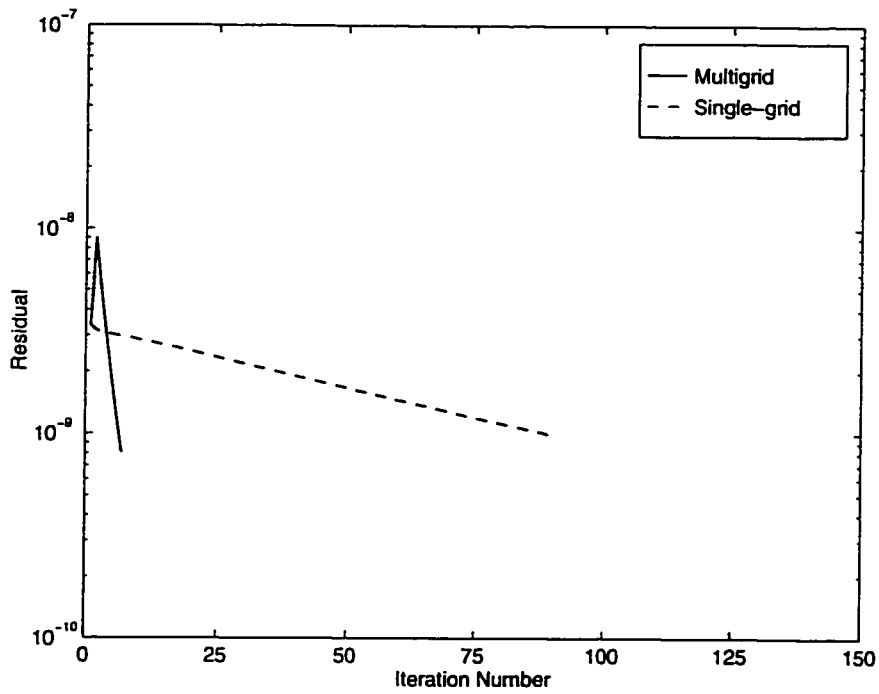


(a) Residual

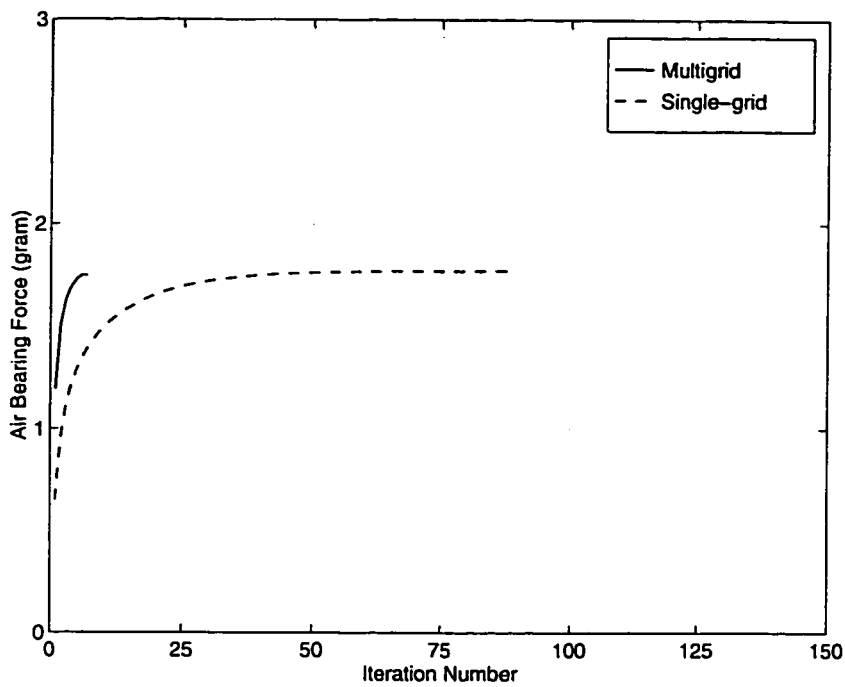


(b) Air bearing force

**Fig. 2.7** Comparison of the convergence rates between the multigrid and single-grid methods for the 50% tripad slider with the finest grids of  $194 \times 194$  and the rotation speed of 5400 rpm



(a) Residual



(b) Air bearing force

**Fig. 2.8** Comparison of the convergence rates between the multigrid and single-grid methods for the 50% tripad slider with the finest grids of  $194 \times 194$  and the rotation speed of 2700 rpm

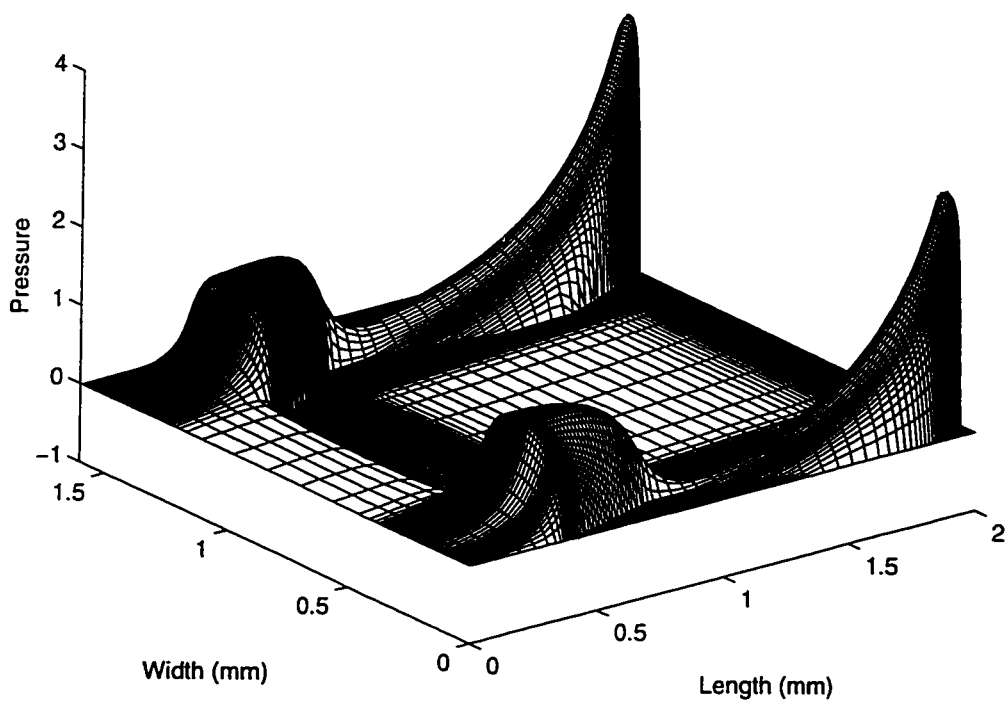
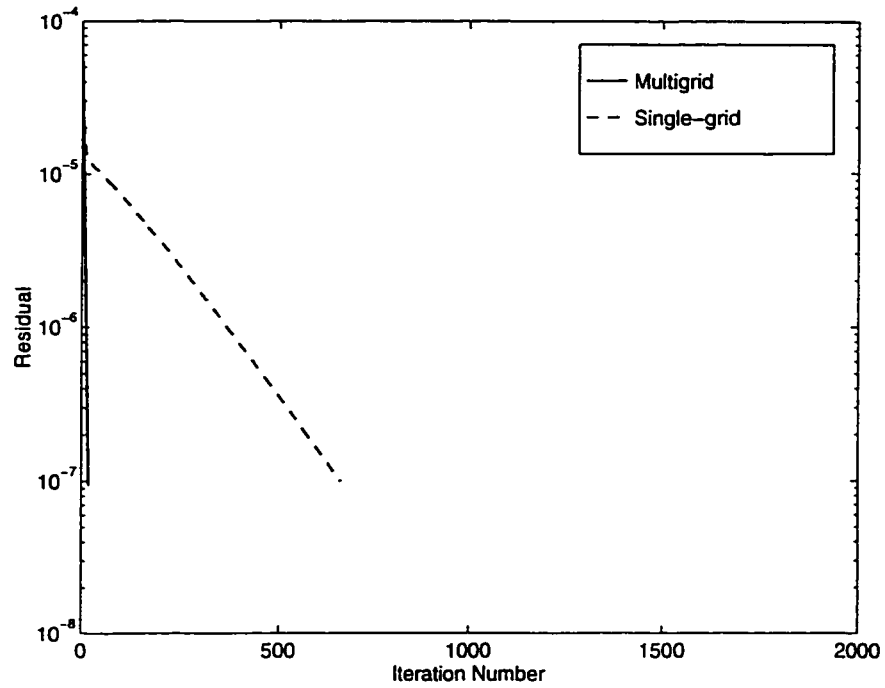
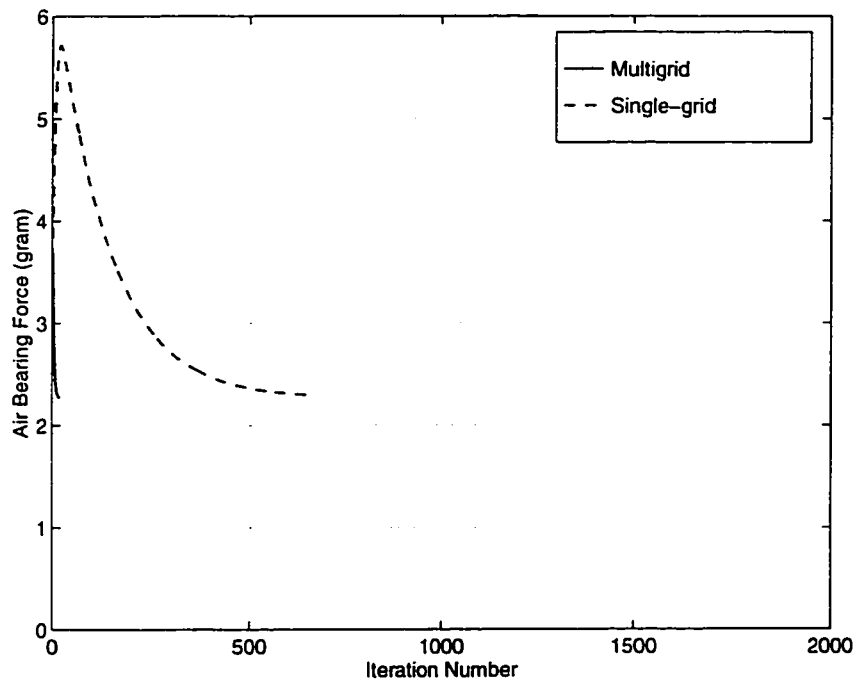


**Fig. 2.9** 3D non-dimensional air bearing pressure profile of the 50% Headway AAB slider. The disk rotates at the speed of 5400 rpm. The nominal trailing edge center fly height, pitch and roll are 40 nm, 48.78  $\mu$ rad and 0 rad, respectively. The grid is 194 $\times$ 194



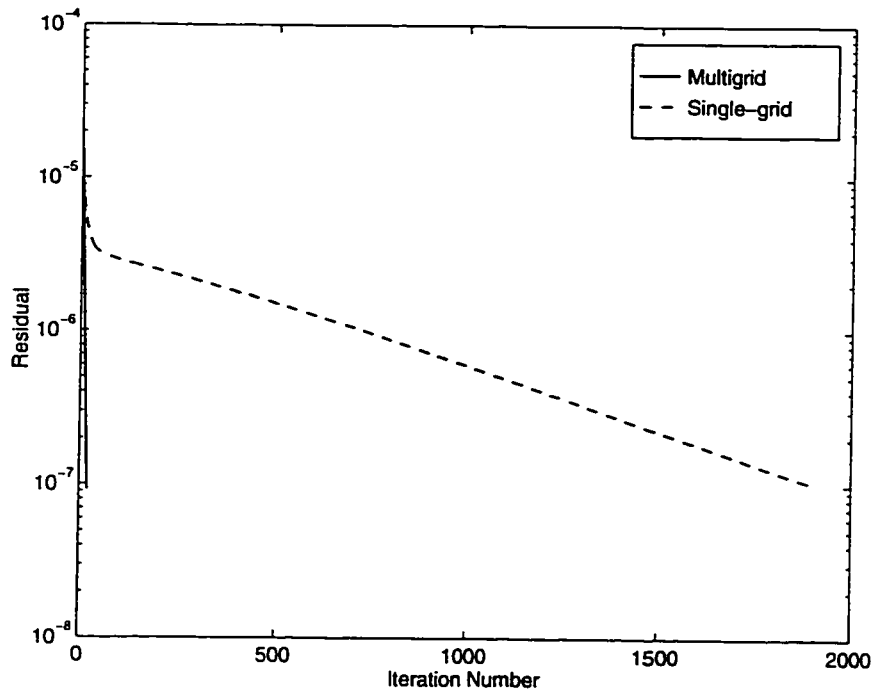


(a) Residual

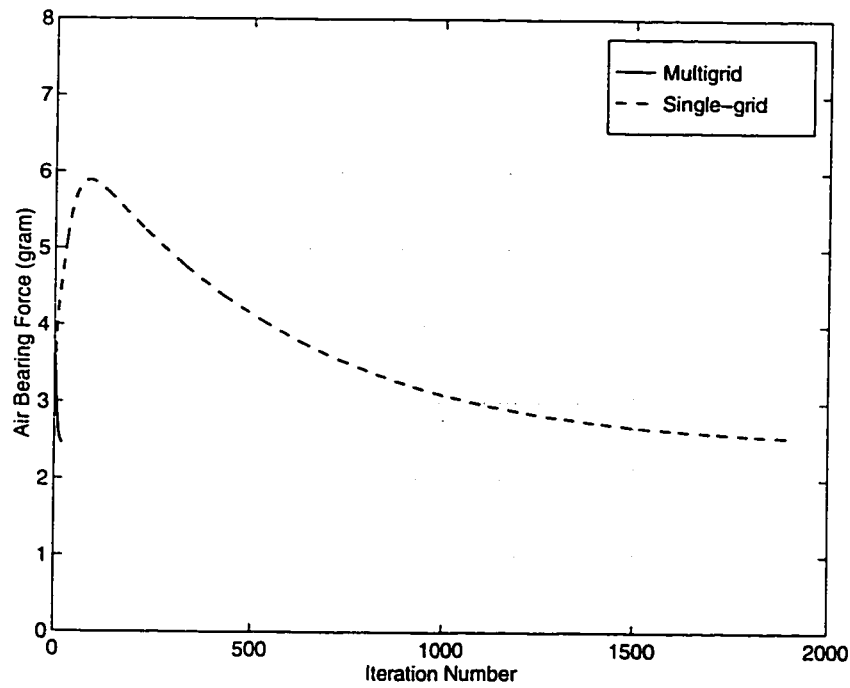


(b) Air bearing force

**Fig. 2.10** Comparison of the convergence rates between the multigrid and single-grid methods for the 50% Headway AAB slider with the finest grids of  $98 \times 98$  and the rotation speed of 5400 rpm

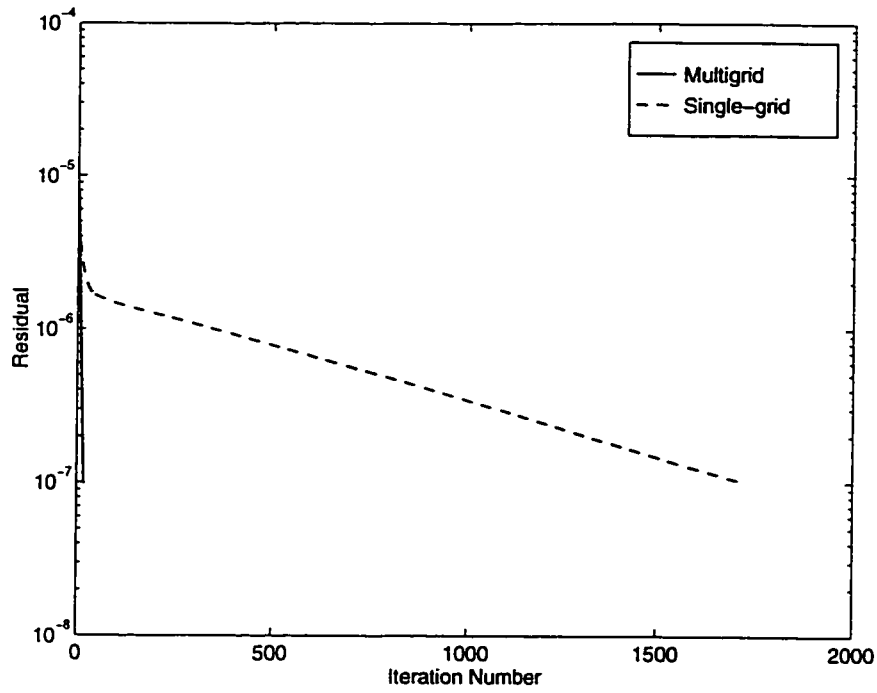


(a) Residual

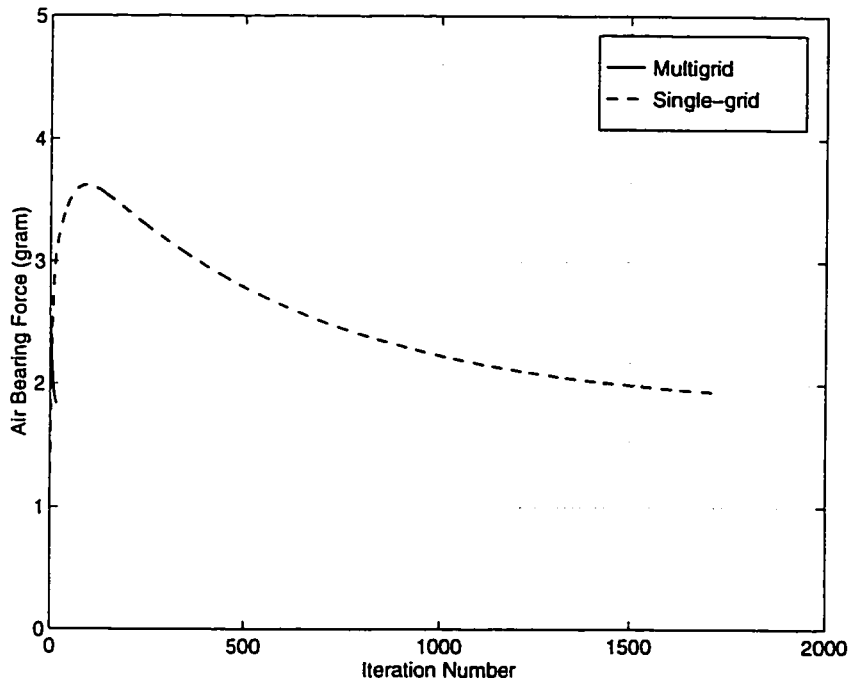


(b) Air bearing force

**Fig. 2.11** Comparison of the convergence rates between the multigrid and single-grid methods for the 50% Headway AAB slider with the finest grids of  $194 \times 194$  and the rotation speed of 5400 rpm



(a) Residual



(b) Air bearing force

**Fig. 2.12** Comparison of the convergence rates between the multigrid and single-grid methods for the 50% Headway AAB slider with the finest grids of  $194 \times 194$  and the rotation speed of 2700 rpm

## **CHAPTER 3**

### **THE CML AIR BEARING DYNAMIC SIMULATOR**

#### **3.1 Introduction**

This chapter briefly describes the Air Bearing Dynamic Simulator developed in the Computer Mechanics Laboratory at the University of California at Berkeley.

The code provides the numerical analysis of head-suspension assembly dynamics for arbitrarily shaped-rail sliders with multiple recess levels including wall profile and edge blend. The program simultaneously solves the generalized Reynolds equation and the equations of motion of the head-suspension assembly. The time-dependent nonlinear generalized Reynolds equation is directly discretized using Patankar's control volume method (Patankar, 1980). The final discretization equations are solved using the alternating direction line sweep method combined with a multi-grid method. This results in a dramatic reduction of solution time, especially for the dynamic simulation, since it involves repeated solutions of the discretized Reynolds equation. An adaptive mesh method is also implemented in the simulator, which can adjust the grid distribution according to the pressure gradient. This usually results in a better usage of the available grid points. The slider's motion is determined by the balance of the air bearing pressure, the suspension force, the contact forces and the inertia. The suspension force can be represented using either the flexure stiffness and damping coefficients or the suspension dynamics. As an alternative to the finite element solution for the suspension, a modal truncation method is used to include the contribution of the suspension assembly

dynamics in the dynamic analysis. The suspension assembly equations of motion are transformed into modal coordinates. The method is very effective in reducing the dimensions of the numerical scheme for solving the equations of motion while retaining essential dynamic characteristics of the problem.

## 3.2 Numerical Models

**3.2.1 Generalized Reynolds Equation.** As described in the previous chapter, the generalized forms of the Reynolds equation, which governs the pressure distribution between the slider and the disk can be written as

$$\frac{\partial}{\partial X} \left[ \hat{Q}PH^3 \frac{\partial P}{\partial X} - \Lambda_x PH \right] + \frac{\partial}{\partial Y} \left[ \hat{Q}PH^3 \frac{\partial P}{\partial Y} - \Lambda_y PH \right] = \sigma \frac{\partial}{\partial T} [PH] \quad (3.1)$$

where  $\Lambda_x = 6\mu UL/p_a h_m^2$  and  $\Lambda_y = 6\mu VL/p_a h_m^2$  are the bearing numbers in the x and y directions, and  $\sigma = 12\mu\omega L^2/p_a h_m^2$  is the squeeze number.  $\hat{Q}$  is the Poiseuille flow factor, which reflects the type of slip-flow modification used, as indicated after equation (2.2).

The time-dependent generalized Reynolds equation is discretized using Patankar's control volume method (Patankar, 1980; Cha and Bogy, 1995), in which the unsteady term is discretized in the implicit form. To improve the efficiency of solution, the final discretization equations are solved using the alternating direction line sweep method combined with a multi-grid method (Hutchinson and Raithby, 1986). Compared with conventional single-grid methods, the multi-grid methods solve the equations on a hierarchy of grids so that all frequency components of the error are reduced at comparable

rates. Inexpensive iteration on the coarse grid rapidly diminishes exactly those components of the error that are so difficult and expensive to reduce by fine grid iteration alone. This results in a dramatic reduction of solution time, especially for the dynamic simulation, since it involves repeated solutions of the discretized Reynolds equation.

**3.2.2 Dynamics of the Slider.** The two-dimensional equations of motion of the air bearing slider flying in partial contact over a rotating disk are

$$\begin{aligned}
 m \frac{d^2 z}{dt^2} &= F_s + F_c + \int_A (p - p_a) dA \\
 I_\theta \frac{d^2 \theta}{dt^2} &= M_{s\theta} + M_{c\theta} + \int_A (p - p_a) (x_g - x) dA \\
 I_\phi \frac{d^2 \phi}{dt^2} &= M_{s\phi} + M_{c\phi} + \int_A (p - p_a) (y_g - y) dA
 \end{aligned} \tag{3.2}$$

where  $z$  is the vertical displacement, and  $\theta$  and  $\phi$  are pitch and roll angles,  $m$  is the slider's mass,  $I_\theta$  and  $I_\phi$  are the slider's moments of inertia,  $x_g$  and  $y_g$  are the positions of the slider's center of gravity.  $F_s$ ,  $M_{s\theta}$  and  $M_{s\phi}$  are the force and moments exerted by the suspension. Similarly,  $F_c$ ,  $M_{c\theta}$  and  $M_{c\phi}$  are the total contact force and moments exerted by the disk on the slider.

Dynamic analysis of a slider flying over a rotating disk requires simultaneous solution of the generalized Reynolds equation and the equation of motion of the slider and its suspension. When the slider is disturbed from its steady state flying conditions, the suspension applies time-dependent loading force and moments to the slider. One efficient approach for integrating the suspension dynamics into the air bearing simulator is to use modal analysis (Cha and Bogy, 1995). The eigenvalue solution of the

suspension is first sought using the commercial FE code ABAQUS, then the dynamic response of the suspension assembly is represented by a truncated linear combination of mode shapes.

Equation (3.2) is solved using direct numerical integration. The Newmark- $\beta$  method (Cha and Bogy, 1995; Ruiz and Bogy, 1990a, 1990b) is implemented in the numerical simulator for high accuracy and less frequency distortion as compared to other commonly used methods. The numerical integration of the coupled equations begins with the estimated displacements of the slider based on the velocities of the previous time step. Then the new displacements are calculated by considering the air bearing pressure and suspension forces at that configuration. These new displacements are compared with the results of the previous iteration step. The iteration ends when the maximum relative change of displacements is smaller than a certain number, which, then gives the final actual displacements of the slider at that time step.

**3.2.3 Slider/Disk Contact Mechanics.** The contact stresses are assumed to depend on the relative profile of the two surfaces in contact, i.e., upon the shape of the gap between them before loading. The system may then be replaced by a flat, rigid surface in contact with a body having a composite modulus and a profile which results in the same undeformed gap between the surfaces. Two asperity-based contact models are implemented in the program: the GW model (Greenwood and Williamson, 1966) and the elastic-plastic model (Chang, *et al.*, 1987, 1992). Both are probabilistic models. The rough surface is represented by a collection of asperities. The surface roughness is assumed to be random, isotropic and Gaussian. The assumptions used in these models

are: (1) the rough surface is isotropic; (2) asperities are spherical near their summits; (3) all asperity summits have the same radius  $R$  before contact, but their heights vary randomly; (4) asperities are far apart and there is no interaction between them; (5) there is no bulk deformation and only the asperities deform during contact. For the GW model, it is assumed that the contacting asperities deform elastically according to Hertz's theory (Johnson, 1985). The elastic-plastic model is similar to the GW model but requires volume conservation of a certain control volume of plastically deformed asperities. The friction force is assumed to follow Coulomb's law, the product of the normal contact force and a friction coefficient  $\gamma$ . Let  $h(x, y)$  denote the slider/disk separation at  $(x, y)$ , and let  $\eta$  denote the areal density of asperities. The contact force and moments are:

**G-W Model** (see Greenwood and Williamson, 1966, for more details)

$$\begin{aligned}
 F_c &= \frac{4}{3} R^{1/2} \eta E \iint_A \int_h^\infty (\xi - h)^{3/2} \varphi(\xi) d\xi dA \\
 M_{c\theta} &= \frac{4}{3} R^{1/2} \eta E \iint_A \left\{ (x - x_g) \int_h^\infty (\xi - h)^{3/2} \varphi(\xi) d\xi + h_{cg} \gamma \cos \psi \int_h^\infty (\xi - h)^{3/2} \varphi(\xi) d\xi \right\} dA \\
 M_{c\phi} &= \frac{4}{3} R^{1/2} \eta E \iint_A \left\{ (y - y_g) \int_h^\infty (\xi - h)^{3/2} \varphi(\xi) d\xi + h_{cg} \gamma \sin \psi \int_h^\infty (\xi - h)^{3/2} \varphi(\xi) d\xi \right\} dA
 \end{aligned} \tag{3.3a}$$

**Elastic-Plastic Model** (see Chang, *et al.*, 1987, 1992, for more details)

$$\begin{aligned}
 F_c &= \eta E \iint_A \left\{ \frac{4}{3} R^{1/2} \int_h^{h+\delta_c} (\xi - h)^{3/2} \varphi(\xi) d\xi + \pi R K \frac{Y}{E} \int_{h+\delta_c}^\infty [2(\xi - h) - \delta_c] \varphi(\xi) d\xi \right\} dA \\
 M_{c\theta} &= \eta E \iint_A \left\{ (x - x_g) \left[ \frac{4}{3} R^{1/2} \int_h^{h+\delta_c} (\xi - h)^{3/2} \varphi(\xi) d\xi + \pi R K \frac{Y}{E} \int_{h+\delta_c}^\infty [2(\xi - h) - \delta_c] \varphi(\xi) d\xi \right] + \right.
 \end{aligned}$$



$$\begin{aligned}
& h_{cg} \gamma \left[ \frac{4}{3} R^{1/2} \int_h^{h+\delta_c} (\xi - h)^{3/2} \varphi(\xi) d\xi + \pi RK \frac{Y}{E} \int_{h+\delta_c}^{\infty} [2(\xi - h) - \delta_c] \varphi(\xi) d\xi \right] \cos \psi \} dA \\
M_{c\phi} = \eta E \iint_A \left\{ (y - y_g) \left[ \frac{4}{3} R^{1/2} \int_h^{h+\delta_c} (\xi - h)^{3/2} \varphi(\xi) d\xi + \pi RK \frac{Y}{E} \int_{h+\delta_c}^{\infty} [2(\xi - h) - \delta_c] \varphi(\xi) d\xi \right] + \right. \\
& \left. h_{cg} \gamma \left[ \frac{4}{3} R^{1/2} \int_h^{h+\delta_c} (\xi - h)^{3/2} \varphi(\xi) d\xi + \pi RK \frac{Y}{E} \int_{h+\delta_c}^{\infty} [2(\xi - h) - \delta_c] \varphi(\xi) d\xi \right] \sin \psi \right\} dA
\end{aligned} \tag{3.3b}$$

where  $\psi$  is the skew angle,  $x_g$  and  $y_g$  are the coordinates of the slider's gravity center, and  $h_{cg}$  is the vertical distance between the point  $(x, y)$  and the center point of gravity. The critical interference,  $\delta_c$ , at which onset of plastic deformation occurs is

$$\delta_c = \left( \frac{\pi KY}{2E} \right)^2 R$$

where  $E$  is the composite Young's modulus,  $Y$  is the yield strength and  $K$  is the yield coefficient, which is a function of Poisson's ratio.  $\varphi(\xi)$  is the asperity height distribution function. In our study, a Gaussian probability distribution is assumed

$$\varphi(\xi) = \frac{1}{\sqrt{2\pi}\sigma} \exp\left(-\xi^2 / 2\sigma^2\right)$$

where  $\sigma$  is the standard deviation of the asperity heights.

**3.2.4 Incorporation of Surface Roughness.** There are various averaging techniques for analyzing the surface roughness effects, which usually tend to smear out the finer details. In order to provide the most realistic simulation of flying characteristics of a slider over the rough disk surface, we directly incorporate the measured disk track profile into the numerical simulator. The film thickness distribution under the slider is obtained through

interpolation of the disk track profile. With this new film distribution, the coupled system of equations is solved.

**3.2.5 Transition Zone Profile.** The transition zone profile from the air bearing surface level is implemented in the simulator using three points in the radial direction. A parabolic functional relationship is assumed to exist for the three points.

### **3.3 Main Features**

The CML Air Bearing Dynamic Simulator offers essentially all the capabilities necessary to characterize the head-disk-suspension dynamics. The dynamic analysis starts with the initialization of the fly height, pitch, roll and the corresponding velocities. The simulator then solves the slider's response to one or a combination of dynamic inputs. A number of dynamic effects on the slider's flying performance can be studied using the simulator (see Hu and Bogy, 1995b, for more details). Among these are:

**3.3.1 Disk Asperities:** This type of analysis tracks the slider's response to the passage of asperities on the disk surface. Five types of asperities are available; the sinusoidal asperity, the ellipsoidal asperity, the cylindrical asperity, the rectangular asperity and manually generated asperity. Their lateral size, height, orientation and location are adjustable.

**3.3.2 Initial Impulse:** Initial impulses are realized numerically by applying initial velocities to the slider. The slider's initial impulse response can be used to characterize the air bearing damping.

**3.3.3 Point by Point Disk Track Profile:** To have the most realistic simulation of a

slider flying over a rough disk surface, the simulator allows the direct input of point by point track profile data. One application of this feature is a numerical estimation of the head-disk spacing modulation caused by the moving disk surface roughness.

**3.3.4 Integration of Suspension Dynamics:** With the head-disk spacing in hard disk drives rapidly approaching sub-25 nm levels, the suspension assembly dynamics may contribute significantly to the overall dynamics of the slider. To obtain an analysis of this contribution, modal analysis of the suspension is employed in the simulator to represent the suspension's effect on the slider dynamics. The dynamic response of the suspension assembly is represented by a linear truncated combination of mode shapes.

**3.3.5 Numerical Generation of Waviness on Disk Surface:** Five types of disk waviness can be numerically generated by the program. They are the sinusoidal wave, the ellipsoidal asperity wave, the cylindrical asperity wave, the rectangular asperity wave, and the manually generated asperity wave. The laser texture profile can be created using the manually generated asperity wave. The waviness can be either one dimensional or two dimensional. They have adjustable wavelength, amplitude and orientation. The radial zone where each waviness exists can also be defined by the input.

**3.3.6 Time-Dependent Disk Velocity:** The program allows the disk velocity to be variable with time. This is usually used for landing/take-off simulations. The time-dependent velocity data consists of pairs of (time, velocity) points. A linear relationship between adjacent data points is assumed. For landing/take-off studies, the simulation can be performed to/from zero disk speed. However, in these cases, an asperity-based contact model should be invoked to ensure a meaningful result.

**3.3.7 Asperity Contact:** Two asperity-based contact models are implemented in the program: the GW model (Greenwood and Williamson, 1966) and the elastic-plastic model (Chang, *et al.*, 1987, 1992). During the simulation, the program computes at each time step the expected values of the normal contact force, the contact moments and the friction force based on the film thickness distribution. These forces and moments are then used to calculate the motion of the slider.

**3.3.8 Track Seeking Motion:** Track access is a process for the slider to move from one track to another. This process involves head motion as well as the dynamics of the suspension. The radial displacement of the slider changes its skew angle and the relative disk velocity, while the slider's accelerations introduce inertia forces. Both of these can adversely affect the spacing between the slider and disk. In the simulation, a time dependent head accessing acceleration profile is imposed and the head velocities are obtained by numerical integration. During the track access motion, the program calculates at each time step the updated radial location, skew angle and relative velocity of the disk surface at each grid point in the bearing. The inertia force acting on the suspension assembly may have significant influence on the spacing modulation for today's high performance disk drives. To effectively include this contribution, we perform the integration of the suspension assembly dynamics using modal analysis.

**3.3.9 Crash Stop Impact:** The crash stop or carriage slam is a mechanism that limits the motion of the actuator either at the extreme inner diameter (ID) or outer diameter (OD). It occurs when a power failure is suddenly applied during a track seek, resulting in uncontrolled collision of the actuator with a mechanical limit stop. The maximum

acceleration/deceleration during crash stop is more than an order of magnitude greater than during track seeking. Therefore, it is considered the most severe dynamic loading in the drive. The actuator acceleration/deceleration produces a roll torsion to the air bearing, which tends to push the outer rail towards the disk surface for the case of the mechanical limit stop located at the ID. The crash resistance of the air bearing is the acceleration required to cause slider/disk contact. To simulate the crash resistance of an air bearing, a time dependent acceleration profile is applied to stop the moving actuator. Since the inertia roll torsion force acting on the suspension plays an important role during the crash stop process, the suspension dynamics need to be included for this type simulation.

**3.3.10 Zone Texture/Transition Zone Profile:** So-called “zone texturing” is one of the approaches to reduce the stiction force during take-off and still allow the use of very smooth disk surfaces in the data region. In this approach, a small annular ring of texture with relatively large surface roughness is provided for the area where the slider starts and stops, while in the data zone, where the slider flies over the disk, the surface is made very smooth. There is a transition zone between the texture zone and the smooth data zone, which is produced during the manufacturing process. The radial zone surface profile is defined by three points in the radial direction. This feature can also be used to describe the radial disk edge profile.

**3.3.11 Numerical Generation of Waviness/Asperities on the Slider:** Similarly to the disk surface, waviness/asperities can also be numerically generated for the slider surface. This feature can be used to model the textured air bearing surfaces.

**3.3.12 Disk Flutter:** The disk flutter simulation provides information on how the slider

responds to disk vibrations. Here a vertical sinusoidal flutter is used. The flutter frequency and amplitude can be adjusted.

### **3.4 Summary**

The CML Air Bearing Dynamic Simulator is a powerful and versatile tool for the study of the head-disk-suspension dynamics. The multiple features including the partial contact, suspension dynamics and laser texture are presented, and the numerical models behind those features are described.

## CHAPTER 4

# DYNAMIC STABILITY AND SPACING MODULATION OF SUB-25NM FLY HEIGHT SLIDERS\*

### 4.1 Introduction

Since the introduction of the first magnetic hard disk drive storage product in 1957, the head-disk spacing has consistently diminished in order to meet the demand for increased data storage. The spacing in new designs is being reduced at an accelerating rate and is expected soon to reach sub-25 nm levels. At such a low spacing, the dynamic spacing fluctuation is a potential cause of occasional head-disk contacts and the spacing fluctuation results in output modulation, so greater dynamic stability becomes an essential design requirement. Furthermore, these low spacings introduce stronger disk surface runout and roughness effects on spacing variation, and track accessing may also force the slider dangerously close to the disk. To meet the demands of these higher performance drives, designers must enhance the dynamic stability and control the spacing modulation with strict design requirements.

The head-disk assembly dynamics have been numerically studied by several researchers over the past decade. Miu and Bogy (1986a, 1986b) implemented the factored implicit scheme of White and Nigam (1980) for the numerical simulation of full size taper-flat sliders. The slider's response due to an impact-induced crater-like depression with a complicated geometry and a deposited aluminum oxide surface step

---

\* Parts of this chapter are published in *IEEE Transactions on Magnetics* (Lu, S., Hu, Y., *et al.*, 1996) and submitted for publication, see Hu and Bogy (1995d)

with a well-defined profile were simulated. Good correlation between the numerical results and the experimental data was observed for the localized step. Ruiz and Bogy (1990a, 1990b) improved this program by including the second order slip effect and the FK modification (Fukui and Kaneko, 1988) to the classical Reynolds equation. They also introduced a slider-disk contact model and surface roughness effects into the simulator. Most importantly, they integrated a finite element model of the entire head-suspension assembly into the simulation program. Using this program, they presented simulations of taper-flat sliders flying over a step bump on the disk, the slider's response during track accessing and during a crash-stop. Jeong and Bogy (1993) simulated the dynamic load-unload procedure and investigated the effects of various parameters on slider-disk contacts during loading. They obtained good agreement between experimental measurements and the simulation results. More recently, Cha and Bogy (1995) developed a factored implicit scheme for the shaped rail sliders using the linearized generalized lubrication equation. They studied the fly height dynamic response of shaped-rail Guppy and IBM tripad sliders to the bump and sinusoidal disk runout as well as slider-asperity contact by incorporating a control volume scheme and an interpolation method to treat rail shapes that are not parallel to the grids. As an alternative to the finite element solution, they presented a modal truncation technique to include the contribution of the suspension assembly dynamics in the dynamic analysis. They also implemented Patankar's power-law scheme in calculating the mass flows.

In this chapter, the CML Air Bearing Dynamic Simulator described in Chapter 3 (see Hu and Bogy, 1995b for more details) is employed to study the dynamic flying



characteristics of three shaped-rail negative pressure sub-25 nm fly height sliders. The air bearing stiffnesses are first calculated using a linear perturbation approach and associated with the air bearing lifting force. Then, the sliders' impulse responses are calculated, and their air bearing damping characteristics are compared by examining the power spectral magnitude plots. To understand the disk surface roughness effect on the head/disk spacing modulation, the transient fly height histories over a "supersmooth" disk are simulated by directly incorporating a measured disk track profile into the simulator. The sliders' responses to a passing bump are simulated and correlated with the air bearing stiffness and damping characteristics. In addition, the critical bump heights without contact are determined. The motion of the head during track accessing is also simulated for the case of Hutchinson 1650E and FX30U type suspensions. Modal analysis of the suspension is employed to integrate the suspension dynamics into the air bearing dynamic simulator. Various conclusions are drawn from these results.

## **4.2 Numerical Simulation**

The generalized Reynolds equation and the equation of motion of the slider and its suspension are numerically solved using the CML Air Bearing Dynamic Simulator. Due to the sub-25 nm spacing in slider air bearings the no-slip boundary condition at the wall is no longer satisfied. In our simulation the modification proposed by Fukui and Kaneko (1988) based on the linearized Boltzmann equation is used.

### 4.3 Results and Discussions

Three shaped-rail sub-ambient pressure type sliders are used in our study. Their air bearing surfaces are illustrated in Fig. 4.1. The 50%/25 nm design has a center rail that carries the read-write element. The design target fly height is about 25 nm under 3 grams of loading force. It is designed with a positive camber so that the closest point is near the center rail trailing edge. The 50%/15 nm and the 30%/15 nm designs are both bi-rail type with the read-write element at the outer rail trailing edge. The load points in these two designs are offset towards the outer rail to guarantee that the minimum fly height is always on the outer rail. They fly at about 15 nm under 3 grams and 1.2 grams of loading force respectively. The disk rotating speed is 5400 rpm. In all three designs, the rail shapes are drawn in on both sides to minimize the fly height change across the disk. The connected front regions of the air bearing surfaces enable the efficient generation of the sub-ambient pressure in the central recessed regions, and also increase fly pitch. A higher pitch angle results in a greater average head-disk separation which would minimize the interaction of the slider with the disk topography. At the radius of 23 mm, the slider's pitch angles are 143.6, 191.6, 306.1  $\mu$ rad for 50%/25 nm, 50%/15 nm and 30%/15 nm designs respectively. The corresponding 3D non-dimensional air bearing pressure profiles are drawn in Fig. 4.2. We note that the trailing edge peak pressures of the 50%/15 nm and 30%/15 nm sliders are much higher than that of the 50%/25 nm slider, this is mainly due to their higher pitch angles and lower trailing edge spacings.

**4.3.1 Air Bearing Stiffness.** The air bearing stiffnesses of the three slider designs are summarized in Table 4.1. They are obtained by use of a linear perturbation at the steady

state fly height. The disk radius at which the head flies is 23 mm giving a speed of 13 m/s. Table 4.2 details the air bearing forces of the three slider designs. The air bearing stiffness is strongly dependent on the lifting force on the air bearing surfaces. For a given net load, a larger sub-ambient pressure force implies a larger lifting force, so a stiffer air bearing is achieved (Kogure, *et al.*, 1983; White, 1983). The results of Tables 4.1 and 4.2 indicate that the air bearing stiffnesses follow the same order as the air bearing lifting forces. The smaller air bearing roll stiffness of the 50%/25 nm slider is also attributed to the three pressure peaks at the trailing edge as compared to the two side pressure peaks of the 50%/15 nm design. Because of the smallest air bearing lifting force and size, the 30%/15 nm slider has the smallest air bearing stiffnesses.

**4.3.2 Impulse Responses.** Figure 4.3 shows the sliders' responses to the vertical, pitch and roll impulses. Their corresponding power spectral magnitudes are plotted in Figs. 4.4, 4.5 and 4.6. The comparison of the fly height and roll oscillation decaying rates as shown in Fig. 4.3 indicates that the 30%/15 nm slider has the highest vertical and roll air bearing damping ratio, followed by 50%/15 nm and 50%/25 nm designs, which agrees well with the relative second peak values in the power spectral magnitudes plotted in Figs. 4.4 and 4.6 (the first peak in Fig. 4.4 corresponds to the pitch resonant frequency). For the pitch motion, both the time and frequency domain plots (Figs. 4.3 and 4.5) imply that the 50%/15 nm design has the smallest air bearing damping ratio in pitch direction, followed by the 50%/25 nm and 30%/15 nm designs.

**4.3.3 Fly Height Modulation over a Supersmooth Disk.** When the slider flies over a real disk, the inevitable surface roughness causes fluctuations in the head-disk spacing.

In our simulation, a measured disk track profile is directly incorporated. Figure 4.7 shows a measured supersmooth disk track profile with a long wavelength cut-off of 350  $\mu\text{m}$ . The corresponding fly heights of the three slider designs over the period of 16 ms are also plotted in the same figure and their fly height modulations are summarized in Table 4.3. The total fly height modulation of the 50%/15 nm design is only about 68.2% of that of the 50%/25 nm design. This is mainly due to the much stiffer air bearing generated by its much higher air bearing lifting force as shown in Table 4.2. However, the 30%/15 nm design exhibits the smallest fly height modulation even though it has the least stiff air bearing. This is because of its shorter length, which is a dominant factor in fly height modulation (Zhu and Bogy, 1989b).

**4.3.4 Bump Responses.** Figure 4.8 illustrates the sliders' responses to the passage of a rectangular bump on the disk surface. The bump has a height of 10 nm and width of 25  $\mu\text{m}$ . For all three designs, the slider reacts slightly as the bump travels under the front taper and then experiences larger oscillation as the bump encounters the more sensitive lower film thickness portions of the bearing. The 50%/25 nm slider flies 10 nm higher than the 50%/15 nm slider, therefore, its bump excitation level is significantly lower than that of the 50%/15 nm slider, which is responsible for its smaller fly height oscillation over the bump. Figure 4.8 also shows that the 30%/15 nm slider has a larger amplitude and faster decaying oscillation compared with the 50%/15 nm slider, which flies at about the same fly height. This is attributed to the smaller air bearing stiffness and higher damping ratio of the 30%/15 nm design versus the 50%/15 nm design. Table 4.4 summarizes the minimum spacing and the maximum bump heights for the slider to fly

over without contact. The maximum bump height is determined by gradually increasing the bump height for the bump response simulation. Any bump higher than those heights will result in a slider/bump contact. The air bearing stiffness, minimum fly height and slider size are the key factors that determine the maximum bump heights. Among the three slider designs, the 50%/15 nm slider has the smallest bump height, followed by the 30%/15 nm and 50%/25 nm designs.

**4.3.5 Track Seeking Dynamics.** Track seeking is the process for the slider to move from one track to another. This process involves head motion as well as the dynamics of the suspension. The radial displacement of the slider changes the skew angle and the relative disk velocity, while the slider's accelerations introduce the inertia force. Both of these can adversely affect the spacing between the slider and disk. In our study, the HTI 1650E type suspension is used for the two 50% sliders. Its FEM mesh is displayed in Fig. 4.9. 3331 nodes are used to model this suspension with a dense mesh distribution in the portion of the integrated gimbal. Figure 4.10 shows FEM mesh of the HTI FX30U type suspension for the 30%/15 nm design, in which 4742 nodes are employed to discretize the suspension. The eigenvalue solution is first obtained using ABAQUS, then the first 10 modes are used in the air bearing simulation to represent the suspension dynamics during the track seeking event. Figure 4.11 presents the track accessing profile. To move the slider from 23 mm to 32.52 mm in the radial direction, it is first accelerated to 2.243m/s, followed by a short period of constant velocity, then decelerated to 0 velocity. The maximum acceleration/deceleration is 60G. During the whole process, the geometrical skew angles change from -6.95 to -17.42 degrees for the 50%/15 nm design

and the 30%/15 nm design, and from -8.32 to -18.39 degrees for the 50%/25 nm design. Figure 4.12 shows the flying characteristics of the three designs during the track seeking process characterized in Fig. 4.11. Also plotted in Fig. 4.12 is the steady-state flying height as a function of radius (but plotted on the corresponding time scale for the dynamic process, dotted line) for comparison. The steady-state results are calculated using the effective skew angle and the relative disk velocity at the appropriate radius. The effective skew angle is the angle between the slider's length axis and the relative disk velocity vector. Positive skew implies that the air flows from the inner rail to the outer rail. When accessing from ID to OD, the seeking velocity decreases the relative disk velocity component in the slider's width axis direction and increases the relative disk velocity component in its length axis direction, which results in a smaller effective skew angle than the geometric skew angle. The difference between the dynamic flying characteristics and the steady state flying characteristics is due to this effect together with the contribution of inertia to the laterally moving slider. We define the dynamic fly height modulation as this difference. The inertia force of the moving head during acceleration stage produces a negative roll motion, while the inertia force during the deceleration stage generates a positive roll motion. The amount of the dynamic roll change increases with the level of the inertia force. Also, it is inversely proportional to the air bearing roll stiffness for a given inertia force. Figure 4.12 shows that the 50%/15 nm slider has a smaller dynamic roll modulation as a result of its higher air bearing roll stiffness as compared with the 50%/25 nm slider. However, the 30%/15 nm slider has a smaller dynamic roll modulation than the 50%/25nm slider even though it has a smaller air

bearing roll stiffness. This is because of its lower level of inertia force associated with its smaller slider size. The dynamic fly height modulation is closely related to the roll motion caused by the inertia force. A larger roll motion leads to a larger dynamic fly height variation. The fly height modulation pattern shown depends on the read-write element location, the accessing direction and the pitch motion. In our study, the slider moves from ID to OD. For the 50%/15 nm design and the 30%/15 nm design whose read-write elements are located at the outer rail trailing edge, the negative roll motion produced during the acceleration stage decreases the fly height, while the positive roll motion generated during deceleration stage increases the fly height. For the 50%/25 nm design, the roll motion results in a decrease of the fly height during the acceleration stage even though the read-write transducer is located at center trailing edge. This is because the inertia force also produces a pitch increase as shown in Fig. 4.13. The pitch and the fly height change do not appear to be related for the 50%/15 nm and 30%/15 nm designs. The pitch is affected very little by the slider's inertia in the off-track direction. The only noticeable effect is a small decrease from the steady state pitch.

#### **4.4 Summary**

The dynamic characteristics of three sub-25 nm fly height sliders are studied in this chapter using the CML Air Bearing Dynamic Simulator. The implementation of a multi-grid method results in a dramatic reduction of the solution time, which enables us to perform these more sophisticated simulations than would otherwise be feasible on our workstations. The air bearing stiffnesses are first calculated using a linear perturbation

approach. The results indicate a strong dependence of the air bearing stiffness on the air bearing lifting force. Then, the sliders' impulse responses are calculated, and their air bearing damping characteristics are compared by examining the power spectral magnitude plots. To understand the disk surface roughness effect on the head/disk spacing variation, the transient fly height history over a supersmooth disk is simulated by directly incorporating the measured disk track profile into the simulator. The results show that the spacing modulation induced by disk roughness decreases with an increase in air bearing stiffness and decrease in slider size. The sliders' responses to a passing bump are simulated and correlated with the air bearing stiffness and damping characteristics. In addition, the maximum bump heights without contact are determined. It is found that the maximum bump heights decrease as the air bearing stiffness and the slider size increase, and increases with the minimum spacing. The motion of the slider during a track accessing event is also calculated using the HTI 1650E and FX30U type suspensions. Modal analysis is employed to integrate the suspension dynamics into the air bearing simulation. It is concluded that the fly height modulation is attributed to many factors such as the effective skew angle, the seeking velocity, the accessing direction, and the roll motion caused by the inertia of the moving head. The extent of the roll motion effect depends on the air bearing roll stiffness and the inertial force of the moving head. Smaller roll stiffness and larger inertia force produce a larger roll motion effect on the head-disk spacing modulation during a track access event.



Sliders	Vertical (kN/m)	Pitch (mN-m/rad)	Roll (mN-m/rad)
50%/25 nm	975.2	632.8	225.8
50%/15 nm	2188.2	1706.7	983.4
30%/15 nm	589.4	161.7	88.8

**Table 4.1** Air bearing stiffness

Sliders	Positive Force (gram)	Negative Force (gram)	Net Force (gram)
50%/25 nm	5.56	2.56	3.0
50%/15 nm	10.0	7.0	3.0
30%/15 nm	2.89	1.69	1.2

**Table 4.2** Air bearing forces: lifting force, suction force and net force

Sliders	Mean Fly Height (nm)	FH Modulation (nm)	Standard Deviation (nm)
50% / 25 nm	23.84	+6.359 (26.67%) -4.486 (18.82%)	1.185
50% / 15 nm	14.25	+4.484 (31.47%) -2.908 (20.41%)	0.689
30% / 15 nm	16.17	+3.074 (19.01%) -2.027 (12.54%)	0.472

**Table 4.3** Summary of fly height modulation

Sliders	50%/25 nm	50%/15 nm	30%/15 nm
Minimum Spacing (nm)	22.94	11.78	13.85
Maximum Bump Height Without Contact (nm)	28	14	21

**Table 4.4** Minimum spacing and maximum bump height for the slider to fly over without contact

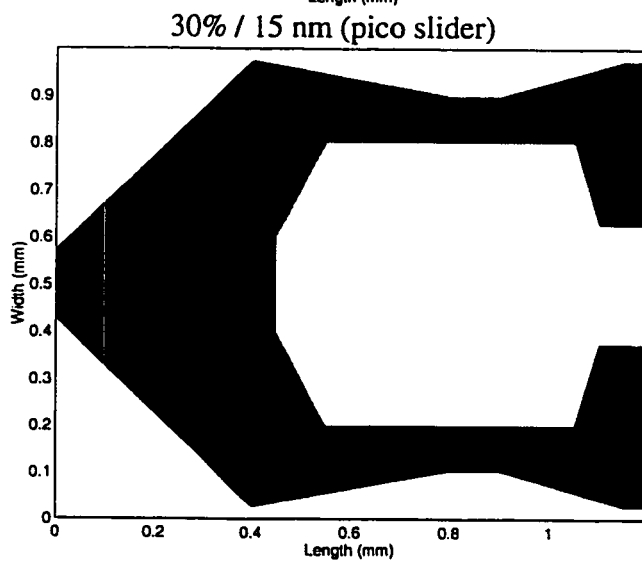
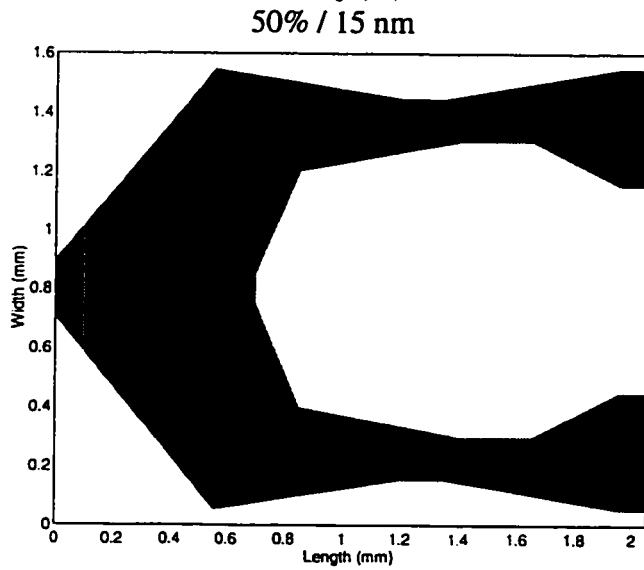
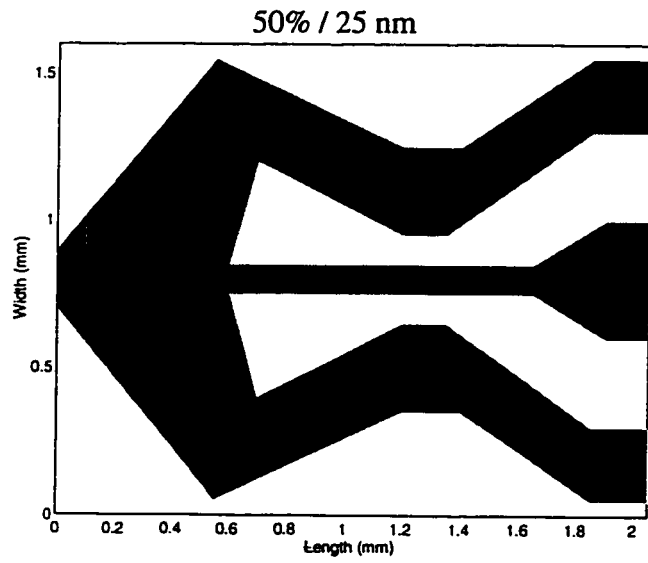
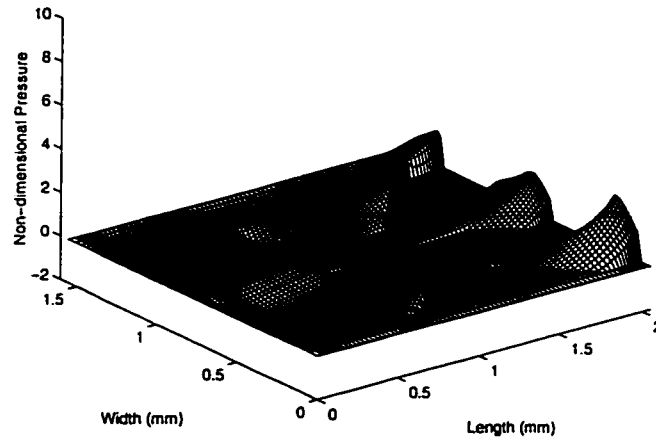
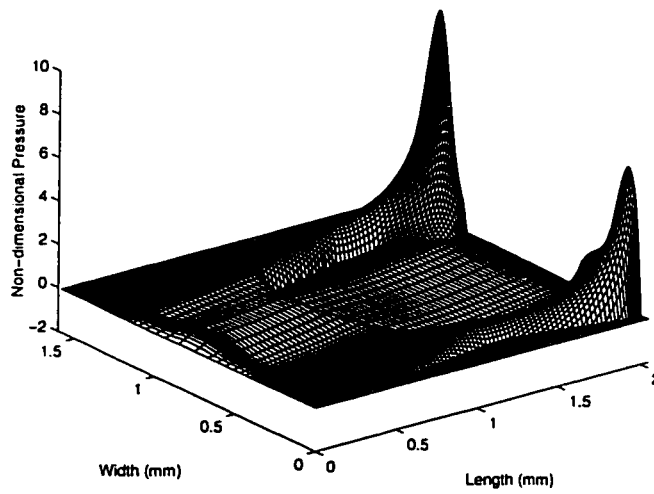


**Fig. 4.1** Three sub-25 nm fly height slider designs

50% / 25 nm



50% / 15 nm



30% / 15 nm

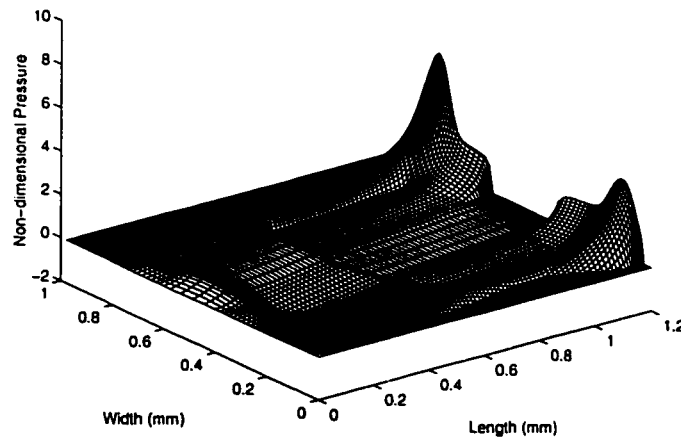


**Fig. 4.2** 3D non-dimensional air bearing pressure profiles

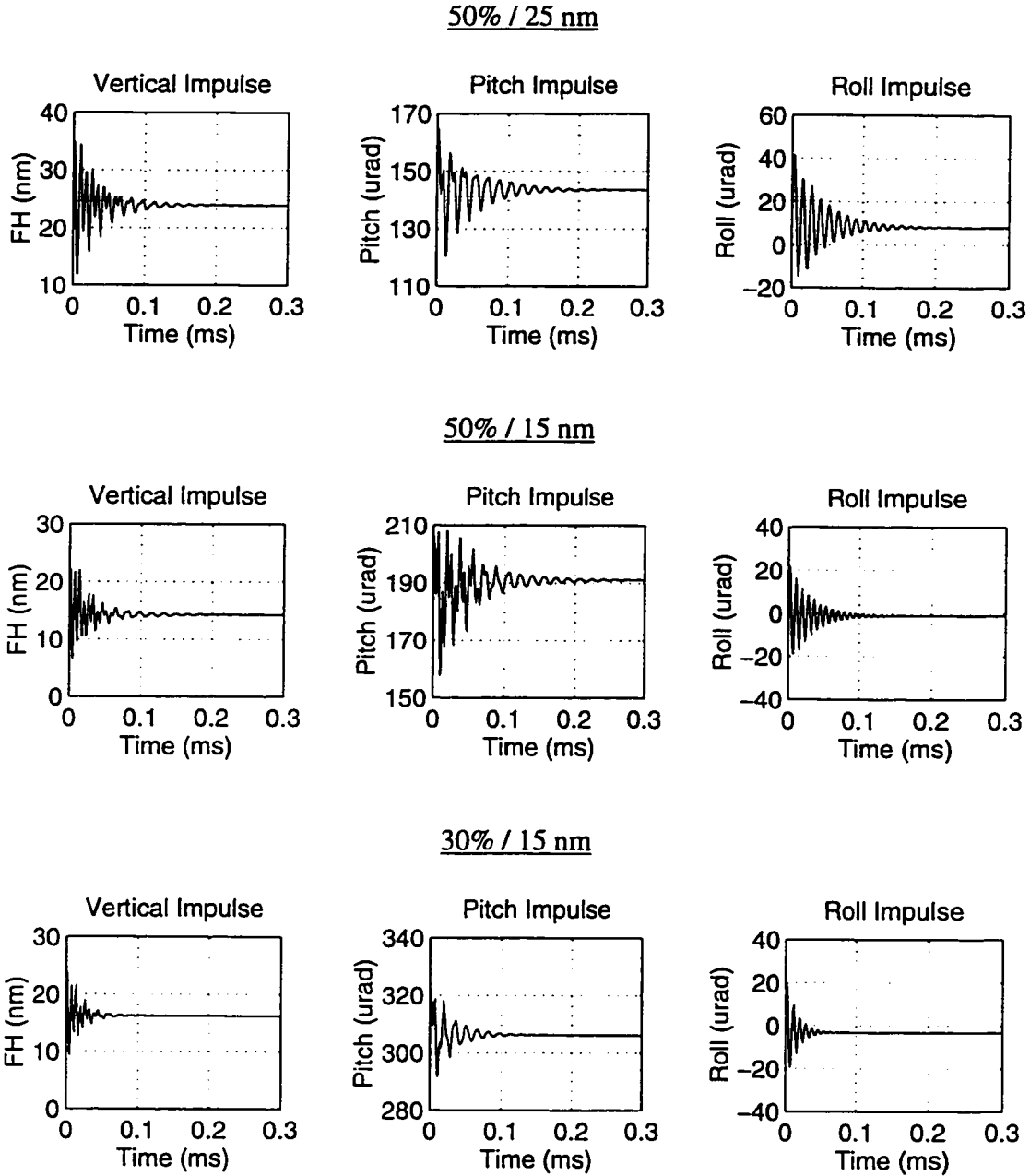


**Fig. 4.3** Impulse responses. Initial vertical velocity = 10 mm/s for vertical impulse responses, initial pitch angular velocity = 20 rad/s for pitch impulse responses, initial roll angular velocity = 20 rad/s for roll impulse responses

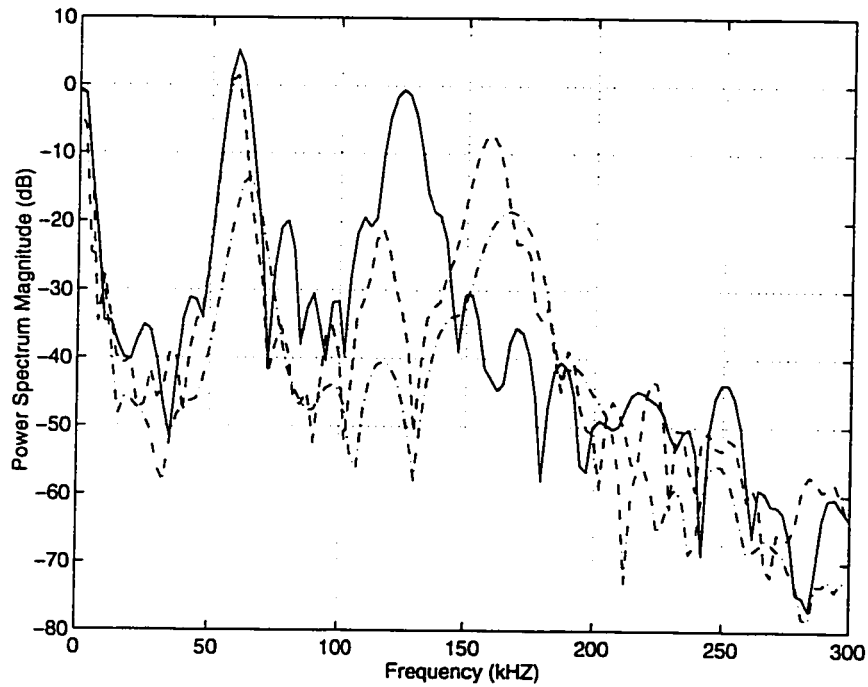


**Fig. 4.4** Power spectral magnitude plots of vertical impulse responses. Initial vertical velocity = 10 mm/s, 50%/25 nm design (solid line), 50%/15 nm design (dash line) and 30%/15 nm design (dash dot line)

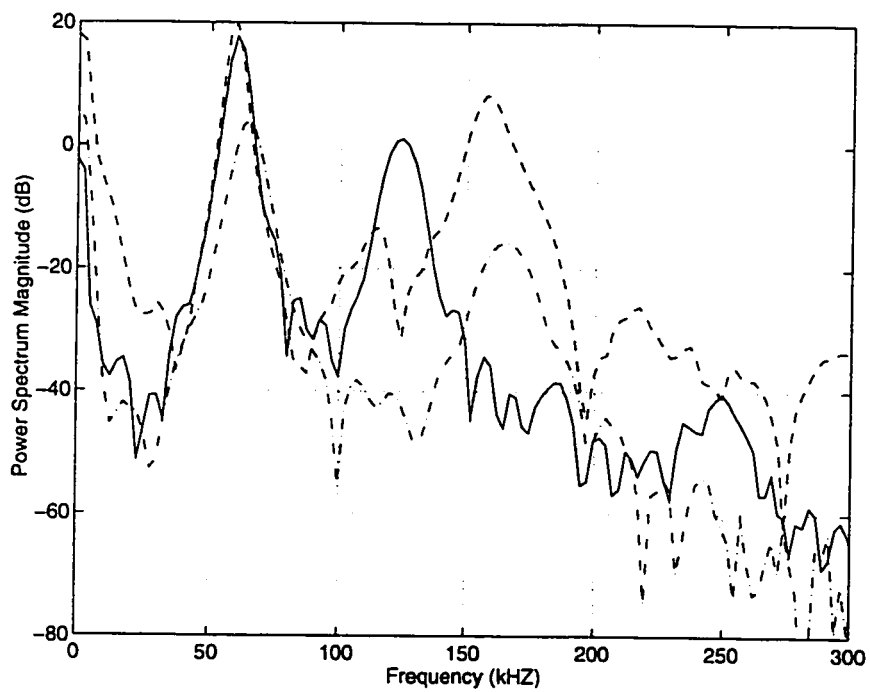


**Fig. 4.5** Power spectral magnitude plots of pitch impulse responses. Initial pitch angular velocity = 20 rad/s, 50%/25 nm design (solid line), 50%/15 nm design (dash line) and 30%/15 nm design (dash dot line)

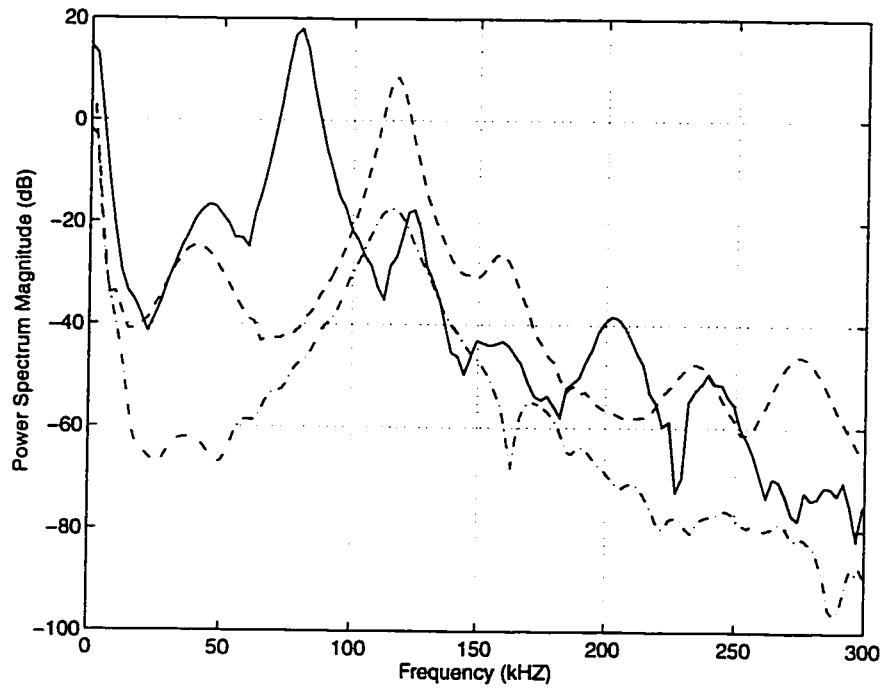


**Fig. 4.6** Power spectral magnitude plots of roll impulse responses. Initial roll angular velocity = 20 rad/s, 50%/25 nm design (solid line), 50%/15 nm design (dash line) and 30%/15 nm design (dash dot line)

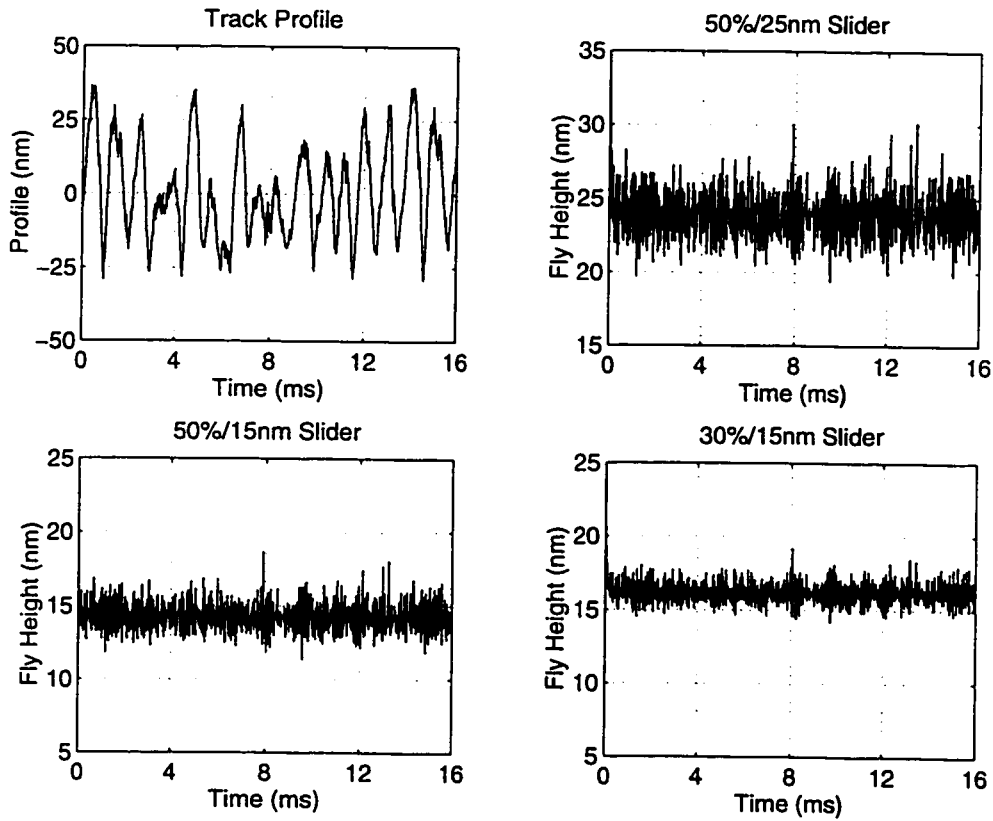


**Fig. 4.7** Fly height modulation

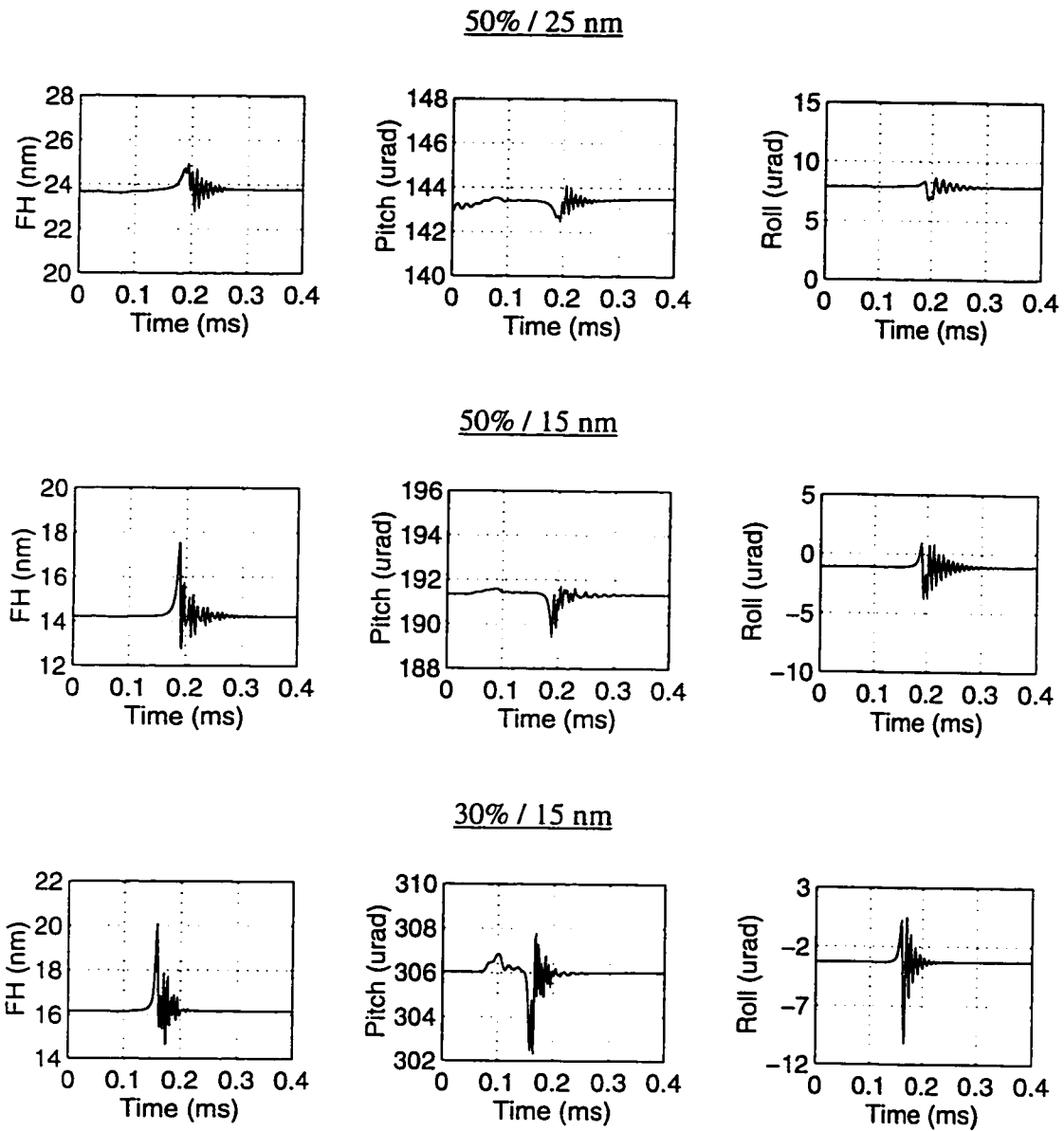


**Fig. 4.8** Bump responses. Bump height = 10 nm, width = 25  $\mu\text{m}$

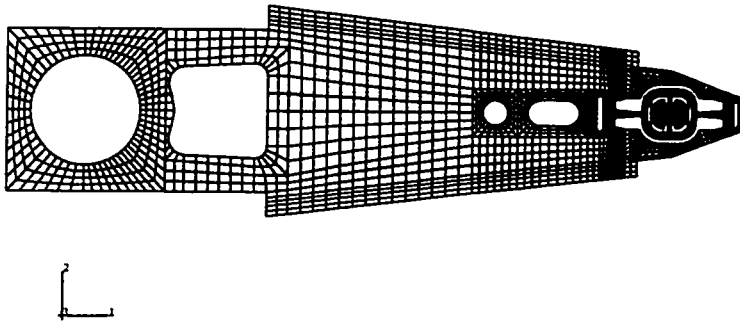


**Fig. 4.9** FEM mesh of a HTI 1650E type suspension

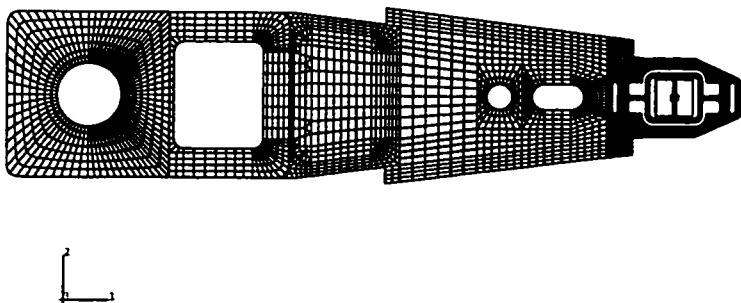


**Fig. 4.10** FEM mesh of a HTI FX30U type suspension



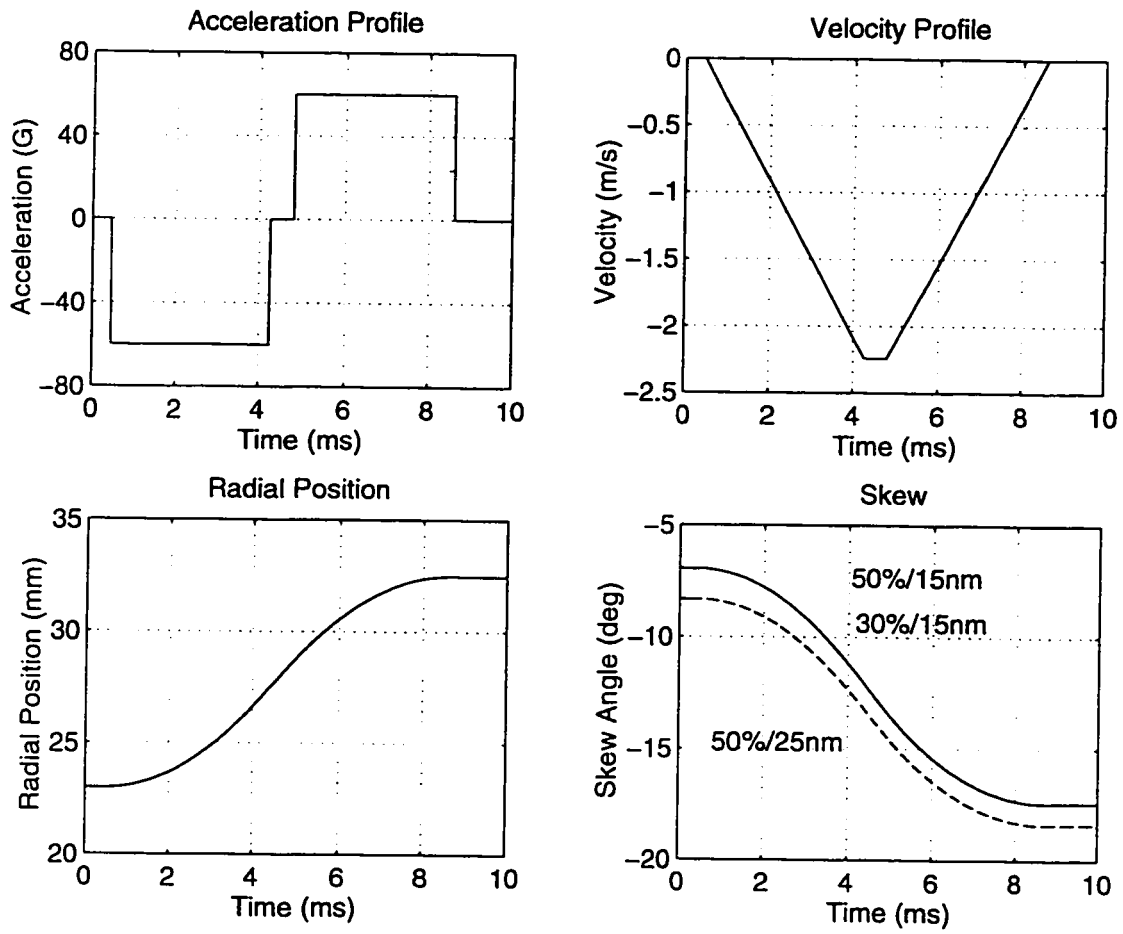


**Fig. 4.11** Track seeking profile

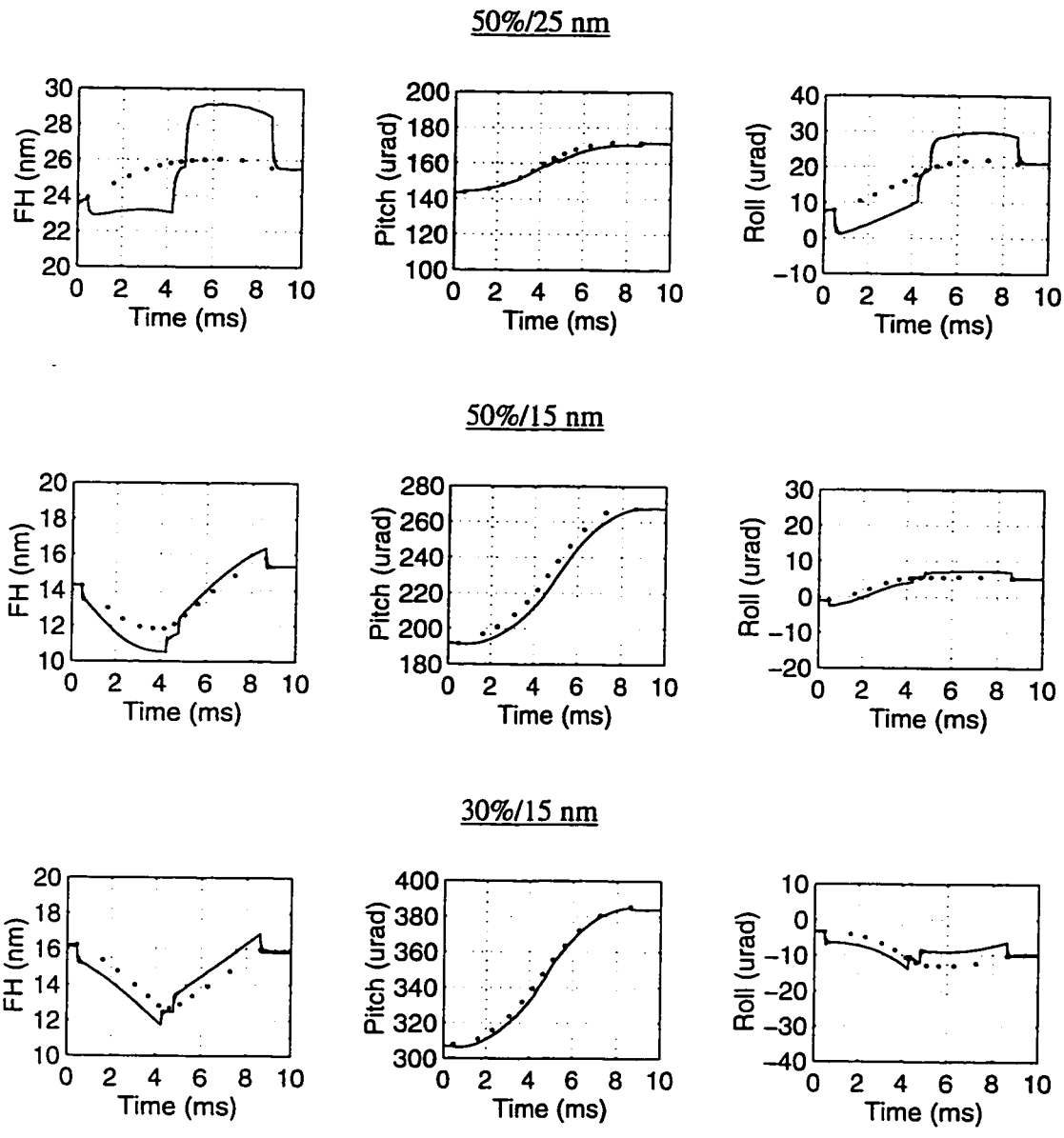


**Fig. 4.12** Fly characteristics during a track seeking event. The dotted lines represent the steady state flying characteristics calculated using the effective skew angle and the relative disk velocity as seen from the head at the radius appropriate to the time shown

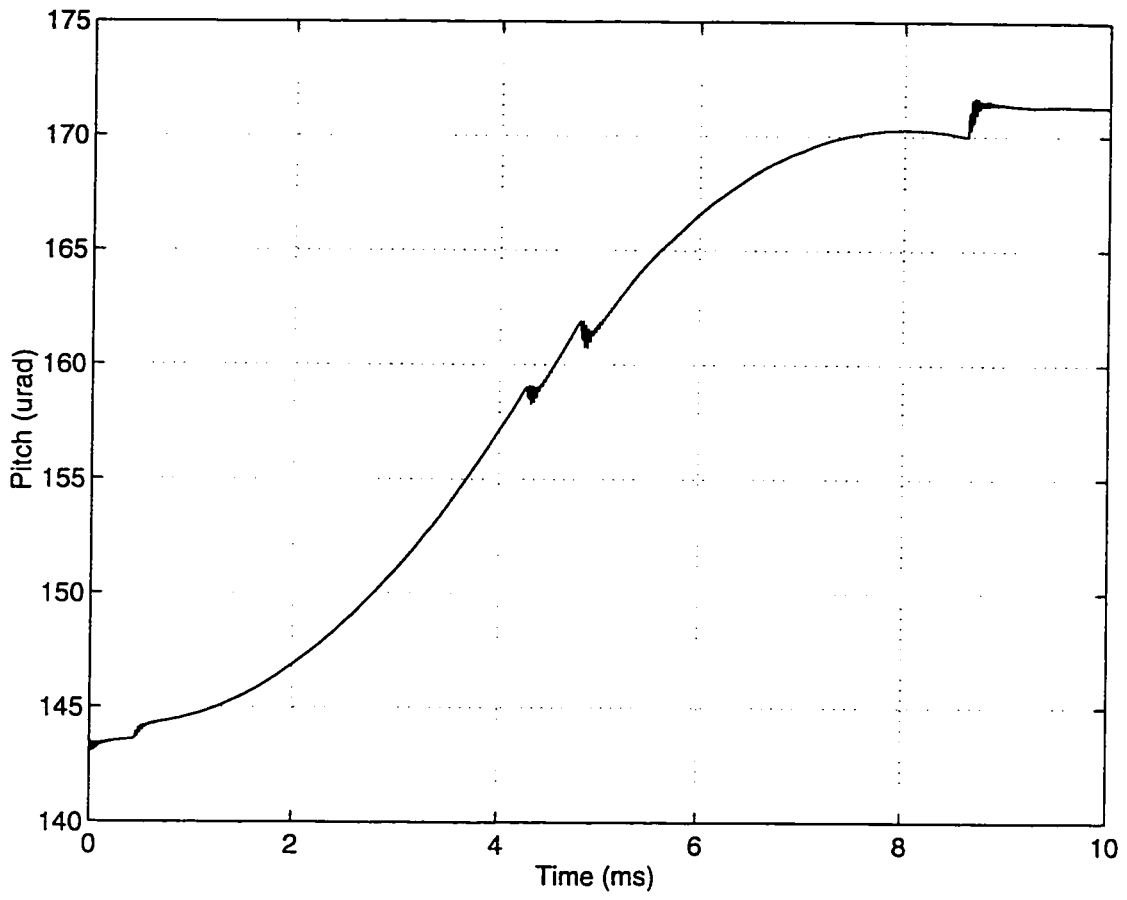


**Fig. 4.13** Pitch during a track seeking event for the 50%/25 nm slider

# CHAPTER 5

## NUMERICAL STUDY OF A SLIDER'S CONTACT TAKE-OFF PROCESS\*

### 5.1 Introduction

With progressive size miniaturization and performance enhancements, magnetic recording on a hard disk drive has necessitated a smaller and smaller reliable head-disk interface. In recent hard disk drive designs, the spacing approaches sub-25 nm levels. This trend towards lower fly heights puts increased demands on the mechanical durability of the head-disk interface during the contact start/stop (CSS) operation. CSS is a process in which the slider is in sliding contact with the disk as it starts and stops rotating. Therefore, minimizing mechanical wear during the CSS process is a key factor to a successful drive design. Because of these demands, the need for an in-depth understanding of the slider/disk interaction dynamics during the CSS process is apparent.

Two key parameters that characterize the mechanical durability of the CSS operation are the take-off velocity (TOV) and landing velocity (LV). With a higher TOV and LV, the sliding distance between the slider and disk is longer and the wear volume is larger. Methods of decreasing the TOV and LV have been pursued to reduce wear during the CSS operation. Lee *et al.* (1989) showed by use of strain gage transducers that the stiction and the TOV depend on the crown and rail width of the slider. Zhu and Bogy (1989a) found that negative crown on the rails produces more disk wear than positive

---

\* Parts of this chapter are submitted for publication, see Hu and Bogy (1995c)

crown. They also explained the motion of crowned sliders during the CSS operation, where it is generally accepted that the slider initially pitches forward during take-off for positive crown sliders, but not for negative crown sliders. Suk *et al.* (1992) investigated the influence of crown on slider dynamics during the take-off stages of disk drives using the multi-channel laser interferometer. They concluded that positive crown sliders are less susceptible to undesirable disturbances caused by surface defects, and positive crown sliders may cause less disk wear due to their shorter sliding distance and less probability of point contacts with the disk in the initial stage of the take-off process. For comparison with the above-mentioned experimental investigation, there are very limited numerical studies of the slider's contact take-off/landing process due to the lack of a reliable model. Bolasna (1990) used an air bearing simulation to analyze the effects of slider/suspension parameters on the TOV of a taper flat slider and a shaped IBM 3380 K slider. In his study, the actual slider/disk contact is ignored, and take-off from the disk is assumed to take place at a given fly height. Using this criterion, he found that crown is the most significant slider/suspension parameter affecting the TOV.

A newly developed mixed lubrication model is presented in this chapter and the effects of the air bearing and other design parameters on the slider's take-off process are investigated using this model. We use a pre-defined percent of the suspension load as a criterion to determine a slider's take-off from a disk. A sub-25 nm fly height slider with shaped-rails is used in this study. We present a simulation analysis of the effects of the slider's crown, camber, twist, taper angle, the disk surface roughness and the head/disk interface friction coefficient on the slider's take-off velocity, take-off fly height, and

initial flying characteristics. It is concluded that the slider's crown and disk surface roughness are the most significant parameters affecting the take-off velocity. Larger crowns and smoother disk surfaces reduce the take-off velocity. The initial take-off flying characteristics are mostly determined by the slider's crown and the contact friction coefficient. Smaller crowns and friction coefficients produce a smoother initial take-off performance.

## 5.2 Mixed Lubrication Model

The Fukui-Kaneko linearized Boltzmann equation is used to model the nonlinear rarefaction effects in the modified Reynolds equation for the ultra-low fly heights in CSS. An elastic-plastic asperity-based contact model (Chang, *et al.*, 1987, 1992) is employed to extract the slider/disk contact forces and moments during the take-off process.

## 5.3 Results and Discussions

The "Nutcracker" slider designed in CML and built by Read-Rite Corporation is used for the sample calculations. It is a shaped-rail 50% sub-ambient pressure type slider. Figure 5.1 shows the shape of its air bearing surface. The slider has a 24 degrees wall angle from horizontal. The design target fly height is about 25 nm under 3.5 grams of suspension load. The slider design has a center rail that carries the read-write element. The read-write point is offset 25  $\mu\text{m}$  forward from the trailing edge. The slider used in our calculations is assumed to have a 15 nm crown. It is also designed with a positive 10 nm camber so that the closest point of separation with the disk is near the center rail

trailing edge. The rail shapes are concave on both sides to minimize the fly height change across the disk. The connected front region of the air bearing surfaces allows the air to expand to a rather low (sub-ambient) pressure, and the recession zone then produces a suction force which attracts the slider to the disk. The disk rotational speed is 5400 rpm. In our simulation, the Hutchinson 1650E type suspension is used. Its FEM mesh is displayed in Fig. 5.2. 3331 nodes are used to model this suspension with a dense mesh distribution in the portion of the integrated gimbal. The eigenvalue solution is first obtained using ABAQUS, then the first 10 modes are used in the air bearing simulation to represent the suspension dynamics during the take-off event.

Figures 5.3 and 5.4 show the slider's contact take-off dynamics during the early moments of the start-up through the first 16 ms. As seen in Fig. 5.3, the slider is initially at rest on the disk surface, when at 0.01 ms, the disk begins to rotate. Due to the positive crown and the sudden action of the contact friction force at the interface, the slider oscillates mainly in the pitch mode for about 0.1 ms. After the initial transient oscillation, the slider's pitch decreases under the contact friction force at the interface, resulting in an increase in the trailing edge fly height. As shown in Fig. 5.4, the trailing edge fly height reaches a maximum of 15.2 nm at about 1.5 ms, and then decreases as the disk speed is increasing. Figure 5.5 shows the continuation of the flying characteristics as functions of the disk speed after the start-up. As the disk speed increases, the air bearing pressure builds up in the front taper region, increasing the pitch of the slider. The trailing edge fly height thus decreases, attaining a minimum of 5.1 nm at the disk speed of 0.44 m/s, which is well below the at-rest spacing, and then it increases with the disk speed as

it takes off. The disk velocity at which the slider takes off from the disk is referred to as the take-off velocity (TOV) of the slider. The practice of using a given fly height to determine the TOV assumes that the take-off fly height is independent of the air bearing and other design parameters. This assumption does not reflect the slider/disk contact conditions during the take-off process. It will be shown later that the take-off fly height, just like the TOV, depends on many air bearing and other design parameters. The more physically realistic criterion for determining the process of a slider taking off from a disk is a pre-defined contact force as a percent of the preload. Throughout this study, it is assumed that take-off from a disk takes place at the disk speed at which the normal contact force reduces to only 1% of the preload. The fly height at the read-write point at take-off is referred to as the take-off fly height. Using this definition, we calculated the TOV and the take-off fly height for the case shown in Figs. 5.3, 5.4 and 5.5. The slider takes off at a TOV of 0.98 m/s and the take-off fly height at the read-write point is 7.1 nm.

**5.3.1 Effect of Slider Crown.** The crown is a longitudinal parabolic surface superimposed lengthwise on the slider's ABS. Figure 5.6 shows the TOV as a function of crown height. As expected, the larger crown sliders take off faster (at a lower disk velocity) than sliders with smaller crown. The plot also shows that the decrease in the TOV is nonlinear in the range from 0 to 30 nm. The rate of TOV decrease with crown drops rapidly as the crown increases. At the higher crown heights, the crown effect on the TOV is less. This agrees with results obtained by Bolasna (1990). Figure 5.7 shows that the take-off fly height increases with the crown height. The effect of crown on the



initial flying characteristics during the contact start-up are shown in Fig. 5.8. The trailing edge fly height and pitch changes from the at-rest values for the slider with two different crown heights are plotted. The slider with 30 nm crown experiences a much larger amplitude transient oscillation and has a greater pitch drop than the slider without crown.

**5.3.2 Effect of Slider Camber.** The camber is a deviation from flatness of the ABS similar to crown, except that it is in the transverse direction. Figure 5.9 is a plot of the TOV versus camber heights from 5 nm to 25 nm. The TOV increases almost linearly with camber height at a rate of about 0.034 m/s/nm, while the take-off fly height decreases as camber height increases (Fig. 5.10). During the contact start-up, an increase of the camber height reduces slightly the amplitudes of the transient flying height and pitch oscillations from their static values as shown in Fig. 5.11.

**5.3.3 Effect of Slider Twist.** The twist is given in terms of the relative height of four corners to the center. A positive twist increases the separation between the slider and the disk at the inner leading edge and the outer trailing edge, and decreases the separation at the outer leading edge and inner trailing edge. Figure 5.12 shows the TOV as a function of the twist. The effect of twist on the TOV is smaller than the crown and camber. The TOV decreases nearly linearly as the twist changes from -10 nm to 10 nm. The take-off fly height does not appear to change much with twist, as illustrated in Fig 5.13. Figure 5.14 shows the transient oscillations from rest values of the trailing edge fly height and pitch during the contact start-up for twist values of 0 and 5 nm. The slider with larger twist has less initial pitch drop.

**5.3.4 Effect of Slider Taper Angle.** In this study, the taper length is kept constant, and

different taper angles are achieved through changing the taper height at the leading edge. Figure 5.15 shows the TOV versus taper angle. The corresponding take-off fly height is plotted in Fig. 5.16. The sliders with smaller taper angle take off at a lower disk velocity and a lower take-off fly height than the sliders with larger taper angle. This is because a smaller taper angle improves the generation of the air bearing pressure in the front taper region during the take-off stage. As the taper angle increases, the rate of change of the TOV decreases. During the initial contact start-up, the larger taper angle sliders have a smaller increase of trailing edge fly height than the smaller taper angle sliders as shown in Fig. 5.17.

**5.3.5 Effect of Disk Surface Roughness.** Figure 5.18 shows the TOV as a function of the standard deviation of the asperity heights ( $\sigma$ ). As expected, the sliders take off at higher TOV's from rougher disk surfaces than from smoother disk surfaces. The rate of change of the TOV increases as  $\sigma$  increases. The take-off fly height increases linearly with  $\sigma$  (Fig. 5.19). Figure 20 illustrates the initial transient flying characteristics during the contact start-up for  $\sigma=3$  nm and 6 nm. When taking off from a rougher disk surface, the sliders endure a larger amplitude and slower decaying oscillation. The rougher disk surface also results in a higher increase of the trailing edge fly height.

**5.3.6 Effect of Head/Disk Interface Friction Coefficient.** Figures 5.21 and 5.22 show the TOV and the take-off fly height versus the friction coefficient, respectively. It is seen that the friction coefficient does not have any influence on the TOV. The only noticeable effect is a slight increase of the take-off fly height with the friction coefficient. Even though the friction coefficient has the least effect on the TOV and the take-off fly height,

it has a substantial influence on the initial flying characteristics during the start-up, as shown in Fig. 5.23. The larger friction coefficient introduces a larger amplitude and slower decaying oscillation. This is expected since the contact start-up oscillation is mainly generated by the sudden action of the friction force at the interface at start-up. The increase of the trailing edge fly height for the friction coefficient of 0.5 is more than twice that for the friction coefficient of 0.2.

#### **5.4 Summary**

A mixed lubrication model is developed for investigating various air bearing and other design parameter effects on the slider's take-off performance. The Fukui-Kaneko linearized Boltzmann equation is used to model the nonlinear rarefaction effects in the modified Reynolds equation for fly heights down to contact. An elastic-plastic asperity-based contact model is employed to extract the slider/disk contact forces and moments during the take-off process. The criterion for take-off from a disk is defined as a specified percent of the suspension preload. A sub-25nm fly height slider with shaped-rails is used in this study. The effects of the slider's crown, camber, twist, taper angle, the disk surface roughness and the head/disk interface friction coefficient on the slider's take-off velocity and take-off fly height, as well as transient flying characteristics during start-up, are studied. Among the many air bearing and other design parameters affecting the take-off velocity, the slider's crown and disk surface roughness are particularly important. Larger crowns and smoother disk surfaces reduce the take-off velocity. The contact start-up take-off flying characteristics are mostly affected by the slider's crown

and the contact friction coefficient. Smaller crowns and friction coefficients produce a smoother initial take-off performance.

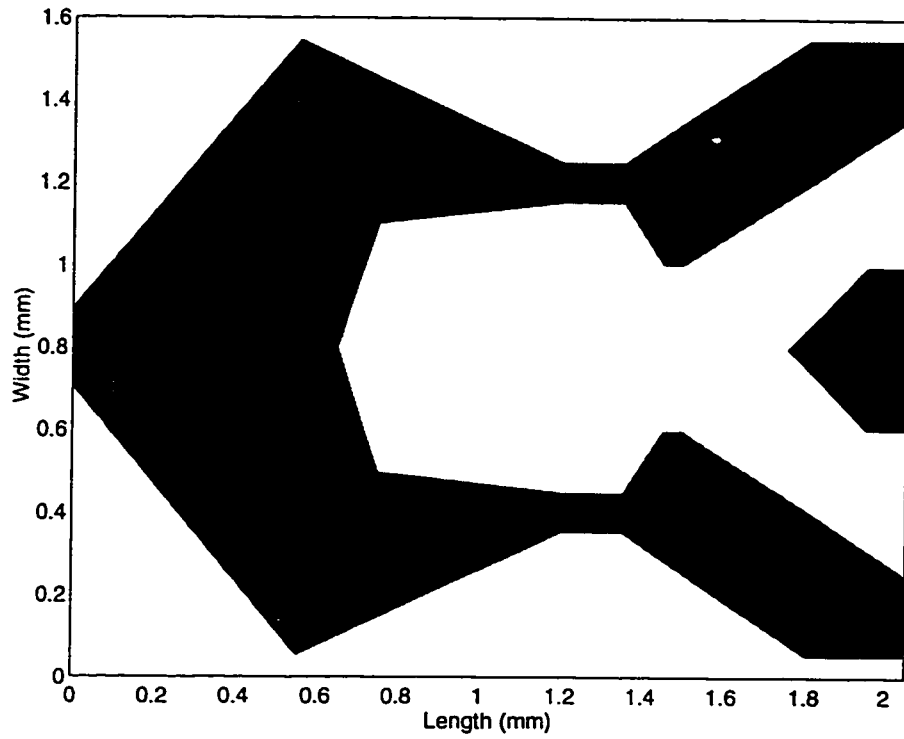


**Fig. 5.1** Air bearing surface for the Nutcracker slider

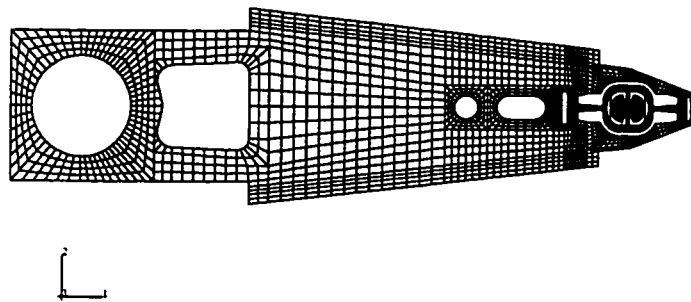


**Fig. 5.2** FEM mesh of a Hutchinson 1650E type suspension

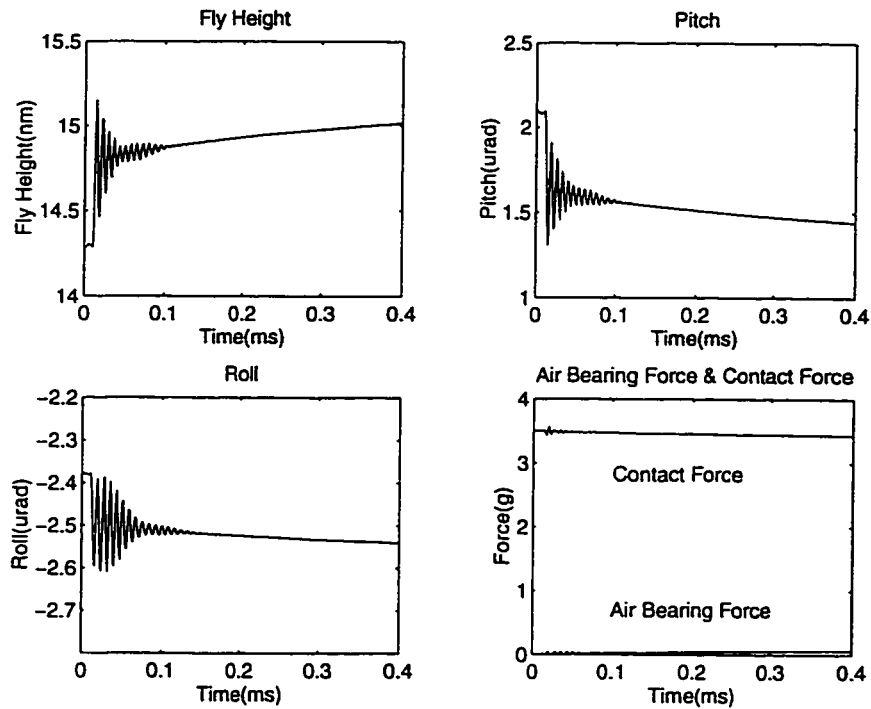


**Fig. 5.3** Flying characteristics during the contact start-up (up to the disk speed of 0.0018 m/s). Crown = 15 nm, camber = 10 nm, twist = 0, taper angle = 0.01 rad,  $\gamma = 0.2$  and  $\sigma = 3$  nm

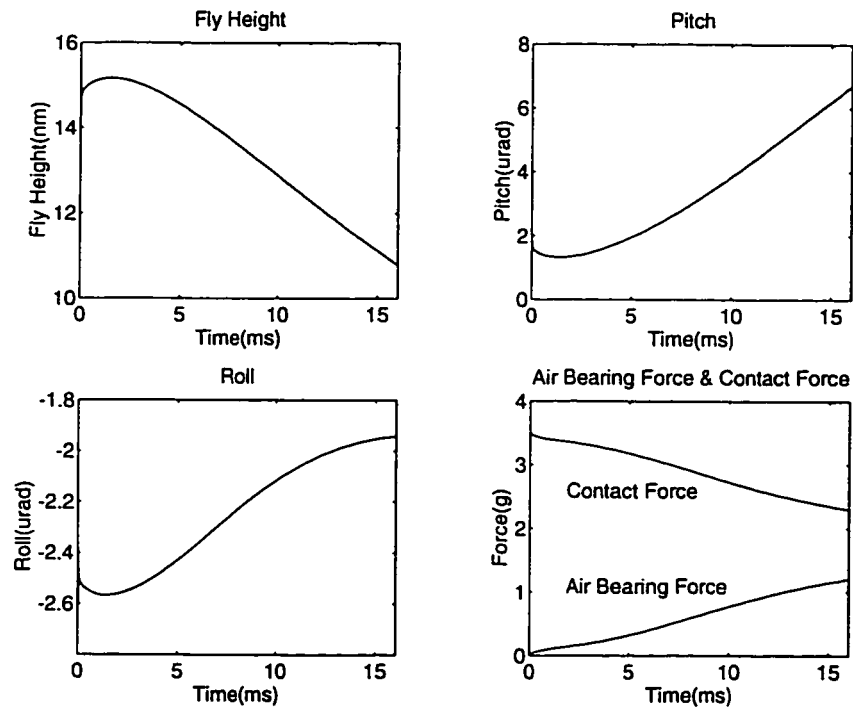


**Fig. 5.4** Flying characteristics during the contact start-up (up to the disk speed of 0.072 m/s). Crown = 15 nm, camber = 10 nm, twist = 0, taper angle = 0.01 rad,  $\gamma = 0.2$  and  $\sigma = 3$  nm

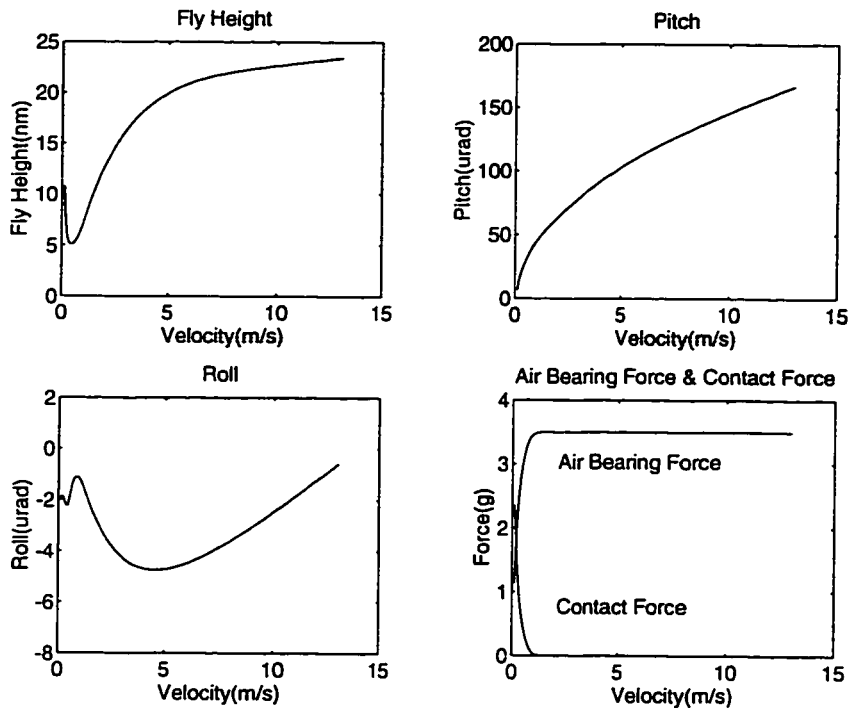


**Fig. 5.5** Fly characteristics after the start-up. Crown = 15 nm, camber = 10 nm, twist = 0, taper angle = 0.01 rad,  $\gamma = 0.2$  and  $\sigma = 3$  nm

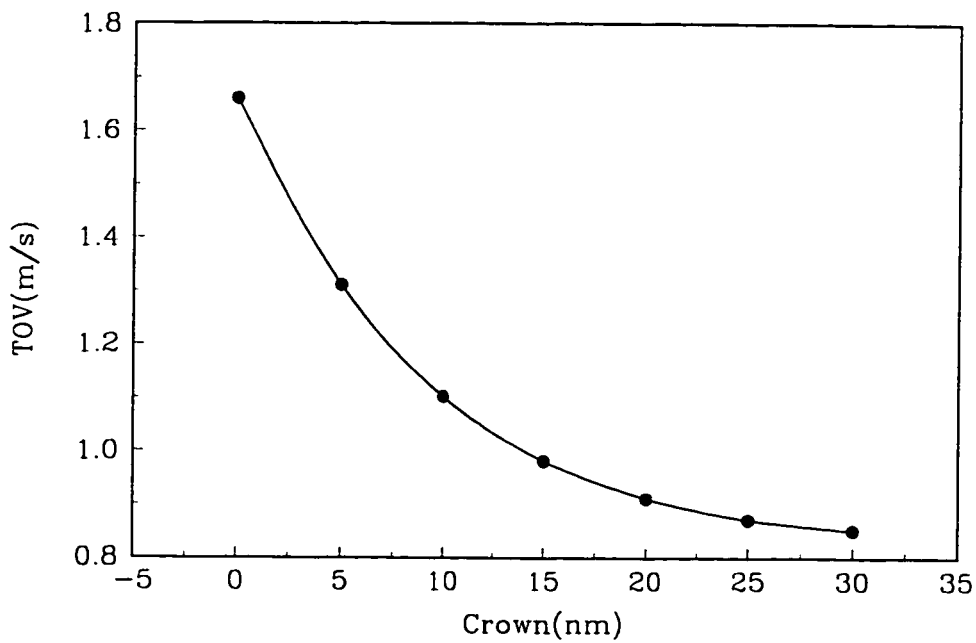


**Fig. 5.6** Take-off velocity versus crown. Camber = 10 nm, twist = 0, taper angle = 0.01 rad,  $\gamma = 0.2$  and  $\sigma = 3$  nm

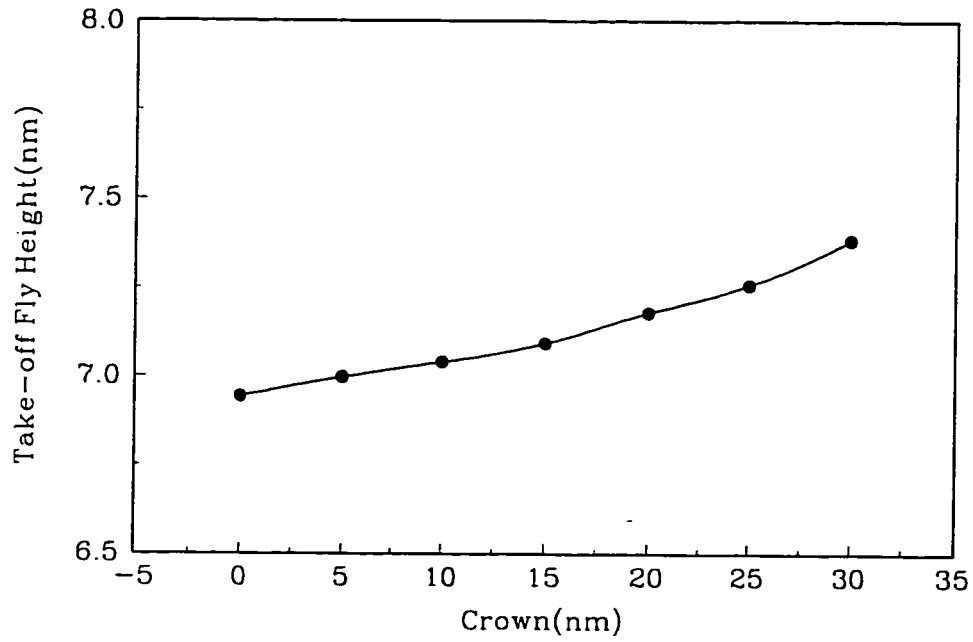


**Fig. 5.7** Take-off fly height versus crown. Camber = 10 nm, twist = 0, taper angle = 0.01 rad,  $\gamma = 0.2$  and  $\sigma = 3$  nm

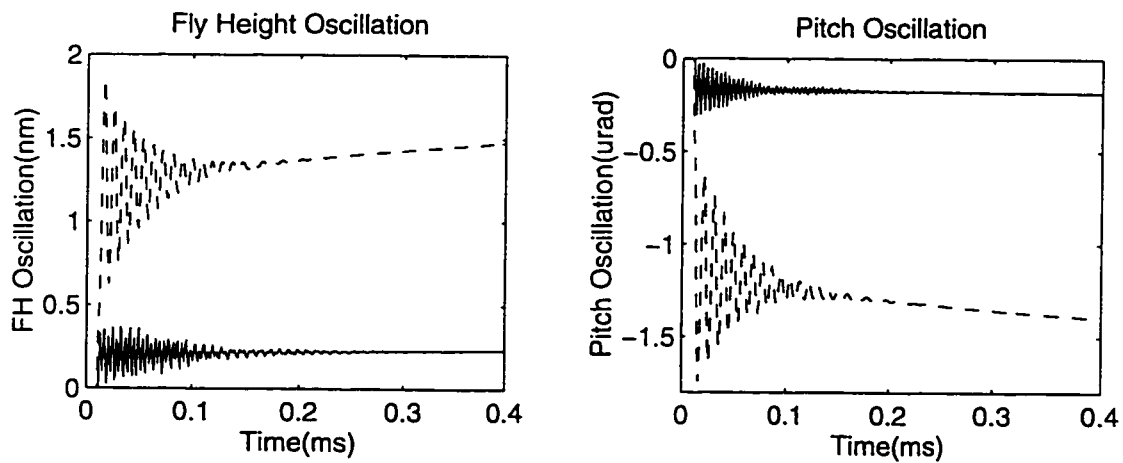


**Fig. 5.8** Fly height and pitch oscillations during the contact start-up for two crown heights. Crown = 0 (solid lines) and crown = 30 nm (dash lines)



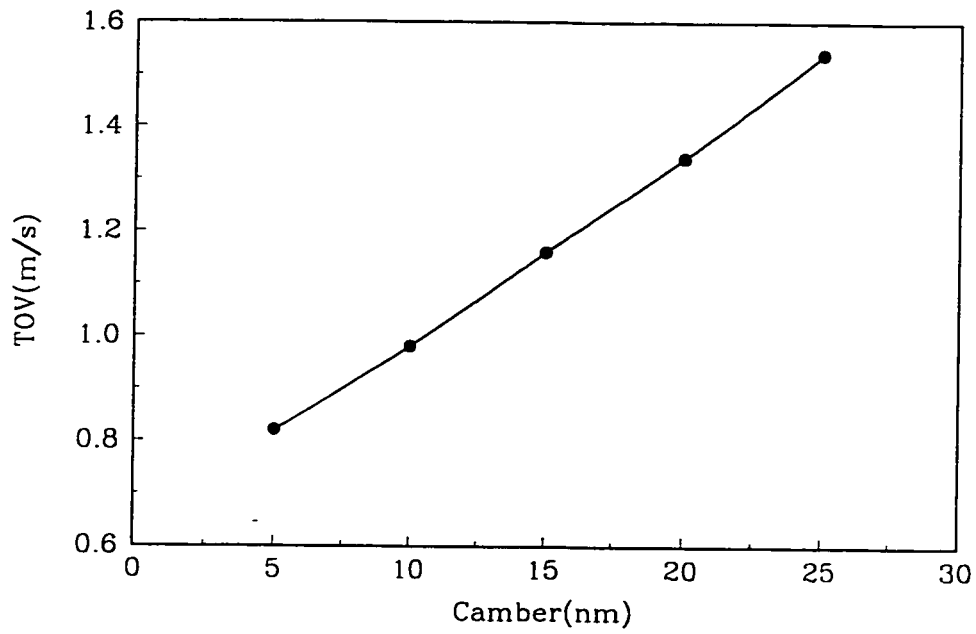


**Fig. 5.9** Take-off velocity versus camber. Crown = 15 nm, twist = 0, taper angle = 0.01 rad,  $\gamma = 0.2$  and  $\sigma = 3$  nm

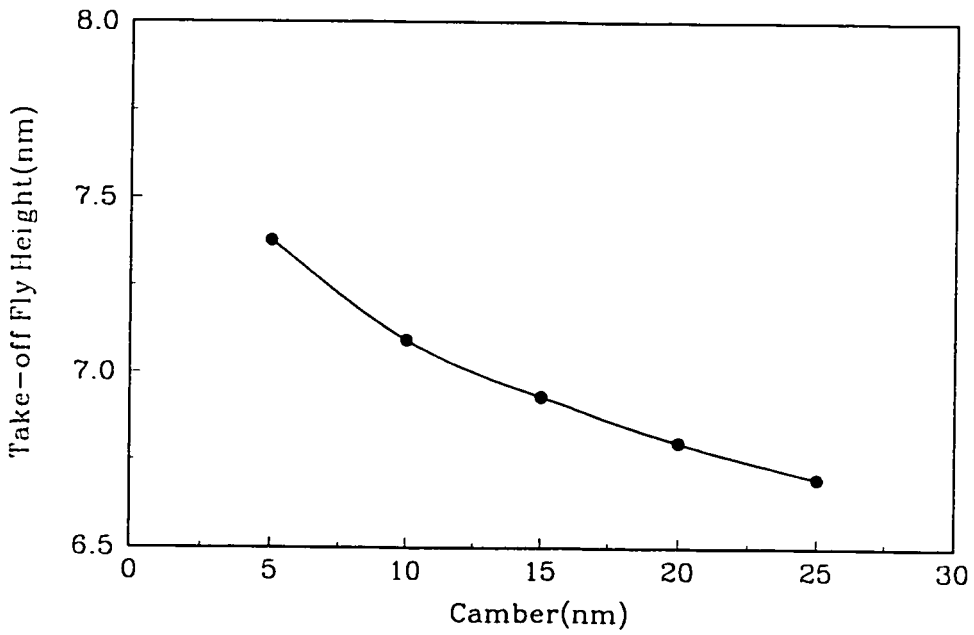


**Fig. 5.10** Take-off fly height versus camber. Crown = 15 nm, twist = 0, taper angle = 0.01 rad,  $\gamma = 0.2$  and  $\sigma = 3$  nm

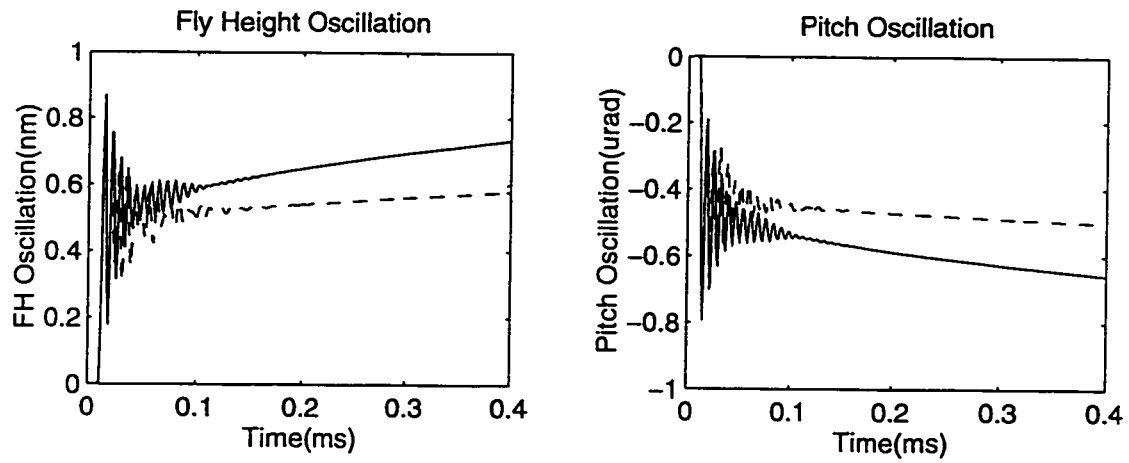


**Fig. 5.11** Fly height and pitch oscillations during the contact start-up for two camber heights. Camber = 10 nm (solid lines) and camber = 20 nm (dash lines)

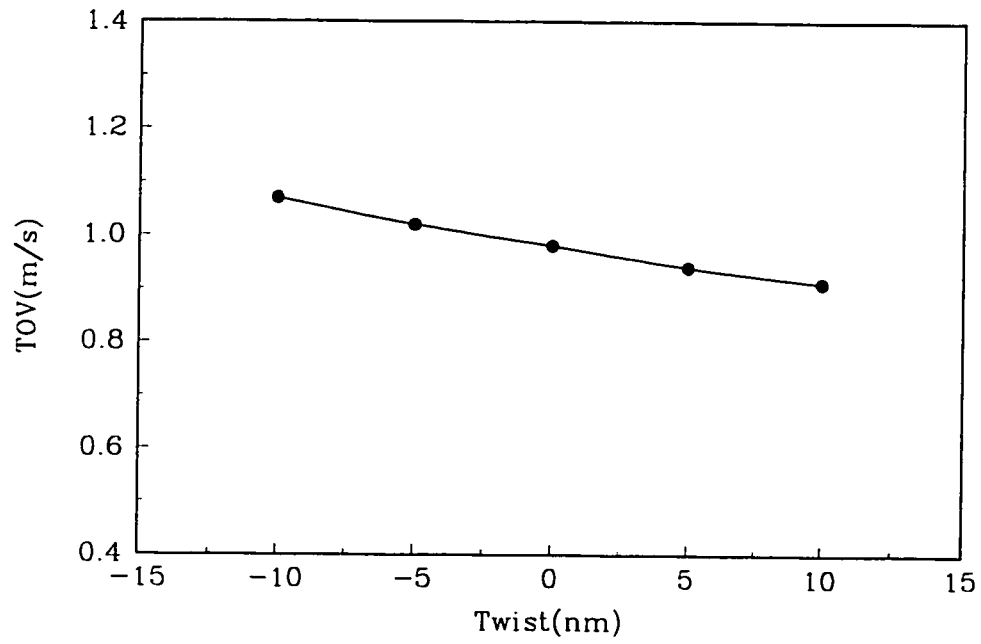


**Fig. 5.12** Take-off velocity versus twist. Crown = 15 nm, camber = 10 nm, taper angle = 0.01 rad,  $\gamma = 0.2$  and  $\sigma = 3$  nm

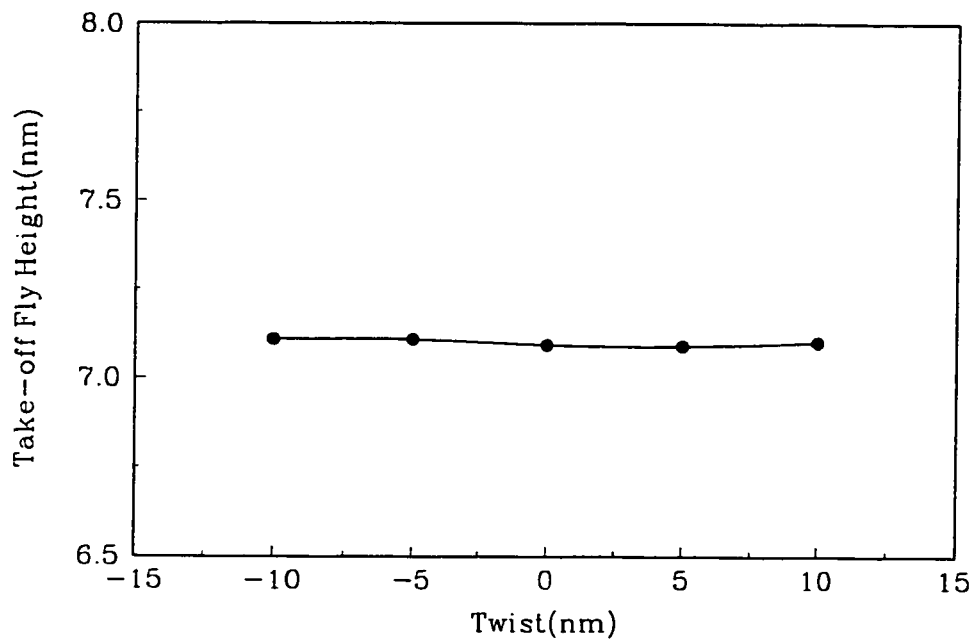


**Fig. 5.13** Take-off fly height versus twist. Crown = 15 nm, camber = 10 nm, taper angle = 0.01 rad,  $\gamma = 0.2$  and  $\sigma = 3$  nm

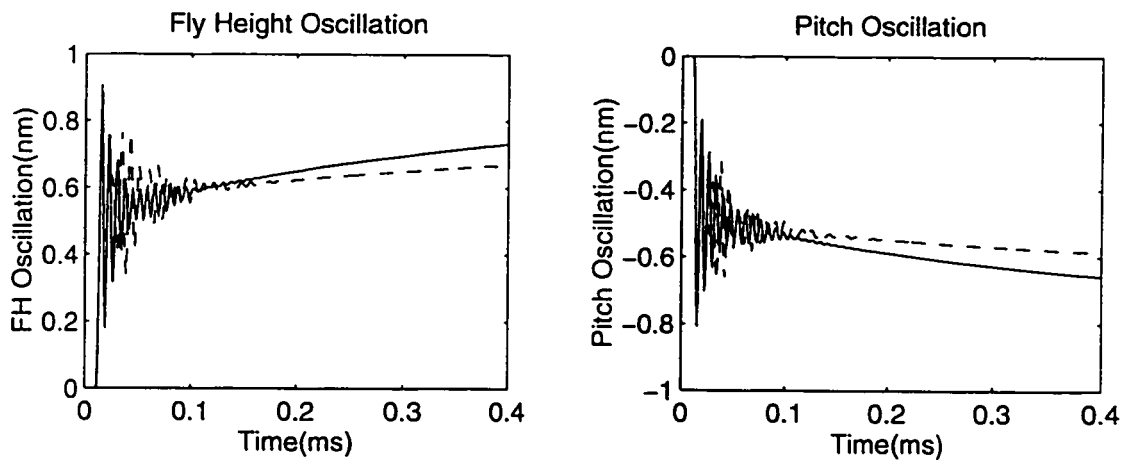


**Fig. 5.14** Fly height and pitch oscillations during the contact start-up for two twist values. Twist = 0 (solid lines) and twist = 5 nm (dash lines)

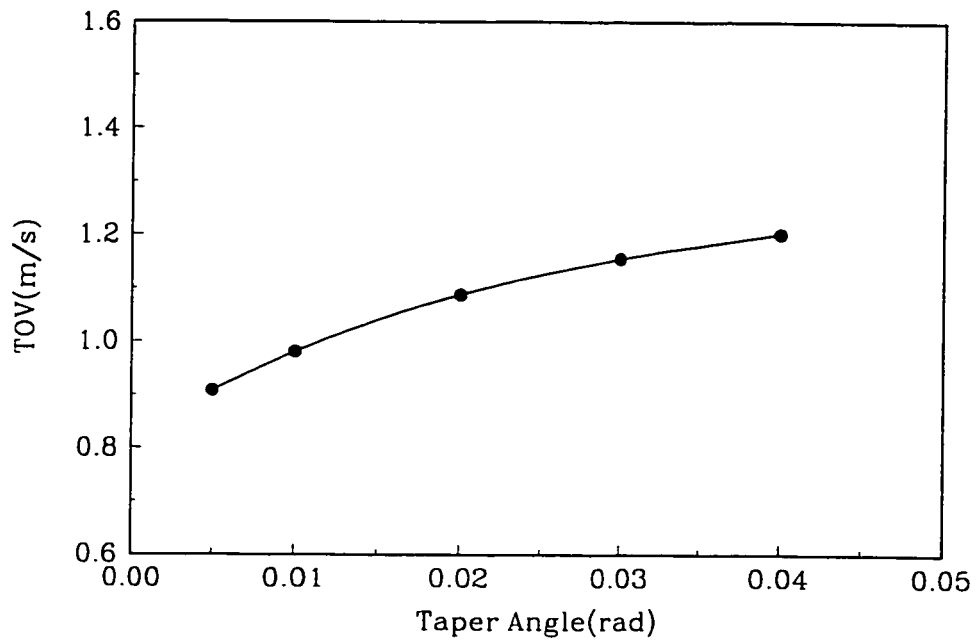


**Fig. 5.15** Take-off velocity versus taper angle. Crown = 15 nm, camber = 10 nm, twist = 0,  $\gamma = 0.2$  and  $\sigma = 3$  nm

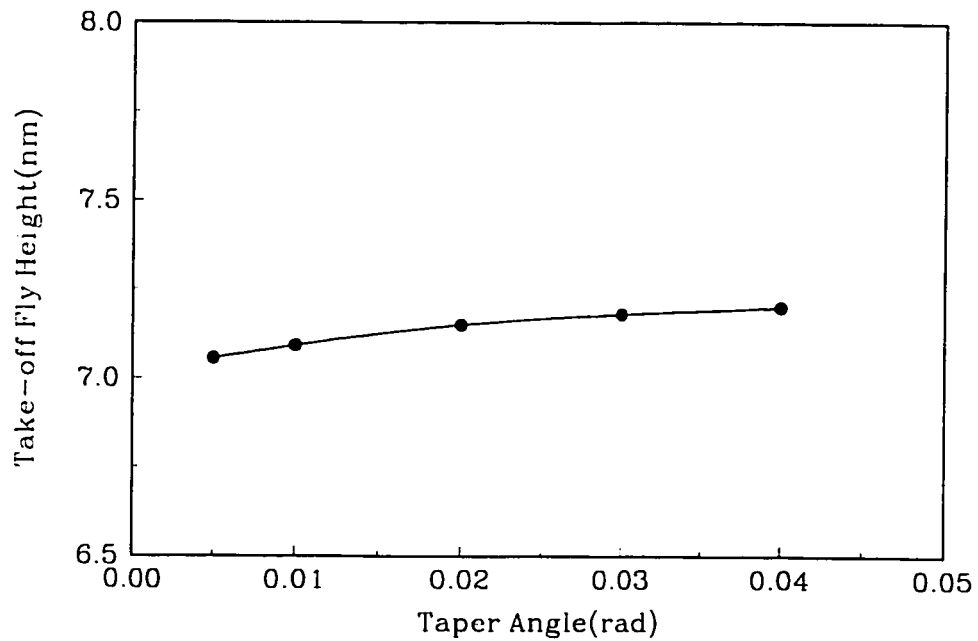


**Fig. 5.16** Take-off fly height versus taper angle. Crown = 15 nm, camber = 10 nm, twist = 0,  $\gamma = 0.2$  and  $\sigma = 3$  nm

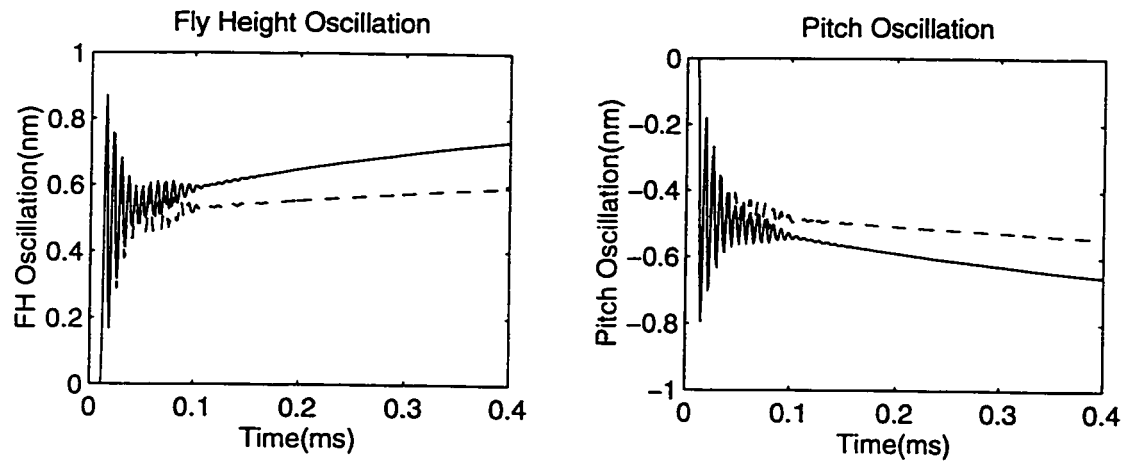


**Fig. 5.17** Fly height and pitch oscillations during the contact start-up for two taper angles. Taper angle = 0.01 rad (solid lines) and taper angle = 0.02 rad (dash lines)

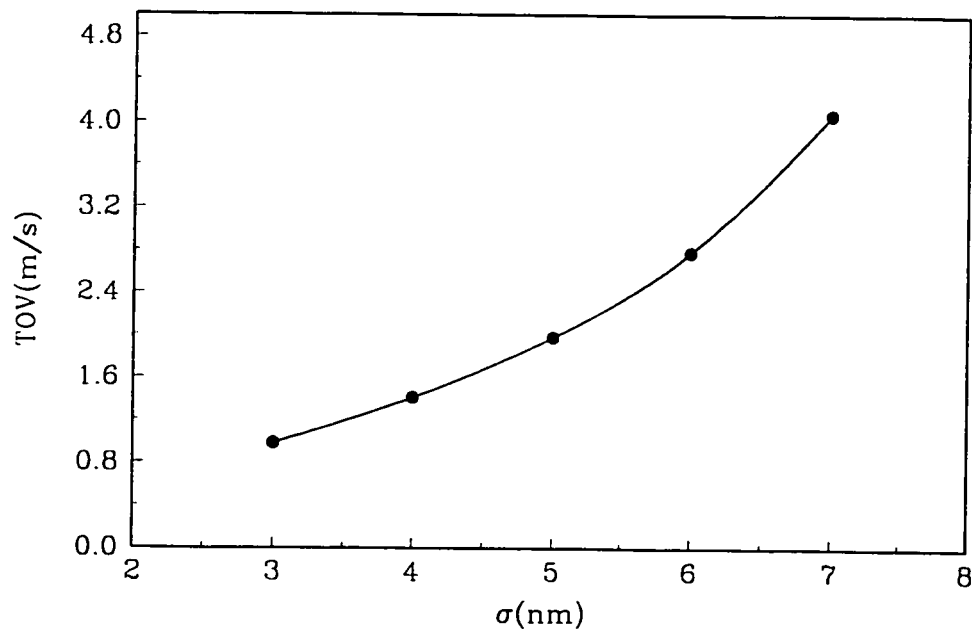


**Fig. 5.18** Take-off velocity versus the standard deviation of surface roughness. Crown = 15 nm, camber = 10 nm, twist = 0, taper angle = 0.01 rad, and  $\gamma = 0.2$

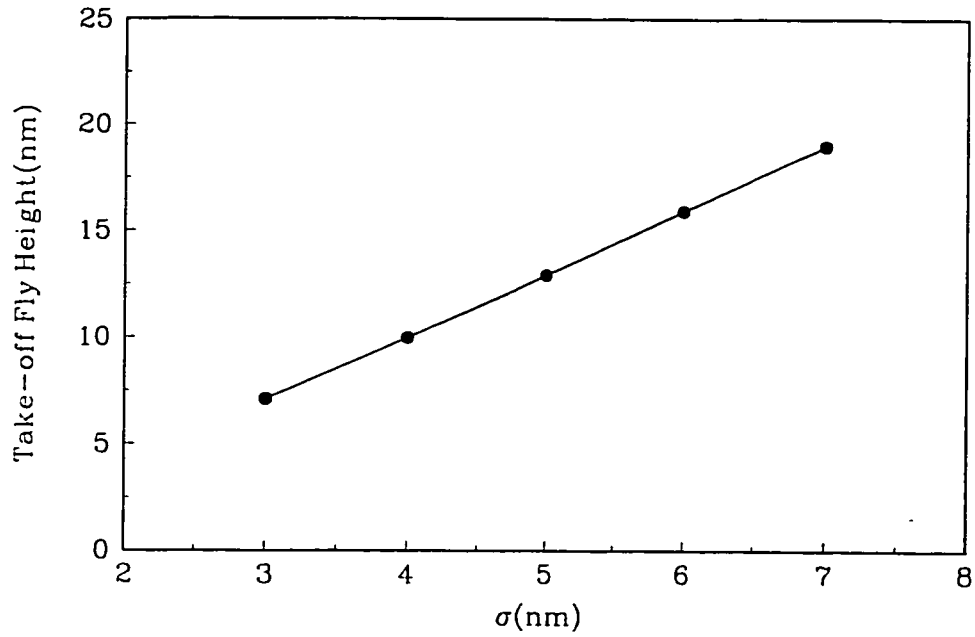


**Fig. 5.19** Take-off fly height versus the standard deviation of surface roughness. Crown = 15 nm, camber = 10 nm, twist = 0, taper angle = 0.01 rad and  $\gamma = 0.2$

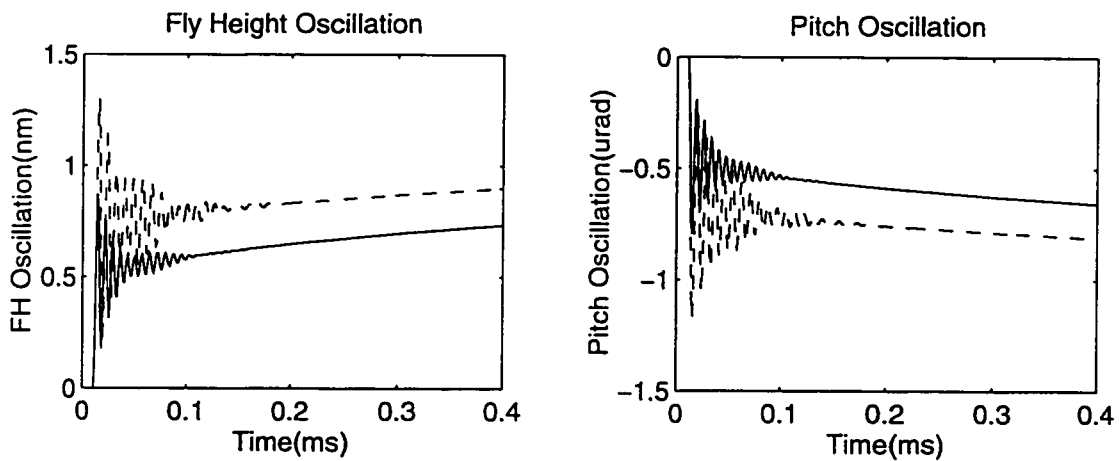


**Fig. 5.20** Fly height and pitch oscillations during the contact start-up for two  $\sigma$  values.  $\sigma = 3$  nm (solid lines) and  $\sigma = 6$  nm (dash lines)

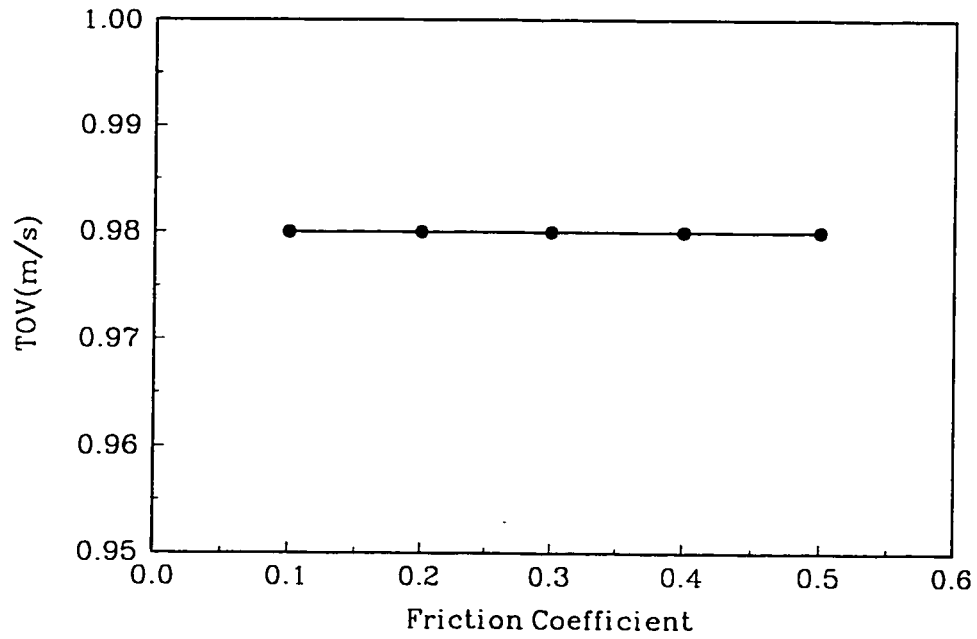


**Fig. 5.21** Take-off velocity versus friction coefficient. Crown = 15 nm, camber = 10 nm, twist = 0, taper angle = 0.01 rad and  $\sigma = 3$  nm

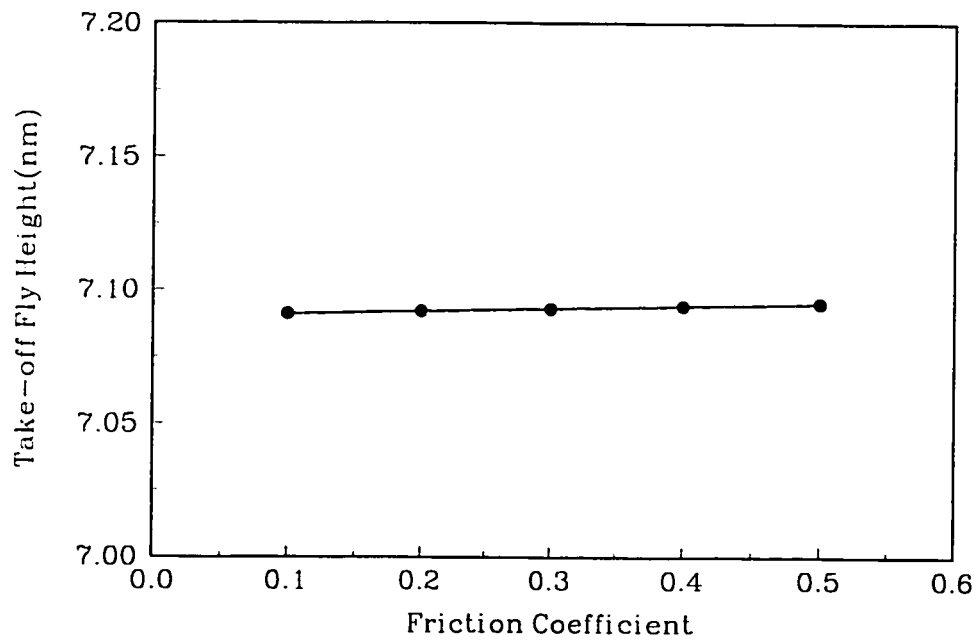


**Fig. 5.22** Take-off fly height versus friction coefficient. Crown = 15 nm, camber = 10 nm, twist = 0, taper angle = 0.01 rad and  $\sigma = 3$  nm

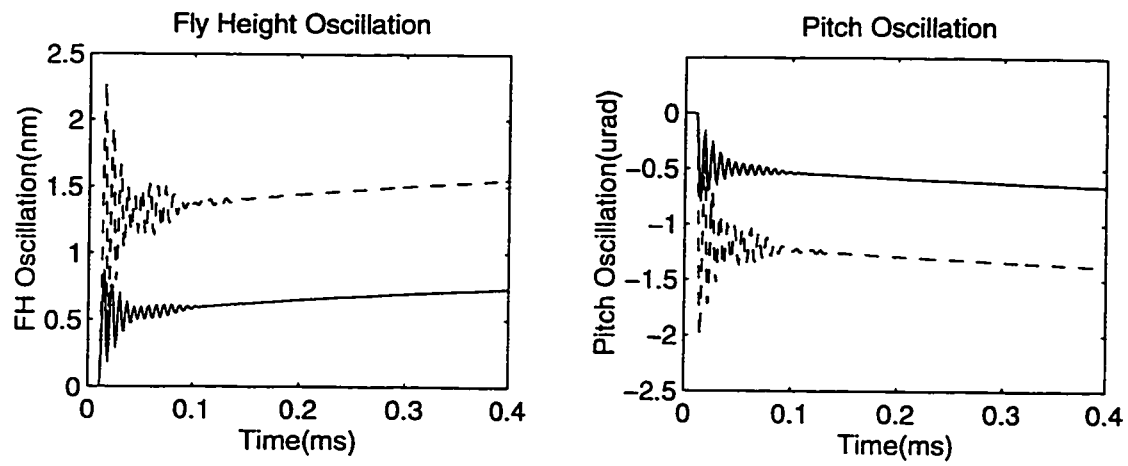


**Fig. 5.23** Fly height and pitch oscillations during the contact start-up for two friction coefficients.  $\gamma = 0.2$  (solid lines) and  $\gamma = 0.5$  (dash lines)



## CHAPTER 6

# SPACING MODULATION OF A SLIDER FLYING ACROSS A TRANSITION BETWEEN LANDING AND DATA ZONES\*

### 6.1 Introduction

Increases in disk drive storage capacity have historically been accompanied by smaller spacing between the transducer and recording medium. The reduction in head-disk spacing has recently accelerated and is approaching near-contact condition. At such a low spacing, surface roughness of the slider/disk interface, lubricant thickness and carbon overcoat thickness contribute substantially to the effective flying height between the slider and disk. Therefore, the trend towards lower fly height puts increasing demands on the use of smoother disks with thinner protective overcoats. This, in turn, creates severe tribological problems such as stiction and wear between the slider and disk when the conventional contact start/stop (CSS) process is employed. There are several alternatives for CSS such as zone texturing, textured air bearing surface (ABS), ramp loading, coated ABS and smaller and lighter loaded sliders, which can be used to largely overcome these tribological problems. Among them, the zone texturing is considered a very good approach since it reduces the stiction force and wear during start-up and still allows the use of very smooth disk surfaces in the data region.

In the zone texturing approach, a small annular ring of texture with relatively large surface roughness is provided for the area where the slider starts and stops. The texture

---

\* Parts of this chapter are to appear in *IEEE Transactions on Magnetics* (Hu and Bogy, 1995a)

provides a well-controlled amount of surface contact between the slider and disk, thereby reducing stiction, friction and wear during start-up of the disk drive when the slider is in sliding contact with the disk. In the data zone, where the slider flies over the disk, the surface is made very smooth to assist the reduction of the head-disk spacing. There is a transition zone between the texture zone and the smooth data zone, which is produced during the manufacturing process. The zone texture is produced by grinding, which removes some material, leaving behind a rough surface that is lower than the original surface. The tools used for grinding are positioned to a finite dynamic tolerance, and the width of the transition zone is determined by the dynamic positioning tolerance. The zone texture/transition zone introduces a spacing modulation, and track accessing across a transition zone may force the slider to fly dangerously close to the disk. To avoid slider/disk contact during accessing across the transition zone, designers need to better understand and control the transition zone induced spacing modulation.

In the present chapter, we study the spacing modulation of a sub-25 nm fly height slider flying across a transition zone using the CML Air Bearing Dynamic Simulator. The transition zone is represented as a parabolic surface defined by three points in the radial direction. The HTI 1650E type suspension assembly dynamics are integrated for the accessing motion. During the accessing event the spacing modulation is produced by the seeking acceleration, effective skew angle, surface roughness and transition zone profile. In this study, the spacing modulation due to the transition zone surface profile is extracted, and the effects of the transition zone height, width and shape on this spacing modulation are discussed.

## 6.2 Numerical Simulation

The generalized Reynolds equation and the equation of motion of the slider and its suspension are numerically solved using the CML Air Bearing Dynamic Simulator. Due to the sub-25nm spacing in slider air bearings the no-slip boundary condition at the wall is no longer satisfied. In our simulation the modification proposed by Fukui and Kaneko (1988) based on the linearized Boltzmann equation is used. The transition zone profile is implemented in the simulator using three points in the radial direction. A parabolic functional relationship is assumed to exist for the three points.

## 6.3 Results and Discussions

The “Nutcracker” slider described in Chapter 5 is used for the sample calculations. It is a shaped-rail 50% sub-ambient pressure type slider. Figure 6.1 shows the shape of its air bearing surface. The design target fly height is about 25 nm under 3.5 grams of loading force. The disk rotational speed is 5400 rpm. The 3D non-dimensional air bearing pressure profile for smooth disk surface is plotted in Fig. 6.2. In our simulation, the Hutchinson 1650E type suspension is used. Its FEM mesh is displayed in Fig. 6.3. 3331 nodes are used to model this suspension with a dense mesh distribution in the portion of the integrated gimbal. The eigenvalue solution is first obtained using ABAQUS, then the first 10 modes are used in the air bearing simulation to represent the suspension dynamics during the accessing event.

Figure 6.4 plots the accessing profile of the slider flying across a transition zone. Initially, the slider flies at the radius of 19 mm. At 0.1 ms, the slider is accelerated

radially outward to the velocity of  $-0.882$  m/s at 2 ms. The minimum acceleration (maximum amplitude) is  $-50G$ . During the process, the slider moves 2.78 mm in the radial direction, and the geometrical skew angle changes from 1.74 to  $-2.182$  degrees. The transition zone is a constant slope plane with a height of 20 nm. It starts at the radius of 20.32 mm and ends at the radius of 20.72 mm. The CSS zone and transition zone have a circumferential texture with sinusoidal cross-section in the radial direction with an amplitude of 2.5 nm and a wavelength of  $118.6$   $\mu\text{m}$ . Figure 6.5 shows the slider's flying characteristics during the event of accessing across the transition zone. The fly height at the center trailing edge (CTE) reaches a maximum of 31.86 nm at the moment when the CTE flies over the starting point of the transition zone. After entering the transition zone, the CTE fly height decreases, attaining a minimum of 10.85 nm at the time when the CTE is gliding over the ending point of the transition zone, and then increases as the slider leaves the transition zone. To fly over the transition zone, the slider has to conform to the slope of the transition zone surface. As a result, the slider's roll first increases, reaching a maximum of  $18.23$   $\mu\text{rad}$ , and then decreases to a minimum as the slider leaves the transition zone. The slight roll drop at 0.1 ms is due to the sudden action of the slider's inertia force. The fly height modulations at the inner rail trailing edge (IRTE) and outer rail trailing edge (ORTE) follow a reversed pattern as compared to the CTE fly height modulation as shown in Fig. 6.6. The fly heights at these two points first decrease to a minimum, and then increase. After reaching a maximum, the spacing decreases as the slider leaves the transition zone. The overall spacing modulation is produced by the surface roughness, effective skew angle, inertia force of laterally moving slider and

transition zone profile. To obtain the contribution due to the transition zone profile, we simulate the same accessing process using the same disk surface without the transition zone. The roll and fly height differences between the two simulations are defined as the roll and fly height modulations produced by the transition zone only, respectively. Figure 6.7 shows the contributions of the transition zone to the roll and fly height modulations. It is seen that the maximum spacing decrease among the three points occurs at the ORTE. Since the maximum head/disk spacing reduction is the main concern to the drive designers, we choose the ORTE to study the effects of the transition zone parameters on its spacing modulation.

**6.3.1 Effect of Transition Zone Width.** The transition zone induced ORTE spacing modulations for three values of zone width are plotted in Fig. 6.8. Among the three cases, the transition zone with zero width produces the largest spacing reduction, which is 20.02 nm. As the zone width increases, the slope of the zone surface decreases, and the maximum spacing drop decreases. Furthermore, the wider zone delays the occurrence of the minimum and maximum spacings. There is a slight drop of the maximum increase of the spacing as the zone width increases from 0 to 0.4 mm. There is also a noticeable small fly height oscillation as the slider leaves the transition zone for the case of the zero zone width. This is due to the abrupt change in bearing separation in the radial direction.

**6.3.2 Effect of Transition Zone Height.** Figure 6.9 shows the ORTE spacing modulation produced by the transition zone surface for three zone heights of 20 nm, 30 nm and 40 nm. In all these simulations, the zone width is 0.4 mm. As the zone height increases from 20 nm to 40 nm, the maximum fly height reduction increases from 10.36

to 19.61 nm. This is because the slope of the zone surface increases as the zone height increases.

**6.3.3 Effect of Transition Zone Shape.** The zone surface profile is represented by a parabolic surface defined by three points in the radial direction. The effect of the zone surface shape on the transition zone induced ORTE spacing modulations is plotted in Fig. 6.10. The case of the middle point height of 10 nm corresponds to the constant slope plane, while the cases of the middle point heights of 5 nm and 15 nm imply concave and convex surfaces, respectively. Among the three zone surfaces, the constant slope plane has the smallest spacing decrease and increase. Even though the concave and convex surfaces have about the same maximum spacing increase, their maximum spacing reductions are noticeably different. The concave surface increases the maximum spacing reduction by about 2.46 nm as compared to the convex surface.

## 6.4 Summary

The spacing modulation of a slider flying across a transition zone is investigated in this chapter using the CML Air Bearing Dynamic Simulator. The transition zone is represented in the simulator as a parabolic surface defined by three radial points. The suspension assembly dynamics are integrated for the accessing motion. A sub-25 nm fly height slider with shaped-rails is used in our calculations. The spacing modulation due to the transition zone profile is extracted. A simulation analysis of the effects of the transition zone height, width and shape on the transition zone induced spacing modulation is presented. It is concluded that the maximum slider/disk spacing reduction

occurs at the outer rail trailing edge when the slider climbs up the transition zone. The spacing reduction increases as the slope of the transition zone surface increases. A concave zone surface produces a larger spacing decrease than either a convex or constant slope zone. Smaller zone widths and larger zone heights also force the slider to fly closer to the disk. The combination that produces the least spacing modulation is increased zone width, decreased zone height, and constant slope transition plane.

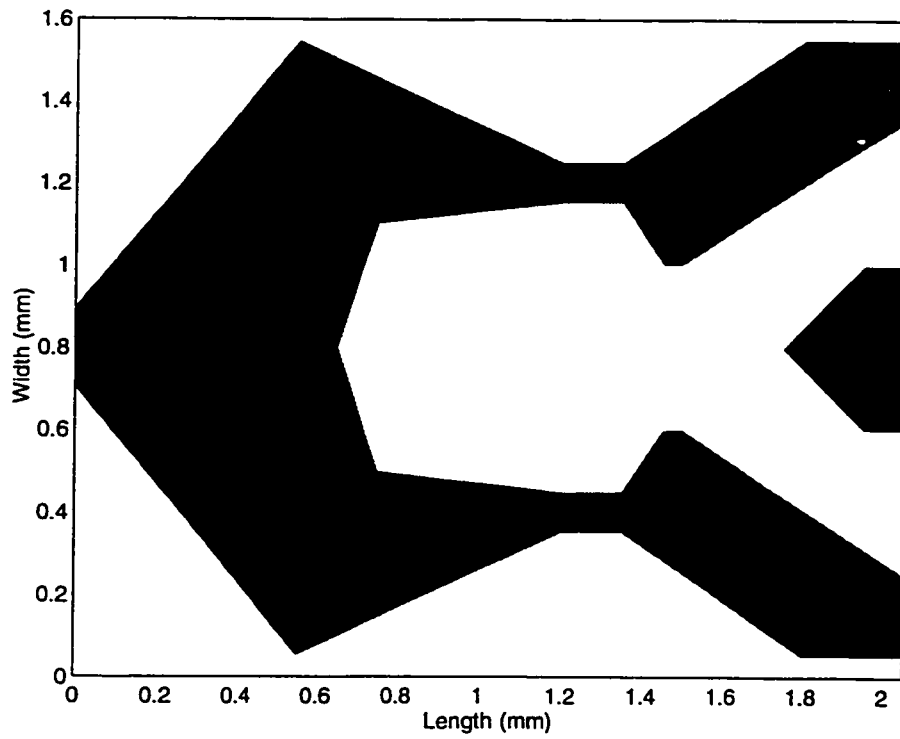


**Fig. 6.1** Air bearing surface for the Nutcracker slider

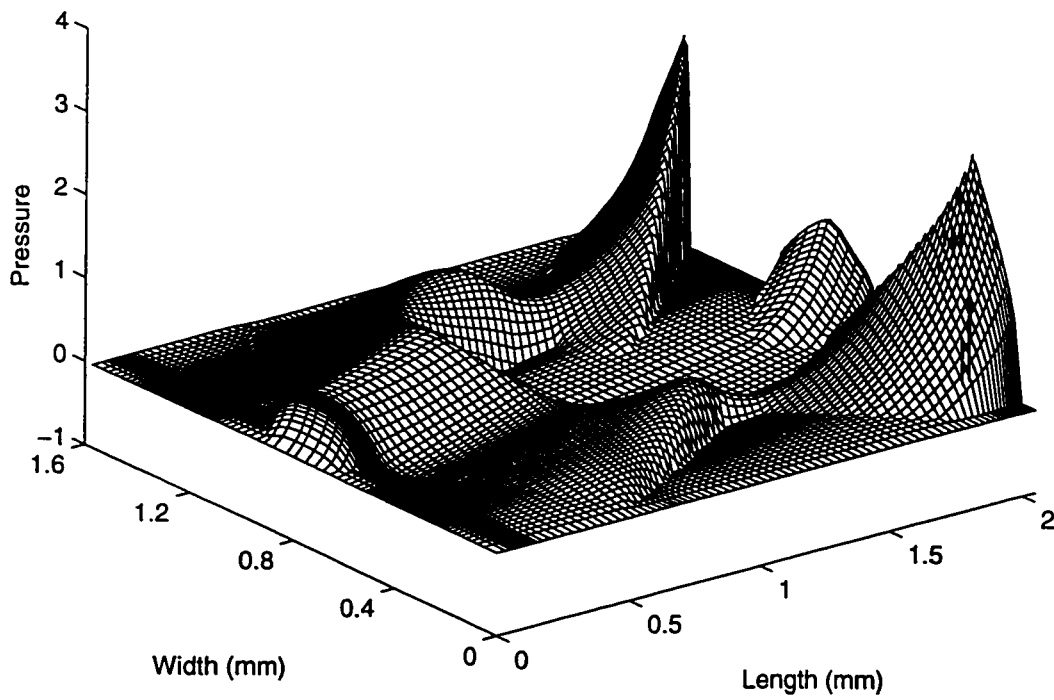


**Fig. 6.2** 3D non-dimensional air bearing pressure profile



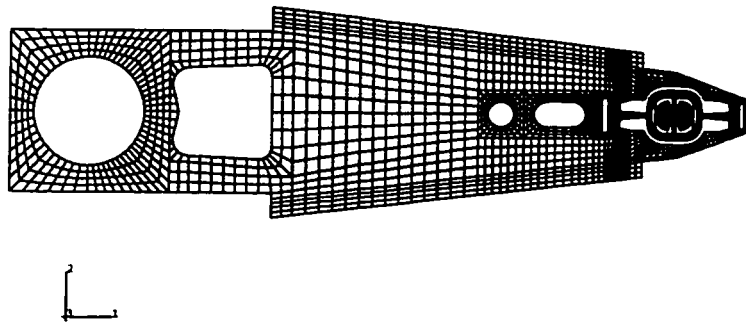


**Fig. 6.3** FEM mesh of a Hutchinson 1650E type suspension

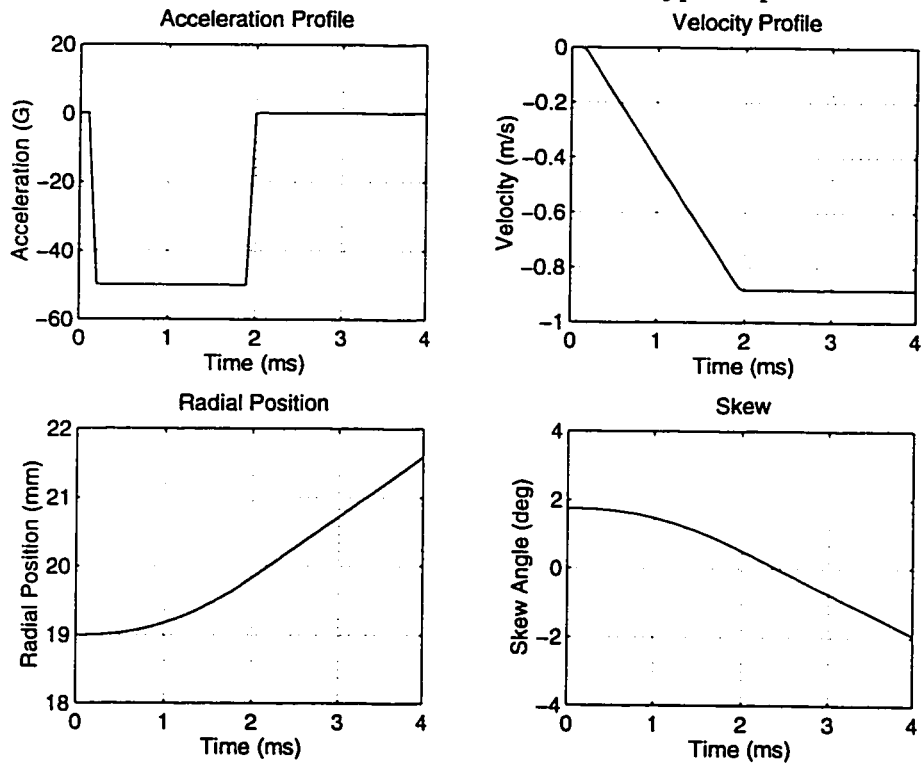


**Fig. 6.4** Accessing profile

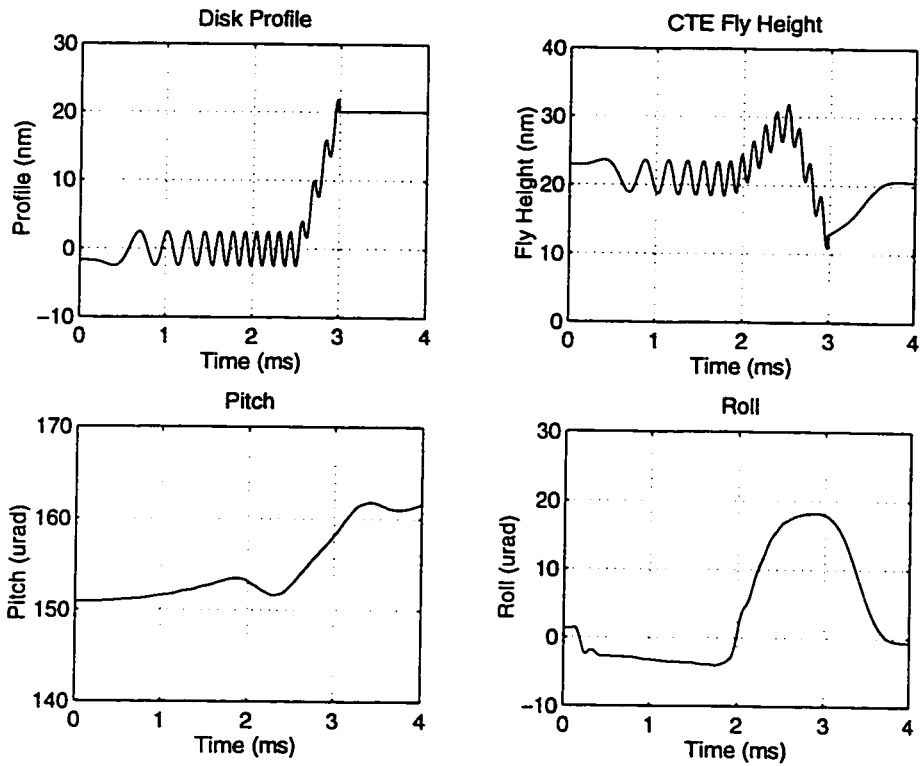


**Fig. 6.5** Flying characteristics of a slider flying across a transition zone. The transition zone is a constant slope plane with a height of 20 nm and a width of 0.4 mm

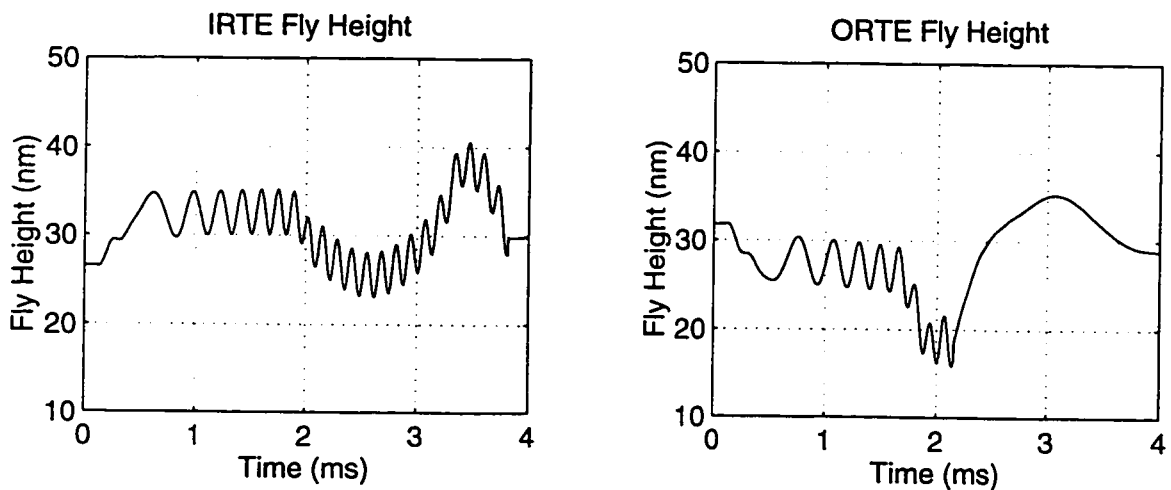


**Fig. 6.6** IRTE and ORTE fly heights of a slider flying across a transition zone. The transition zone is a constant slope plane with a height of 20 nm and a width of 0.4 mm

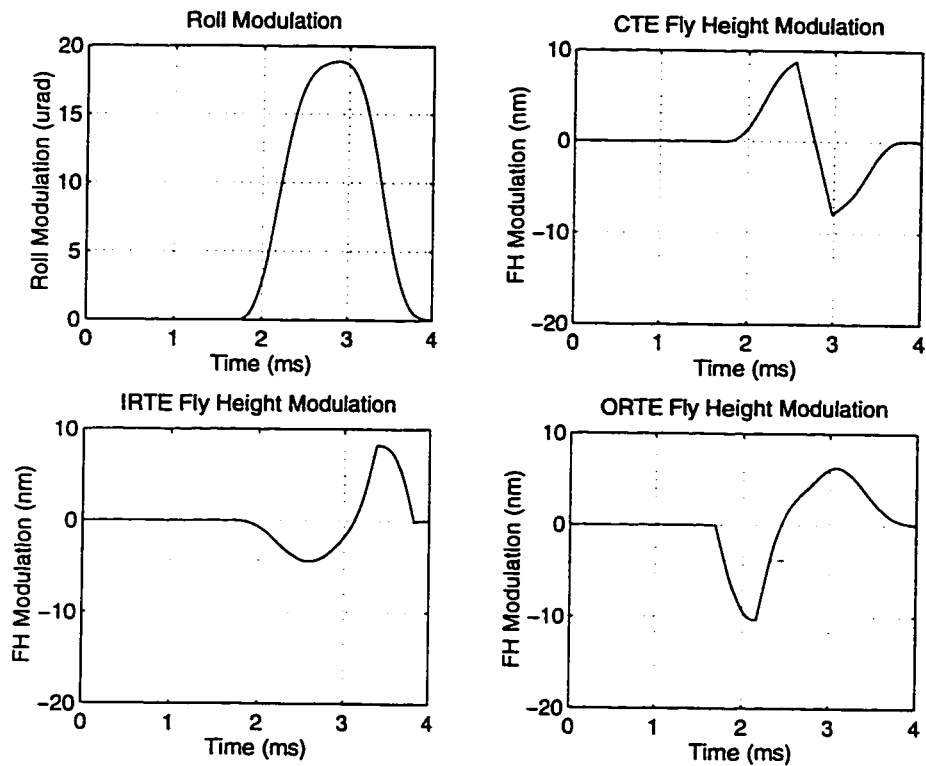


**Fig. 6.7** The contributions of a transition zone to the fly characteristics. The transition zone is a constant slope plane with a height of 20 nm and a width of 0.4 mm

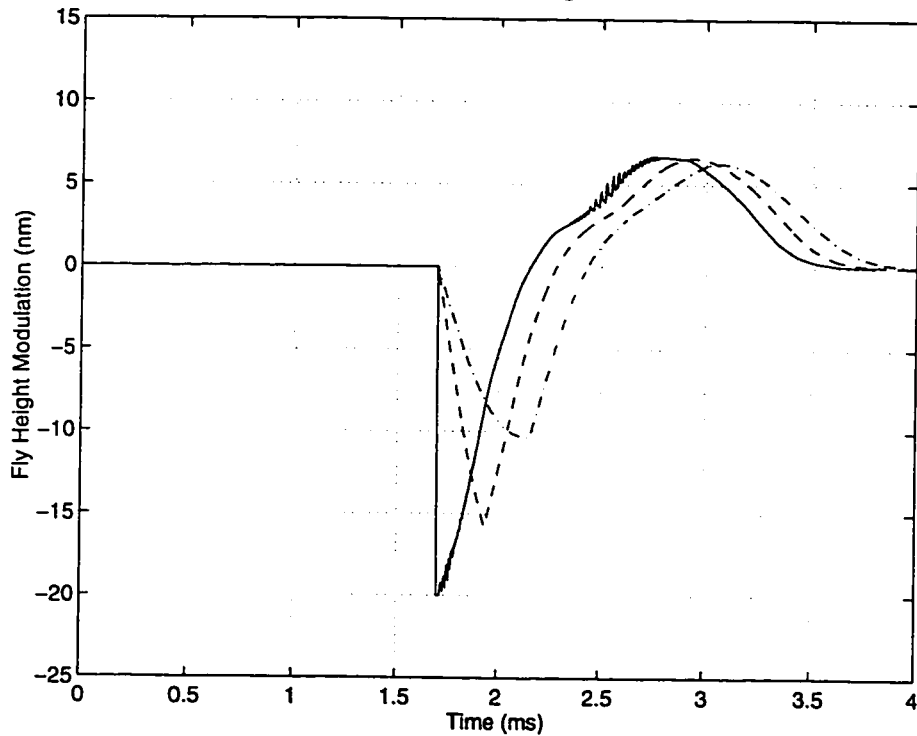


**Fig. 6.8** The effect of the zone width on the transition zone induced ORTE spacing modulation. Width = 0 (solid lines), 0.2 mm (dash lines) and 0.4 mm (dash dotted lines)

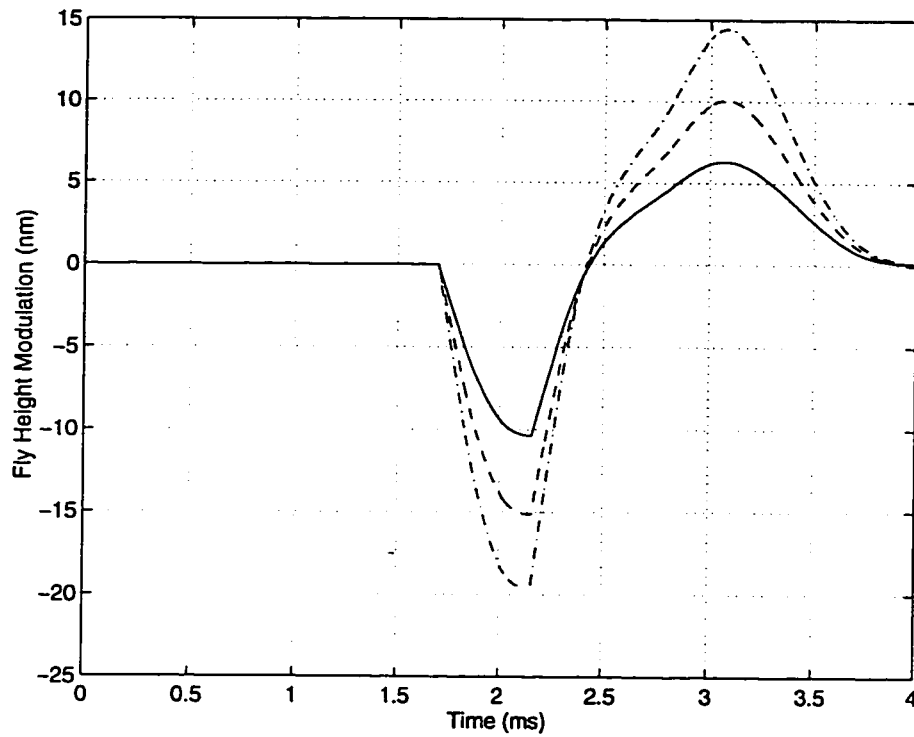


**Fig. 6.9** The effect of the zone height on the transition zone induced ORTE spacing modulation. Height = 20 nm (solid lines), 30 nm (dash lines) and 40 nm (dash dotted lines)

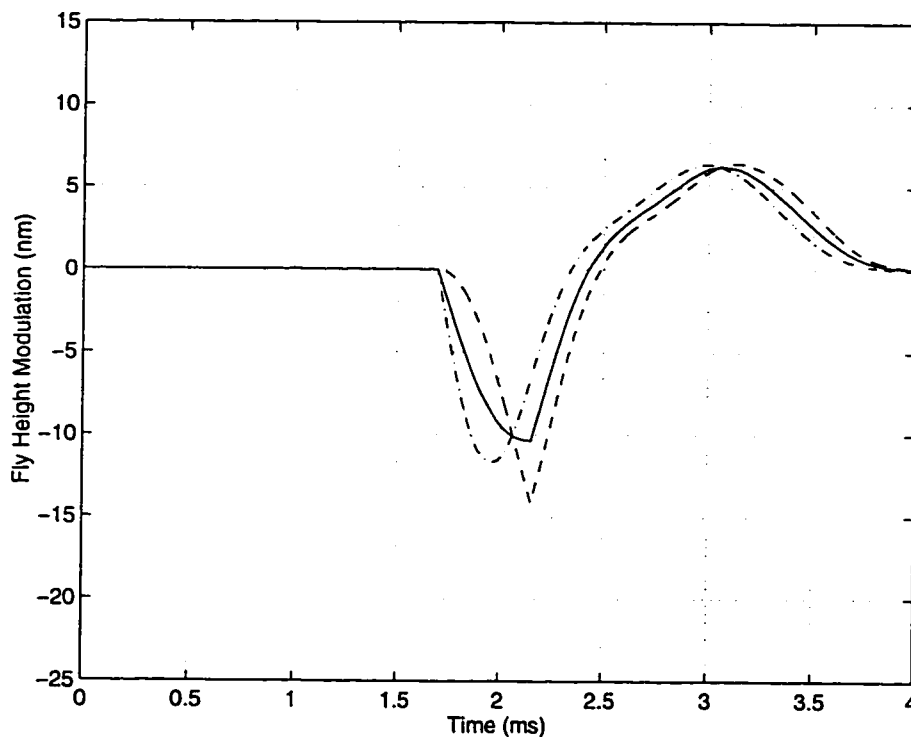


**Fig. 6.10** The effect of the zone shape on the transition zone induced ORTE spacing modulation. The height of middle point = 10 nm (solid lines), 5 nm (dash lines) and 15 nm (dash dotted lines)

## CHAPTER 7

# FLYING CHARACTERISTICS OF A SLIDER OVER TEXTURED SURFACE DISKS\*

### 7.1 Introduction

Increasing areal densities in magnetic hard disk drive create an array of challenges for the disk drive designer, one being the tribological performance of the head/disk interface. Higher storage densities require smaller head/media spacing, which translates into lower fly heights for the slider. This trend towards lower fly height generates severe stiction and wear problems between the slider and disk, especially due to the advances in ultra fine surface finish technology. Stiction not only can lead to damage of the head/disk interface, but also, in smaller form drives, can be high enough to prevent the spindle from starting. To avoid these problems, artificial surface treatment, for example, well-defined surface textures provide a possible approach since it greatly reduces sliding friction and also eliminates initial start-up “stiction”. However, this, in turn, raises the issues of surface texture effects, especially in connection with ultra-thin gas films, since surface irregularities normally considered minor and, therefore, negligible, may have to be considered when the slider-disk separation becomes very small. Therefore, understanding the effects of surface textures on the slider’s flying characteristics becomes essential to texturing the disk surface.

The well-defined disk surface texture can be classified as a special type of moving

---

\* Parts of this chapter are submitted to *ASME Journal of Tribology*

roughness. The field of surface roughness effects on hydrodynamic lubrication has received considerable attention. To date, several approaches have been developed to account for the presence of roughness on the surface of the slider and/or the disk. Christensen and Tonder (1971) introduced a statistical film averaging concept for striated roughness. Applying a two-scale expansion method, Elrod (1973) confirmed the film averaging concept mathematically. Furthermore, Rhow and Elrod (1974) employed this approach to the two-sided roughness problem. Mitsuya *et al.* (1984, 1989, 1990) extended this concept for two-dimensional roughness using a mixed-averaging technique. Another approach to surface roughness effects, the average flow model, was developed by Patir and Cheng (1978,1979), who proposed an ensemble-averaged Reynolds equation in which roughness effects are built into pressure and shear flow factors. Their flow factors were obtained by numerical simulations with carefully developed surface roughness models. After that, Elrod (1979) generalized the flow factors analytically. Tripp (1983) also showed analytical expressions of flow factors using a perturbation approach with a Green function technique. The flow factor method was also extended to thin film gas lubrication in the slip flow regime by Crone *et al.* (1991) and Makino *et al.* (1993). In the area of experimental study, Ohkubo and Mitsuya (1991) investigated the effects of moving surface textures on the static flying characteristics of self-acting gas-lubricated sliders at the clearance of about one micro-meter. Three types of surface textures ( 1-D square wave, 2-D rectangular groove and 2-D rectangular bump) were used in their study. The experimental results were compared with numerical results based on an averaged film thickness model that takes the effect of moving textures into account. Tanaka and

Bogy (1994) investigated the effects of disk texture on slider flying characteristics using disks with well-defined texture. The texture has circumferential or regular dot array ridges with uniform height. It was concluded that the fly height of the slider, defined from the bottom surface of the texture, increases with increases in both the height and area ratio of the ridges. The fly height difference between smooth and textured disks becomes more significant at lower fly heights, especially in the near contact region. Although various averaged models are capable of predicting the global characteristics of rough surface gas lubrication, they fail to provide data revealing the local behavior of surface texture effects. Therefore, an alternative approach, i.e., to use a deterministic description of the texture in the calculations instead of using some averaged Reynolds equation is adopted here to perform the most realistic simulations of a slider flying over the disks with well-defined surface textures.

In this study, the effects of well-defined surface texture on the slider's flying characteristics are numerically investigated using the CML Air Bearing Dynamic Simulator in conjunction with the experimental work done by Tanaka and Bogy (1994). The slider-disk interface dynamics are simulated numerically for the three dimensional surface textures generated in the simulator, which are circumferential ridges with different heights and area ratios. The effects of the area ratio and height of the ridges as well as the disk velocity on the slider's flying height and pitch are simulated, and texture effect mechanisms (side-flow restriction and reduced flow area) are discussed. The effects of the ridged disk surfaces on slider's air bearing damping characteristics are examined using the impulse responses and their power spectral magnitude plots. It is

concluded that the air damping ratio increase for the textured disks is attributed to the enhancement of the transverse viscous shearing across the ridges.

## **7.2 Numerical Simulation**

The generalized Reynolds equation and the equation of motion of the slider are numerically solved using the CML Air Bearing Dynamic Simulator. Due to the ultra-low spacing in slider air bearings the no-slip boundary condition at the wall is no longer satisfied. In our simulation the modification proposed by Fukui and Kaneko (1988) based on the linearized Boltzmann equation is used. There are various averaging techniques for analyzing the surface texture effects, which usually tend to smear out the finer details. In order to perform the most realistic simulation of flying characteristics of a slider over the textured disk surfaces, we directly generate the three-dimensional surface texture in the numerical simulator. At each time step, the film thickness distribution under the slider is obtained through interpolation of the disk surface texture profile. With this new film distribution, the coupled system of equations is solved. To resolve the smallest wavelength of surface texture, the air bearing mesh is refined until there are at least six grid points per wavelength. The circumferential ridges with a varied heights and area ratios are used to study their effects on the slider's flying characteristics.

## **7.3 Results and Discussions**

The disk surface texture pattern used in this study is shown in Fig. 7.1. It consists of circumferential ridges with uniform height. By changing the ridge width while



keeping the wavelength constant, the ridge area ratio (percent of ridge area to total area) is varied from 25% to 75%. The wavelength is 30  $\mu\text{m}$  and the ridge height is varied from 0 to 80 nm. A 70% taper-flat slider with the rail width of 350  $\mu\text{m}$  is used for the sample calculations. Figure 7.3 shows the shape of its air bearing surface. The suspension preload is 8 grams. The slider used in our simulations is assumed to have a 23 nm crown and zero camber and twist. The disk radius at which the slider flies is 42 mm, and the skew angle is assumed to be zero. The suspension heave, pitch and roll stiffnesses are 26 N/m, 0.0001705 N $\times$ m/rad and 0.0002131 N $\times$ m/rad, respectively. In this study, the fly height at the center of the outer rail trailing edge, measured from the bottom surface of the texture, is referred to as the fly height of the slider.

Figures 7.4 and 7.5 show the changes of the fly height and pitch from the values obtained using the smooth disk in the disk velocity range from 1 to 10 m/s for three textured disk surfaces. The circumferential ridge surfaces introduce an increase of the fly height and a decrease of the pitch. These changes increase as the ridge height and ridge area ratio increase. The rates of the changes increase rapidly as the disk velocity decreases. This agrees well with the experimental results obtained by Tanaka and Bogoy (1994). Among the three circumferential ridge surfaces, the disk with a ridge area ratio of 25% and a height of 40 nm has the largest rate of the fly height change in the velocity range from 1 to 5 m/s. For the two disks with the same ridge height of 40 nm, even though the difference of the pitch decreases is hardly noticeable in the velocity range from 5 to 10 m/s, it is significant at the velocities smaller than 5 m/s, as shown in Fig. 7.5. The changes of the fly height and pitch are attributed to the reduced flow area associated with

the presence of the ridges and restrictions in the side-flows due to channeling of flow in the air bearing. Figure 7.2 illustrates a schematic of these two mechanisms. The ridges on the disk surface function like the reduced flow area, which tends to increase the slider-disk separation. The air flow in the region I is physically trapped between two ridge walls. In the region II, the higher pressure on the top of the ridges generated by the reduced film thickness impedes the side-leakage across the ridges. This is because the negative pressure gradients are established in the side-flow directions. Both mechanisms encourage the pressure generation, thus increase the slider-disk spacing. Lower pitch angles are expected since the reductions in the side-flows are greatest near the trailing edge. The side-flow restriction mechanism can be further illustrated by examining the pressure distributions for the circumferential ridge surface disks. Figures 7.6, 7.7, 7.8 and 7.9 show the dimensionless 3-D air bearing pressure distributions beneath the inner rail at the disk velocity of 2 m/s for a smooth disk surface and three circumferential ridge disk surfaces, respectively. Along the length of the slider rail, zero is defined as the leading edge. Though the overall shapes of the pressure distributions for the smooth and textured surfaces are similar, their local shapes are dramatically different. As a comparison to the smooth pressure profile for the smooth disk surface, the textured disk surfaces generate the stippled pressure ridges embedded on the smooth pressure distributions, thus establish a series of local negative pressure gradients in the side-flow directions, which substantially restrict the side leakage across the ridges. These local transverse pressure gradients gradually increase from the leading edge to trailing edge, reaching a maximum in the region near the trailing edge. This confirms that the largest

side-flow restriction occurs near the trailing edge. It is seen that these negative pressure gradients increase as the ridge height and area ratio increase, as shown in Figs. 7.7, 7.8 and 7.9. The effects of the textured disk surfaces on the slider's air bearing damping characteristics are also simulated. Figure 7.10 shows the slider's vertical, pitch and roll impulse responses at the disk velocity of 10 m/s. There is no noticeable difference of the oscillation decaying characteristics between the smooth disk and the textured disk (with the 25% ridge area ratio and 40 nm height). This is further illustrated by the corresponding power spectral magnitude plots as shown in Figs. 7.11, 7.12 and 7.13. The impulse responses at the disk velocity of 2 m/s are plotted in Fig. 7.14. Their corresponding power spectral magnitude plots are shown in Figs. 7.15, 7.16 and 7.17. As a comparison to the negligible difference at the disk velocity of 10 m/s, both the time-domain and frequency-domain plots at the disk velocity of 2 m/s indicate that the textured disk surfaces (with the 25% ridge area ratio and 20 & 40 nm heights) produce a substantial increase of the air bearing damping ratios, especially for the roll and vertical oscillations. The increased air bearing damping ratios for the textured disk surfaces appear to be related to the enhanced viscous shearing across the circumferential ridges. In contrast with the smooth disk, the ridged surface disk increases the transverse viscous shearing through several ways. First of all, the flow gradient on the ridge top is higher due to the reduced slider-disk separation. Ridge side walls increase the effective shearing area. Finally, the increased pressure gradient across the ridges results in a larger transverse flow rate. Among the three types of slider's motions, the vertical and roll motions contribute more to the side flow at the trailing edge, which is more directly

associated with the transverse viscous shearing effect. This shearing effect increases as the disk velocity decreases mainly due to the decreased slider-disk spacing.

**7.3.1 Effect of the Ridge Height.** The fly characteristics of a slider flying over disks with the 25% ridge area ratio and heights from 0 to 80 nm are simulated. The results are plotted in Figs. 7.18 and 7.19. Increasing the ridge height reduces the effective flow area and imposes more restrictions to the side-flows, thus increases the fly height and decreases the pitch. The rates of the fly height and pitch changes increase as the ridge height increases. This also agrees with the measurement results by Tanaka and Bogoy (1994). Smaller disk velocities have larger rates of the fly height and pitch changes. This is because the textured surface effects are greater at the lower velocities due to the reduced slider-disk separation. The effects of the ridge heights on the air bearing damping characteristics are demonstrated in Figs. 7.14, 7.15, 7.16 and 7.17. We see a significant increase of the air bearing damping ratios as we increase the ridge height from 0 to 40 nm. The rates of the changes increase as the ridge height increases.

**7.3.2 Effect of the Ridge Area Ratio.** The disks with a 20 nm ridge height and ridge area ratios from 25% to 75% are used in the simulations. Figures 7.20 and 7.21 plot the fly height increase and pitch decrease versus the ridge area ratio. The increase of the fly height increases almost linearly with the ridge area ratio at a rate of about 0.21 nm per unit percent, which confirms the experimental observation by Tanaka and Bogoy (1994). The linear increase is believed to be mainly associated with the linear increase of the reduced flow area with the ridge area ratio. It is seen that the rate of the fly height change does not depend on the velocity. The ridge area ratio has a minor effect on the pitch

decrease, as shown in Fig. 7.13. The pitch decrease reaches a maximum at a ridge area ratio of about 45%. Smaller velocities result in a larger pitch decrease. The ridge area ratio also affects the air bearing damping characteristics. Figure 7.22 plots the vertical, pitch and roll impulse responses at the disk velocity of 2 m/s for the textured disks with the height of 40 nm and area ratios of 25% & 50%. Their corresponding power spectral magnitude plots are shown in Figs. 7.23, 7.24 and 7.25. Both the time-domain and frequency-domain results imply a decrease of the vertical and roll damping ratios as we increase the ridge area ratio from 25% to 50%. Similarly to the effect on the steady state pitch, the ridge area ratio has a secondary effect on the air bearing damping ratio for the slider's pitch motion.

## 7.4 Summary

The effects of well-defined surface texture on a slider's flying characteristics are studied in this chapter using the CML Air Bearing Dynamic Simulator. The slider-disk interface dynamics are simulated numerically for the three dimensional surface textures generated in the simulator, which are the circumferential ridges with different heights and area ratios of the ridges. The effects of the ridge area ratio and height, as well as the disk velocity on the slider's flying characteristics are investigated. Adding the circumferential ridge surfaces increases the trailing edge fly height and decreases the pitch because of the reductions in the effective flow area and the restrictions in side-flows. The rates of fly height and pitch change increase rapidly as the disk velocity decreases. The ridge height has a substantial influence on the slider's steady state fly

characteristics. A larger ridge height produces a larger trailing edge fly height increase and pitch decrease. The simulation results also indicate a nearly linear increase of the fly height with the ridge area ratio, but the ridge area ratio has a minor effect on the pitch decrease. The ridged disk surfaces increase the air bearing damping ratios through the enhancement of the viscous shearing across the circumferential ridges. The rates of the effects increase as the disk velocity decreases and ridge height increases. A larger ridge area ratio results in a decrease of the air bearing damping ratios. The slider's vertical and roll motions are more subject to the enhanced transverse viscous shearing generated by the textured disk surfaces than the pitch motion.

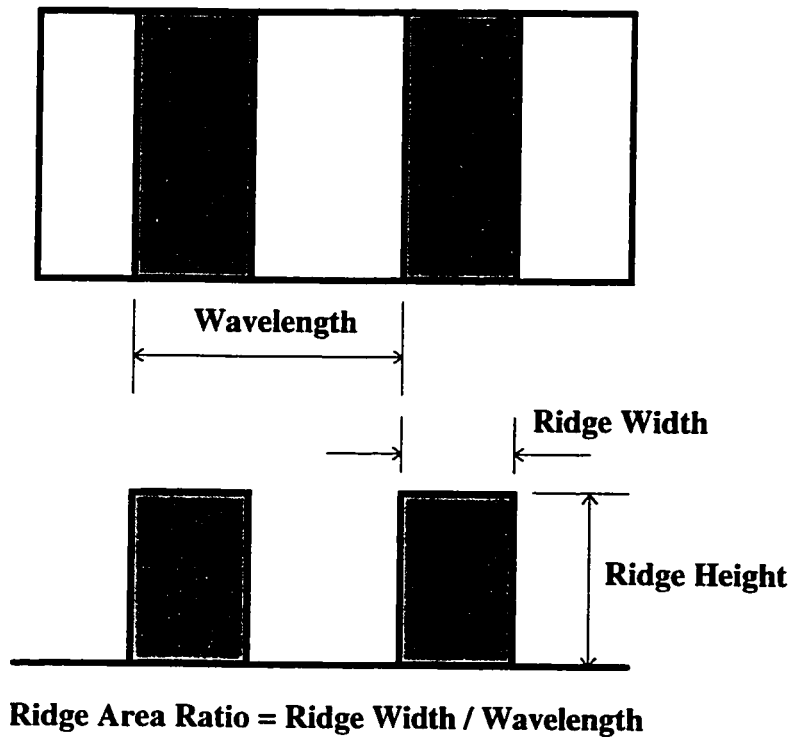
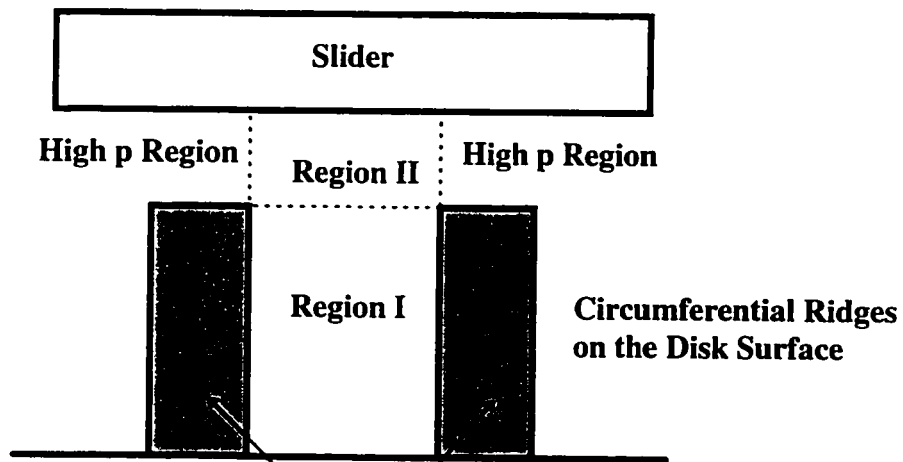


**Fig. 7.1** The circumferential ridge disk surface



**Side-Flow Restrictions:**

**Region I: Physically Trapped**

**Region II: Restricted by the Negative Pressure**

**Gradients Across the Ridges**

**Fig. 7.2** A schematic of two mechanisms of the texture effects: side-flow restriction and reduced flow area

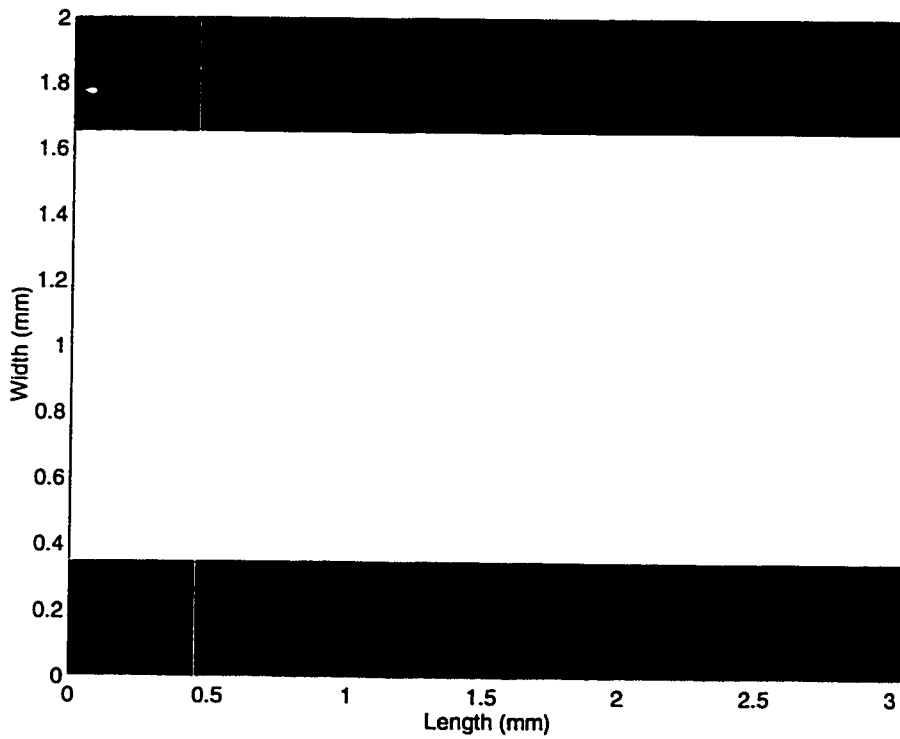


**Fig. 7.3** Air bearing surface of the taper-flat slider

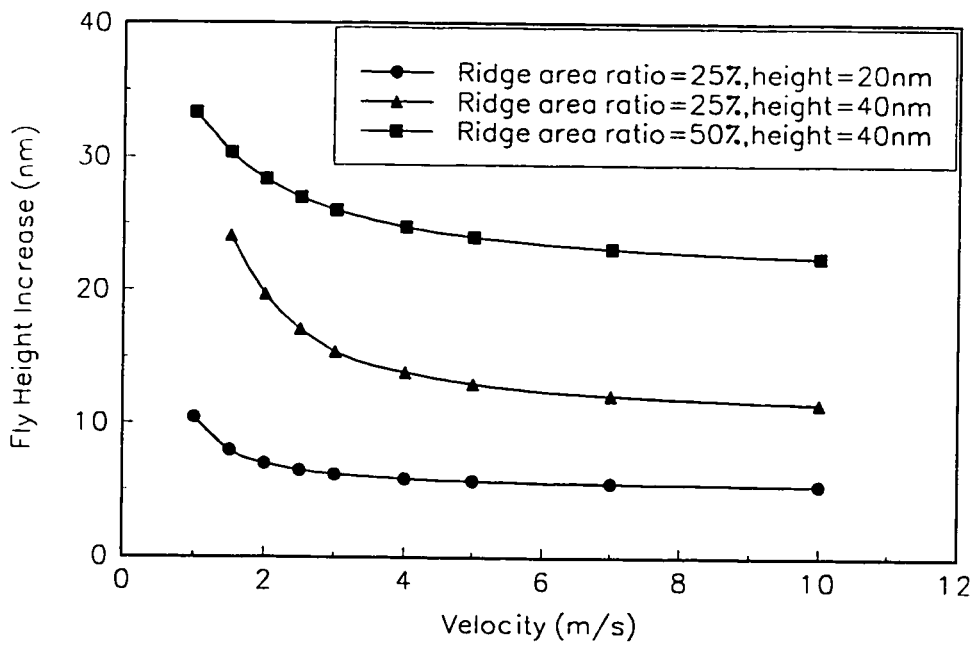


**Fig. 7.4** Fly height increase versus the disk velocity for three circumferential ridge disk surfaces



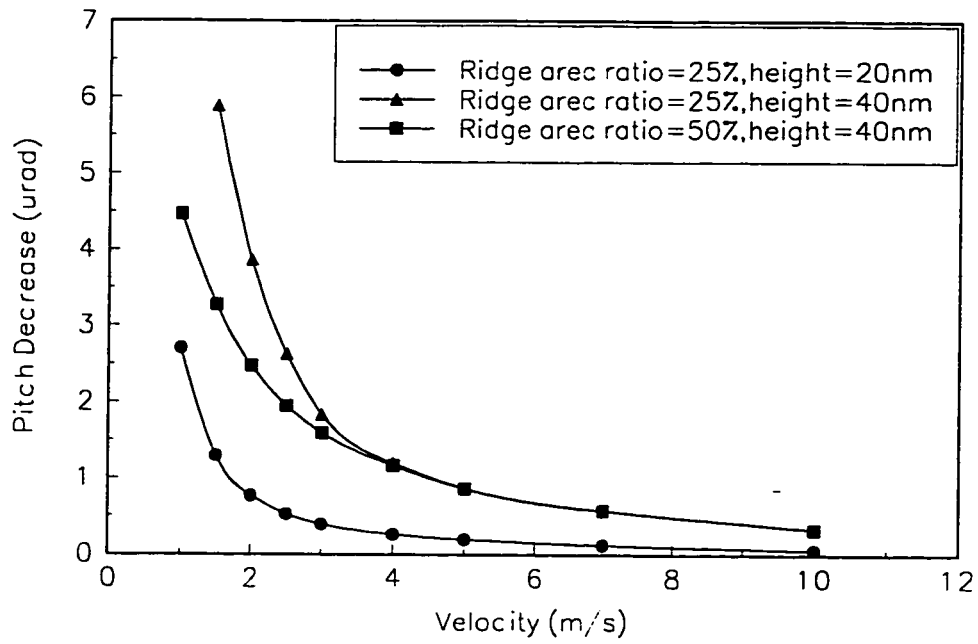


**Fig. 7.5** Pitch decrease versus the disk velocity for three circumferential ridge disk surfaces

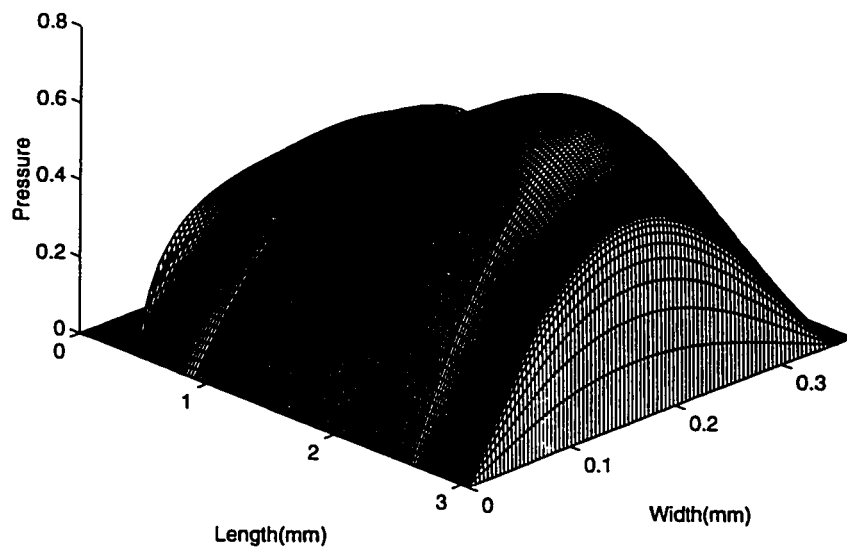


**Fig. 7.6** Dimensionless 3-D air bearing pressure profile beneath the inner rail for the smooth disk surface. The disk velocity is 2 m/s

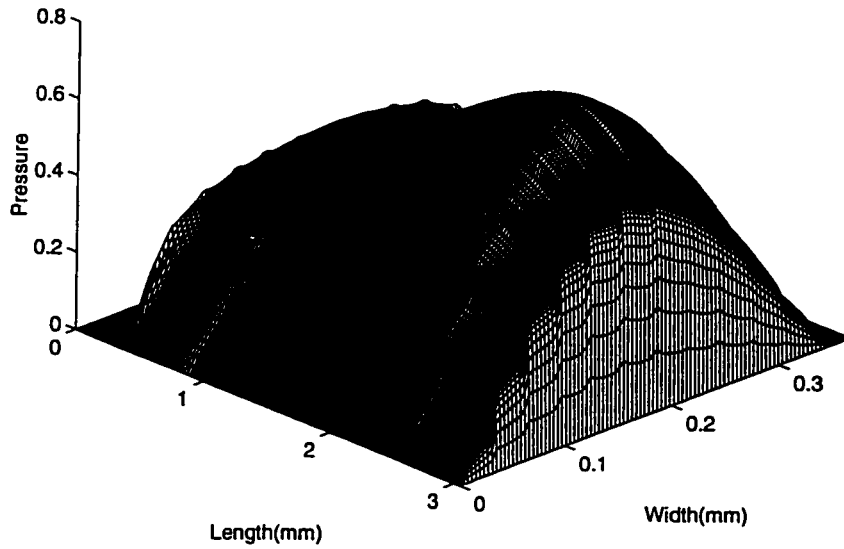


**Fig. 7.7** Dimensionless 3-D air bearing pressure profile beneath the inner rail for the circumferential ridge disk surface with a ridge height of 20 nm and a ridge area ratio of 25%. The disk velocity is 2 m/s

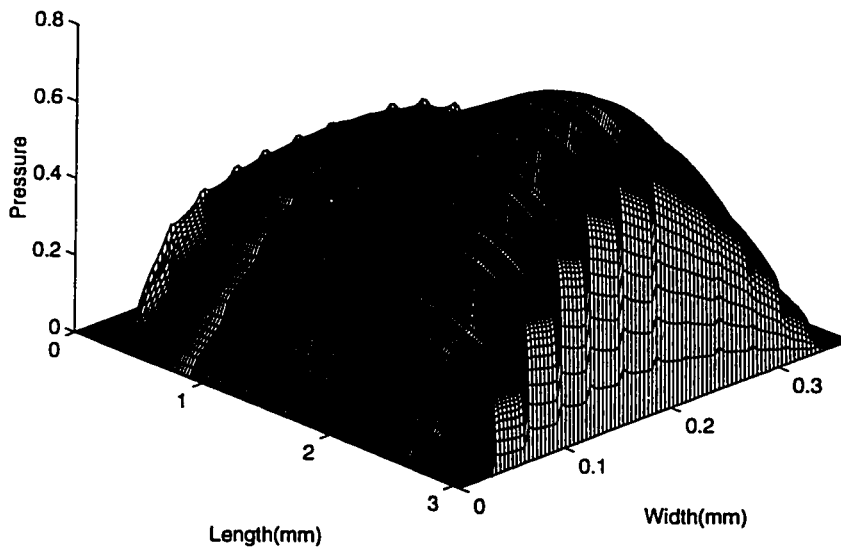


**Fig. 7.8** Dimensionless 3-D air bearing pressure profile beneath the inner rail for the circumferential ridge disk surface with a ridge height of 40 nm and a ridge area ratio of 25%. The disk velocity is 2 m/s

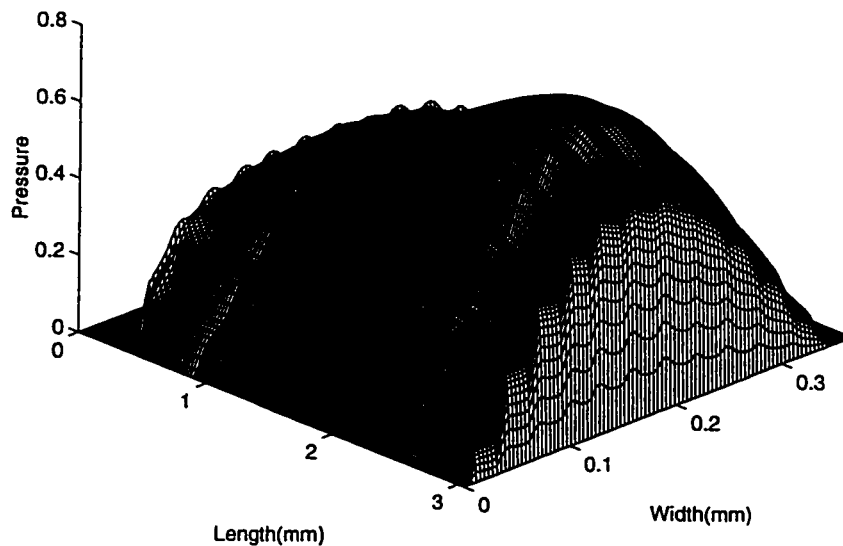


**Fig. 7.9** Dimensionless 3-D air bearing pressure profile beneath the inner rail for the circumferential ridge disk surface with a ridge height of 40 nm and a ridge area ratio of 50%. The disk velocity is 2 m/s

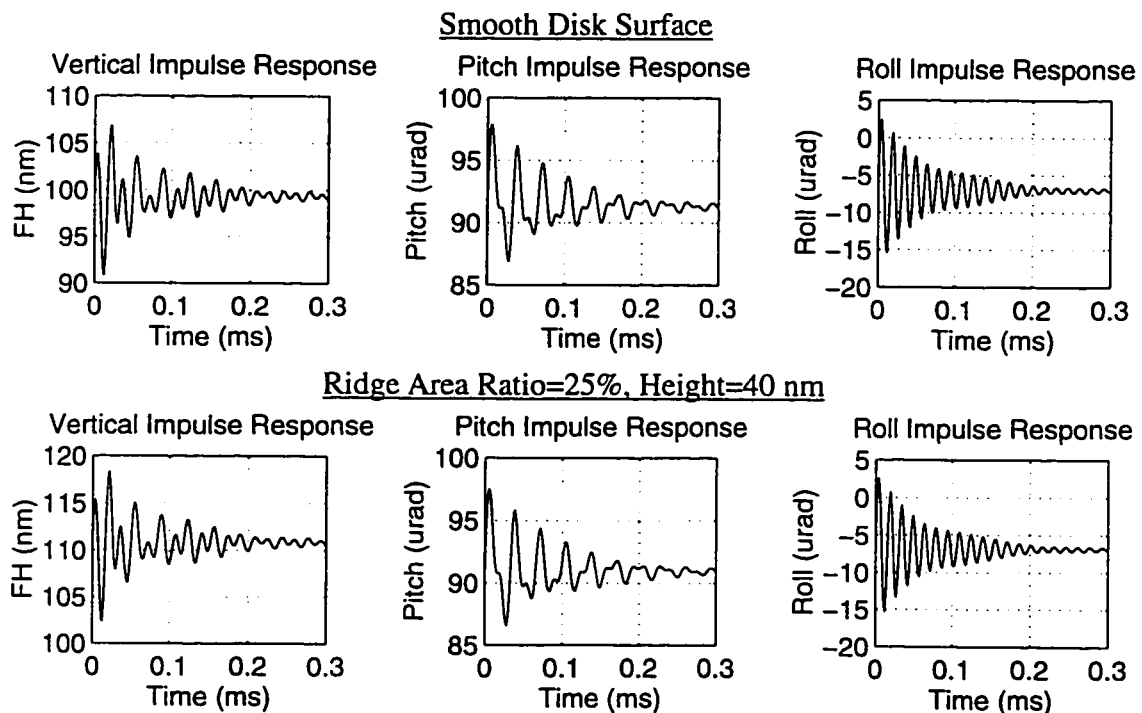


**Fig. 7.10** Vertical, pitch and roll impulse responses at the disk velocity of 10 m/s. Initial vertical velocity = 2 mm/s for vertical impulse response, initial pitch angular velocity = 2 rad/s for pitch impulse response, initial roll angular velocity = 4 rad/s for roll impulse response

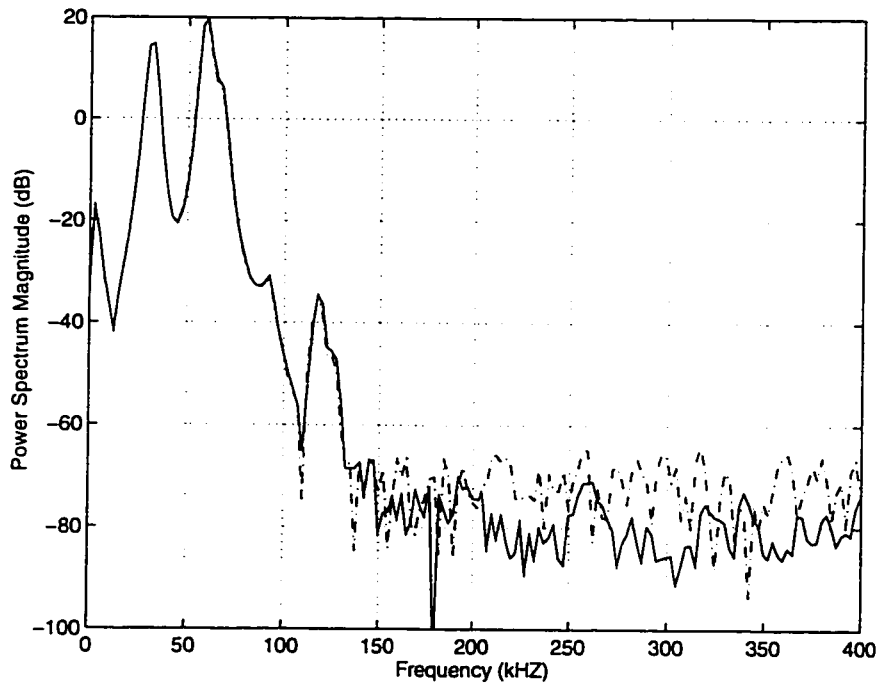


**Fig. 7.11** Power spectral magnitude plots of the vertical impulse responses at the disk velocity of 10 m/s. Initial vertical velocity = 2 mm/s, smooth surface (solid line), ridge area ratio = 25%, height = 40 nm (dash dot line)

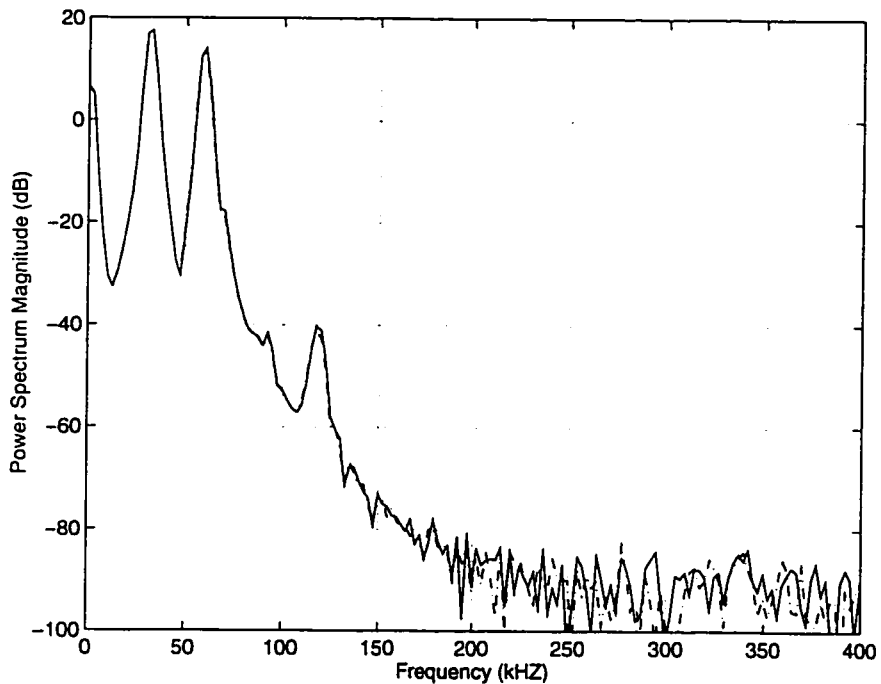


**Fig. 7.12** Power spectral magnitude plots of the pitch impulse responses at the disk velocity of 10 m/s. Initial pitch angular velocity = 2 rad/s, smooth surface (solid line), ridge area ratio = 25%, height = 40 nm (dash dot line)

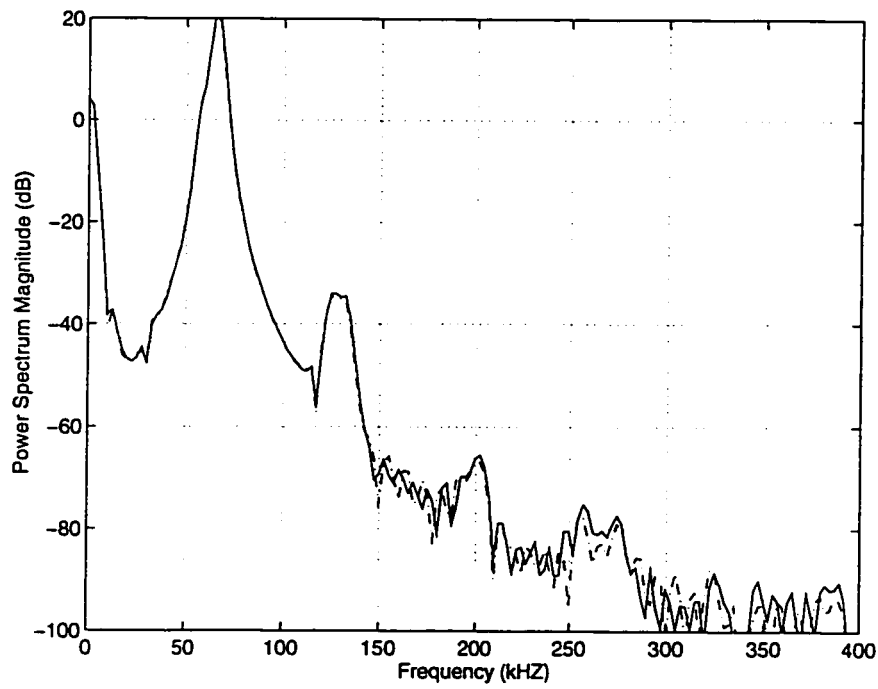


**Fig. 7.13** Power spectral magnitude plots of the roll impulse responses at the disk velocity of 10 m/s. Initial roll angular velocity = 4 rad/s, smooth surface (solid line), ridge area ratio = 25%, height = 40 nm (dash dot line)

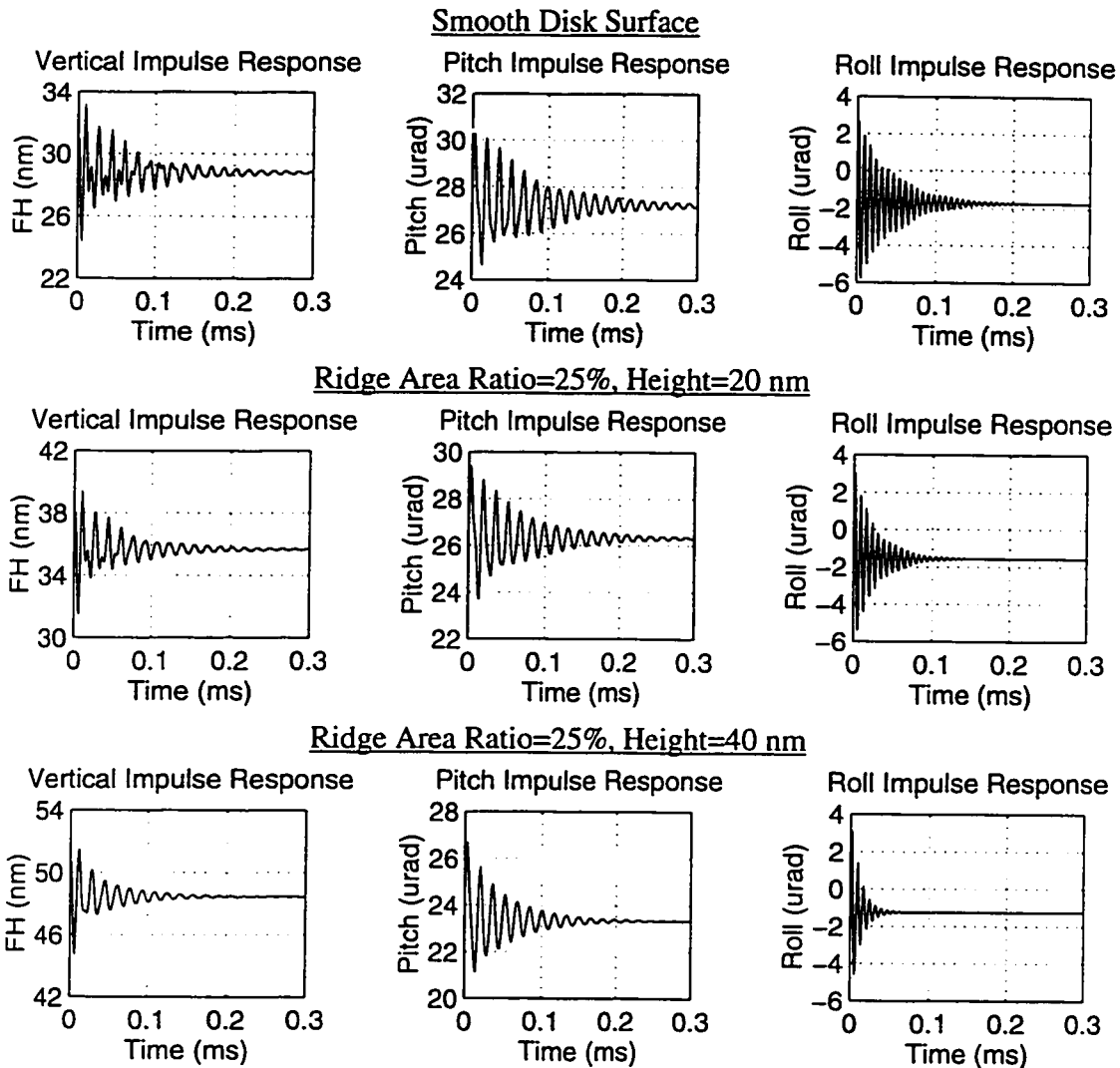


**Fig. 7.14** Vertical, pitch and roll impulse responses at the disk velocity of 2 m/s. Initial vertical velocity = 2 mm/s for vertical impulse response, initial pitch angular velocity = 2 rad/s for pitch impulse response, initial roll angular velocity = 4 rad/s for roll impulse response

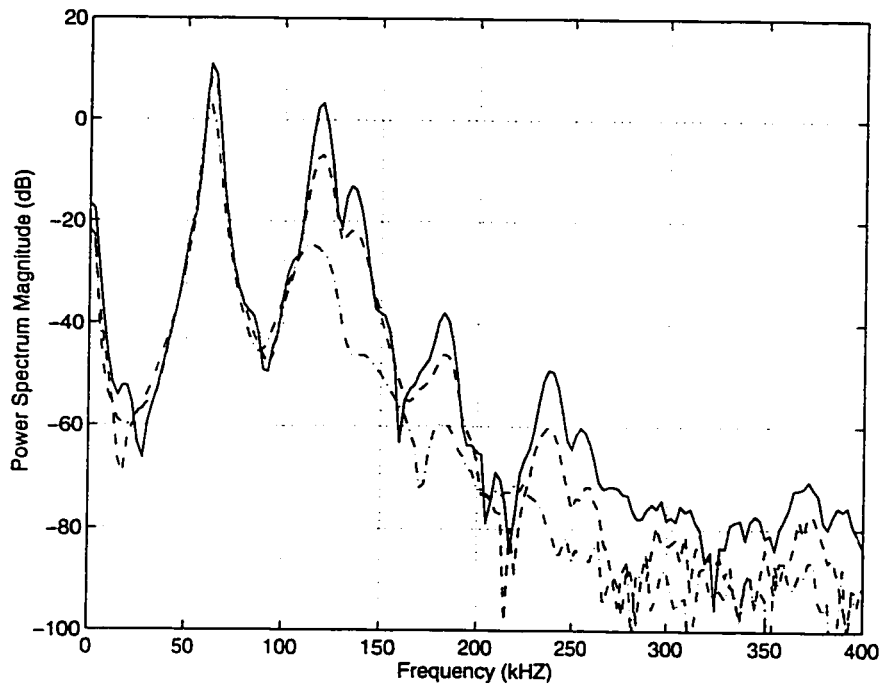


**Fig. 7.15** Power spectral magnitude plots of the vertical impulse responses at the disk velocity of 2 m/s. Initial vertical velocity = 2 mm/s, smooth surface (solid line), ridge area ratio=25%, height = 20 nm (dash line), ridge area ratio = 25%, height = 40 nm (dash dot line)

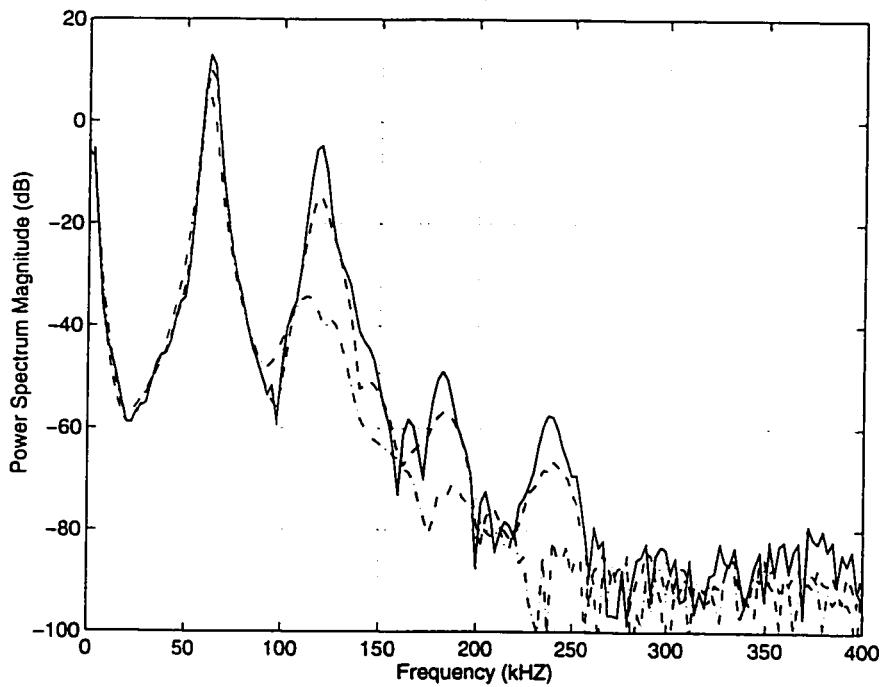


**Fig. 7.16** Power spectral magnitude plots of the pitch impulse responses at the disk velocity of 2 m/s. Initial pitch angular velocity = 2 rad/s, smooth surface (solid line), ridge area ratio=25%, height = 20 nm (dash line), ridge area ratio = 25%, height = 40 nm (dash dot line)

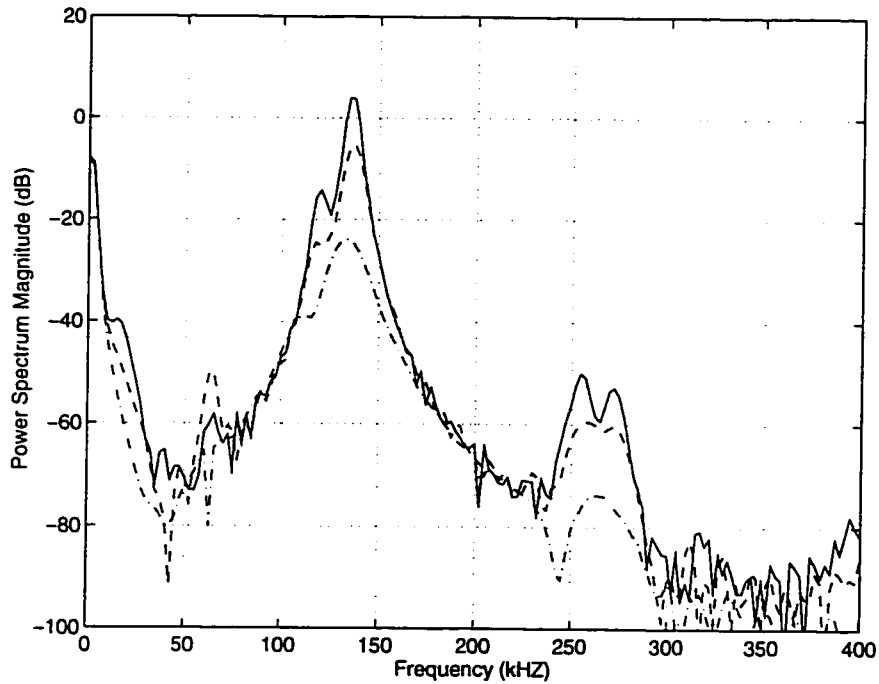


**Fig. 7.17** Power spectral magnitude plots of the roll impulse responses at the disk velocity of 2 m/s. Initial roll angular velocity = 4 rad/s, smooth surface (solid line), ridge area ratio=25%, height = 20 nm (dash line), ridge area ratio = 25%, height = 40 nm (dash dot line)

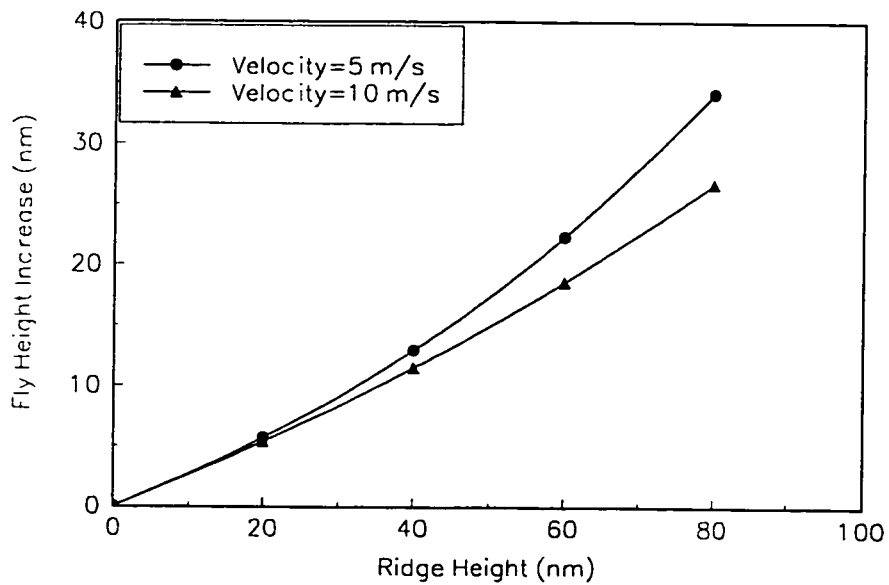


**Fig. 7.18** Effects of the ridge height on the fly height increase for two disk velocities of 5 and 10 m/s. The ridge area ratio is 25%



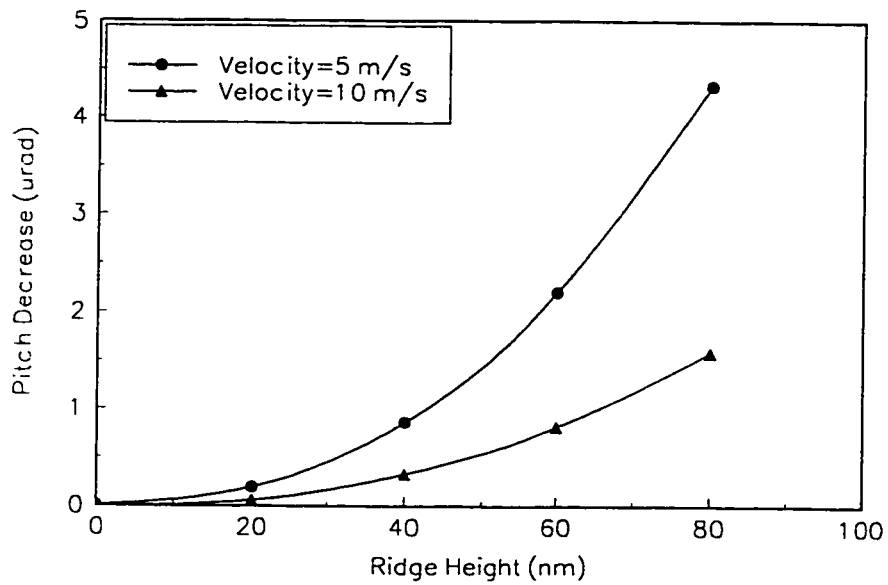


**Fig. 7.19** Effects of the ridge height on the pitch decrease for two disk velocities of 5 and 10 m/s. The ridge area ratio is 25%

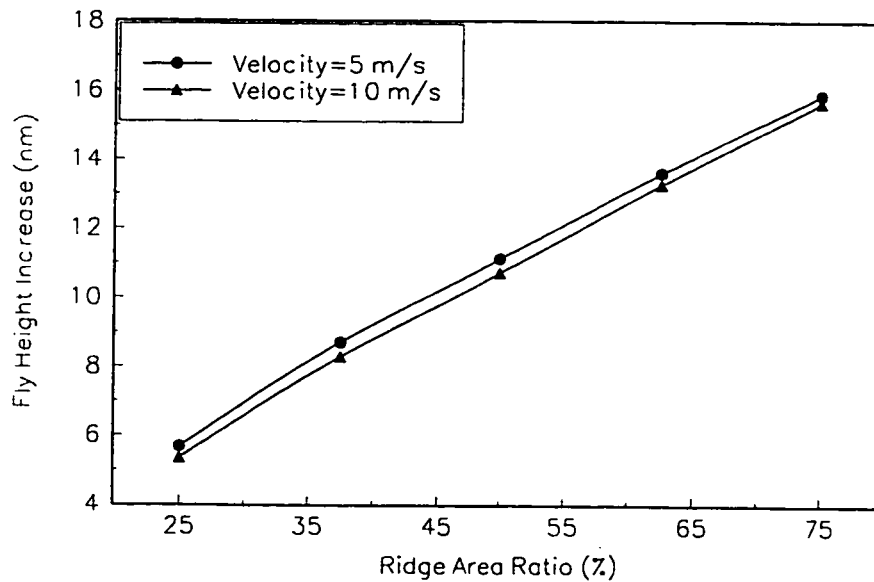


**Fig. 7.20** Effects of the ridge area ratio on the fly height increase for two disk velocities of 5 and 10 m/s. The ridge height is 20 nm.

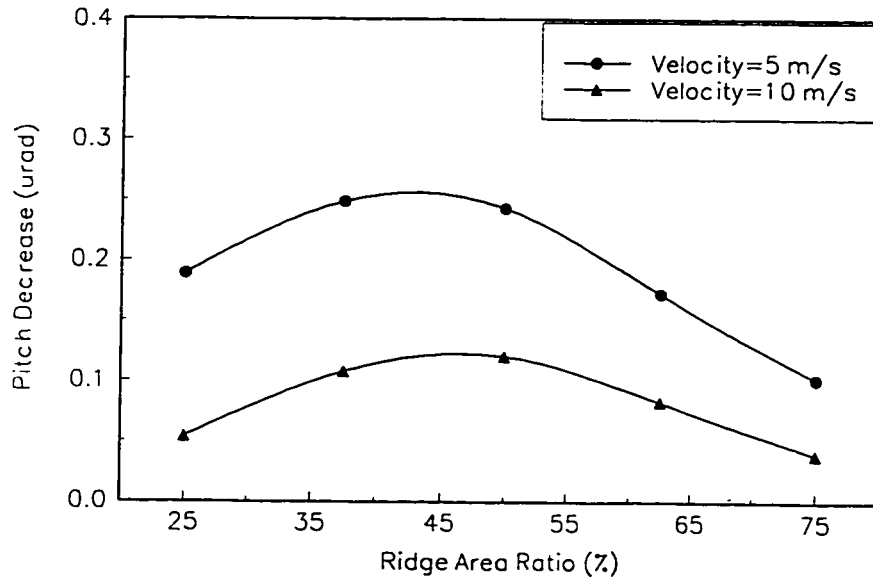


**Fig. 7.21** Effects of the ridge area ratio on the pitch decrease for two disk velocities of 5 and 10 m/s. The ridge height is 20 nm

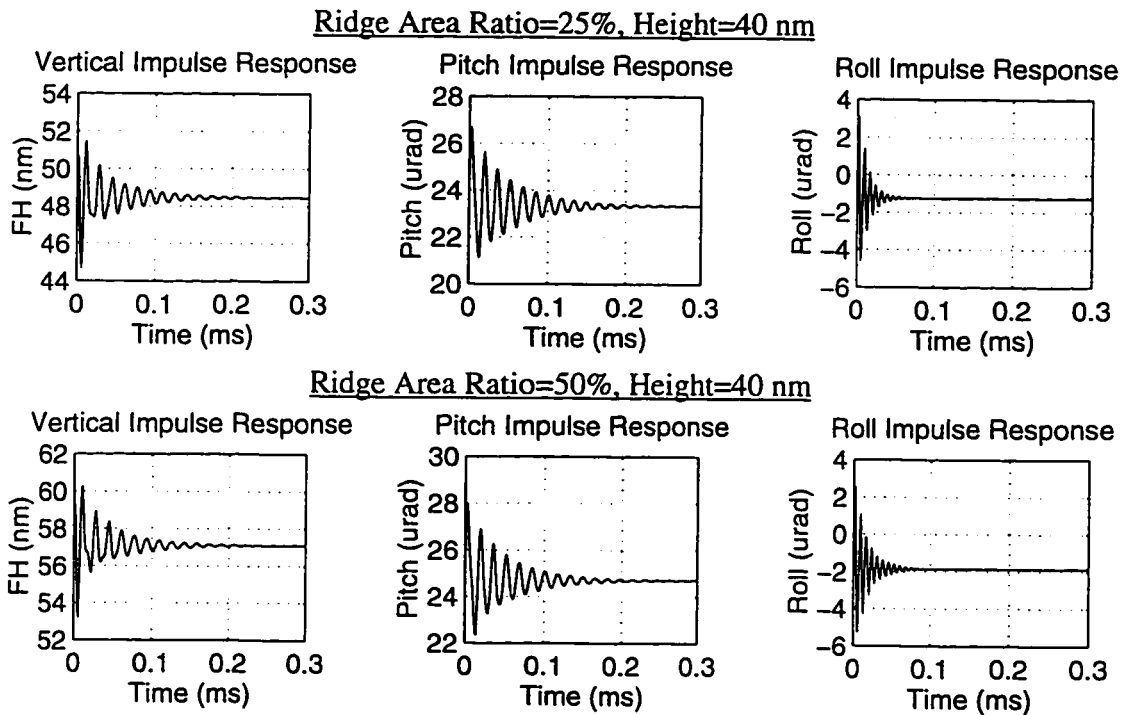


**Fig. 7.22** Vertical, pitch and roll impulse responses at the disk velocity of 2 m/s. Initial vertical velocity = 2 mm/s for the vertical impulse response, initial pitch angular velocity = 2 rad/s for the pitch impulse response, initial roll angular velocity = 4 rad/s for the roll impulse response

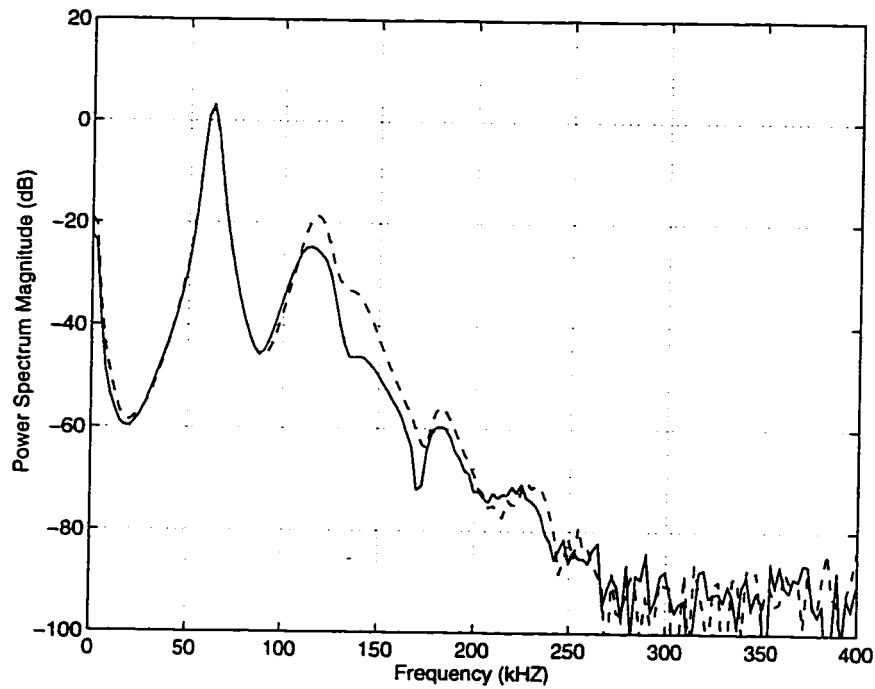


**Fig. 7.23** Power spectral magnitude plots of the vertical impulse responses at the disk velocity of 2 m/s. Initial vertical velocity = 2 mm/s, ridge area ratio=25%, height = 40 nm (solid line), ridge area ratio = 50%, height = 40 nm (dash line)

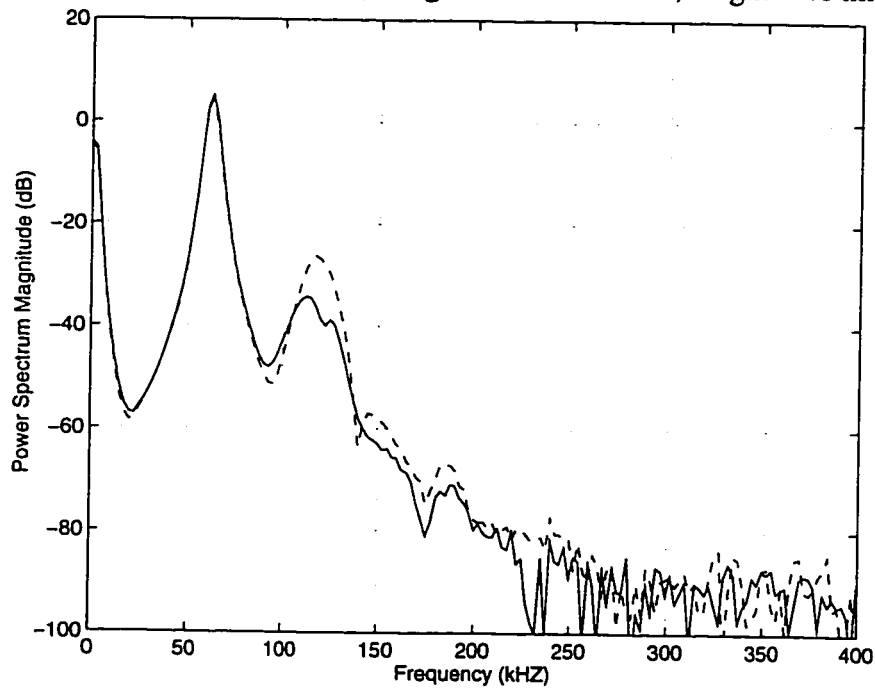


**Fig. 7.24** Power spectral magnitude plots of the pitch impulse responses at the disk velocity of 2 m/s. Initial pitch angular velocity = 2 rad/s, ridge area ratio=25%, height = 40 nm (solid line), ridge area ratio = 50%, height = 40 nm (dash line)

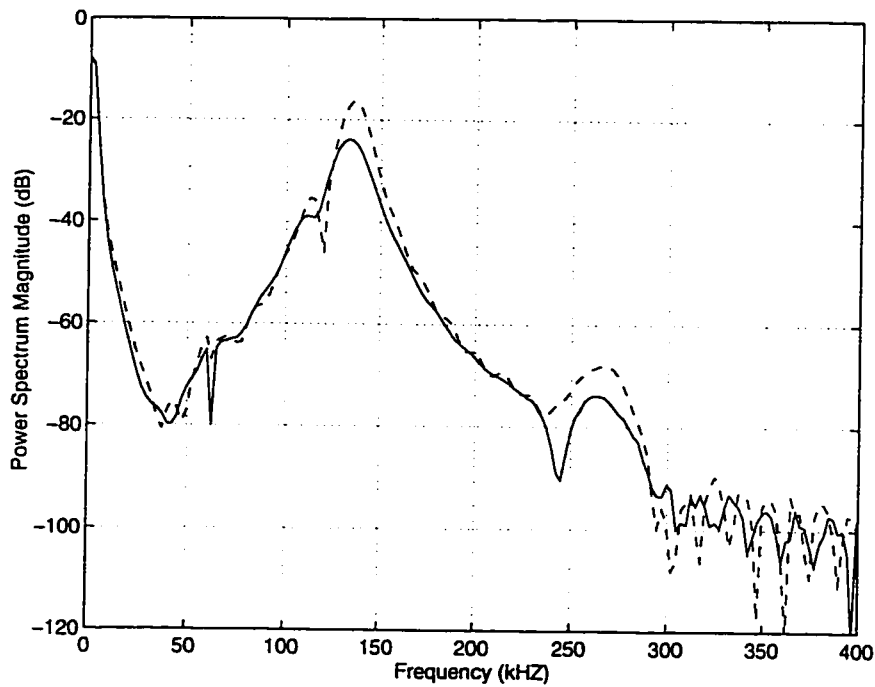


**Fig. 7.25** Power spectral magnitude plots of the roll impulse responses at the disk velocity of 2 m/s. Initial roll angular velocity = 4 rad/s, ridge area ratio=25%, height = 40 nm (solid line), ridge area ratio = 50%, height = 40 nm (dash line)

## **CHAPTER 8**

# **DYNAMICS OF TRIPAD SLIDER PARTIAL CONTACT AIR BEARINGS\***

### **8.1 Introduction**

The hard disk drive industry has been enjoying a period of exponential density growth. The areal density of current state-of-the-art production drives is around 1Gb/in<sup>2</sup>, with 10 Gb/in<sup>2</sup> drives predicted in early next century. While past density increases have come from evolutionary advances, future increases will require radical breakthroughs in the head/disk interface technology. Partial contact recording is one of the challenges the industry is currently pursuing. Conceptually, partial contact recording occurs when an air bearing slider operates at or below the glide height of the media by design or by consequence of drive design. One of the partial contact slider designs is the so-called tripad pseudo-contact slider. It is a modified bi-rail taper-flat design with two shortened side rails and a small pad located at the center of the trailing edge that carries the read/write element. Besides insensitivity to roll motion, the shortened side rails shift the air bearing force center towards the leading edge, resulting in a high pitch angle and low spacing at the rear pad. By appropriate design, the rear pad flies at or slightly below glide height, which maximizes the data recording density. However, the non-zero head/disk interference height produces a constant contact between the head and media. This contact may create severe tribological problems such as wear and mechanical durability as compared to the conventional non-contact air bearing interface between the slider and the

---

\* Parts of this chapter are submitted for publication, see Hu and Bogy (1996)

disk. In order to minimize these adverse effects due to the contact, designers must have a thorough understanding of the dynamics of partial contact air bearings.

In this chapter, the dynamics of tripad slider partial contact air bearings are analyzed using the CML Air Bearing Dynamic Simulator. The GW asperity-based contact model is employed to model the slider/disk contact. The slider's fly height, pitch, contact force and partial contact air bearing stiffnesses are calculated, and the effects of radial position, surface roughness, glide height and altitude on them are summarized. The tripad slider's responses to a passing bump and initial impulses are simulated, and its partial contact air bearing resonant frequencies are obtained by examining the power spectral density plots. To understand the disk surface roughness effect on the head/disk spacing and contact force modulations, the transient fly height histories over a "supersmooth" disk are calculated by directly incorporating a measured disk track profile into the simulator. The motions of the slider during track seeking and accessing over a transition between landing and data zones are also simulated for the case of a Hutchinson 850AK type suspension. Modal analysis of the suspension is employed to integrate the suspension dynamics into the air bearing simulator. To evaluate the crash resistance of tripad slider partial contact air bearings, the crash stop impact processes for two deceleration values of 500G and 800G are analyzed. Finally, the slider's contact take-off dynamics during the start-up are simulated.

## **8.2 Numerical Models**

The generalized Reynolds equation and the equation of motion of the slider and its

suspension are numerically solved using the CML Air Bearing Dynamic Simulator. Due to the partial contact condition in slider air bearings the no-slip boundary condition at the wall is no longer satisfied. The modification proposed by Fukui and Kaneko (1988) based on the linearized Boltzmann equation is employed in this study for the ultra-low fly height application. The GW asperity-based contact model (Greenwood and Williamson, 1966) is employed to extract the contact forces and moments.

### **8.3 Results and Discussions**

The tripad slider air bearing surface is shown in Fig.8.1. In our study, a Hutchinson 850AK type suspension is used. Its FEM mesh is displayed in Fig. 8.2. 3238 nodes are used to model this suspension with a dense mesh distribution in the flexure portion. The eigenvalue solution is first obtained using ABAQUS, then the first 10 modes are used in the partial contact air bearing simulation to represent the suspension dynamics. The disk rotation speed is 5200 rpm. At the inner radius of 20.73 mm, the slider has a skew of 4.508 degrees, and the closest point of separation with the disk is in the center line of the rear pad offset 6.35  $\mu\text{m}$  from the trailing edge where the edge blend starts. The spacing at this point is about 10.86 nm under 3.5 grams of loading force acting at the slider's center. In this simulation, we assume that the asperity heights have a Gaussian probability distribution and their standard deviation is 6 nm. The 3D non-dimensional air bearing pressure profile is drawn in Fig. 8.3. We note that the pressure at the rear pad is much higher than that on the two side rails. Figure 8.4 displays the corresponding 3D non-dimensional contact pressure distribution. The total contact force is 64.77 mg, which is

1.85% of the suspension load. The contact pressure is concentrated at the rear pad mainly because of the high pitch angle ( $176.46 \mu\text{rad}$ ) and low spacing at the rear pad. The slight tilt of the contact pressure profile in the slider width direction is due to the slider's roll angle.

**8.3.1 Fly Height, Pitch and Contact Force.** The fly height, pitch and contact force at three radial positions are summarized in Table 8.1. The minimum spacing at the middle radius of 32.46 mm is slightly higher than those at the inner and outer radii. However, the pitch increases dramatically from the inner radius position to the outer radius position. A smaller pitch angle produces a larger contact area at the trailing edge. This is why the contact force at the inner radius is the largest among the three radial positions. Table 8.2 shows the effects of surface roughness on the fly height, pitch and contact force. As anticipated, a rougher interface generates a larger contact force and larger spacing between the head and the disk. As the contact force increases, the slider's pitch angle gradually decreases. The effects of the glide height on the fly height, pitch and contact force are presented in Table 8.3. Decreasing the glide height results in the reduction of both the contact force and fly height. This agrees with the intuitive expectation that burnishing the slider/disk interface over time knocks down the high asperities and reduces the slider/disk interference. As the glide height increases to a certain value (15 nm in this case), the effect of the glide height on the contact force drops to almost zero. Altitude also has a significant effect on the fly height and contact force as shown in Table 8.4. At high altitude, the loss of the air bearing force due to the increase of the molecular mean free path is compensated by the supply of the contact force generated by the fly height and



pitch decreases. As we increase the altitude from 0 to 3000 meters, the contact force is nearly tripled. We also note that the contact force increases almost linearly with altitude at a rate of about 0.0409 mg/m.

**8.3.2 Partial Contact Air Bearing Stiffness.** The stiffnesses are obtained by use of a linear perturbation at the steady state fly height. Table 8.5 summarizes the partial contact air bearing stiffnesses at three radial positions. At the inner radius the slider has the highest stiffnesses, followed by the outer radius and middle radius except in the roll direction. Effects of interface roughness are presented in Table 8.6. Vertical and pitch stiffnesses increase as the roughness magnitude increases. The roll stiffness changes slightly. As shown in Table 8.7, decreasing the glide height results in a considerable increase of the vertical and pitch stiffnesses and a minor increase of roll stiffness. As a comparison, altitude has a major effect on partial contact air bearing stiffnesses. As the altitude increases from 0 to 3000 meters, the vertical and pitch stiffnesses increase by 49.5% and 78.7%, respectively.

**8.3.3 Bump and Impulse Responses.** Figure 8.5 shows the slider's responses to the passage of a rectangular bump on the disk surface. The bump has a height of 30 nm and width of 25  $\mu\text{m}$ . The glide height is 25 nm. The slider reacts slightly as the bump travels under the front part of the slider due to the high pitch angle and then experiences larger oscillation as the bump encounters the rear pad portions of the bearing as a result of its below-glide height spacing. At the moment of the bump passing the rear pad, the contact force reaches a maximum value of about 888.2 mg. It is also noted that the roll oscillation starts a little earlier than the vertical and pitch oscillations. This is because the

bump exerts a roll excitation to the skewed slider as it passes the trailing edge of the two shortened side rails. Overall, the dominating motion due to the passing bump is in the pitch mode. Figure 8.6 shows the vertical, pitch and roll impulse responses. The initial vertical velocity is 2 mm/s, and the initial pitch and roll velocities are 2 rad/s. Also shown in the figure are their corresponding power spectral densities (PSD). The time-domain plots show that the vertical oscillation is damped out more quickly than the pitch and roll motions, which agrees well with the relative peak values in the PSD plots. The PSD results also indicate that the roll motion is decoupled from the vertical and pitch motions, while the pitch and vertical oscillations are closely coupled together. The decoupling between the roll and the vertical/pitch motions is especially important, since it makes the magnetic spacing at the rear pad insensitive to the roll motion. From the PSD plots, we also calculated partial contact air bearing resonant frequencies. Table 8.9 presents these resonant frequencies at three radial positions. Among the three radial positions, the slider flying at the inner radius has the highest resonant frequencies. The vertical frequency at the outer radius is higher than that at the middle radius, while its pitch and roll frequencies are slightly lower than those at the middle radius. The effects of the slider/disk interface roughness on the resonant frequencies are summarized in Table 8.10. The vertical resonant frequency increases as the slider/disk interface gets rougher, whereas the pitch and roll resonant frequencies do not appear to be related much to the roughness. Table 8.11 shows the resonant frequencies at two altitudes. The vertical resonant frequency increases from 110 kHz to 134 kHz as we move the hard disk drive from the sea level to 3000m above, which is a 21.8% increase. Again, the effects of

altitude on the pitch and roll resonant frequencies are minor. As shown in Table 8.12, decreasing glide height increases significantly the vertical resonant frequency, but does not affect the pitch and roll resonant frequencies.

**8.3.4 Fly Height Modulation over a Supersmooth Disk.** When the tripad slider flies over a real disk, the inevitable surface roughness and surface contact causes fluctuations in the head-disk spacing. In our simulation, a measured disk track profile is directly incorporated. Figure 8.7 shows a measured supersmooth disk track profile with a long wavelength cut-off of 350  $\mu\text{m}$ . The corresponding fly height, roll and contact force over the period of 16 ms are also plotted in the same figure and their modulations are summarized in Table 8.13. The fly height fluctuates between 10.91 - 1.49 nm and 10.91 + 2.90 nm, and the contact force oscillates between 64.89 - 43.24 mg and 64.89 + 55.80 mg.

**8.3.5 Track Seeking Dynamics.** Track seeking is the process for the slider to move from one track to another. This process involves head motion as well as the dynamics of the suspension. The radial displacement of the slider changes the skew angle and the relative disk velocity, while the slider's accelerations/decelerations introduce inertia forces. Both of these can adversely affect the head/disk spacing and the contact force. Figure 8.8 presents the track accessing profile. To move the slider from 20.73 mm to 30.53 mm in the radial direction, it is first accelerated to 2.595 m/s, followed by a short period of constant velocity, then decelerated to 0 velocity. The maximum acceleration/deceleration is 80G. During the whole process, the geometrical skew angles change from 4.508 to -5.538 degrees. Figure 8.9 shows the roll motion during the track seeking process

characterized in Fig. 8.8. Positive roll is defined such that the outer rail flies higher than the inner rail. The inertia force of the laterally moving slider produces a negative roll motion during the acceleration stage and a positive roll motion during the deceleration stage. The amount of the roll motion mainly depends on the partial contact air bearing roll stiffness for a given acceleration/deceleration profile (Hu and Bogy, 1995d). The magnitude difference between the two stages shown in Fig. 8.9 correlates well with the roll stiffness trend from the inner radius to outer radius as presented in Table 8.5. Figure 8.9 also shows that a roll oscillation follows the sudden roll change. The low frequency motion following the high frequency and quickly damped-out oscillation corresponds to the first torsion mode of the suspension. The fly height during the track seeking process is plotted in Fig. 8.10. The fly height modulation is closely related to the roll motion shown in Fig. 8.9. Since the fly height is measured at the point in the center line near the trailing edge, a roll motion always results in an increase of the fly height. The magnitude of fly height modulation is small, this is mainly attributed to the insensitivity of center pad fly height to slider's roll motion. Figure 8.11 shows the contact force modulation during track seeking. The contact force modulation follows a reversed pattern as compared to the fly height modulation. This is because a larger spacing at the rear pad indicates a smaller interference height for a given slider/disk interface. Overall, the contact force decreases from 64.77 mg to 19.86 mg.

**8.3.6 Crash Stop Impact Performance.** The crash stop or actuator slam stop occurs when a power failure is applied during a track seek, resulting in uncontrolled collision of the actuator with a mechanical limit stop. The maximum deceleration during crash stop

is typically more than an order of magnitude greater than that during track accessing. Therefore, it is considered the most severe dynamic loading in the drive. In this study, the mechanical limit stop is placed at the inner radius of 20.19 mm. To study the effect of different deceleration values, an inline actuator moving toward the rotation center of the disk at 2.54 m/s is stopped at the radius of 20.19 mm using a rectangular deceleration profile. Two maximum deceleration values (500G and 800G) are used in our simulation. Figure 8.12 shows two deceleration and velocity profiles during the crash stop. The roll motion during crash stop is plotted in Fig. 8.13. The amount of roll decrease increases with the deceleration level. In the 800G case, roll drops about 103.20  $\mu\text{rad}$  as compared to 57.86  $\mu\text{rad}$  in the 500G case. The corresponding pitch motions of the slider during crash stop are displayed in Fig. 8.16. The deceleration introduces a pitch increase. Figures 8.15 and 8.16 show the fly heights at the rear pad and back center point of the outer rail during the two crash stops. As expected, the spacing at the rear pad increases during the deceleration stage. The roll inertia torsion tends to push the outer rail towards the disk surface. In the two simulated cases, the 800G deceleration pushes the trailing edge of the outer rail about 19.18 nm closer to the disk surface than that of the 500G deceleration. The contact force during crash stop is plotted in Fig. 8.17. Large contact force oscillations are observed right after the start and the end of the deceleration. A larger deceleration value results in a larger amplitude contact force oscillation. However, the 800G produces a smaller contact force during the deceleration stage even though it generates a larger roll inertia torsion. This is because of larger increases in the pitch and spacing at the rear pad as shown in Figs. 8.14 and 8.15, which are dominant factors in

contact force modulation.

### **8.3.7 Analysis of Accessing Across a Transition Between Landing and Data Zones.**

As a good alternative for the conventional contact start/stop drive, the zone texturing approach provides a relatively large surface roughness for the takeoff/landing zone and a very smooth surface for the data zone. There is a transition zone between the texture zone and the smooth data zone, which is produced during the manufacturing process. The zone texture/transition zone introduces spacing and contact force modulations, and track accessing across a transition zone may force the slider to fly dangerously close to the disk (Hu and Bogy, 1995a). Figure 8.18 shows the slider's flying characteristics during the event of accessing across a transition zone. Initially, the slider flies at the radius of 20.73 mm. At 0.1 ms, the slider is accelerated radially outward to the velocity of -1.96 m/s at 2.7 ms. The minimum acceleration (maximum amplitude) is -80G. During the whole process, the slider moves 7.05 mm in the radial direction, and the geometrical skew angles change from 4.508 to -3.067 degrees. The transition zone is a constant slope plane with a height of 20 nm. It starts at the radius of 23 mm and ends at the radius of 23.4 mm. The CSS zone and transition zone have a circumferential texture with sinusoidal cross-section in the radial direction with an amplitude of 2.5 nm and a wavelength of 118.6  $\mu\text{m}$ . To fly over the transition zone, the slider has to conform to the slope of the transition zone surface. As a result, the slider's roll first increases, reaching a maximum of 20  $\mu\text{rad}$ , and then decreases to a minimum as the slider leaves the transition zone. Correspondingly, the fly height at the rear pad reaches a maximum of 16.2 nm at the moment when the rear pad flies over the starting point of the transition zone. After

entering the transition zone, the rear pad fly height decreases, attaining a minimum of 8.45 nm at the time when the rear pad is gliding over the ending point of the transition zone, and then increases as the rear pad leaves the transition zone. The contact force modulation follows a reversed pattern as compared to the fly height. The maximum and minimum values of the contact force during the event are 80.63 and 32.55 mg, respectively.

**8.3.8 Contact Take-off Simulation.** Contact start/stop is a process in which the slider is in sliding contact with the disk as it starts and stops rotating. Figure 8.19 shows the flying characteristics during the start-up (up to the disk speed of 0.1303 m/s). Due to the positive crown, the slider's pitch decreases under the contact friction force at the interface, resulting in an increase in the rear pad fly height (Hu and Bogy, 1995c). The fly height reaches a maximum of 36.06 nm at about 3.31 ms, and then as the disk speed increases, the air bearing pressure builds up in the front taper region, increasing the pitch and decreasing the rear pad fly height. The contact force modulates in a way similar to the rear pad fly height. The slider's contact take-off dynamics during the early moments of the start-up through the first 0.25 ms (up to the disk speed of 0.00097717 m/s) are shown in Fig. 8.20. As seen in the figure, the slider is initially at rest on the disk surface, when at 0.01 ms, the disk begins to rotate. The sudden action of the contact friction force causes the slider to oscillate. The amplitudes of the pitch and fly height oscillations are much larger than that of the roll oscillation, indicating the oscillation is mainly in the pitch mode. The initial rear pad fly height increase is about 4.5 nm, and corresponding contact force drop is about 0.37 gram.

## 8.4 Summary

The dynamics of tripad slider partial contact air bearings are studied in this chapter using the CML Air Bearing Dynamic Simulator. In this study, the GW asperity-based contact model is employed to model the slider/disk contact. The effects of radial position, surface roughness, glide height and altitude on the slider's fly height, pitch, contact force and partial contact air bearing stiffnesses are summarized. The contact force increases with altitude and decreases after burnishing. The slider's responses to a passing bump and impulses are simulated, and its partial contact air bearing resonant frequencies are obtained by examining the power spectral density plots. The power spectral density plots also indicate a decoupling between the roll and vertical/pitch motions and the largest partial contact air bearing damping for the vertical motion. The spacing and contact force modulations over a "supersmooth" disk are calculated by directly incorporating a measured disk track profile into the simulator. The motions of the slider during track seeking and accessing over a transition between landing and data zones are also simulated for the case of a Hutchinson 850AK type suspension. It is found that the roll and contact force modulations strongly depend on the partial contact air bearing roll stiffness. To evaluate the slider's crash resistance during actuator's slam stop, the crash stop impact processes for two deceleration values of 500G and 800G are analyzed. Finally, the slider's contact take-off dynamics during start-up are numerically examined.



Radial position (mm)	Minimum FH (nm)	Pitch ( $\mu$ rad)	Contact Force (mg)
20.73	10.86	176.46	64.77
32.46	12.26	242.58	20.39
42.80	10.62	267.74	40.54

**Table 8.1** Fly height, pitch and contact force versus radial positions.  $\sigma = 6$  nm, glide height = 25nm and altitude = 0

$\sigma$ (nm)	Minimum FH (nm)	Pitch ( $\mu$ rad)	Contact Force (mg)
0	8.76	179.02	0
6	10.86	176.46	64.77
12	23.29	162.55	271.59

**Table 8.2** Fly height, pitch and contact force versus roughness. Radial position = 20.73 mm and altitude = 0

Glide Height (nm)	Minimum FH (nm)	Pitch ( $\mu$ rad)	Contact Force (mg)
10	9.51	178.09	25.51
15	10.75	176.59	61.63
20	10.86	176.46	64.65
25	10.86	176.46	64.76

**Table 8.3** Fly height, pitch and contact force versus glide height.  $\sigma = 6$  nm, radial position = 20.73 mm and altitude = 0

Altitude (m)	Minimum FH (nm)	Pitch ( $\mu$ rad)	Contact Force (mg)
0	10.86	176.46	64.76
1000	9.99	170.01	103.72
2000	9.38	163.23	145.34
3000	8.95	156.26	187.46

**Table 8.4** Fly height, pitch and contact force versus altitude.  $\sigma = 6$  nm, glide height = 25nm and radial position = 20.73 mm

Radial Position (mm)	Vertical (kN/m)	Pitch (mN-m/rad)	Roll (mN-m/rad)
20.73	1081.38	610.82	189.81
32.46	740.13	394.05	136.48
42.80	816.79	556.00	106.45

**Table 8.5** Partial contact air bearing stiffnesses versus radial positions.  $\sigma = 6$  nm, altitude = 0 and glide height = 25nm

$\sigma$ (nm)	Vertical (kN/m)	Pitch (mN-m/rad)	Roll (mN-m/rad)
0	844.26	388.72	187.11
6	1081.38	610.82	189.81
12	1290.75	777.18	189.30

**Table 8.6** Partial contact air bearing stiffnesses versus roughness. Altitude = 0 and radial position = 20.73 mm

Glide Height (nm)	Vertical (kN/m)	Pitch (mN-m/rad)	Roll (mN-m/rad)
10	1319.54	753.11	192.17
15	1104.30	637.28	189.93
20	1081.89	611.62	189.82
25	1081.40	610.83	189.81

**Table 8.7** Partial contact air bearing stiffnesses versus glide height.  $\sigma = 6$  nm, altitude = 0 and radial position = 20.73 mm

Altitude (m)	Vertical (kN/m)	Pitch (mN-m/rad)	Roll (mN-m/rad)
0	1081.40	610.83	189.81
1000	1251.85	775.57	180.60
2000	1446.60	938.28	186.76
3000	1616.61	1091.74	176.41

**Table 8.8** Partial contact air bearing stiffnesses versus altitude.  $\sigma = 6$  nm, radial position = 20.73 mm and glide height = 25 nm

Radius (mm)	Vertical (kHz)	Pitch (kHz)	Roll (kHz)
20.73	110	42	61
32.46	90	35	52
42.80	102	34	48

**Table 8.9** Partial contact air bearing resonant frequencies versus radial positions.  $\sigma = 6$  nm, altitude = 0 and glide height = 25 nm

$\sigma$ (nm)	Vertical (kHz)	Pitch (kHz)	Roll (kHz)
0	95	41	61
6	110	42	61
12	118	43	61

**Table 8.10** Partial contact air bearing resonant frequencies versus roughness. Altitude = 0 and radial position = 20.73 mm

Altitude (m)	Vertical (kHz)	Pitch (kHz)	Roll (kHz)
0	110	42	61
3000	134	42	59

**Table 8.11** Partial contact air bearing resonant frequencies versus altitude.  $\sigma = 6$  nm, glide height = 25nm and radial position = 20.73 mm

Glide Height (nm)	Vertical (kHz)	Pitch (kHz)	Roll (kHz)
10	142	42	61
25	110	42	61

**Table 8.12** Partial contact air bearing resonant frequencies versus glide height.  $\sigma = 6$  nm, altitude = 0 and radial position = 20.73 mm

	Mean	Modulation	Standard Deviation
Fly Height (nm)	10.91	+2.90 , -1.49	0.45
Roll ( $\mu$ rad)	5.82	+1.54, -1.75	0.57
Contact Force (mg)	64.89	+55.80 , -43.24	12.57

**Table 8.13** Summary of the fly height, roll and contact force modulations

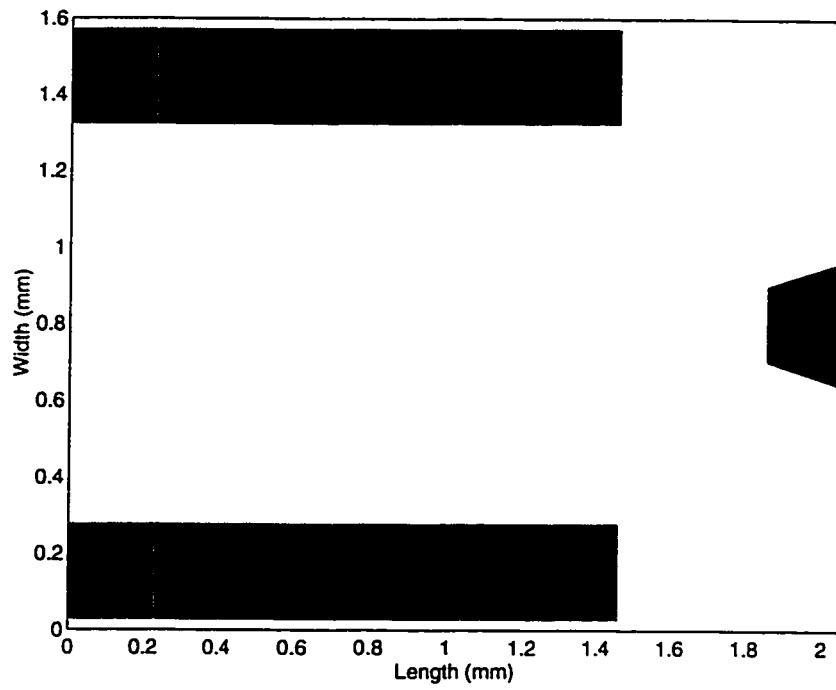


**Fig. 8.1** Tripad slider air bearing surface

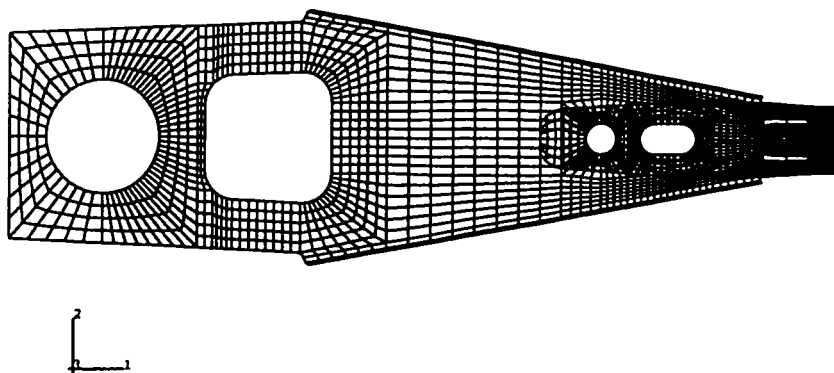


**Fig. 8.2** FEM mesh of a Hutchinson 850AK type suspension

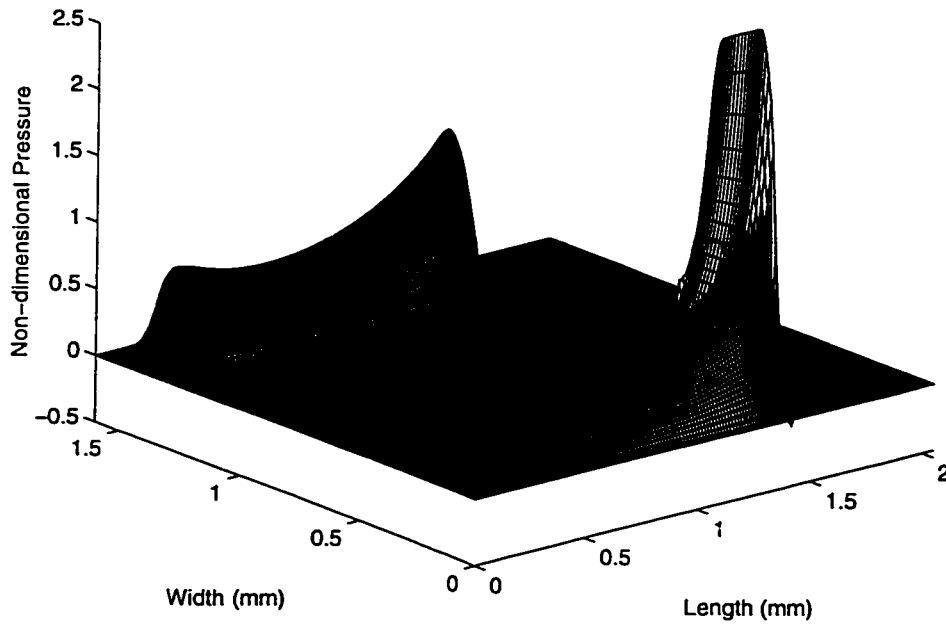


**Fig. 8.3** 3D non-dimensional air bearing pressure profile. Radial position = 20.73 mm,  $\sigma = 6$  nm, glide height = 25 nm and altitude = 0

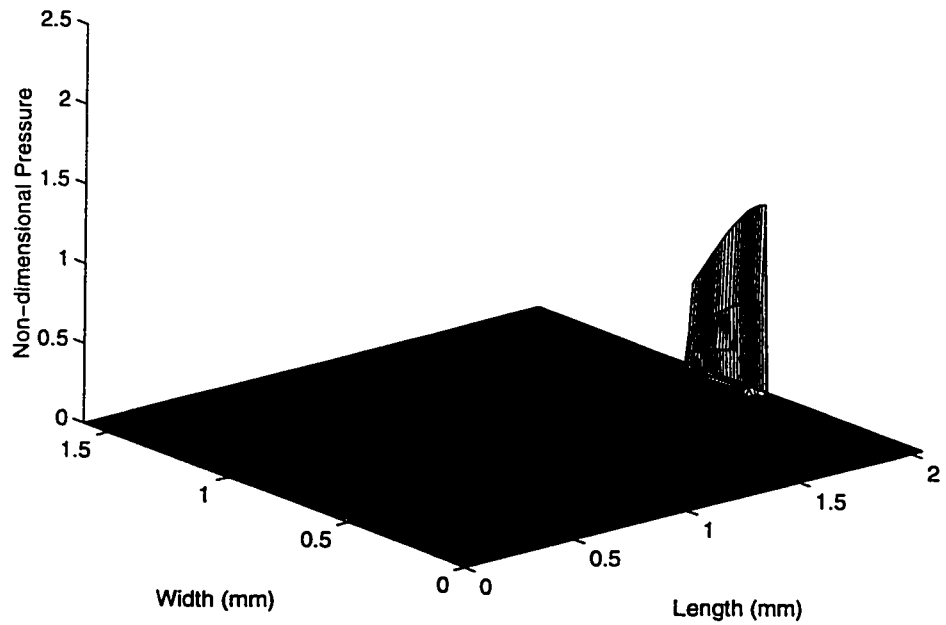


**Fig. 8.4** 3D non-dimensional contact pressure profile. Radial position = 20.73 mm,  $\sigma = 6$  nm, glide height = 25 nm and altitude = 0

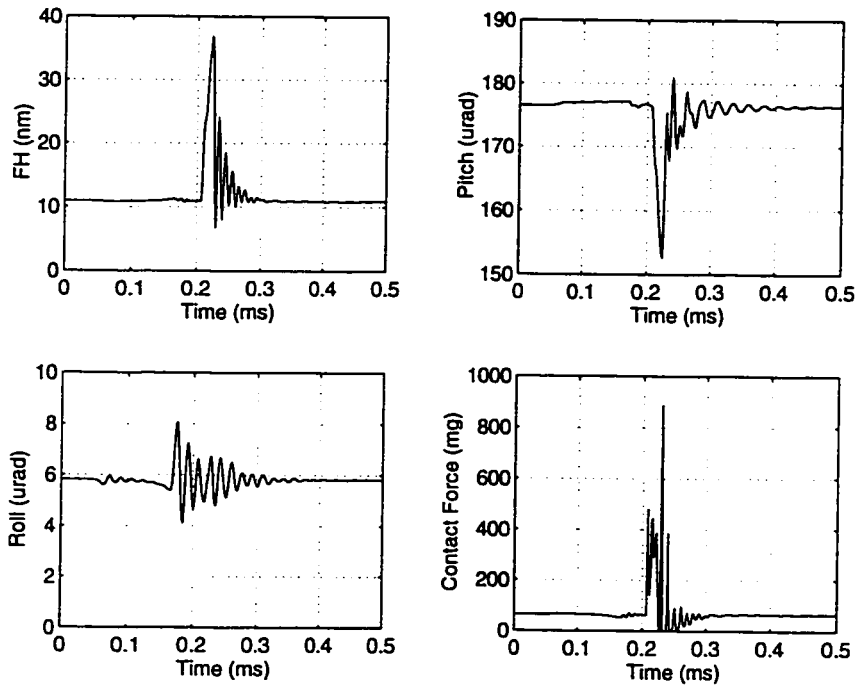


**Fig. 8.5** Bump response. Bump height = 30 nm, width = 25  $\mu\text{m}$ ,  $\sigma = 6$  nm, glide height = 25 nm, radial position = 20.73 mm and altitude = 0

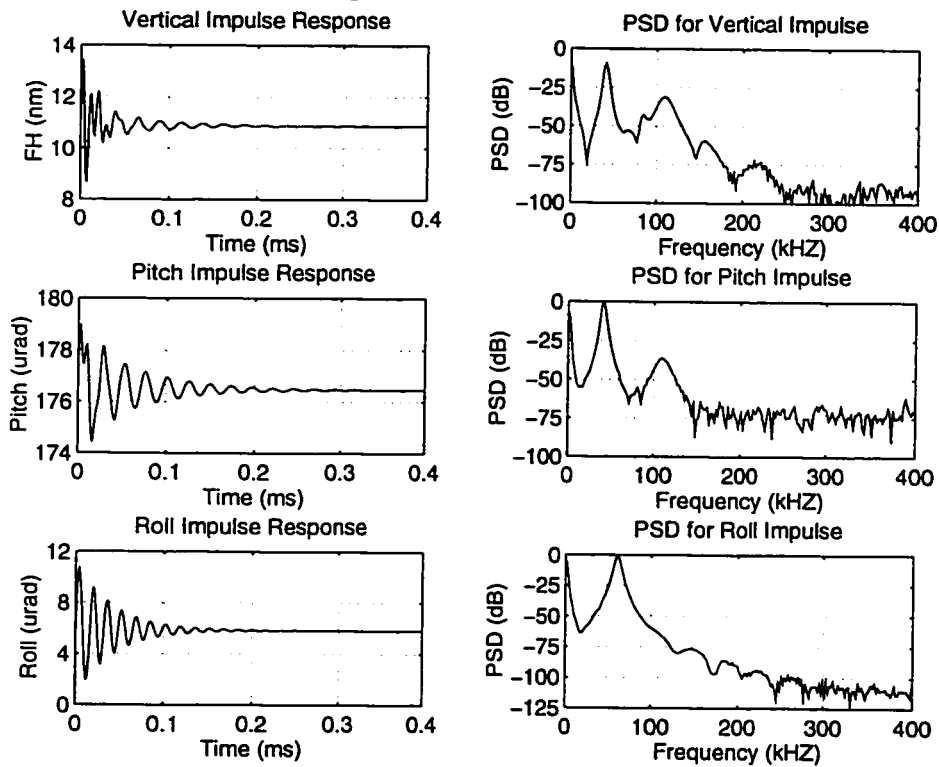


**Fig. 8.6** Vertical, pitch and roll impulse responses and their corresponding power spectral density plots. Initial vertical velocity = 2 mm/s, initial pitch and roll angular velocities = 2 rad/s, radial position = 20.73 mm,  $\sigma = 6$  nm, glide height = 25 nm, altitude = 0

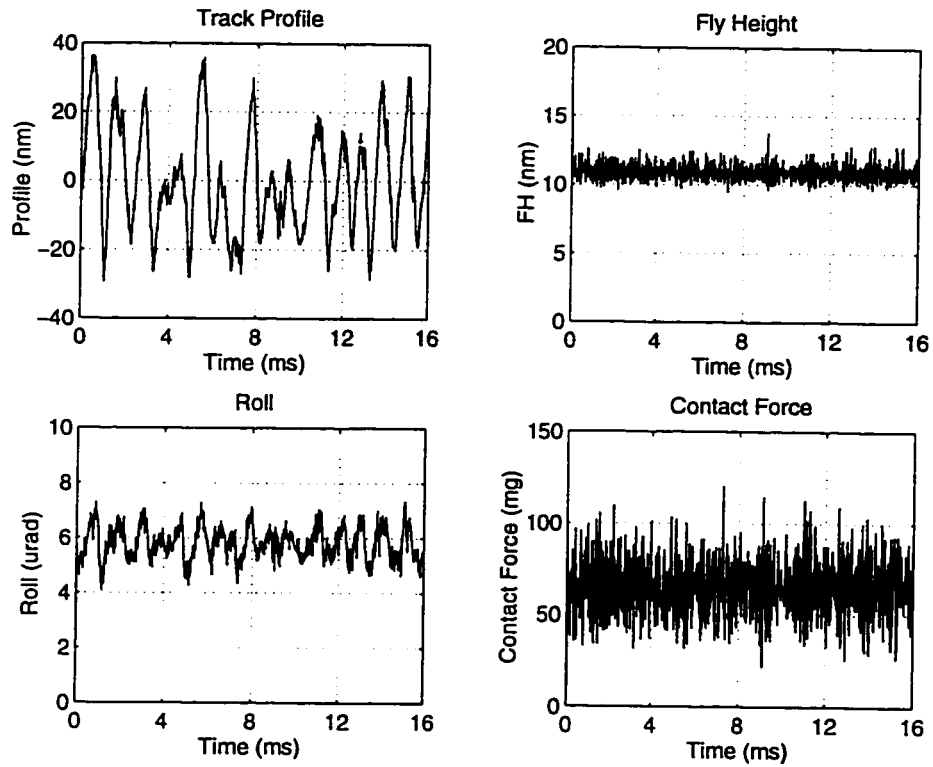


**Fig. 8.7** Fly height, roll and contact force modulations. Radial position = 20.73 mm and altitude = 0

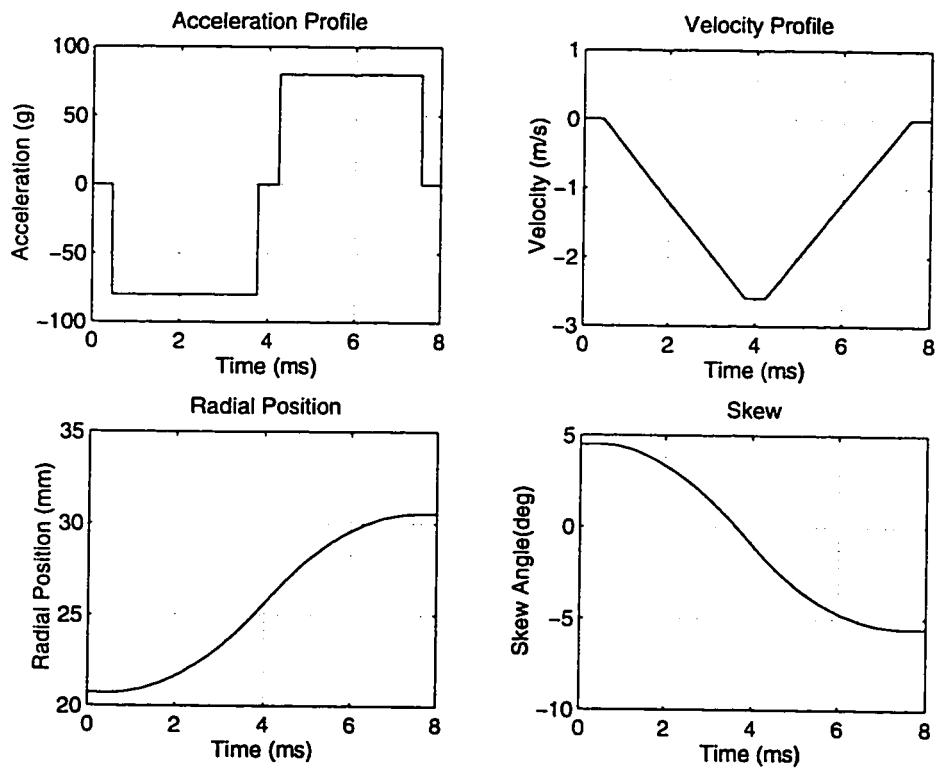


**Fig. 8.8** Track seeking profile

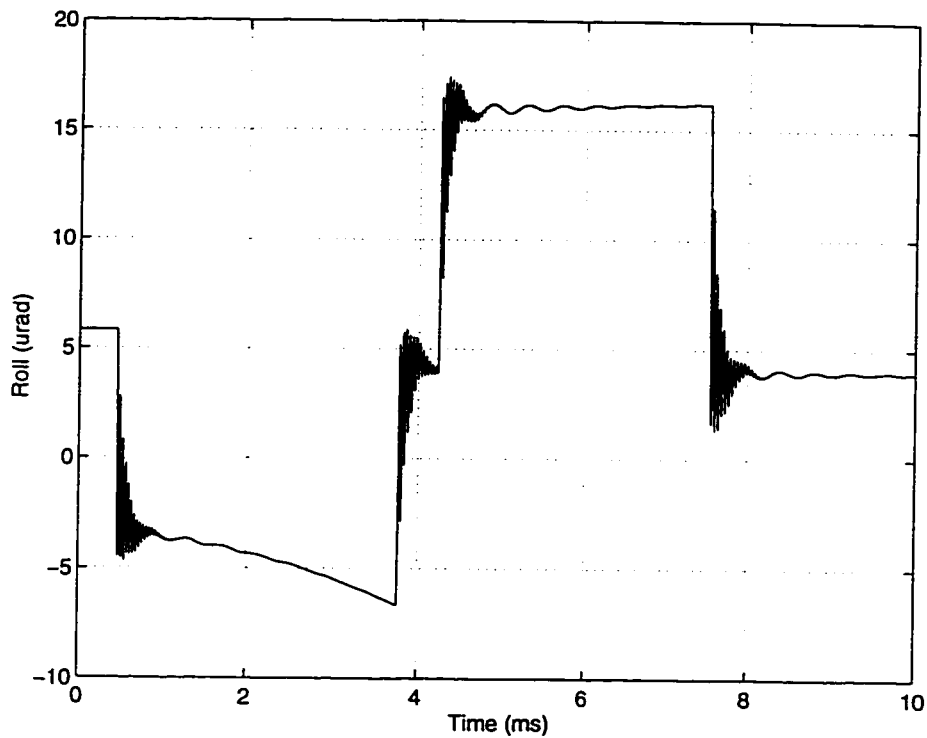


**Fig. 8.9** Roll motion during track seeking.  $\sigma = 6$  nm, glide height = 25 nm and altitude = 0

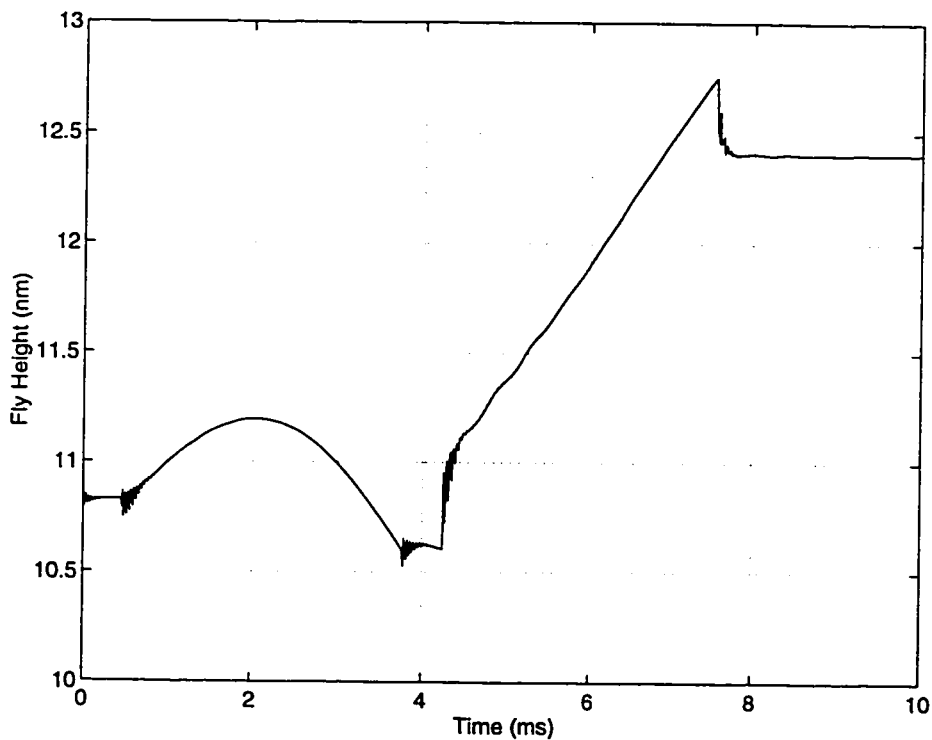


**Fig. 8.10** Fly height during track seeking.  $\sigma = 6$  nm, glide height = 25 nm and altitude = 0



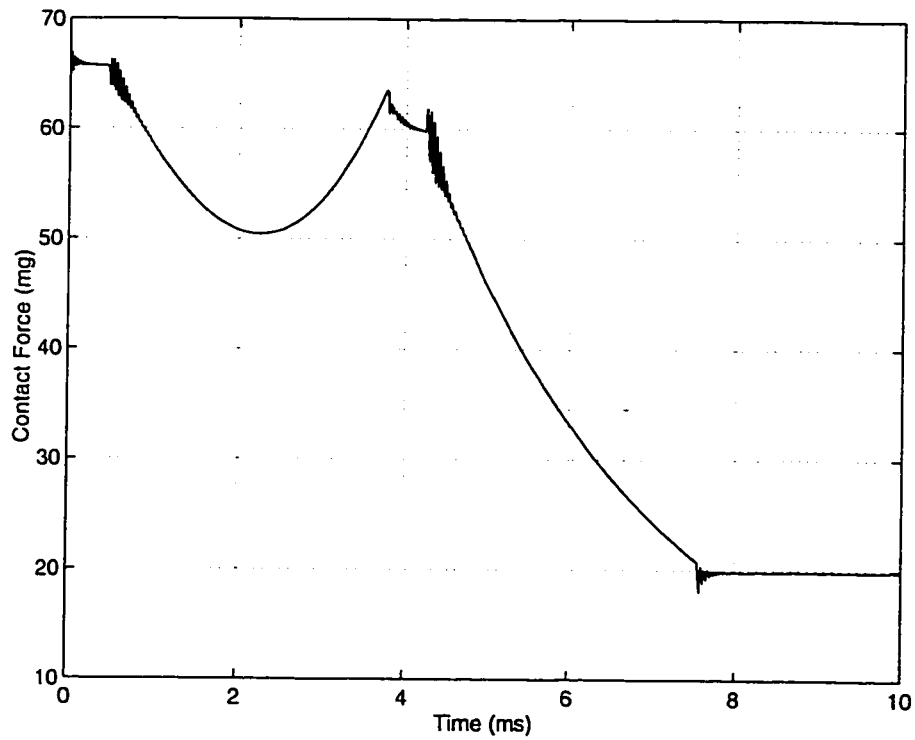


**Fig. 8.11** Contact force during track seeking.  $\sigma = 6$  nm, glide height = 25 nm and altitude = 0

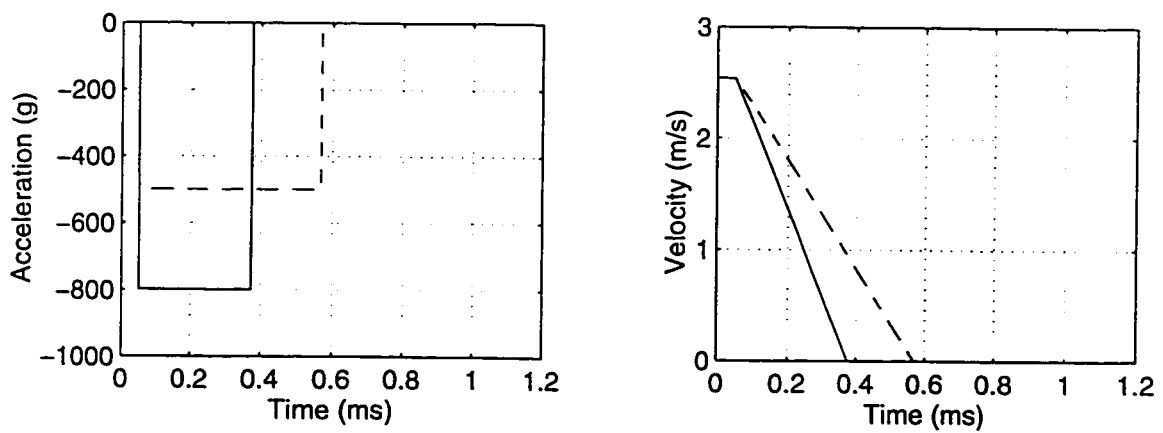


**Fig. 8.12** Deceleration and velocity profiles for the two crash stop processes

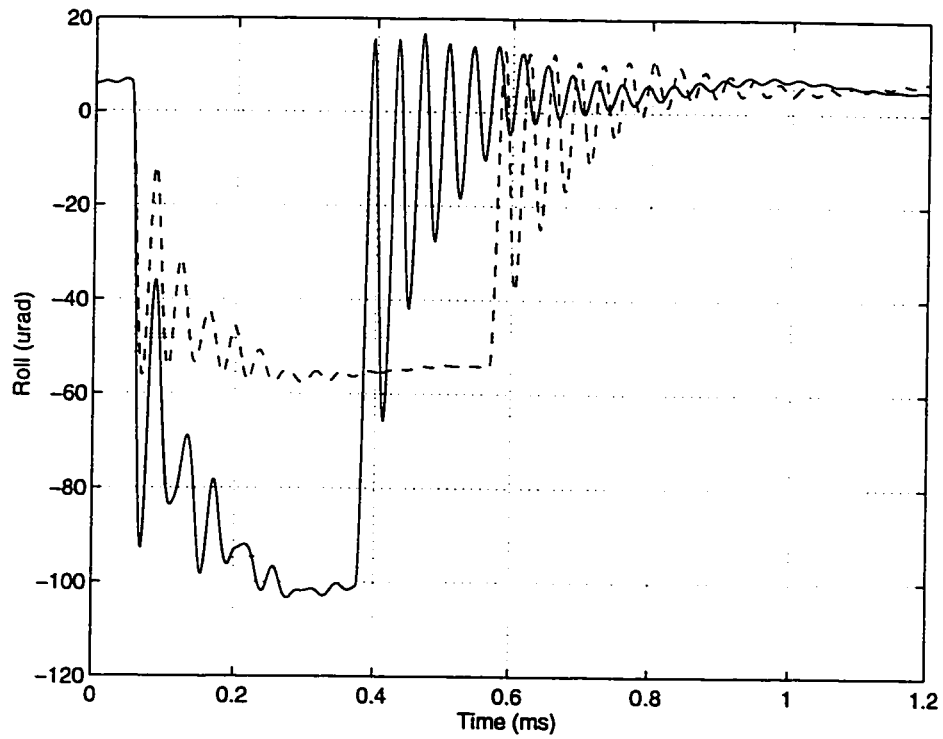


**Fig. 8.13** Roll motions during the two crash stop processes.  $\sigma = 6$  nm, glide height = 25 nm and altitude = 0. Maximum deceleration = 800G (solid line), 500G (dash line)

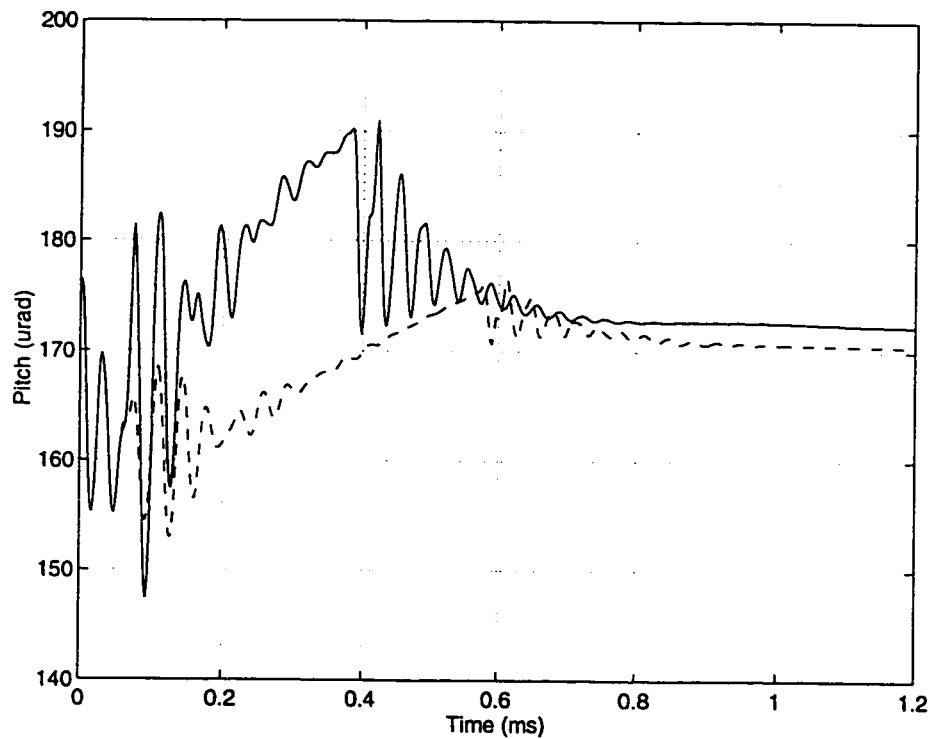


**Fig. 8.14** Pitch motions during the two crash stop processes.  $\sigma = 6$  nm, glide height = 25 nm and altitude = 0. Maximum deceleration = 800G (solid line), 500G (dash line)

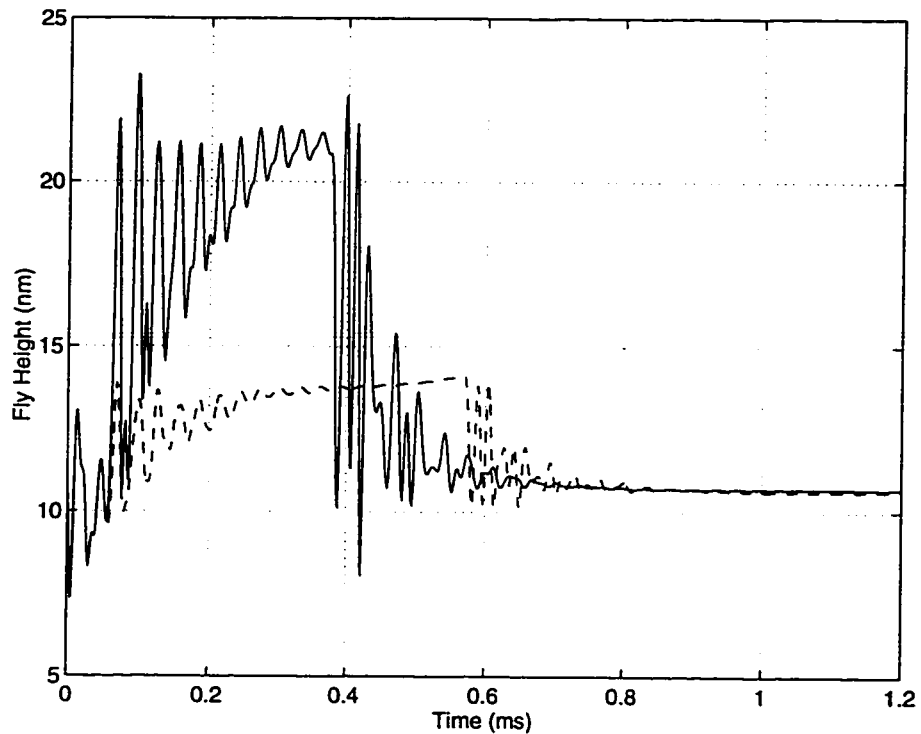


**Fig. 8.15** Fly heights at the rear pad during the two crash stop processes.  $\sigma = 6$  nm, glide height = 25 nm and altitude = 0. Maximum deceleration = 800G (solid line), 500G (dash line)

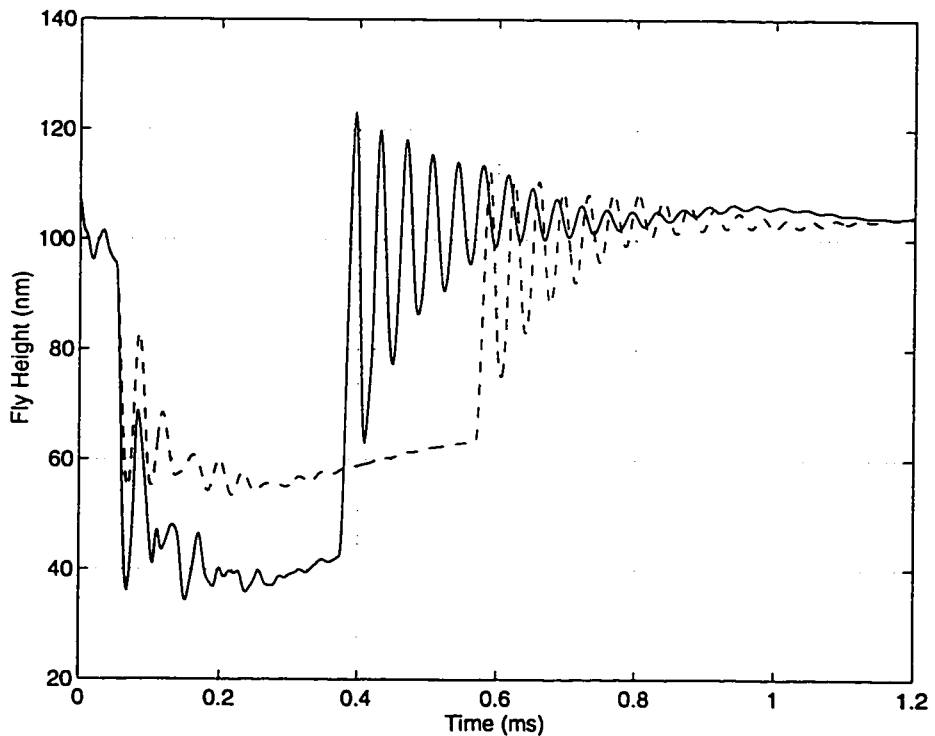


**Fig. 8.16** Fly heights of back center point of the outer rail during the two crash stop processes.  $\sigma = 6$  nm, glide height = 25 nm and altitude = 0. Maximum deceleration = 800G (solid line), 500G (dash line)

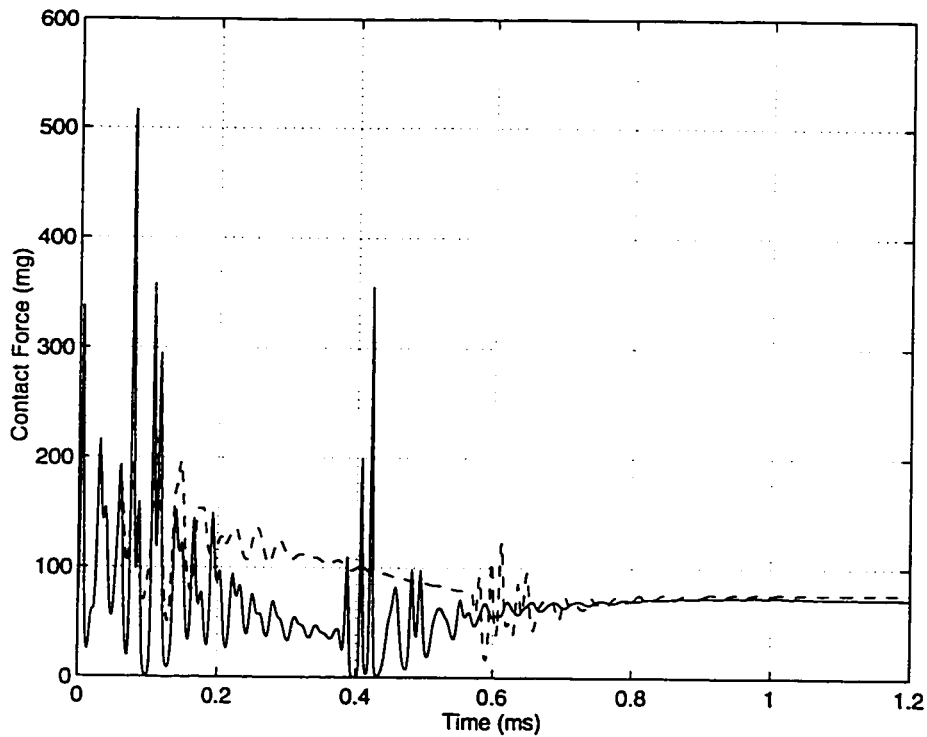


**Fig. 8.17** Contact forces during the two crash stop processes.  $\sigma = 6$  nm, glide height = 25 nm and altitude = 0. Maximum deceleration = 800G (solid line), 500G (dash line)

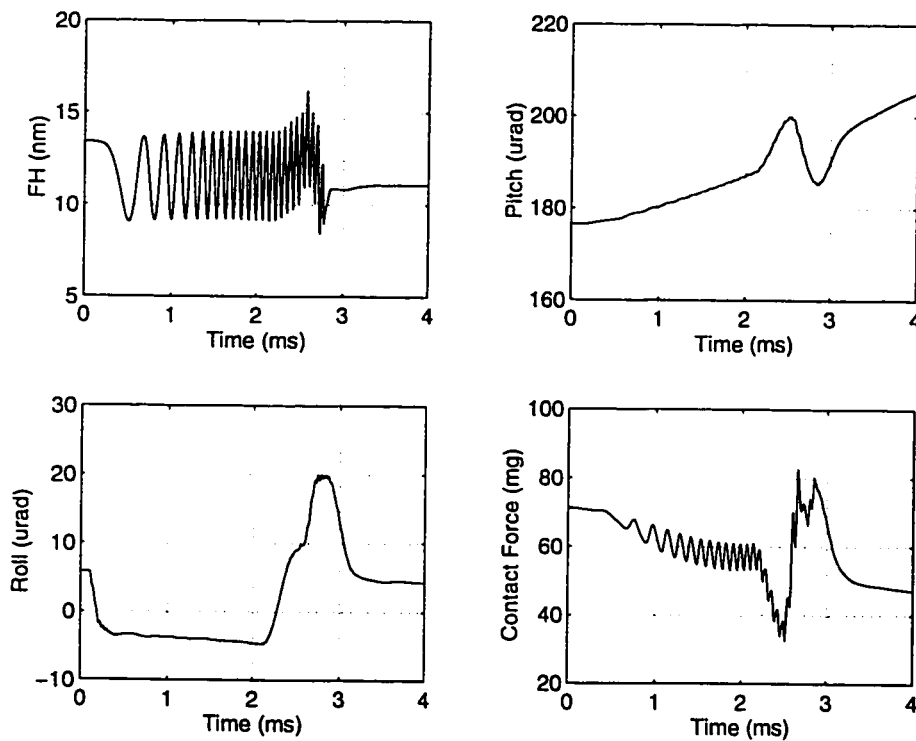


**Fig. 8.18** Fly height and contact force during accessing across a transition zone.  $\sigma = 6$  nm, glide height = 25 nm and altitude = 0

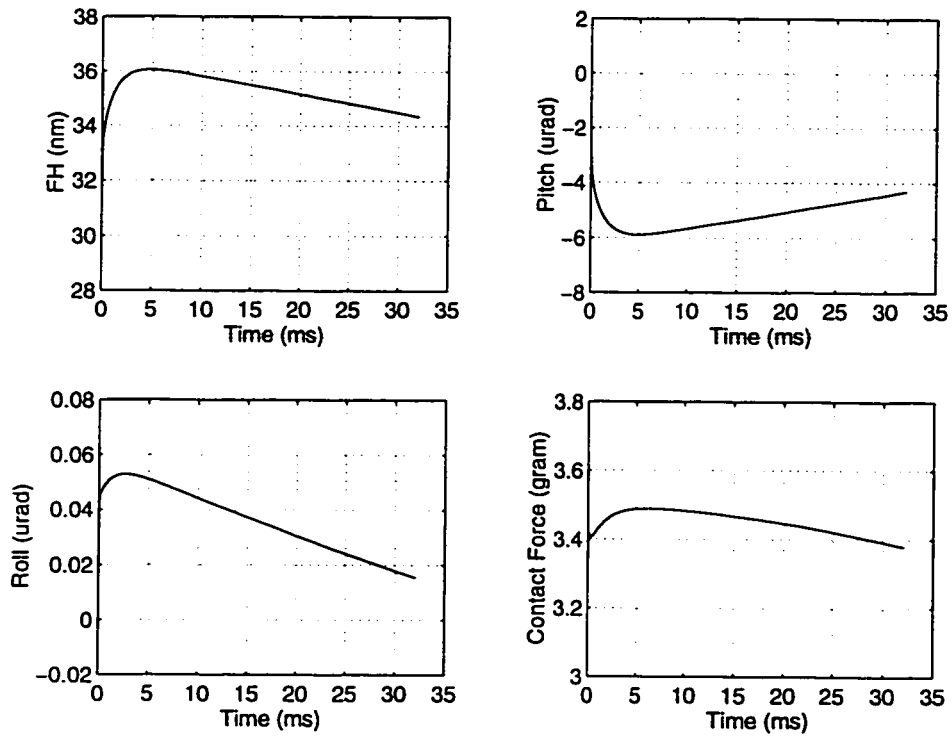


**Fig. 8.19** Flying characteristics during the contact start-up (up to the disk speed of 0.072 m/s).  $\sigma = 6$  nm, radial position = 20.73 mm, glide height = 25 nm and altitude = 0

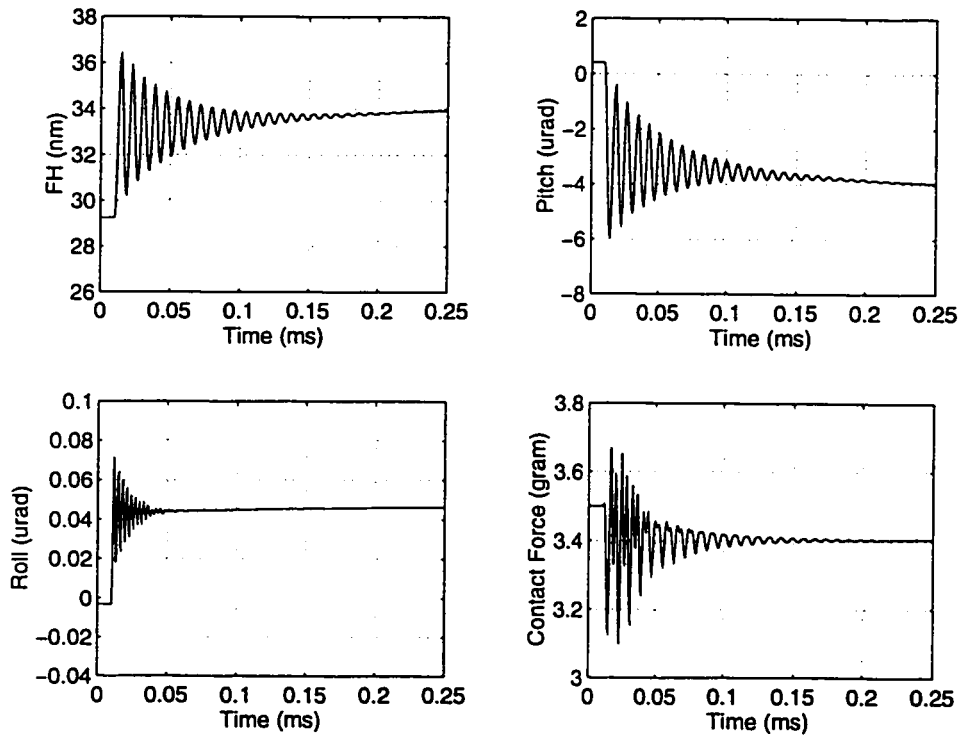


**Fig. 8.20** Flying characteristics during the early moments of the contact start-up (up to the disk speed of 0.00097717 m/s).  $\sigma = 6$  nm, radial position = 20.73 mm, glide height = 25 nm and altitude = 0

## CHAPTER 9

# EFFECTS OF LASER TEXTURED DISK SURFACES ON A SLIDER'S FLYING CHARACTERISTICS\*

### 9.1 Introduction

The storage density of magnetic hard disk drives has been increasing at an explosive rate requiring decreases in the slider-disk spacing. As densities exceed 1 Gb/in<sup>2</sup> the slider/disk spacing requirement and the tribological performance must be jointly optimized. One approach that allows lowering the fly height without affecting the tribological reliability is the creation of a dedicated take-off/landing zone near the disk inner diameter, where the slider can be parked as the drive is shut down. The mechanical means of fabricating such take-off/landing zones as studied in Chapter 6 do not provide the required precision and reliable control of contact area needed in high density magnetic recording. Of additional concern is the disk surface area that is required to accommodate the transition between the landing and data zones produced during the mechanical manufacturing process. In contrast to the mechanical texturing approach, the laser texturing technique employs a pulsed laser beam to produce "pits", "craters", or some form of depression on a material surface (Baumgart, *et al.*, 1995; Ranjan, *et al.*, 1991). The textured landing zone created by a laser consists of spatially separated micro-domes or "bumps" laid down, e.g., in a spiral pattern on the disk substrate, which can be placed precisely thus eliminating the transition zone of a mechanically textured landing zone. It

---

\* Parts of this chapter are submitted to *ASME Journal of Tribology*

is well known that these well-placed laser bumps under the slider air bearing surface serve as gentle and smooth support points for the contacting slider and therefore provide excellent tribological performance in terms of low contact start/stop stiction and good durability (Baumgart *et al.*, 1995; Ranjan *et al.*, 1991). However, our knowledge of the laser texture effects on the slider's flying characteristics is very limited.

In this chapter, the effects of laser bumps and laser textured disk surfaces on the flying characteristics of a shaped-rail sub-ambient pressure slider are numerically investigated using the CML Air Bearing Dynamic Simulator. Two laser bump profiles and various texture patterns are numerically generated in the simulator. The effects of bump shape on the slider's bump responses are studied. The slider's flying dynamics over the laser textured disk surface are simulated, and the effects of the texture pattern and shape on the slider's fly height, pitch, roll and their modulations are summarized. To understand the laser texture mechanism, the air bearing pressure profiles induced by the laser bumps are examined. Finally, the slider's flying characteristics with one rail over the laser textured landing zone and another rail over the smooth data zone are simulated.

## **9.2 Numerical Simulation**

The generalized Reynolds equation and the equation of motion of the slider are numerically solved using the CML Air Bearing Dynamic Simulator. Due to the ultra-low spacing in slider air bearings the no-slip boundary condition at the wall is no longer satisfied. In our simulation the modification proposed by Fukui and Kaneko (1988) based on the linearized Boltzmann equation is used. In stead of using various averaging

techniques for analyzing the surface texture effects, we directly generate the three-dimensional laser bump and texture in the numerical simulator. The mesh size and time step are refined such that they are comparable to the bump dimension. At each time step, the film thickness distribution under the slider is obtained through interpolation of the bump and the disk surface texture profiles. With this new film distribution, the coupled system of equations is solved.

### **9.3 Results and Discussions**

The Headway Advanced Air Bearing (AAB) slider shown in Figure 9.1 is used in this study. This air bearing has the following features; negative pressure cavity, hour glass shaped rails, relieved leading edge, and partially stepped wall angle profile. The large leading edge area increases the slider's pitch, to minimize the interaction between the slider and the disk. The hour glass shaped rails reduce the air bearing sensitivity to skew angle operation. This, combined with the partially stepped wall angle profile, prevents the loss of lift which occurs at skew due to the inefficient pressurization of the slider rails. The suspension preload is 3.5 grams. The air bearing geometric measurements including wall profiles, acquired using the Zygo New View 100 surface characterization system, are directly input into the CML air bearing dynamic simulator. The slider has a 22.9 nm crown and 8.5 nm camber. The disk radius at which the slider flies is 25 mm, and the skew angle is assumed to be zero. The disk rotation speed is 5400 rpm. For these operating parameters, the steady-state outer trailing edge fly height, pitch and roll over the smooth disk surface are calculated to be 45.04 nm, 125.65  $\mu$ rad and 3.97  $\mu$ rad,



respectively. Figures 9.2 and 9.3 show the corresponding non-dimensional 3D air bearing pressure profile and 2D air bearing pressure contour.

**9.3.1 Laser Bump Responses.** The laser bumps are created by a process involving material redistribution rather than removal. A variety of topographical shapes can be achieved by varying the laser parameters such as energy, pulse-width and beam profile. Currently, two types of the laser bumps are commonly used to texture the landing zone for their property of very small contact area. The “Sombrero” type bump has a positive-extending dome accompanied by a positive-extending rim of lower height as shown in Fig. 9.4, while the ridge bump shape consists of a central depression and a surrounding rim as displayed in Fig. 9.5. Figures 9.6 shows the slider’s responses to the passage of the “Sombrero” and ridge type bumps. Both bumps have the rim height of 15 nm and diameter of 40  $\mu\text{m}$ . The center dome height for the “Sombrero” bump is 30 nm. Because of the positive-extending central dome, the “Sombrero” bump has a higher excitation than the ridge bump, which is responsible for its larger outer trailing edge fly height oscillation. The bump responses for two central dome heights of the “Sombrero” type bump are plotted in Fig. 9.7. The oscillation of the 30 nm center height bump is slightly larger than that of the 20 nm center height bump. Compared to the bump type and central dome height, the rim diameter has much larger effect on the bump responses as shown in Fig. 9.8. Perturbations to the slider’s motion due to the compression of air between the slider and the bump increase with increasing the bump’s cross-sectional areas due to circumferential flow. Overall, the maximum magnitude of the oscillation is less than 0.45% of the steady-state fly height. As we further increase the central dome height

beyond 40 nm, the slider starts to contact the passing bump mainly because the small bump is unable to generate enough air bearing compression force to separate the slider and the central dome of the “Sombrero” type bump as shown in Fig. 9.9. As a result of the contact between the slider and the bump, the oscillation increases substantially.

**9.3.2 Effect of the Laser Textured Disk Surfaces.** The laser texture in a spiral pattern on the disk substrate is generated using a train of high repetition rate laser pulses of proper pulse width focused to a small spot on a moving disk surface (Baumgart, *et al.*, 1995). This laser-created texture consists of evenly spaced, protruding microdomes, or “bumps,” of equal height that minimize the contact area between the slider and the disk. Figures 9.10 and 9.11 display the two types of laser textured disk surfaces: “Sombrero” type and ridge type. The bump spacings in the circumferential and radial directions are 100  $\mu\text{m}$  and 50  $\mu\text{m}$ , respectively. The transient outer trailing edge fly height for a slider dropped over a laser textured disk surface is plotted in Fig. 9.12. The laser texture is of the “Sombrero” type with 30 nm central dome height, 40  $\mu\text{m}$  rim diameter and 15 nm rim height. The result indicates that the trailing edge fly height increases and the slider’s oscillation does not completely die out. After 0.3 ms, the slider starts to oscillate in a mode of constant modulation. The fly height increase and the non-decaying modulation can be explained, if the moving laser textured disk surface is visualized as a series of bumps, each providing additional excitation to the slider. These continuous bump excitations are the driving force that increases the fly height and maintains the constant fly height modulation. The non-dimensional 3D air pressure profile and 2D pressure contour at the time of 0.5 ms are shown in Figs. 9.13 and 9.14. The stippled pressure

peaks embedded on the smooth pressure profile are generated due to the air compression by the moving laser bumps on the disk surface. After entering from the slider's leading edge, these stippled pressure peaks move gradually to the trailing edge portion where they exert the largest perturbation to the slider's motion due to the smallest slider-disk separation there. Table 9.1 summarizes the outer trailing fly height increase (with the reference to the smooth disk surface) and its modulation for the two type laser textures. The "Sombrero" laser textured disk surface produces much larger fly height increase and modulation than the ridge type texture. This agrees well with the single bump response results discussed in previous section. The non-dimensional 2D air bearing pressure contour for the ridge type textured disk surface is displayed in Fig. 9.15. Table 9.2 details the fly height increase and modulation as functions of bump spacing. Larger bump spacing decreases the frequency of the bump excitations, therefore reducing the fly height increase and modulation. The non-dimensional 2D air bearing pressure contour for circumferential bump spacing of 100  $\mu\text{m}$  and radial bump spacing of 200  $\mu\text{m}$  is plotted in Fig. 9.16. The effects of the central dome height for the "Sombrero" type laser texture on the fly height increase and modulation are presented in Table 9.3. Compared to the bump type and spacing, the central dome height has much smaller effect on the slider's flying characteristics. Figure 9.17 displays the non-dimensional 2D air bearing pressure contour for the case of the 20 nm central dome height. Table 9.4 illustrates the fly height increases and modulations for the two rim diameters of 20  $\mu\text{m}$  and 40  $\mu\text{m}$ . The rim diameter has the most significant influence on slider's flying characteristics. As we increase the rim diameter from 20  $\mu\text{m}$  to 40  $\mu\text{m}$ , the fly height increases almost five

times. The dramatic increase comes from the fact that laser bumps with larger rim diameter are much more effective in compressing the air bearing than smaller bumps due to circumferential flow around their sides. This is further confirmed by the smaller stippled pressure peaks on the non-dimensional 2D air bearing pressure contour for the 20  $\mu\text{m}$  rim diameter laser texture (Fig. 9.18).

**9.3.3 Effect of Outer Rail Fly Condition.** Use of the disk area near the landing zone for data recording purpose necessitates an in-depth understanding of the effect of outer rail fly condition on the slider's flying characteristics. Table 9.5 summarizes the simulated flying characteristics for two outer rail fly conditions. Compared to the case of both rails flying over the textured landing zone, the slider with the outer rail flying over the smooth data zone has a much smaller fly height gain/modulation and a substantial decrease of roll. The former is due to the reduced continuous bump excitation to the slider in the vertical direction, while the latter is associated with increased unbalancing excitation in roll direction between the two side rails. Figure 9.19 plots the non-dimensional 2D air bearing pressure contour for the case of outer rail flying over the smooth data zone.

## 9.4 Summary

The effects of laser bumps and laser textured disk surfaces on the Headway AAB slider's flying characteristics are numerically investigated using the CML Air Bearing Dynamic Simulator. Two laser bump profiles ("Sombrero" and ridge types) and various laser texture patterns are numerically generated in the simulator. The passing "Sombrero" type bump produces larger perturbation to the slider's motion than the ridge

type bump. The larger size laser bump produces a larger amplitude and slower decaying oscillation. The moving laser texture generates moving stippled pressure peaks embedded on a smooth pressure profile. These moving pressure peaks increase the slider's trailing edge fly height and maintain a constant magnitude fly height modulation. The effect increases as the bump spacing decreases and the central dome height and rim diameter increase. Flying the outer rail over the smooth data zone, while keeping the inner rail over the textured landing zone, decreases the fly height gain and fly height modulation, but increases the roll loss and roll modulation.

Laser Texture Type	“Sombrero”	Ridge
Fly Height Increase (nm)	0.7439	0.3427
Fly Height Modulation (nm)	0.2231	0.1014

**Table 9.1** Fly height increase and modulation versus laser texture type. Bump spacing = 100×50 μm, rim height = 15 nm, rim diameter = 40 μm and center height = 30 nm (“Sombrero” type)

Bump Spacing (μm)	100×50	200×100
Fly Height Increase (nm)	0.7439	0.1983
Fly Height Modulation (nm)	0.2231	0.1865

**Table 9.2** Fly height increase and modulation versus laser bump spacing. “Sombrero” type, center height = 30 nm, rim height = 15 nm and rim diameter = 40 μm

Center Height (nm)	30	20
Fly Height Increase (nm)	0.7439	0.702
Fly Height Modulation (nm)	0.2231	0.1826

**Table 9.3** Fly height increase and modulation versus laser bump center height. “Sombrero” type, bump spacing = 100×50 μm, rim height = 15 nm and rim diameter = 40 μm

Rim Diameter (μm)	40	20
Fly Height Increase (nm)	0.7439	0.1556
Fly Height Modulation (nm)	0.2231	0.0937

**Table 9.4** Fly height increase and modulation versus rim diameter. “Sombrero” type, bump spacing = 100×50 μm, rim height = 20 nm and center height = 30 nm

Outer Rail Fly Condition	Over Data Zone	Over Landing Zone
Fly Height Increase (nm)	0.0154	0.7439
Fly Height Modulation (nm)	0.0576	0.2231
Roll Decrease ( $\mu\text{rad}$ )	0.5484	0.0207
Roll Modulation ( $\mu\text{rad}$ )	0.1204	0.045

**Table 9.5** Fly height increase, roll decrease and their modulations versus outer rail flying condition. Inner rail flies over the laser textured landing zone, "Sombbrero" type, bump spacing =  $100 \times 50 \mu\text{m}$ , rim height = 20 nm and center height = 30 nm

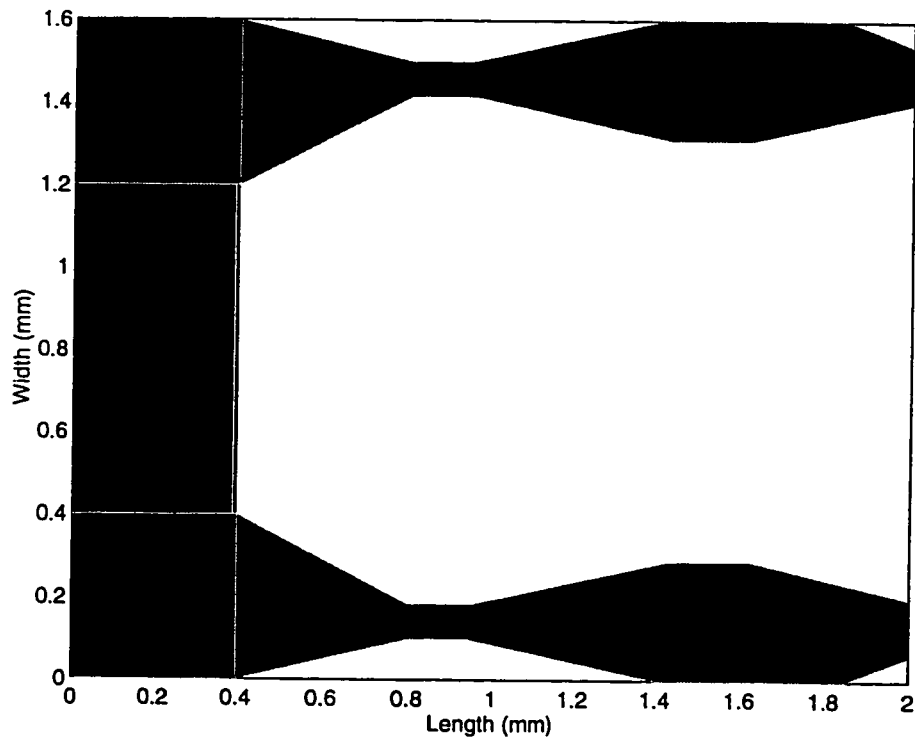


**Fig. 9.1** 50% Headway AAB slider air bearing surface

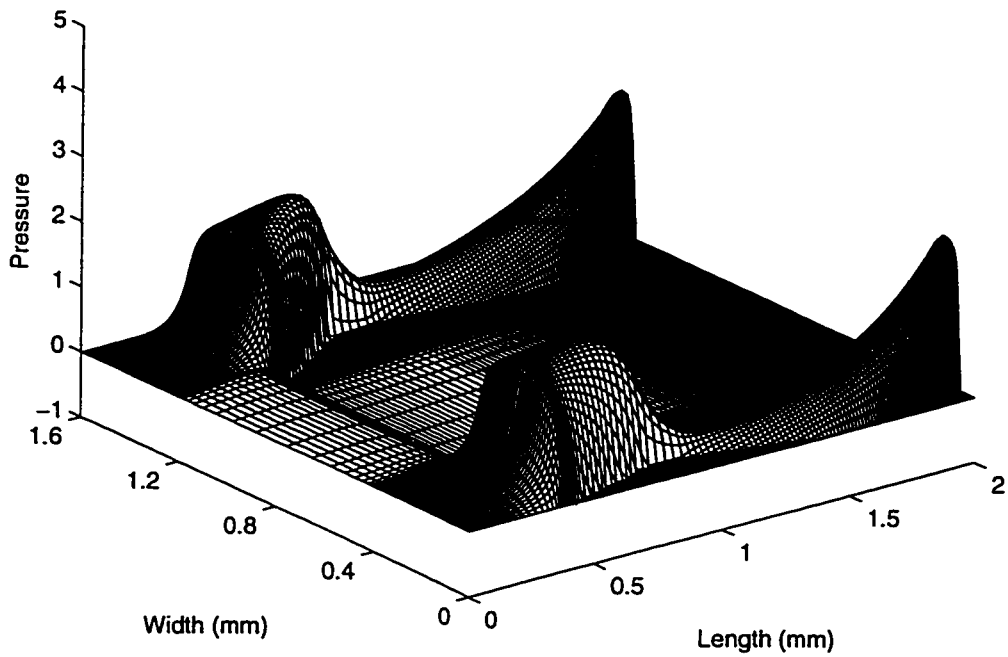


**Fig. 9.2** Headway AAB slider's 3D non-dimensional air bearing pressure profile for smooth disk surface

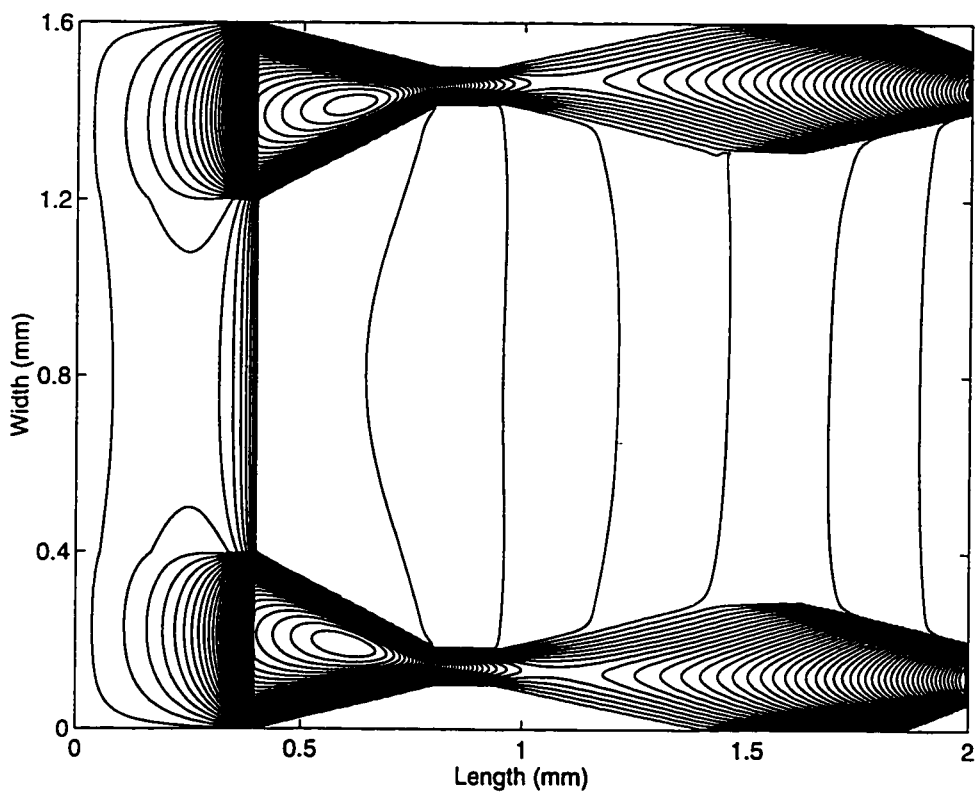


**Fig. 9.3** Headway AAB slider's 2D non-dimensional air bearing pressure contour for smooth disk surface



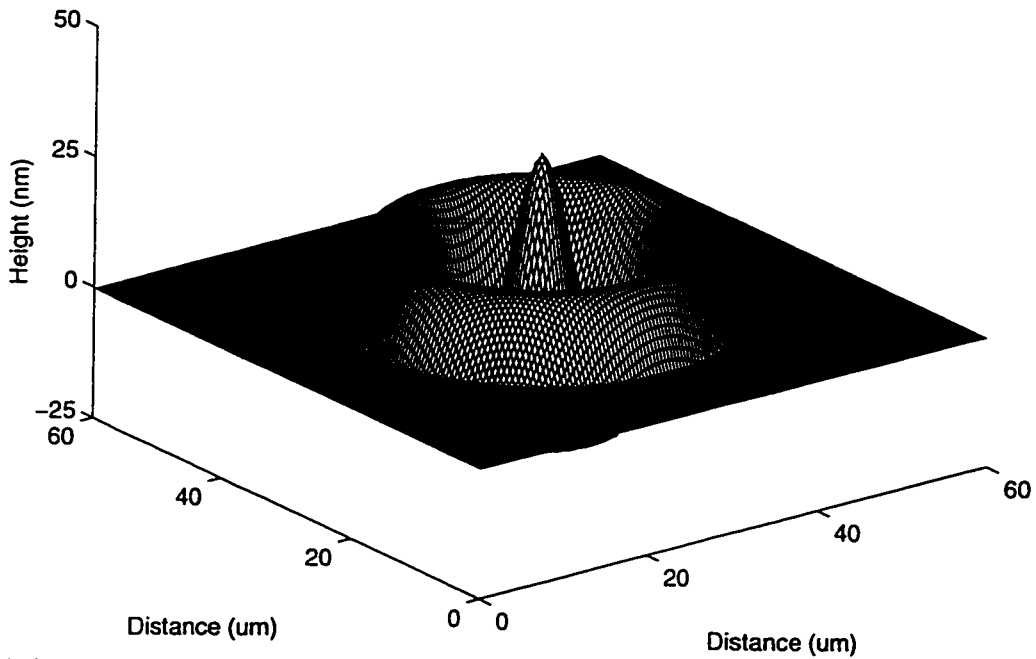


**Fig. 9.4** A 3D representation of "Sombrero" type laser bump. Center height = 30 nm, rim height = 20 nm and rim diameter = 40 μm

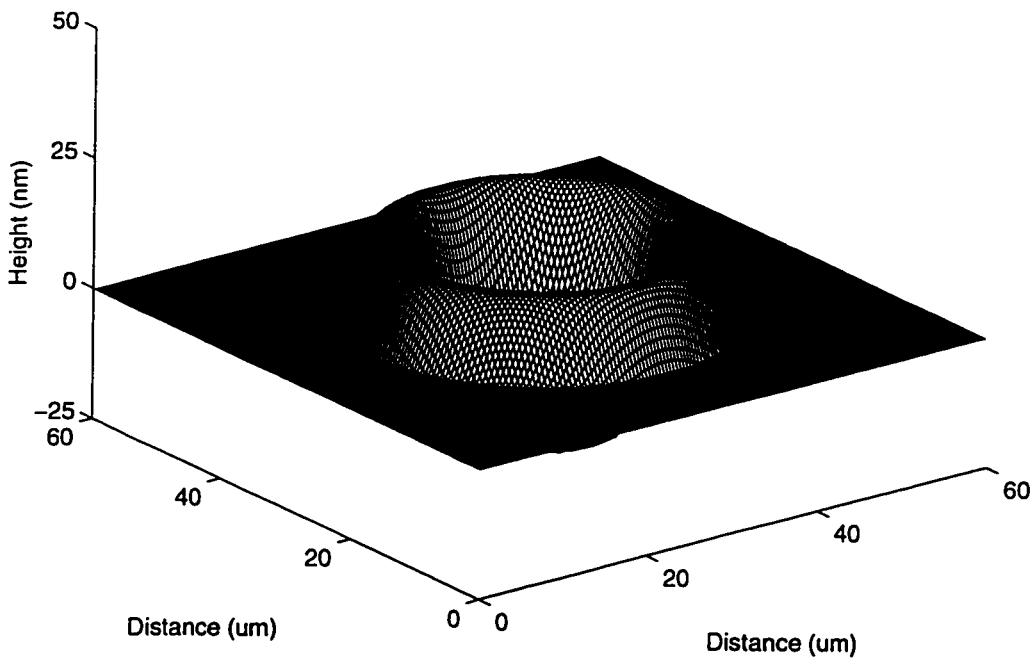


**Fig. 9.5** A 3D representation of ridge type laser bump. Rim height = 20 nm and rim diameter = 40 μm

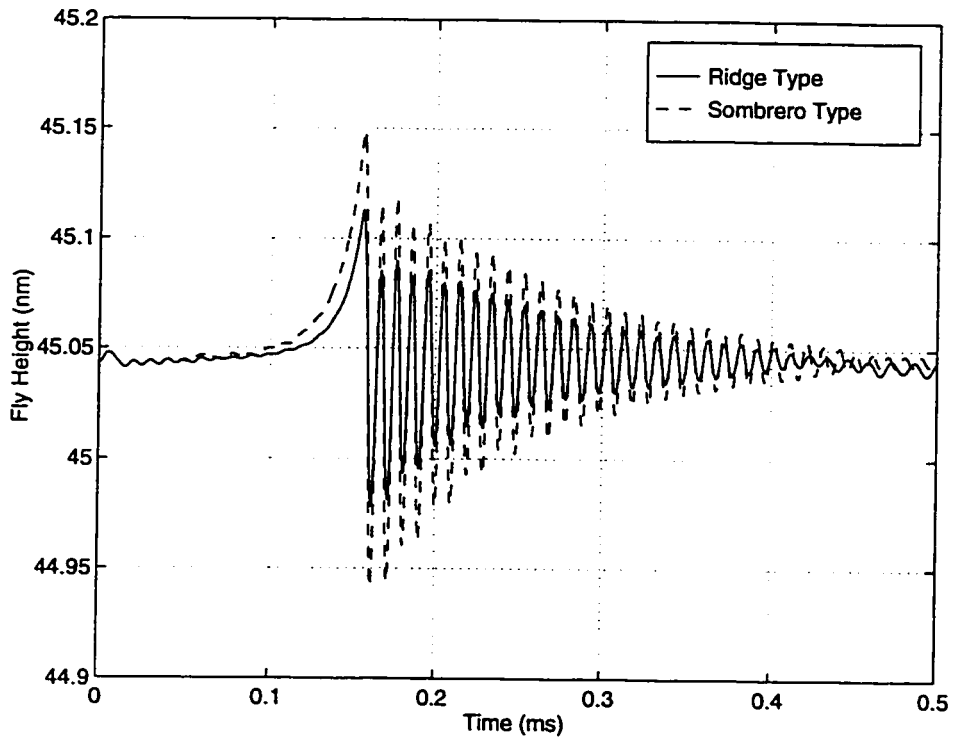


**Fig. 9.6** Bump response versus laser bump type. Center height = 30 nm (“Sombrero” type), rim diameter = 40  $\mu\text{m}$  and rim height = 20 nm

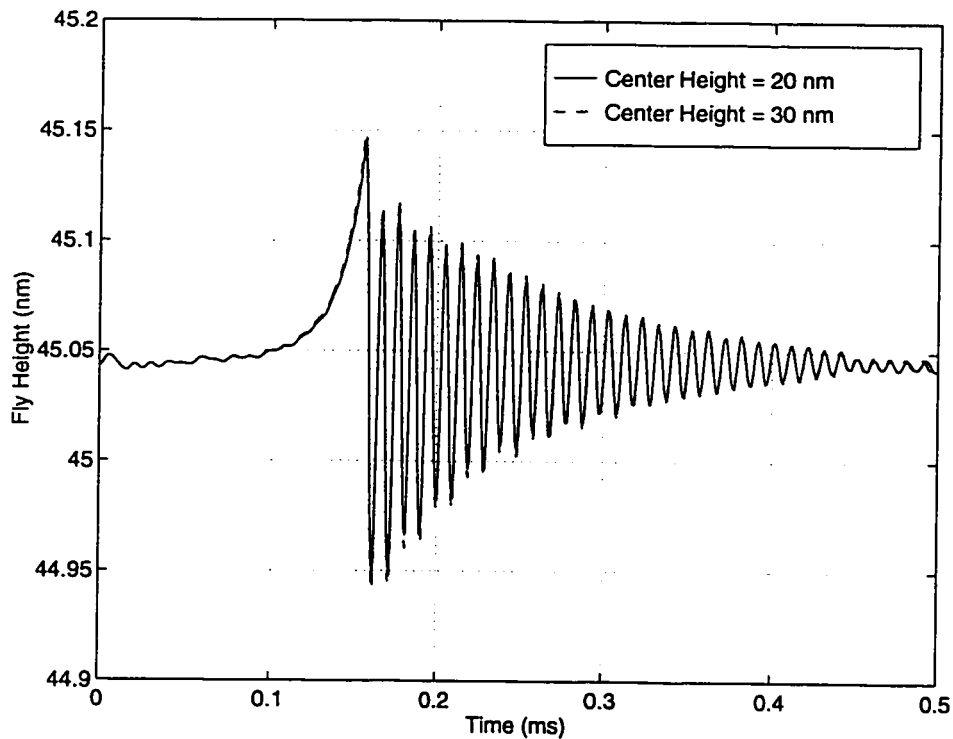


**Fig. 9.7** Bump response versus center height. “Sombrero” type laser bump, rim height = 20 nm and rim diameter = 40  $\mu\text{m}$

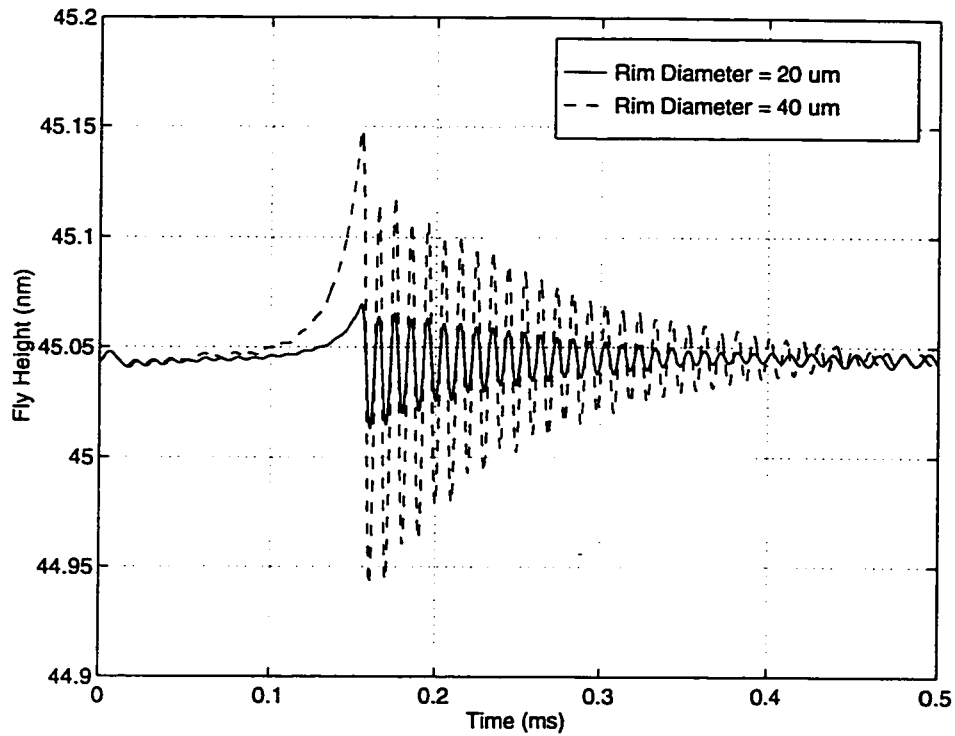


**Fig. 9.8** Bump response versus rim diameter. “Sombrero” type laser bump, center height = 30 nm and rim height = 20 nm

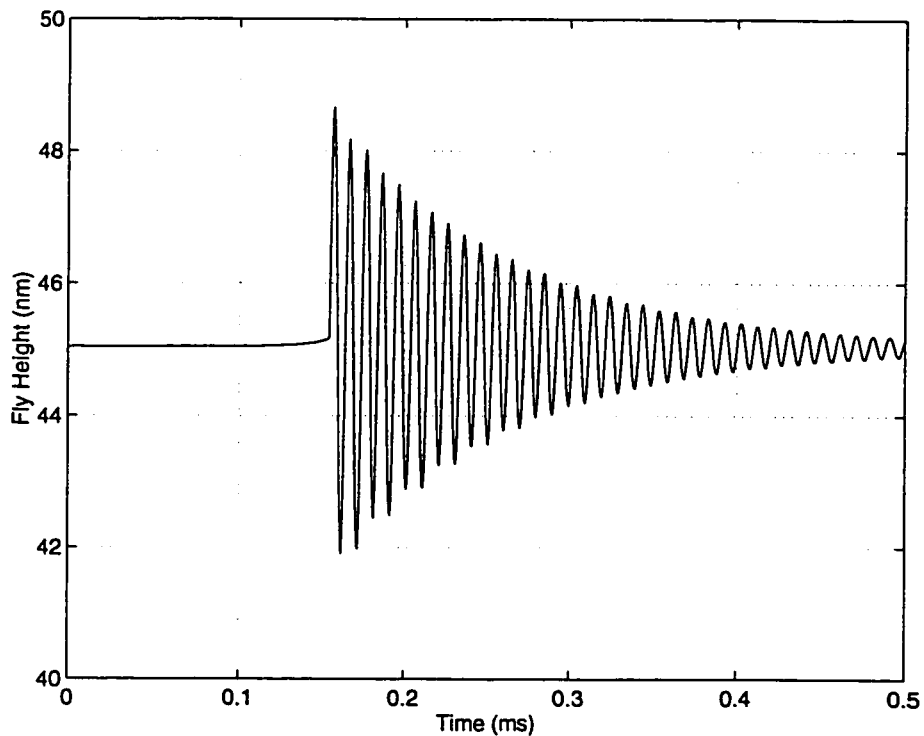


**Fig. 9.9** Contact bump response. “Sombrero” type laser bump with center height = 50 nm, rim diameter = 40 μm and rim height = 20 nm

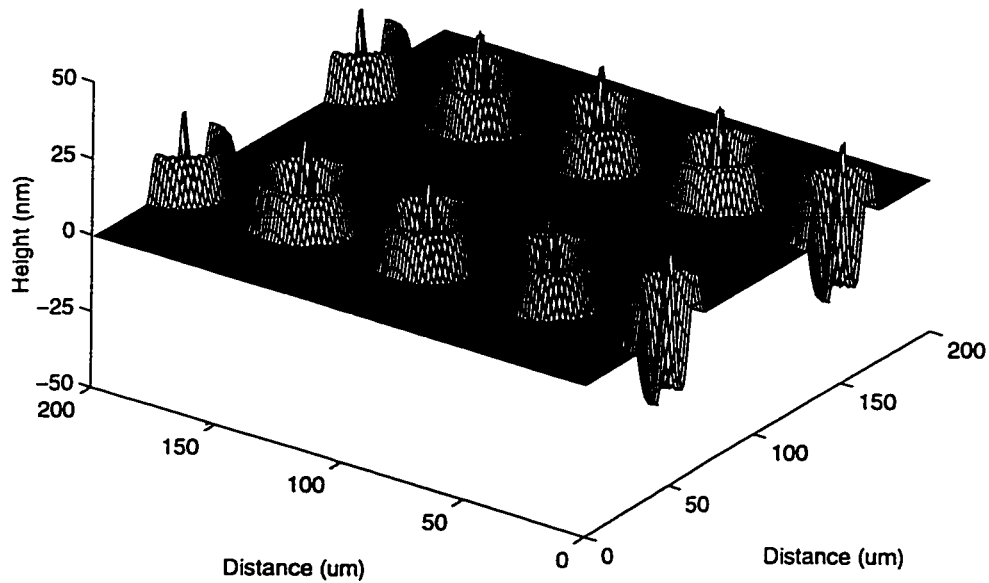


**Fig. 9.10** A 3D representation of “Sombrero” type laser texture. Bump spacing =  $100 \times 50 \mu\text{m}$ , center height = 30 nm, rim height = 20 nm and rim diameter =  $40 \mu\text{m}$

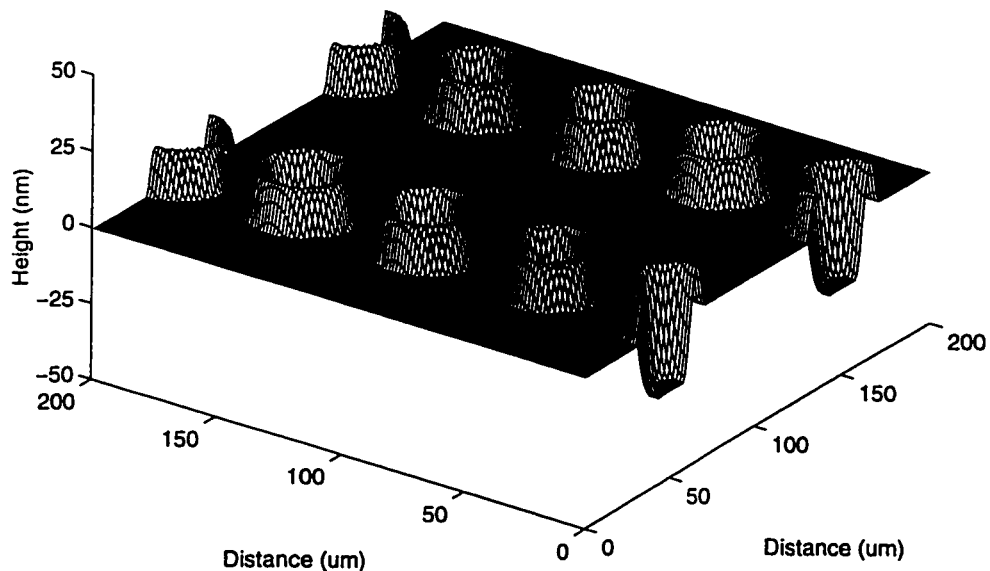


**Fig. 9.11** A 3D representation of ridge type laser texture. Bump spacing =  $100 \times 50 \mu\text{m}$ , rim height = 20 nm and rim diameter =  $40 \mu\text{m}$

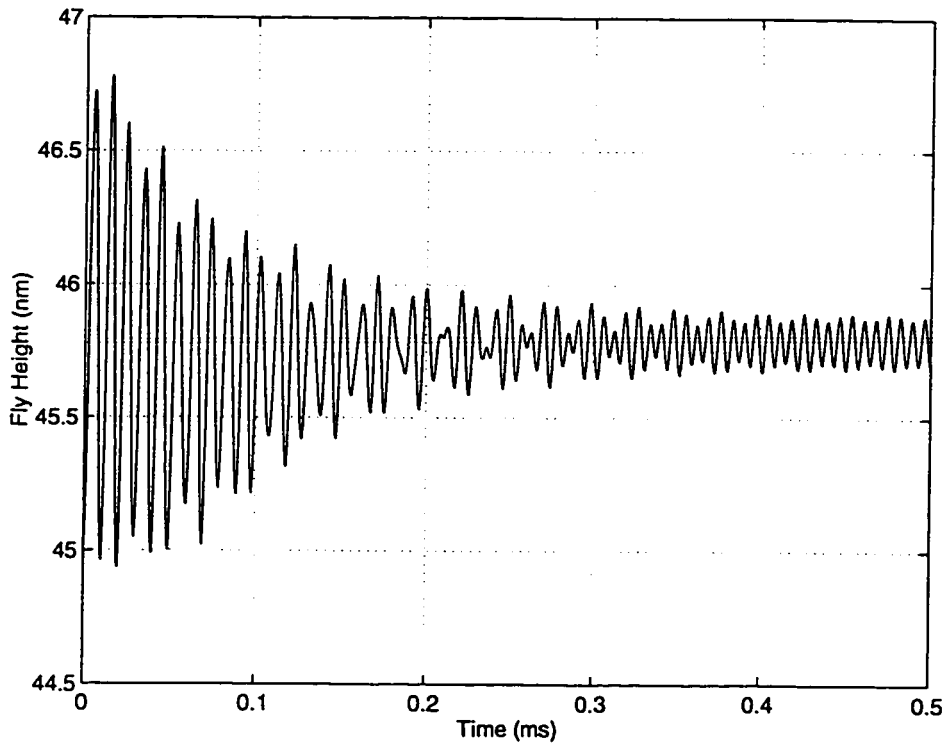


**Fig. 9.12** Slider's fly height settling history over a laser textured ("Sombrero" type) disk surface. Bump spacing =  $100 \times 50 \mu\text{m}$ , center height = 30 nm, rim height = 15 nm and rim diameter =  $40 \mu\text{m}$

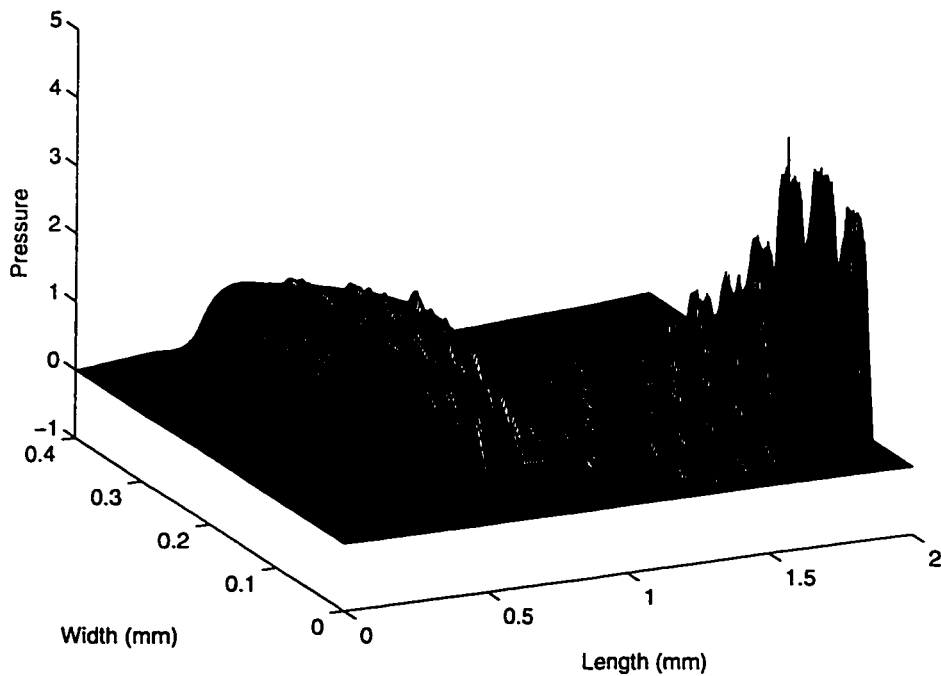


**Fig. 9.13** 3D non-dimensional air bearing pressure profile beneath the inner rail. "Sombrero" type laser texture, bump spacing =  $100 \times 50 \mu\text{m}$ , center height = 30 nm, rim height = 15 nm and rim diameter =  $40 \mu\text{m}$

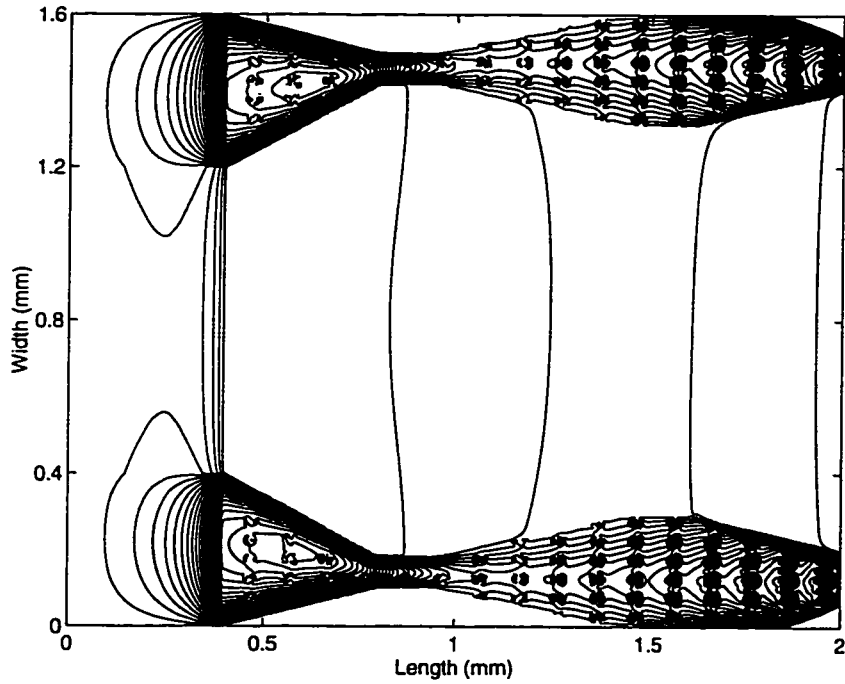


**Fig. 9.14** 2D non-dimensional air bearing pressure contour. “Sombrero” type laser texture, bump spacing =  $100 \times 50 \mu\text{m}$ , center height = 30 nm, rim height = 15 nm and rim diameter =  $40 \mu\text{m}$

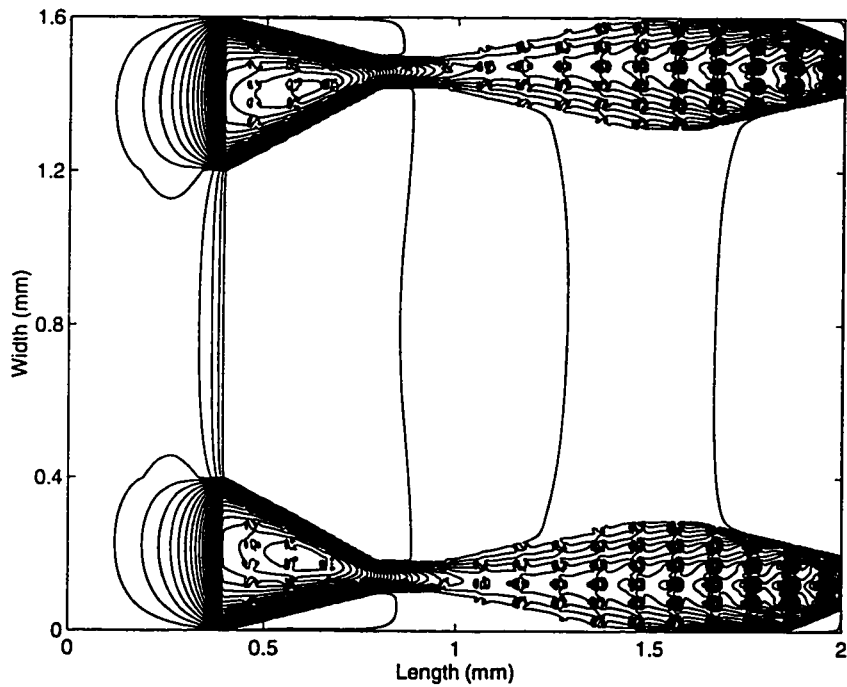


**Fig. 9.15** 2D non-dimensional air bearing pressure contour. Ridge type laser texture, bump spacing =  $100 \times 50 \mu\text{m}$ , rim height = 15 nm and rim diameter =  $40 \mu\text{m}$

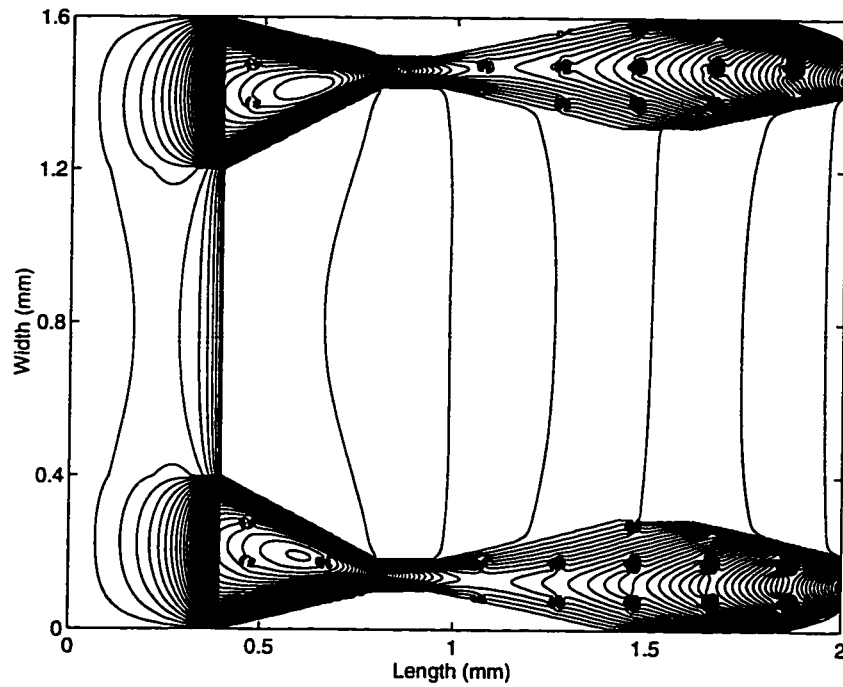


**Fig. 9.16** 2D non-dimensional air bearing pressure contour. “Sombrero” type laser texture, bump spacing =  $200 \times 100 \mu\text{m}$ , center height = 30 nm, rim height = 15 nm and rim diameter =  $40 \mu\text{m}$

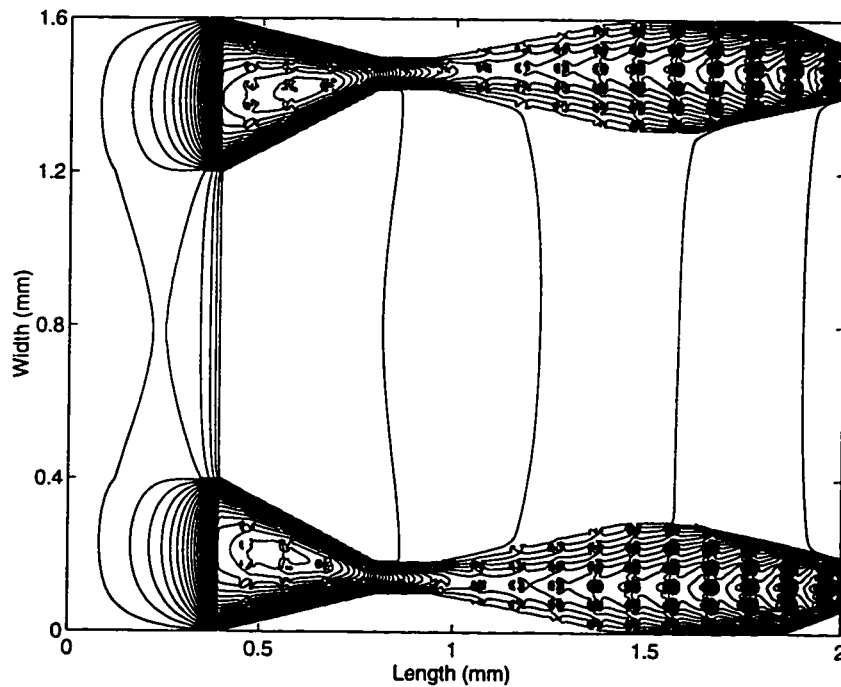


**Fig. 9.17** 2D non-dimensional air bearing pressure contour. “Sombrero” type laser texture, bump spacing =  $100 \times 50 \mu\text{m}$ , center height = 20 nm, rim height = 15 nm and rim diameter =  $40 \mu\text{m}$

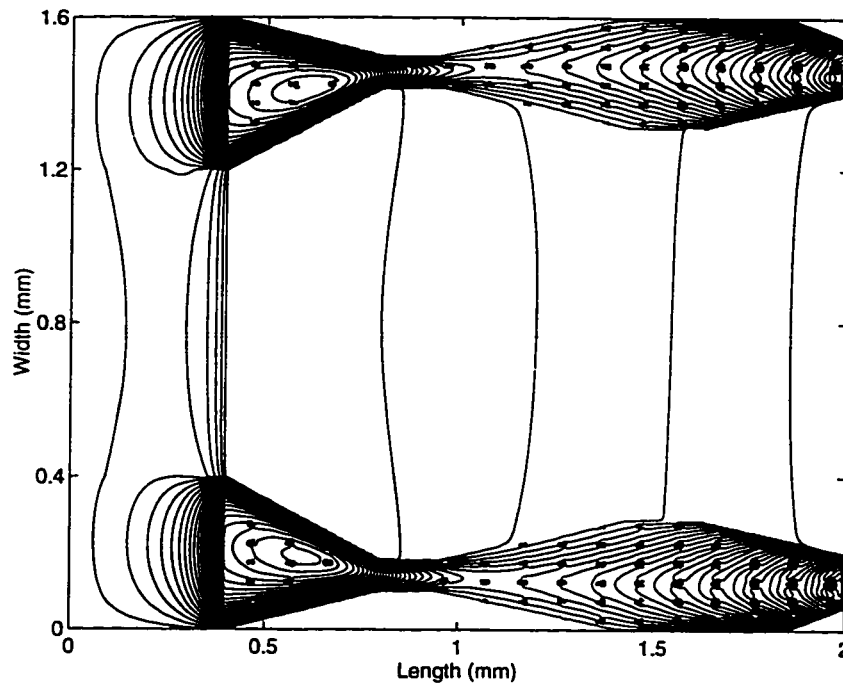


**Fig. 9.18** 2D non-dimensional air bearing pressure contour. “Sombbrero” type laser texture, bump spacing =  $100 \times 50 \mu\text{m}$ , center height = 30 nm, rim height = 15 nm and rim diameter =  $20 \mu\text{m}$

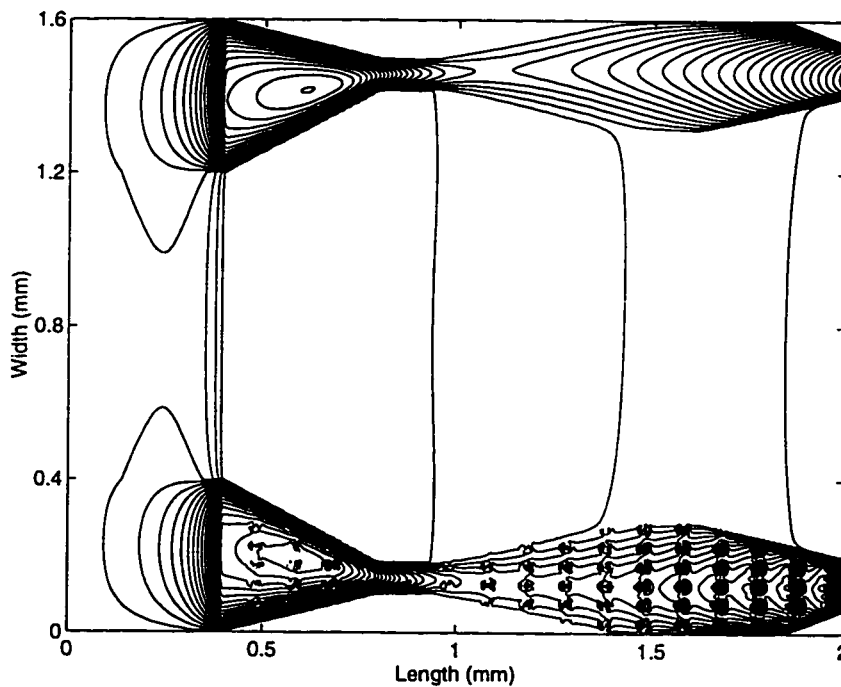


**Fig. 9.19** 2D non-dimensional air bearing pressure contour with inner rail flying over the textured landing zone and outer rail flying over the smooth data zone. “Sombbrero” type laser texture, bump spacing =  $100 \times 50 \mu\text{m}$ , center height = 30 nm, rim height = 20 nm and rim diameter =  $40 \mu\text{m}$



## **CHAPTER 10**

### **CONCLUSION**

Our appetite for stored data seems unbounded. The magnetic hard disk drive industry has responded to this by continually lowering the spacing between the read/write head and the disk. The spacing in new designs is quickly approaching the near-contact condition. At such a low spacing, designing a reliable head/disk interface requires an in-depth understanding of the dynamic behavior of the head-disk-suspension systems. The emphasis of this dissertation is placed on the development of a general purpose numerical simulation program for studying the dynamics of the head-disk-suspension assembly of magnetic hard disk drives. This program, called the CML Air Bearing Dynamic Simulator, can simulate a variety of dynamic effects associated with the head-disk-suspension assembly including partial contact, suspension dynamics and laser texture. In addition, using the simulator we investigate a collection of the dynamic problems in today's head-disk interface.

An additive correction based multigrid control volume method is developed for the solution of the rarefied gas lubrication equation that governs the pressure distribution between the slider and the disk. The control volume schemes for discretizing the lubrication equation are based on convection-diffusion formulations including the central difference, upwind, hybrid, power-law and exponential schemes. To improve the solver's efficiency, an additive correction based multigrid method is implemented for the solution of the resulting discretization equations. The method is based on the principle of deriving

the coarser grid discretization equations from the fine grid discretization equations. The comparison study using the 50% tripod and Headway AAB sliders demonstrates the multigrid method to be rapidly convergent with saving in CPU requirements by a factor ranging from 3.9 to 39.7 depending on the slider type, grid number and bearing number as compared to the single-grid method. The performance gets even better with the increases of the grid number and the bearing number. The efficiency of the multigrid method over the single-grid method is further dramatically improved for today's shaped rail sub-ambient pressure sliders.

The dynamic flying characteristics of three sub-25nm fly height sliders are studied in Chapter 4. The results show that the spacing modulation induced by disk roughness decreases with an increase in air bearing stiffness and decrease in slider size. The sliders' responses to a passing bump correlate very well with the air bearing stiffness and damping characteristics. In addition, the maximum bump heights without contact decrease as the air bearing stiffness and the slider size increase, and increase with the minimum spacing. The motion of the slider during a track accessing event is also calculated using the HTI 1650E and FX30U type suspensions. Modal analysis is employed to integrate the suspension dynamics into the air bearing simulation. It is concluded that the fly height modulation is attributed to many factors such as the effective skew angle, the seeking velocity, the accessing direction, and the roll motion caused by the inertia of the moving head. The extent of the roll motion effect depends on the air bearing roll stiffness and the inertial force of the moving head. Smaller roll stiffness and larger inertia force produce a larger roll motion effect on the head-disk spacing

modulation during a track access event.

In Chapter 5, a mixed lubrication model is developed for investigating various air bearing and other design parameter effects on the Nutcracker slider's take-off performance. The Fukui-Kaneko linearized Boltzmann equation is used to model the nonlinear rarefaction effects in the modified Reynolds equation for fly heights down to contact. An elastic-plastic asperity-based contact model is employed to extract the slider/disk contact forces and moments during the take-off process. The criterion for take-off from a disk is defined as a specified percent of the suspension preload. The Nutcracker slider which flies sub-25 nm fly height is used in this study. Among the many air bearing and other design parameters affecting the take-off velocity, the slider's crown and disk surface roughness are particularly important. Larger crowns and smoother disk surfaces reduce the take-off velocity. The contact start-up take-off flying characteristics are mostly affected by the slider's crown and the contact friction coefficient. Smaller crowns and friction coefficients produce a smoother initial take-off performance.

The spacing modulation of the Nutcracker slider flying across a transition between landing and data zones is investigated in Chapter 6. The transition zone is represented in the simulator as a parabolic surface defined by three radial points. The HTI 1650E type suspension assembly dynamics are integrated for the accessing motion. The spacing modulation due to the transition zone profile is extracted. It is concluded that the maximum slider/disk spacing reduction occurs at the outer rail trailing edge when the slider climbs up the transition zone. The spacing reduction increases as the slope of the transition zone surface increases. The combination that produces the least spacing

modulation is increased zone width, decreased zone height, and constant slope plane.

Chapter 7 is devoted to the study of the effects of well-defined surface texture on a slider's flying characteristics. The slider-disk interface dynamics are simulated numerically for the three dimensional surface textures generated in the simulator, which are circumferential ridges with different heights and area ratios of the ridges. Adding the circumferential ridge surfaces increases the trailing edge fly height and decreases the pitch because of the reductions in the effective flow area and restrictions in side-flows. The rates of fly height and pitch change increase rapidly as the disk velocity decreases. The ridge height has a substantial influence on the slider's steady state fly characteristics. A larger ridge height produces a larger trailing edge fly height increase and pitch decrease. The simulation results also indicate a nearly linear increase of the fly height with the ridge area ratio, but the ridge area ratio has a minor effect on the pitch decrease. The ridged disk surfaces increase the air bearing damping ratios through the enhancement of the viscous shearing across the circumferential ridges. The rates of the effects increase as the disk velocity decreases and ridge height increases. A larger ridge area ratio results in a decrease of the air bearing damping ratios. The slider's vertical and roll motions are more subject to the enhanced transverse viscous shearing generated by the textured disk surfaces than the pitch motion.

The simulated dynamics of tripad slider partial contact air bearings are presented in Chapter 8. In this study, the GW asperity-based contact model is employed to model the slider/disk contact. The effects of radial position, surface roughness, glide height and altitude on the slider's fly height, pitch, contact force, partial contact air bearing

stiffnesses and resonant frequencies are summarized. The contact force increases with altitude and decreases after burnishing. The power spectral density plots of impulse responses indicate that the roll and vertical/pitch motions are decoupled. The spacing and contact force modulations over a “supersmooth” disk are calculated by directly incorporating a measured disk track profile into the simulator. The motions of the slider during track seeking and accessing over a transition between landing and data zones are also simulated for the case of a HTI 850AK type suspension. It is found that the roll and contact force modulations strongly depend on the partial contact air bearing roll stiffness. To evaluate the slider’s crash resistance during actuator’s slam stop, the crash stop impact processes for two deceleration values of 500G and 800G are analyzed. Finally, the slider’s contact take-off dynamics during start-up are numerically examined.

Chapter 9 models the effects of laser bumps and laser textured disk surfaces on Headway AAB slider’s flying characteristics. The passing “Sombrero” type bump generates a larger excitation to slider’s motion than the ridge type bump. Larger size laser bump produces larger amplitude and slower decaying oscillation. The moving laser texture creates moving stippled pressure peaks embedded on smooth pressure profile. These moving pressure peaks increase the slider’s trailing edge fly height and effect a constant magnitude fly height modulation. The effect increases as the bump spacing decreases and the central dome height and rim diameter increase. Flying the outer rail over the smooth data zone, while keeping the inner rail over the textured landing zone, decreases the fly height gain and fly height modulation, but increases the roll loss and roll modulation.

## REFERENCES

Alexander, F. J., Garcia, A. L., and Alder, B. J., 1994, "Direct Simulation Monte Carlo for Thin-film Bearings," *Physics of Fluids*, Vol. 6, No. 12, pp.3854-3860.

Baumgart, P., Krajnovich, D. J., Nguyen, T. A., and Tam, A. C., 1995, "A New Laser Texturing Technique for High Performance Magnetic Disk Drives," *IEEE Transactions on Magnetics*, Vol. 31, pp.2946-2951.

Bolasna, S., 1990, "Air Bearing Parameter Effects on Take-off Velocity," *IEEE Transactions on Magnetics*, Vol. 26, No. 6, pp.3033-3038.

Brandt, A., 1977, "Multi-Level Adaptive Solutions to Boundary-Value Problems," *Mathematics of Computations*, Vol. 31, pp.333-390.

Burgdorfer, A., 1959, "The Influence of the Molecular Mean Free Path on the Performance of Hydrodynamic Gas Lubricated Bearings," *ASME Journal of Basic Engineering*, Vol. 81, pp.94-100.

Castelli, V., and Pirvics, J., 1968, "Review of Numerical Methods in Gas Bearing Film Analysis," *ASME Journal of Lubrication Technology*, Vol.90, pp.777-792.

Cha, E., and Bogy, D. B., 1995, "A Numerical Scheme for Static and Dynamic Simulation of Subambient Pressure Shaped Rail Sliders," *ASME Journal of Tribology*, Vol. 117, pp.36-46.

Chang, W. R., Etsion, I., and Bogy, D. B., 1987, "An Elastic-Plastic Model for the Contact of Rough Surfaces," *ASME Journal of Tribology*, Vol.109, pp.257-263.

Chang, W. R., and Ling, F. F., 1992, "Normal Impact Model of Rough Surfaces," *ASME*

*Journal of Tribology*, Vol.114, pp.439-447.

Christensen, H., and Tonder, K., 1971, "The Hydrodynamic Lubrication of Rough Bearing Surfaces of Finite Width," *ASME Journal of Lubrication Technology*, Vol. 93, pp.324-330.

Crone, R. M., Peck, P. R., Jhon, M. S., Karis, T. E., and Bhushan, B., 1991, "The Flow Factor Approach in Air Bearing Simulation," *ASME Advances in Information Storage Systems*, Vol.4, pp.123-138.

Elrod, H. G., 1973, "Thin-Film Lubrication Theory for Newtonian Fluids with Surface Possessing Striated Roughness or Grooving," *ASME Journal of Lubrication Technology*, Vol.95, pp.484-489.

Elrod, H. G., 1979, "A General Theory for Laminar Lubrication with Reynolds Roughness," *ASME Journal of Lubrication Technology*, Vol.101, pp.8-14.

Fukui, S., and Kaneko, R., 1988, "Analysis of Ultra-Thin Gas Film Lubrication Based on Linearized Boltzmann Equation: First Report-Derivation of a Generalized Lubrication Equation Including Thermal Creep Flow," *ASME Journal of Tribology*, Vol.110, pp.335-341.

Fukui, S., and Kaneko, R., 1990, "A Database for Interpolation of Poiseuille Flow Rates for High Knudsen Number Lubrication Problems," *ASME Journal of Tribology*, Vol.112, pp.78-83.

Gans, R., 1985, "Lubrication Theory at Arbitrary Knudsen Number," *ASME Journal of Tribology*, Vol.107, pp.431-433.

Garcia-Suarez, C., Bogy, D. B., and Talke, F. E., 1984, "Use of an Upwind Finite

Element Scheme for Air Bearing Calculations," *ASLE SP-16*, pp.90-96.

Greenwood, J. A., and Williamson, J. B. P., 1966, "Contact of Nominally Flat Surface," *Proceedings Royal Society (London)*, Series A295, pp.300-319.

Gross, W. A., Matsch, L. A., Castelli, V., Eshel, A., Vohr, J. H., and Wildmann, M., 1980, "*Fluid Film Lubrication*," Wiley, New York.

Harker, J. M., Brede, D. W., Pattison, R. E., Santana, G. R., and Taft, L. G., 1981, "A Quarter Century of Disk File Innovation," *IBM Journal of Research and Development*, Vol.25, No.5, pp.677-689.

Hsia, Y. T., and Domoto, G. A., 1983, "An Experimental Investigation of Molecular Rarefaction Effects in Gas Lubricated Bearings at Ultra-Low Clearances," *ASME Journal of Lubrication Technology*, Vol.105, pp.120-130.

Hu, Y., and Bogy, D. B., 1996, "Dynamics of Tripad Partial Contact Air Bearings," *Technical Report No. 96-001*, Computer Mechanics Laboratory, U. C. Berkeley. Also submitted to *ASME Journal of Tribology*.

Hu, Y., and Bogy, D. B., 1995a, "Spacing Modulation of a Slider Flying Across a Transition Between Landing and Data Zones," *Technical Report No. 95-012*, Computer Mechanics Laboratory, U. C. Berkeley. Also *IEEE Transactions on Magnetics*, to appear.

Hu, Y., and Bogy, D. B., 1995b, "The CML Air Bearing Dynamic Simulator," *Technical Report No. 95-011*, Computer Mechanics Laboratory, U. C. Berkeley.

Hu, Y., and Bogy, D. B., 1995c, "Numerical Study of a Slider's Contact Take-off



Process," *Technical Report No. 95-009*, Computer Mechanics Laboratory, U. C. Berkeley. Also submitted to *ASME Journal of Tribology*.

Hu, Y., and Bogy, D. B., 1995d, "Dynamic Stability and Spacing Modulation of Sub-25nm Sliders," *Technical Report No. 95-004*, Computer Mechanics Laboratory, U. C. Berkeley. Also submitted to *ASME Journal of Tribology*.

Hutchinson, B. R., and Raithby, G. D., 1986, "A Multigrid Method Based on the Additive Correction Strategy," *Numerical Heat Transfer*, Vol. 9, pp.511-537.

Hutchinson, B. R., Galpin, P. F., and G. D. Raithby, 1988, "Application of Additive Correction Multigrid to the Coupled Fluid Flow Equations," *Numerical Heat Transfer*, Vol. 13, pp.133-147.

Jeong, T. G., and Bogy, D. B., 1993, "Numerical Simulation of Dynamic Loading in Hard Disk Drives," *ASME Journal of Tribology*, Vol.115, pp.370-375.

Johnson, K. L., 1985, "*Contact Mechanics*," Cambridge University Press, Cambridge.

Kogure, K., Fukui, S., Mitsuya, Y., and Kaneko, R., 1983, "Design of Negative Pressure Slider for Magnetic Recording Disks," *ASME Journal of Lubrication Technology*, Vol.7, pp.496-502.

Lee, H. J., Hempstead, R. D., and Weiss, J., 1989, "Study of Head and Disk Interface in Contact Start Stop Test," *IEEE Transactions on Magnetics*, Vol. 25, No. 5, pp.2748-2750.

Lu, S., Hu, Y., O'Hara, M., Bogy, D. B., Bhatia, C. S., and Hsia, Y. T., 1996, "Air Bearing Design, Optimization, Stability Analysis and Verification for Sub-25 nm Flying," *IEEE Transactions on Magnetics*, Vol. 32, pp.103-109.

- Makino, T., Morohoshi, S., and Taniguchi, S., 1993, "Application of Average Flow Model to Thin Film Gas Lubrication," *ASME Journal of Tribology*, Vol. 115, pp.185-190.
- Mitsuya, Y., 1984, "A Simulation Method for Hydrodynamic Lubrication of Surfaces with Two-Dimensional Isotropic or Anisotropic Roughness Using Mixed Average Film Thickness," *Bulletin of JSME*, Vol.27, No.231, pp.2036-2044.
- Mitsuya, Y., Ohkubo, T., and Ota, H., 1989, "Averaged Reynolds Equation Extended to Gas Lubrication Possessing Surface Roughness in the Slip Flow Regime: Approximate Method and Confirmation Experiments," *ASME Journal of Tribology*, Vol. 111, pp.495-503.
- Mitsuya, Y., and Hayashi, T., 1990, "Numerical Study of Film Thickness Averaging in Compressible Lubricating Films Incurring Stationary Surface Roughness," *ASME Journal of Tribology*, Vol.112, pp.230-237.
- Miu, D., and Bogy, D. B., 1986a, "Dynamics of Gas-Lubricated Slider Bearings in Magnetic Recording Disk Files: Part I-Experimental Observation," *ASME Journal of Tribology*, Vol.108, pp.584-588.
- Miu, D., and Bogy, D. B., 1986b, "Dynamics of Gas-Lubricated Slider Bearings in Magnetic Recording Disk Files: Part II-Numerical Simulation," *ASME Journal of Tribology*, Vol.108, pp.589-593.
- Ohkubo, T., and Mitsuya, Y., 1991, "An Experimental Investigation of the Moving Roughness Effect on Thin-Film Gas Lubrication for Flying Head Sliders," *ASME Advances in Information Storage Systems*, Vol.2, pp.127-136.
- Patankar, S. V., 1980, " *Numerical Heat Transfer and Fluid Flow*," McGraw-Ridge.

Patankar, S. V., 1981, "A Calculation Procedure for Two-Dimensional Elliptic Situations," *Numerical Heat Transfer*, Vol. 4, pp.409-425.

Patir, N., and Cheng, H. S., 1978, "An Average Flow Model for Determining Effects of Three-Dimensional Roughness on Partial Hydrodynamic Lubrication," *ASME Journal of Lubrication Technology*, Vol.100, pp.12-17.

Patir, N., and Cheng, H. S., 1979, "Application of Average Flow Model to Lubrication Between Rough Sliding Surfaces," *ASME Journal of Lubrication Technology*, Vol.101, pp.220-230.

Ranjan, R., Lambeth, D. N., Tromel, M., Goglia, P., and Li, Y., 1991, "Laser Texturing for Low-Flying-Height Media," *Journal of Applied Physics*, Vol.69, No.8, pp.5745-5747.

Rhow, S. K., and Elrod, H. G., 1974, "The Effects on Bearing Load-Carrying Capacity of Two-Sided Striated Roughness," *ASME Journal of Lubrication Technology*, Vol.96, pp.554-560.

Ruiz, O. J., and Bogy, D. B., 1990a, "A Numerical Simulation of the Head-Disk Assembly in Magnetic Hard Disk: 1. Component Models," *ASME Journal of Tribology*, Vol.112, pp.593-602.

Ruiz, O. J., and Bogy, D. B., 1990b, "A Numerical Simulation of the Head-Disk Assembly in Magnetic Hard Disk: 2. Solution of the Coupled System," *ASME Journal of Tribology*, Vol.112, pp.603-613.

Settari, A., and Aziz, K., 1973, "A Generalization of the Additive Correction Methods for the Iterative Solution of Matrix Equations," *SIAM Journal of Numerical Analysis*, Vol. 10, pp.506-521.

Suk, M., Ishii, T. , and Bogy, D. B., 1992, "The Influence of Air-Bearing Surface Geometry on the Dynamics of Sliders," *ASME Journal of Tribology*, Vol. 114, pp.26-31.

Tanaka, H., and Bogy, D. B., 1994, " Effects of Disk Surface Texture on Slider Flying Characteristics in the Near Contact Interface," *Technical Report No.94-017*, Computer Mechanics Laboratory, U. C. Berkeley.

Tripp, J. H., 1983, "Surface Roughness Effects in Hydrodynamic Lubrication: The Flow Factor Method," *ASME Journal of Lubrication Technology*, Vol.105, pp.458-465.

Vanka, S. P., 1986, "Block Implicit Multigrid Solution of Navier-Stokes Equations in Primitive Variables," *Journal of Computational Physics*, Vol. 65, pp.138-158.

Wallace, R. L., 1951, "The Reproduction of Magnetically recorded Signals," *The Bell System Technical Journal*, Vol.30, pp.1145-1173.

White, J. M., and Nigam, A., 1980, "A Factored Implicit Scheme for the Numerical Solution of the Reynolds Equation at Very Low Spacing," *ASME Journal of Lubrication Technology*, Vol.102, pp.80-85.

White, J. M., 1983, "Flying Characteristics of the "Zero-Load" Slider Bearing," *ASME Journal of Lubrication Technology*, Vol.105, pp.484-490.

Yoneoka, S., Yamada, T., Aruga, K., Ooe, T., and Takahashi, M., 1987, "Fast Take-off Negative Pressure Slider," *IEEE Transactions on Magnetics*, Vol. MAG-23, No.5, pp.3464-3466.

Zhu, L. Y., and Bogy, D. B., 1989a, "A Multi-channel Laser Interferometer and its Use to

Study Head-Disk Interface Dynamics in Magnetic Disk Drives,” *Tribology and Mechanics of Magnetic Storage Systems*, STLE Special Publication, Vol. VI, pp.168-179.

Zhu, L. Y., and Bogy, D. B., 1989b, “Head-Disk Spacing Fluctuation due to Disk Topography in Magnetic Recording Hard Disk Files,” *Tribology and Mechanics of Magnetic Storage Systems*, STLE Special Publication, No. SP-26, pp.160-167.